LUND UNIVERSITY

Probing Atomic Scale Structure and Catalytic Properties of Cobalt Oxide Model Catalysts

Arman, Alif

2016

Probing Atomic Scale Structure and Catalytic Properties of Cobalt Oxide Model Catalysts

MOHAMMAD ALIF ARMAN
DEPARTMENT OF PHYSICS | FACULTY OF SCIENCE | LUND UNIVERSITY

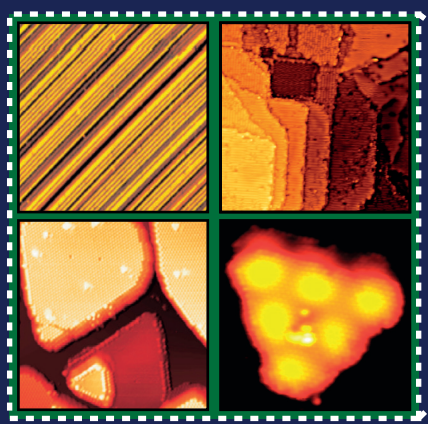

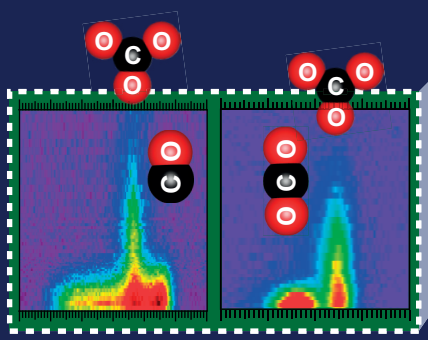

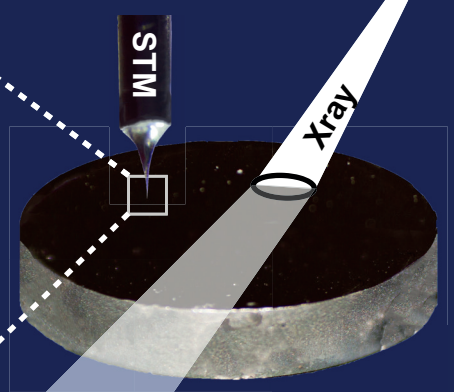

Probing Atomic Scale Structure and Catalytic Properties of Cobalt Oxide Model Catalysts

Mohammad Alif Arman

Division of Synchrotron Radiation Research

LUND UNIVERSITY

DOCTORAL DISSERTATION

by due permission of the Faculty of Science, Lund University, Sweden.

To be defended in the Rydberg Lecture Hall at the Department of Physics.

Friday 27th of January 2017 at 13:00

Dissertation advisors

Dr. Jan Knudsen, Prof. Edvin Lundgren

Faculty opponent

Prof. Herbert Over

Department of Physical Chemistry, Justus Liebig University Giessen

Organization	Document name
LUND UNIVERSITY Division of Synchrotron Radiation Research Department of Physics, BOX 118, S-221 00 Lund	DOCTORAL DISSERTATION
	Date of distribution January 27, 2017
	Sponsoring organization
Author(s): Mohammad Alif Arman	

Title and subtitle: Probing Atomic Scale Structure and Catalytic Properties of Cobalt Oxide Model Catalysts

Abstract

Cobalt oxides are known to be active catalysts for a number of chemical reactions, but very little is known about the atomic scale processes responsible for the activity. The research presented in this thesis is focused on obtaining an atomic scale understanding of the chemistry of well-characterized *cobalt oxide model catalyst surfaces* consisting of pristine and defective CoO and Co_3O_4 thin films with the (111) and (100) terminations supported by Ag(100), Ir(100), and Au(111) single crystal surfaces. The structure and the adsorption properties of probe molecules onto these cobalt oxide model catalyst surfaces are studied under ultra-high vacuum conditions using the interplay of X-ray photoemission spectroscopy (XPS), scanning tunneling microscopy (STM), and low energy electron diffraction (LEED). Further, high pressure XPS (HPXPS) is used to study the stability and phase transitions of the cobalt oxide model catalysts in more realistic gas environments. As a side project to the work on cobalt oxide thin films the thesis gives a comprehensive spectroscopic picture of Ir(100) surface reconstructions and molecular adsorption onto these surfaces.

The adsorption experiments of H_2, CO, CO_2, and H_2O probe molecules give a detailed picture of the surface chemistry of Co oxide surfaces and it is demonstrated that Co ions naturally found on the surface of $Co_3O_4(111)$ and $Co_3O_4(100)$ thin films or artificially created on the CoO(111) surface are extremely important for chemical properties of the surface. Water dissociation, carbonate formation, weak adsorption of CO and CO_2 are examples of processes that only take place in the presence of Co surface ions. The work at more realistic gas pressures in the mbar regime demonstrates that Co oxide thin films should be seen as dynamic films that easily change phase between the CoO and Co_3O_4 structure in response to the gas composition.

To summarize, the work presented in this thesis is important for the fundamental understanding of cobalt oxide surfaces and their catalytic properties, and hopefully, this fundamental understanding can be used to develop new and better cobalt oxide based catalysts.

Key words:catalysis, model systems, $Co_3O_4(111)$, $Co_3O_4(100)$, CoO(111), Ir(100), Ag(100), X-ray photoelectron spectroscopy, Scanning tunneling microscopy, High pressure X-ray photoelectron spectroscopy, Low energy electron diffraction, H_2, O_2, CO_2, CO, H_2O, H_{rad}

Classification system and/or index terms (if any)

Supplementary bibliographical information		Language: English
ISSN and key title		ISBN 978-91-7753-140-1 (print) 978-91-7753-141-8 (pdf)
Recipient's notes	Number of pages 203	Price
	Security classification	

Distribution by Division of Synchrotron Radiation Research, Department of Physics, P.O. Box 118, S-221 00 Lund, Sweden

Signature  Date 2017-12-12

Probing Atomic Scale Structure and Catalytic Properties of Cobalt Oxide Model Catalysts

Mohammad Alif Arman

LUND UNIVERSITY

DOCTORAL DISSERTATION

Division of Synchrotron Radiation Research
Department of Physics, Lund University, Sweden.

Front cover:

Temperature programmed X-ray photoelectron spectroscopy used to identify adsorbed molecules on the $Co_3O_4(111)$ surface and scanning tunneling microscopy images of some of the surfaces I worked with:

Top left: Hydrogen on the Ir(100)-(5×1)-hex surface acquired by Pascal Ferstl.

Bottom left: The $Co_3O_4(111)$ surface grown on Ir(100) surface acquired by Pascal Ferstl.

Top right: $Co_3O_4(100)$ and CoO(100) phases grown Ag(100)

Bottom right: $CoO_2(111)$ nano islands grown on Au(111) acquired by Alex S. Walton and Jakob Fester.

Doctoral Thesis
Division of Synchrotron Radiation Research
Department of Physics, Lund University, Sweden

ISBN 978-91-7753-140-1 (print)
ISBN 978-91-7753-141-8 (pdf)

Printed in Sweden by Media-Tryck, Lund University
Lund 2017

I would like to dedicate this thesis to
my beautiful wife,
my loving mom and dad.

"No one undertakes research in physics with the intention of winning a prize.
It is the joy of discovering something no one knew before."
-Stephen Hawking

Abstract

Cobalt oxides are known to be active catalysts for a number of chemical reactions, but very little is known about the atomic scale processes responsible for the activity. The research presented in this thesis is focused on obtaining an atomic scale understanding of the chemistry of well-characterized *cobalt oxide model catalyst surfaces* consisting of pristine and defective CoO and Co_3O_4 thin films with the (111) and (100) terminations supported by Ag(100), Ir(100), and Au(111) single crystal surfaces. The structure and the adsorption properties of probe molecules onto these cobalt oxide model catalyst surfaces are studied under ultra-high vacuum conditions using the interplay of X-ray photoemission spectroscopy (XPS), scanning tunneling microscopy (STM), and low energy electron diffraction (LEED). Further, high pressure XPS (HPXPS) is used to study the stability and phase transitions of the cobalt oxide model catalysts in more realistic gas environments. As a side project to the work on cobalt oxide thin films the thesis gives a comprehensive spectroscopic picture of Ir(100) surface reconstructions and molecular adsorption onto these surfaces.

The adsorption experiments of H_2, CO, CO_2, and H_2O probe molecules give a detailed picture of the surface chemistry of Co oxide surfaces and it is demonstrated that Co ions naturally found on the surface of Co_3O_4(111) and Co_3O_4(100) thin films or artificially created on the CoO(111) surface are extremely important for chemical properties of the surface. Water dissociation, carbonate formation, weak adsorption of CO and CO_2 are examples of processes that only take place in the presence of Co surface ions. The work at more realistic gas pressures in the mbar regime demonstrates that Co oxide thin films should be seen as dynamic films that easily change phase between the CoO and Co_3O_4 structure in response to the gas composition.

To summarize, the work presented in this thesis is important for the fundamental understanding of cobalt oxide surfaces and their catalytic properties, and hopefully, this fundamental understanding can be used to develop new and better cobalt oxide based catalysts.

Popular Summary

Catalysts are used to produce a large fraction of the materials we use in our modern society. A very famous example is the highly efficient catalysts that are used to fix nitrogen from the air into artificial fertilizer salts. Without this catalytic process, it is difficult to imagine that we could feed the current population of earth. Artificial fertilizers are, however, not the only product that uses a catalyst for its production. In fact, almost all products produced in the chemical industry such as plastic materials, paints, coating materials, gasoline, drugs, etc. use catalysts for their production. Catalysts are also used extensively for cleaning of exhaust gas from power plants, trucks, and cars. As an example, the catalyst in a car convert carbon monoxide gas (CO) to non-toxic carbon dioxide (CO_2). Unfortunately, the catalyst in the car is built partly from very expensive metals such as platinum and palladium.

As discussed above catalysts are used extensively both for the production of modern materials and for reducing the amount of toxic chemicals we release into our environment. Most of the catalyst materials we use today have been found by trial and error methods and knowledge of why and how the chemical process take place on the catalyst material is therefore often very limited or missing fully.

The goal of the present work has been to improve our understanding of chemical processes taking place on cobalt oxide based catalysts. Instead of studying real and complex cobalt oxide catalyst materials we have studied thin and highly idealized cobalt oxide films. Using these highly idealized *model systems* of the real catalysts we studied chemical processes at the atomic scale level. One important take home message of the studies is that single cobalt atoms found on the surface are essential for the function of the catalysts surface and in particular for how it interact with gas molecules.

Hopefully, the present fundamental work on cobalt oxide catalysts can be used to develop new and better catalysts of this material. Furthermore, the work adds knowledge to our general understanding of metal oxide films and their catalytic applications.

Preface

In July 2012 I started my PhD study in the area of surface science and catalysis. The purpose of this project was to link catalytic activity directly to specific atomic scale sites of surfaces. In more detail, my project aims at measuring the catalytic properties of extremely well-defined model systems consisting of thin conductive cobalt oxide films grown on single crystal surfaces. These model systems mimic the metal oxide films that often are formed on real catalysts at reaction conditions. Synchrotron-based X-ray photoemission spectroscopy (XPS) and high pressure XPS (HPXPS) have been used as central techniques in my studies. A large part of the experimental XPS work has been performed at MAX-lab. Moreover, scanning tunneling microscopy (STM) and low energy electron diffraction (LEED) have been used for structural characterization.

The present thesis gives a complete picture of my studies of the surface structure of cobalt oxide based thin films and their chemistry. In addition, I also spent quite some time on characterizing the chemistry of graphene grown on Ir(111), and platinum supported iron oxide films. The results from the graphene and iron oxide project are, however, not included in this thesis.

The results from the cobalt oxide project are summarized in the following papers, which are included in the second part of the thesis.

List of publications

List of papers included in this thesis

I. Adsorption of hydrogen on stable and metastable Ir(100) surfaces
M. A. Arman, A. Klein, P. Ferstl, A.Valookaran, J. Gustafson, K. Schulte, E. Lundgren, K. Heinz, A. Schneider, F. Mittendorfer, L. Hammer, J. Knudsen
Surf. Sci. 2017, 656, 66. http://dx.doi.org/10.1016/j.susc.2016.10.002
I participated in planning and performing the experiments. I acquired the photoelectron spectroscopy data, analyzed the data, and was main responsible for writing the manuscript.

II. Adsorption and activation of CO on Co_3O_4(111) thin films

P. Ferstl, S. Mehl, **M. A. Arman**, M. Schuler, A. Toghan, B. Laszlo, Y. Lykhach, O. Brummel, E. Lundgren, J. Knudsen, L. Hammer, M.A. Schneider, J. Libuda

J. Phys. Chem. C, 2015, 119, 16688 http://dx.doi.org/10.1021/acs.jpcc.5b04145

I participated in planning and performing the experiments. I acquired the photoelectron spectroscopy data, analyzed the data, and took part in the discussion and writing of the manuscript.

III. Adsorption properties of CO and CO_2 onto CoO(111) and Co_3O_4(111) films studied with core level spectroscopy

M. A. Arman, P. Ferstl, M. A. Schneider, L. Hammer, E. Lundgren and J. Knudsen

In Manuscript

I participated in planning and performing the experiments. I acquired the photoelectron spectroscopy measurements, analyzed the data and wrote the manuscript.

IV. Water and hydrogen radical adsorption onto CoO(111) and Co_3O_4(111) surfaces studied by photoemission spectroscopy

M. A. Arman, P. Ferstl, M. A. Schneider, L. Hammer, E. Lundgren, and J. Knudsen

In Manuscript

I participated in planning and performing the experiments. I acquired the photoelectron spectroscopy measurements, analyzed the data and wrote the manuscript.

V. Co_3O_4(100) films grown on Ag(100): Structure and chemical properties

M. A. Arman, L. R. Merte, E. Lundgren, and J. Knudsen

Accepted for publication in Surface Science http://dx.doi.org/10.1016/j.susc.2016.11.011

I planned the experiment, was main responsible for the scanning tunneling microscopy measurements, the photoelectron spectroscopy measurements, analyzed the data, and wrote the manuscript.

VI. Transformation between Co_3O_4 and CoO phases under reaction conditions
M. A. Arman, L. R. Merte, E. Lundgren, and J. Knudsen
In Manuscript
I planned the experiment, was main responsible for the scanning tunneling microscopy measurements, photoelectron spectroscopy measurements, analyzed the data, and wrote the manuscript.

VII. Interface Controlled Oxidation States in Layered Cobalt Oxide Nano-Islands on Gold
A. S. Walton, J. Fester, **M. A. Arman**, J. Osiecki, J. Knudsen, and J. V. Lauritsen
ACS Nano, 2015, 9, 2445 http://dx.doi.org/10.1021/acsnano.5b00158
I was heavily involved in the photoelectron spectroscopy measurements and I participated in the discussions regarding the results.

List of papers I have contributed to and are not included in this thesis

1. The low and high coverage adsorption structure of CO on unreconstructed Ir(100)-(1×1)
M. A. Arman, E. Lundgren, and J. Knudsen
In Preperation

2. Adsorption structure of oxygen on metastable Ir(100) surface
P. Ferstl, **M. A. Arman,** E. Lundgren, A. Schneider, F. Mittendorfer, L. Hammer, and J. Knudsen
In Preperation

3. Ultra-thin stepped iron oxide films grown on high index Pt surfaces - a new catalytic model system
E. Grånäs, N. Johansson, **M. A. Arman,** J. Osiecki, K. Schulte, J. N. Andersen, J. Schnadt, and J. Knudsen
In Manuscript

4. The SPECIES beamline at the MAX IV Laboratory: a facility for soft x-ray RIXS and APXPS
S. Urpelainen, C. Såthe, W. Grizolli, M. Agåker, A. R. Head, M. Andersson, S.-W. Huang, B. N. Jensen, E. Wallen, H. Tarawneh, R. Sankari, R. Nyholm, M. Lindberg, P. Sjöblom, N. Johansson, B. N. Reinecke, **M. A. Arman**, L. R. Merte, J. Knudsen, J. Schnadt, J. N. Andersen, and F. Hennies
J. Synchrotron Radiat. 24 (2017) https://doi.org/10.1107/S1600577516019056.

5. Oxygen intercalation under graphene on Ir(111): energetics, kinetics and the role of graphene edges
E. Grånäs, J. Knudsen, U. A. Schröder, T. Gerber, C. Busse, **M. A. Arman,** K. Thånell, J. N. Andersen, and T. Michely
ACS nano, 2012, 11, 9951 http://dx.doi.org/10.1021/nn303548z

6. CO Intercalation of Graphene on Ir(111) in the Millibar Regime
E. Grånäs, M. Andersen, **M. A. Arman**, T. Gerber, J. Schnadt, J. N. Andersen, T. Michely, and J. Knudsen
J. Phys. Chem. C, 2013, 117, 16438 http://dx.doi.org/10.1021/jp4043045

7. Dissociative Adsorption of Hydrogen on PdO(101) Studied by HRCLS and DFT
N. M. Martin, M. V. Bossche, H. Grönbeck, C. Hakanoglu, J. Gustafson, S. Blomberg, **M. A. Arman**, A. Antony, R. Rai, A. Asthagiri, J. F. Weaver, and E. Lundgren,
J. Phys. Chem. C, 2013, 117, https://doi.org/13510 10.1021/jp4036698

8. Comment on Interfacial Carbon Nanoplatelet Formation by Ion Irradiation of Graphene on Iridium(111)
C. Herbig, E. H. Åhlgren, U. A. Schröder, A. J. Martinez-Galera, **M. A. Arman**, W. Jolie, J. Kotakoski, J. Knudsen, A. V. Krasheninnikov, and T. Michely
ACS Nano, 2015, 9, 4664 https://doi.org/10.1021/acsnano.5b02303

9. Xe Irradiation of Graphene on Ir(111): From Trapping to Blistering
C. Herbig, E. H. Åhlgren, U. A. Schröder, A. J. Martinez-Galera, **M. A. Arman**, J. Kotakoski, J. Knudsen, A. V. Krasheninnikov, and T. Michely
Phys. Rev. B, 2015, 92, 08529 https://doi.org/10.1103/PhysRevB.92.085429

10. Adsorption and Reaction of CO and NO on Ir(111) under Near Ambient Pressure Conditions
K. Ueda, K. Suzuki, R. Toyoshima, Y. Monya, M. Yoshida, K. Isegawa, K. Amemiya, K. Mase, B. S. Mun, **M. A. Arman**, E. Grånäs, J. Knudsen, J. Schnadt, H. Kondoh,
Topics in catalysis, 2016, 59, 487 http://dx.doi.org/10.1007/s11244-015-0523-5

11. Etching of Graphene on Ir(111) with Molecular Oxygen
U. Schröder, E. Grånäs, T. Gerber, **M. A. Arman**, K. Schulte, J. N. Andersen, J. Knudsen, and T. Michely
Carbon, 2016, 96, 320 http://dx.doi.org/10.1016/j.carbon.2015.09.063

12. Core level shifts of intercalated graphene
U. A. Schröder, M. Petrovic, T. Gerber, A. J. Martinez-Galera, E. Grånäs, **M. A. Arman**, C. Herbig, J. Schnadt, M. Kralj, J. Knudsen, and T. Michely
2D Mater. 2017, 4, 015013 http://dx.doi.org/10.1088/2053-1583/4/1/015013

13. Symmetry Driven Band Gap Engineering in Hydrogen Functionalized Graphene
J. Jørgensen, A. G. Čabo, R. Balog, L. Kyhl, M. Groves, A. Cassidy, M. Bianchi, M. Dendzik, **M. A. Arman**, L. Lammich, J. I. Pascual, J. Knudsen, B. Hammer, P. Hofmann, L. Hornekær
Accepted ACS Nano, http://dx.doi.org/10.1021/acsnano.6b04671

14. Water chemistry beneath graphene: formation and trapping of a super-dense OH-H_2O phase
E. Grånäs, U. A. Schröder, **M. A. Arman,** M. Andersen, T. Gerber, K. Schulte, J. N. Andersen, B. Hammer, T. Michely, and J. Knudsen
In manuscript

15. From permeation to cluster arrays: graphene on Ir(111) exposed to carbon vapor
C. Herbig, T. Knispel, S. Simon, U. A. Schröder, A. J. Martinez-Galera, **M. A. Arman,**
C. Teichert, J. Knudsen, A. V. Krasheninnikov, and T. Michely
In manuscript

16. Exciting molecules for graphene functionalization
L. Kyhl, R. Bisson, R. Balog, M. Groves, E. L. Kolsbjerg, A. Cassidy, J. Jørgensen,
S. Halkjær, J. Miwa, A. G. Čabo, T.Angot, P. Hofmann, **M. A. Arman**, S. Urpelainen,
H. Bluhm, J. Knudsen, B. Hammer, L. Hornekær
In manuscript

List of acronyms

AFM	Atomic force microscopy
BE	Binding energy
CCD	Charge-Coupled Device
CHA	Concentric hemispherical analyzer
CLS	Core level shift
DFT	Density functional theory
ESCA	Electron spectroscopy for chemical analysis
HPXPS	High pressure X-ray photoelectron spectroscopy
HRXPS	High resolution X-ray photoelectron spectroscopy
KE	Kinetic energy
L	Langmuir
LEED	Low energy electron diffraction
LDOS	Local density of states
MCP	Microchannel plate detector
ML	Monolayer
MLE	Monolayer equivalent
ORR	Oxygen reduction reaction
OER	Oxygen evolution reaction
PROX	Preferential oxidation
PEEM	Photoemission electron microscopy
STM	Scanning tunneling microscopy
SXRD	Surface X-ray diffraction
TPXPS	Temperature programmed X-ray photoelectron spectroscopy
UHV	Ultra-high vacuum
XPS	X-ray photoelectron spectroscopy
XAS	X-ray absorption spectroscopy

Acknowledgements

Many people have contributed to this thesis directly or indirectly and here I would like to acknowledge them. First of all, my acknowledgment goes to my supervisors Jan Knudsen and Edvin Lundgren for giving me the chance to work with their groups. Having an engineering background before joining as a PhD student in the division of synchrotron radiation research my knowledge about surface science and synchrotron facilities were limited. I want to thank my main supervisor Jan Knudsen from my heart especially for teaching me the essential knowledge on theory and different research techniques, which were essential for me to complete my PhD Furthermore, I would like to express my gratitude to you for giving me enough time to discuss the solutions for the numerous challenges and problems that occurred during the project. I am grateful to you for all the feedback you have given during the writing of articles and the thesis. Thank you for always giving me confidence throughout my work and for your active supervision.
I want to thank my co-supervisor Edvin Lundgren for all of your help and advice during these years, in particular for all your constructive comments on my thesis and articles. I would also like to thank you for organizing the kick-off meetings in excellent locations.

Furthermore, I want to thank all my colleagues at the division of synchrotron radiation research and for making it an enjoyable working place. Especial thanks to Joachim Schnadt for your moral advices and motivation. Lindsay Merte thank you for giving the constructive comments on my articles and also for the scientific consultations. Niclas Johansson for the scientific discussions, Igor macros, and for the conversations, we had during the coffee breaks. Elin Grånäs thanks for introducing me to the fascinating world of graphene and help in the STM lab. I remember the days we (me, Elin, and Niclas) worked together in the STM and beam times on the FeO project. Payam Shayesteh you are really a humble office mate and thanks a lot for sharing the scientific and of course for the non-scientific issues. I am also thankful to Chu Zhang, Shabnam Oghbaiee, Jovanna Colvin, Ashley R. Head, Tripta Kamra, Olesia Snezhkova, Andreas Schaefer, Lisa Rullik, Foteinie Ravani, Bart Oostenrijk, Shilpi Chaudhary, and Andrea Troian for their friendly company. Thanks to Anders Mikkelsen and Rainer Timm for discussing the STM. Thanks to Johan Gustafson for the computer and software related help, and Patrik Wirgin for the advice and our funny discussions.

I am conveying my appreciation to the MAX-lab people: Karina Thånell, Balasubramanian Thiagarajan, Jacek Osiecki, and Karsten Handrup for their help during beam times.

I am grateful to all the people I have collaborated with. In particular, Lutz Hammer, Alexander Schneider, and Pascal Ferstl from Friedrich-Alexander-Universität, Erlangen-Nürnberg, are acknowledged for their help during beam times, for providing STM images, and for their help with manuscripts. I would also like to thank Thomas Michely, Ulrike Schröder, Antonio Martínez-Galera, and Charlotte Herbig from the University of Cologne. I have enjoyed the collaboration with you for the graphene project. Finally, I would like to thank Alex S. Walton, Jakob Fester, and Andrew Cassidy, University of Aarhus for their collaboration on cobalt oxide and graphene projects.

I311 and I511 beamline, you are now gone, and new beamlines are now constructed with new names at the MAX IV laboratory, but I will always remember you for providing outstanding results. Obelix, I have used you for my research and baked you many times. Thanks a lot for giving me many atomically resolved images.

I would also like to thank my friends, Maruf, Chisty, Mehdy, Amit, Deep, Sadek, Saikat, and Zuel for your inspiration and support.

I am cordially thankful to the Bangladeshi community in Lund. You people have filled my life with enjoyments by arranging the countless amount of parties. Special thanks to the “Badminton Masters” and “Lund Summer Cricket” groups for organizing the sports I always prefer to play. I must say that I have enjoyed all of your presence and it was impossible to play these games without your active participation.

Finally, I want to acknowledge my family: Mom, Dad, and siblings from my heart. Mom (Ammu) and Dad (Abbu) thank you a lot for your unconditional love and blessings. I will be forever indebted to you and it is impossible to express my gratefulness in words. Grandma (Dadi and

Nani), thanks for your love and prayers. My greeting goes to my brother-in-law (Mobin) for his good advice.

I also want to acknowledge my in-law's family members for their endless love, blessings, and inspiration. My further acknowledgment goes to Sakhawat vi, Moni apa, and Ruma apa for their incredible supports. I am greatly indebted to you for all you have done for me.

Finally, I am eternally grateful to my beloved wife, Israt Jahan for her infinite patience by staying alone at home when I was at conferences and had night shifts in MAX-lab. My PhD would not be possible without her unlimited supports and encouragements.

Contents

Introduction

In the modern world, almost all the products we use in our daily life are produced with the help of catalysts. For example, catalysts are used to produce drugs in the pharmaceutical industry, in the refinement of crude oil into gasoline, to produce plastics and fertilizers, for the cleaning of water, and to produce many other chemicals. The use of catalysts are also important for the reduction of environmental pollution [1]. One prominent example is here the three-way catalyst that performs three tasks simultaneously, (i) Reduction of nitrogen oxides (NO_x) to nitrogen (N_2) and oxygen (O_2), (ii) Oxidation of carbon monoxide (CO) to carbon dioxide (CO_2), and (iii) Oxidation of unburnt hydrocarbons (HC) to carbon dioxide (CO_2) and water (H_2O).
One of the most important catalytic processes is the ammonia (NH_3) synthesis used to produce fertilizers. In nature, ammonia is generated from nitrogen (N_2) in the soil from bacterial processes, but ammonia can also be formed from the decomposition of organic matters from plants, animals, and animal dung. Before the 20^{th} century, animal dung and other organic waste were the only way farmers could fertilize their crop field, and it is difficult to imagine that the limited amount of ammonia given to the crop fields by these methods would be enough to feed billions of people. However, Fritz Haber invented the artificial process of ammonia synthesis in 1909 and the process was further developed by Carl Bosch. Using an iron based catalysts and high pressures of hydrogen and nitrogen it became possible to synthesize ammonia from nitrogen in the air. Fritz Haber was awarded the Nobel Prize in 1918 for the invention of ammonia synthesis and later in 1931, Carl Bosch was awarded the Nobel Prize for transforming this process into industrial scale production.

The term *catalyst* was coined by Swedish chemist Jöns Jacob Berzelius in 1835 [2]. Later, in 1900 the German chemist Friedrich Wilhelm Ostwald proposed a definition for a catalyst: "*A catalyst is a substance, which affects the rate of a chemical reaction without being part of its end products*" [3]. Later in 1909 Ostwald was awarded the Nobel Prize for his contributions to catalysis.

In brief, a catalyst helps to produce the desired product by stimulating the chemical process. As an example, hydrogen can be produced from steam (H_2O) and methane (CH_4) using a nickel based catalyst:

$$CH_4 + H_2O \xrightarrow{Ni} CO + 3H_2$$

Catalysts can be classified into two categories: homogeneous and heterogeneous catalysts. The homogeneous catalysts denote the cases where there only is one phase involved in the catalytic reaction. As an example, carboxylic acid treated with an alcohol under the presence of sulfuric acid as a catalyst produce the corresponding ester. Here, the Sulfuric acid, as well as the carboxylic acid and alcohol are in the (same) liquid phase.

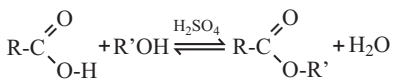

In contrast, the catalyst and the reactants are in different phases in a heterogeneous catalytic reaction. As an example, we can think of a platinum catalyst used to oxidize carbon monoxide (CO) to carbon dioxide (CO_2). In this case, the platinum catalyst is in the solid phase, while the reactants (O_2 and CO) are in gas phase. In this case, the reaction takes place at the surface of the platinum.

$$2CO + O_2 \xrightarrow{Pt} 2CO_2$$

The reaction mechanisms of catalytic processes are complex. However, the general principles are well-established. Different types of reaction mechanisms are illustrated in figure 1. Figure 1(a) shows the Langmuir-Hinshelwood mechanism for the CO oxidation on a metal surface. In the first step of this reaction, CO and O_2 adsorb onto the catalyst surface. Afterward, the adsorbed O_2 molecules dissociate into individual O atoms. The CO molecules and O atoms start to diffuse on the surface, and once a CO molecule and O atom meet each other, they recombine and form CO_2. In the last step, CO_2 desorbs into the gas phase. The Eley-Rideal mechanism is shown in figure 1(b). Here one of the reactant molecules adsorbs first onto the catalyst surface and the reaction takes place when another reactant molecule hits it from the gas phase. Finally, the Mars-van Krevelen mechanism is shown in figure 1(c). Here gas phase molecules react with the oxidized surface. As an example, we can think of CO oxidation on a trilayer FeO_2 film grown on Pt(111).

In this process, CO reacts with the topmost oxygen lattices and leaves the surface by forming CO_2. This reaction reduced the FeO_2 surface to FeO. Subsequent, oxidation by O_2 recover the FeO_2 surface and the catalytic cycle is closed [4].

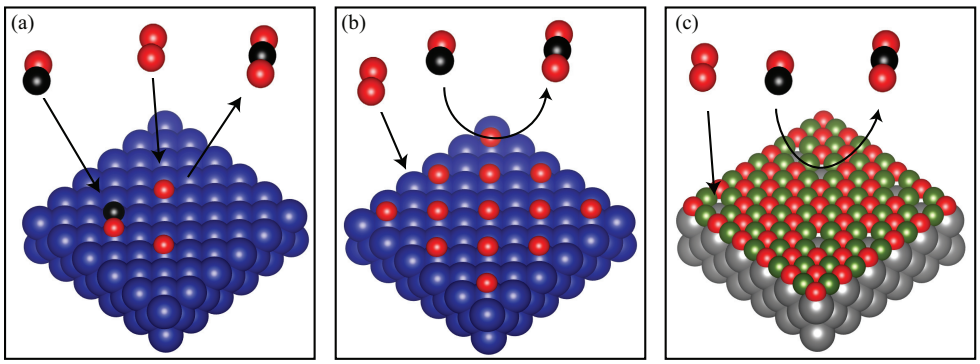

Figure 1: Illustration of (a) Langmuir-Hinshelwood mechanism, (b) Eley-Rideal mechanism, and (c) Mars-Van Krevelen mechanisms. As an example, of the reaction of CO with O_2 to form CO_2 is used. In (a) and (b) the blue spheres correspond to the catalyst atoms. (c) shows a metal oxide film grown on top of a substrate (gray atoms). The green spheres correspond to metal atoms. The red and black spheres in (a, b, and c) correspond to oxygen and carbon atoms, respectively.

The goal of the research work presented in this thesis is to obtain a profound atomic scale understanding of cobalt oxide based catalysts. Cobalt oxide nanomaterials are good candidates for low-cost heterogeneous catalyst [5, 6, 7] for many applications such as energy-related materials [8], and electrocatalysis [9, 10]. Cobalt oxide nanomaterials can also be used for some specific applications, for example, the low temperature CO oxidation [5, 11, 12, 13], selective oxidation of CO (PROX reaction) [14], for hydrocarbon oxidation [15], and for both the oxygen reduction reaction (ORR) and the oxygen evolution reaction (OER) in electrocatalysis [16, 17].

The surface science approach to catalysis and single crystal surfaces as model catalysts

Most of the catalysts we know today have been designed and developed by *trial and error*. For the design of better catalysts for future generations, it is essential to obtain an atomic scale understanding of catalysts and the chemical process taking place on them. Consequently, a significant amount of research is currently focused on this.

Many of the real catalysts we use today contain late transition metal nanoparticles dispersed on a suitable oxide support to maximize the surface area, as shown in figure 2(a). Using such supported catalysts particles decrease the amount of active and expensive transition metals. Atomic scale characterization of real and complex catalyst surface under working conditions, is, unfortunately, difficult. Therefore, we often mimick the structure of the complex catalyst systems by a simpler *model system.* Such model systems can be single crystal surfaces of metals of the same metal as the active nanoparticles in the real catalyst. The surfaces of these model systems can now be characterized with standard surface science techniques. It is, for example, possible to study how the reactants and products bind to the model system surface at ultra-high vacuum (UHV) conditions. The surface science approach to catalysis was recognized by awarding the Nobel Prize in chemistry in 2007 to Gerhard Ertl for his ground-breaking surface science studies of catalysts [18].

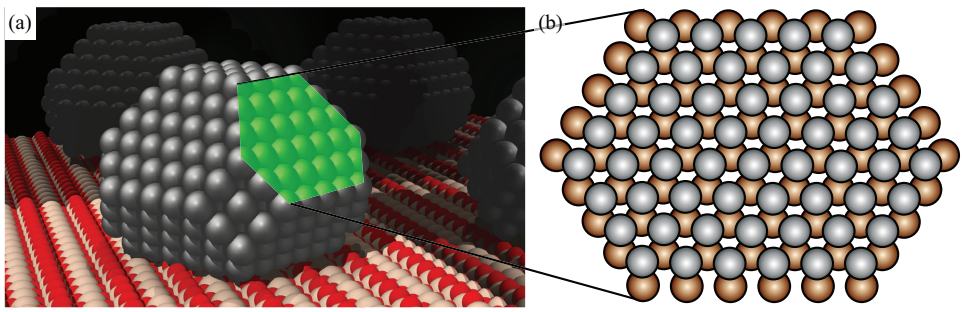

Figure 2: (a) Ball model of nano particles supported by an oxide surface. The image is taken from ref. [19]. (b) Ball model of a single crystal surface used as model system for one of the surface terminations of the nano particle.

A broad range of surface sensitive techniques that can be used to characterize a surface exists today. X-ray photoelectron spectroscopy (XPS), X-ray absorption spectroscopy (XAS), and infrared spectroscopy (IRAS) can be used to probe the atoms of the surface and the molecules adsorbed, while temperature programmed desorption (TPD) yields information about how strong an adsorbate is bound. The local atomic scale structure can be studied with scanning tunneling microscopy (STM) and atomic force microscopy (AFM). The surface periodicity can be found using low energy electron diffraction (LEED) and surface X-ray diffraction (SXRD). Theoretically, density functional theory (DFT) calculation can be used to calculate the energy of surface structures, diffusion barriers, reaction barriers, and adsorption energies.

Although some studies have reported a good agreement between UHV measurements and real catalytic environments [20, 21, 22] UHV studies often fail to mimic the activity found in a real catalytic process [23, 24]. New surface structures might form at high pressure condition [25] giving rise to a so-called *pressure gap*. To study the model catalyst at high-pressure conditions closer to the real conditions used for industrial catalysts, surface science techniques have been developed such as high-pressure scanning tunneling microscopy (HPSTM) [26], high pressure X-ray photoelectron spectroscopy (HPXPS) [27], and surface X-ray diffraction (SXRD) [28].

Thin metal oxide films as model systems

Metal oxide surfaces are used both as support material of active catalyst particles and as the active catalyst material itself. Unfortunately, they are difficult to study with electron based surface science techniques (XPS, STM, LEED) because of their low conductivity. To overcome this problem thin oxide films grown on metal surfaces can be used instead. These thin oxide films should ideally be thick enough to mimic the metal oxide of the real oxide, but thin and thereby conductive enough to allow electron based techniques to be used. Such thin metal oxide films are often produced by depositing and oxidizing a metal on a single crystal surface. Examples are oxide films of titanium [29], manganese [30], iron [31], and cobalt [32] that can be grown on noble metal surfaces with a variety of different structures.

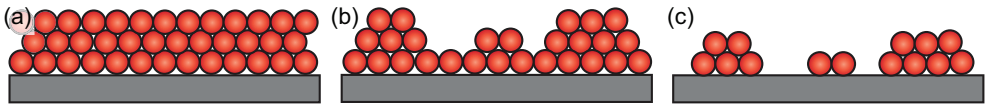

Figure 3: Illustration of (a) Frank-van-der Merwe, (b) Stranski-Krastanov, and (c) Vollmer-weber. The image is modified from ref. [33]

The growth of thin films on a substrate often follow one of the following growth modes: (a) Frank-van-der Merwe, (b) Stranski-Krastanov, and (c) Vollmer-weber growth mode as illustrated in figure 3. In the Frank-van-der Merwe growth mode, the film grows layer by layer. In contrast 3D islands form after the completion of the first layer in Stranski-Krastanov growth mode, as shown in figure 3(b). The growth of cobalt oxide films follows the Stranski-Krastanov growth mode [34,35]. In contrast to thin film growth, separate islands are formed in the Vollmer-weber growth mode, and the film does not cover the entire surface (see figure 3(c)).

Gas surface interaction

To understand a catalytic reaction on the surface of a solid catalyst the gas surface interaction need to be studied [36]. This includes the study of gas adsorption, dissociation, diffusion, and desorption.

Figure 4 shows a simplified illustration of the potential energy curves of the gas adsorption process proposed by Lennard-Jones [37]. Gas adsorption can be classified into two different categories depending on the strength of the adsorbate-surface interaction: (i) If the adsorbate is bound to the surface by weak Van der Waals bonds we refer to the adsorption process as physisorption, and (ii) if real chemical bonds are formed between the adsorbate and the surface we refer to the adsorption process as chemisorption [38]. In the physisorption process, the adsorbates are trapped at a certain distance from the surface, and no valence electrons are exchanged with the surface. In contrast, exchange of valence electrons occurs between the surface and adsorbate for the chemisorption process.

Depending on the nature of the surface, molecular adsorption can occur, or the molecules spontaneously dissociate upon adsorption. For example, H_2 molecules dissociate into hydrogen atoms onto the surface of Ir(100) substrate [39] while CO adsorbs molecularly [25].

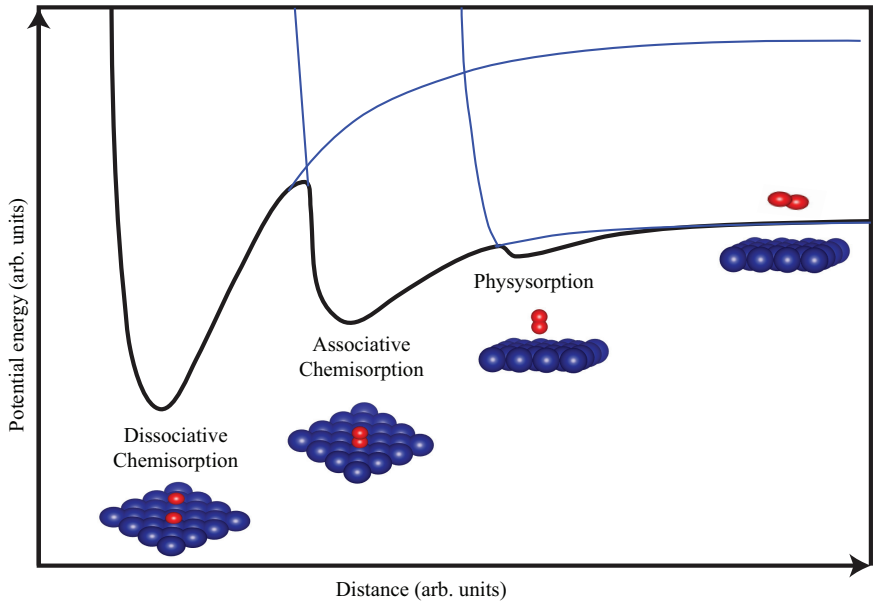

Figure 4: Simplified illustration of the potential energy curves of gas adsorption process proposed by Lennard-Jones.

Chapter 1

Surface structures

Solid materials consist of grains with randomly oriented crystal lattices. The surface of such a complex material is challenging to study with standard surface science techniques since it has many different surface facets and grain boundaries. Instead, single crystal surfaces can be used as simplified model systems.

1.1 Crystal structures and surfaces

In a perfect single crystal, the atoms are positioned in one crystal lattice. The smallest repeating unit of the lattice is called the unit cell. Most metals adopt one of the three different cubic Bravais lattices: simple cubic (sc), body-centered cubic (bcc), and face-centered cubic (fcc). The unit cell of the fcc lattice is shown in figure 5.

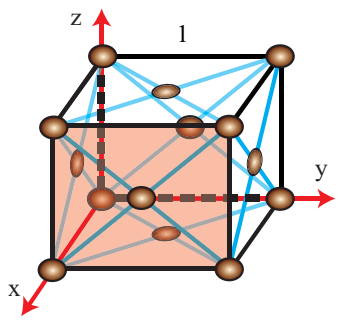

Figure 5: Face centered cubic lattice with the (100) plane highlighted with transparent red color.

The atomic orientation of a surface plane can be specified by using the so-called Miller indices (hkl), where h, k, and l are integers. The Miler indices of a particular plane are determined in two

steps. First, the interception points of the plane and the x, y, and z axis are determined. As an example, the plane highlighted with transparent red in figure 5 intercepts only at the x-axis at 1. Secondly, the reciprocal values of the interception points of this particular plane are determined. Thus, the Miller indices of the transparent red plane in figure 5 is:

$\frac{1}{1}, \frac{1}{\infty}, \frac{1}{\infty} = (100)$

1.2 Wood notation

Atoms or molecules often create ordered overlayer structures when adsorbed on solid surfaces. The Wood notation is used to characterize a given overlayer structure. If the unit cell vectors of a substrate surface are given with $\overrightarrow{a_1}$, $\overrightarrow{a_2}$ and the unit cell vectors of the over layer structure with $\overrightarrow{b_1}$, $\overrightarrow{b_2}$ (see figure 6(a)) the Wood notation becomes:

$$\left(\frac{\left|\overrightarrow{b_1}\right|}{\left|\overrightarrow{a_1}\right|} \times \frac{\left|\overrightarrow{b_2}\right|}{\left|\overrightarrow{a_2}\right|}\right) \tag{1}$$

If the unit cell of the overlayer structure is primitive, “p” is added in front of equation (1), while an adsorbate in the center leads to the prefix “c”. Moreover, if the unit cell vectors of the adsorbates are rotated with respect to the unit cell vectors of the substrate surface then “Rθ" is added, at the end of equation (1).

The use of the Wood notation requires that the angle between $\overrightarrow{a_1}$ and $\overrightarrow{a_2}$ is identical to the angle between $\overrightarrow{b_1}$ and $\overrightarrow{b_2}$. However, the Wood notation only gives the symmetry of a certain structure *i.e.* the number of adsorbed atoms and their adsorption site is not given by the Wood notation.

The surface structure of a clean and CO covered Ir(100)-(1×1) surface is shown in figure 6(b) and (c), respectively. The unit cell for the clean Ir(100)-(1×1) surface is marked with a black square. Adsorbed CO forms a primitive p$\left(\sqrt{2} \times \sqrt{2}\right)R45^{o}$ unit cell (marked with purple). However, the structure of the adsorbed CO can also be denoted as c(2×2) unit cell (marked with white dotted).

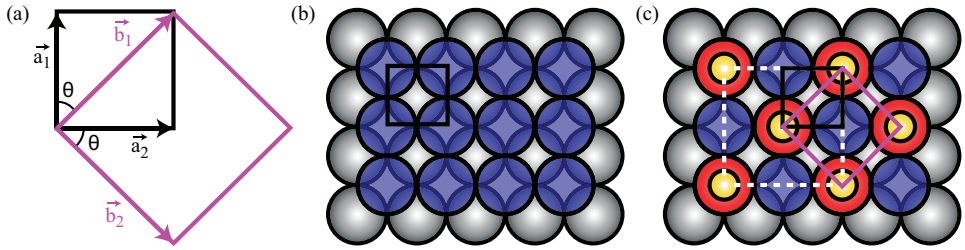

Figure 6: (a) $\overrightarrow{a_1}$ and $\overrightarrow{a_2}$ are the unit cell vectors of the substrate surface while $\overrightarrow{b_1}$ and $\overrightarrow{b_2}$ are the unit cell vectors of the over layer structure. (b) Surface structure of clean Ir(100)-(1×1) and (c) with a CO overlayer structure. The gray, blue, red, and yellow spheres correspond to iridium bulk, iridium surface, iridium surface atoms bonded with CO, and CO molecules, respectively.

1.3 Surface reconstruction

Atoms in a single crystal surface often displace or rearrange from the bulk lattice positions. These displacements and rearrangements are driven by the energy gain originating from the increased coordination of surface atoms to the substrate to compensate for the missing neighbors towards the vacuum side [40]. Two types of surface rearrangements may occur (i) both in and out of plane relaxation, and (ii) surface reconstruction. No change in the periodicity of the surface structure occurs due to surface relaxations since the surface atoms just are displaced a little with respect to the bulk lattice positions. In contrast, surface reconstructions lead to a change in the periodicity of the surface structure and a new surface unit cell will form, as atoms are added or removed from the surface layer. As an example, the Ir(100) surface can be prepared both in a metastable Ir(100)-p(1×1) phase (figure 7(a)) or in a reconstructed Ir(100)-(5×1)-hex phase (figure 7(b)) [41].

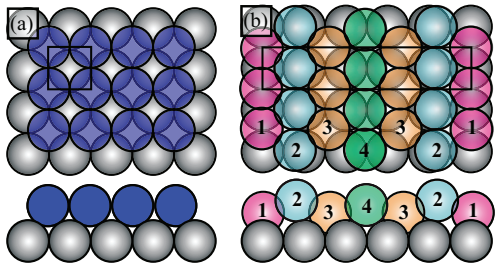

Figure 7: (a) The Ir(100)-(1×1) phase with no surface reconstruction and (b) the Ir(100)-(5×1)-hex formed upon surface reconstruction. The gray and blue spheres of Ir(100)-(1×1) structure correspond to iridium bulk, and iridium surface atoms, respectively. The different color code of the Ir(100)-(5×1)-hex surface atoms relates to their height difference and position with respect to the bulk atoms. The image is modified from ref. [41].

Chapter 2

Experimental methods

Determining the chemical structures and processes occurring on a catalyst surfaces using electron based surface science techniques is a challenging task and require special experimental setups. This chapter discusses the working principles of the following techniques: X-ray photoelectron spectroscopy (XPS), high pressure XPS (HPXPS), scanning tunneling microscopy (STM), and low energy electron diffraction (LEED).

2.1 X-ray photoelectron spectroscopy (XPS)

2.1.1 Generation of X-ray light

In 1895 Wilhelm Conrad Röntgen discovered X-rays and later in 1901 he was awarded the Nobel Prize. One way to produce X-rays is to bombard a metal target with a high-energy beam of electrons. This method is used extensively in laboratory based X-ray sources. Often such sources use Mg or Al targets (anodes) giving photon energies of 1253.6 eV (Mg K_α) and 1486.6 eV (Al K_α).

Laboratory based X-ray sources are small and rather inexpensive. In contrast, synchrotron radiation facilities are much more expensive to build and operate. However, there are numerous benefits of using synchrotron radiation: (i) the photon energy is tunable, (ii) much high intensity and brilliance of the light, (iii) smaller spot size, (iv) polarization control, (v) ultraclean source with zero degassing, and (vi) a time-structured source.

In synchrotron radiation facilities, electrons circulate in an electron storage ring. The electrons circulate near the speed of light in vacuum and are kept in their orbit by a series of bending magnets separated by straight sections. In the bending magnets, the electrons are deflected, and X-rays are emitted (figure 8(a)). The X-ray spectrum generated from bending magnets is continuous and

photons with an energy between a few eV to several keV are produced simultaneously. Higher intensity for selected photon energies can be achieved by using different insertion devices such as wiggler and undulator in the straight sections. In the case of an undulator, it contains a periodic array of alternating magnets (figure 8(b)). Electron bunches pass through the trajectory of the undulator, and constructive interference of photons created at different locations along the undulator can occur. The energy spectrum of an undulator has a series of sharp peaks (harmonics) and the photon energy position for these harmonics can be tuned by changing the gap between the magnetic arrays. As an example, the energy spectrum from the undulator used at the I311 beamline is shown in figure 8(c) and the energy shifts of undulator peaks for different (color coded) gap values are visible.

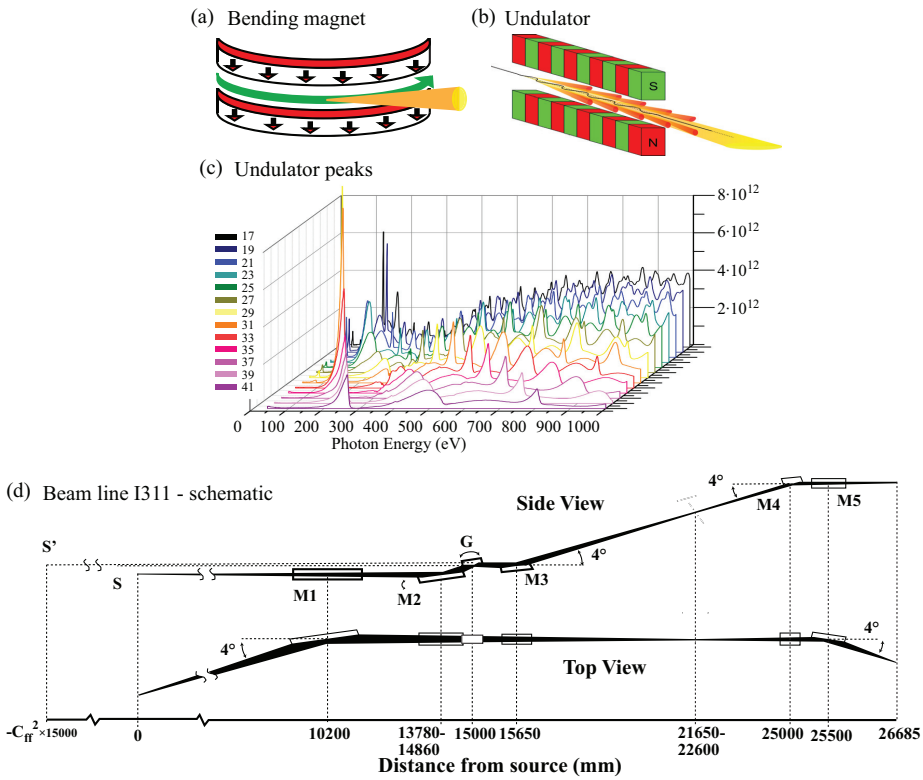

Figure 8: Illustration of (a) bending magnet, (b) an undulator [42], (c) undulator spectrum from the I311 beamline [43], and (d) optical layout of the I311 beamline [44].

The optical layout of the I311 beamline used to obtain a large fraction of the results in this thesis is shown in figure 8(d). This beamline is described in more detail elsewhere [44]. The light produced in the undulator is focused onto the sample position by a set of mirrors (M1-M5). Further a grating (G) is used to select a particular photon energy, while an exit slit is used both to control the energy resolution and the intensity of the light. The energy resolution of the photon from the monochromator (ΔE_{MONO}) depends on the photon energy, the size of the exit slit, the C_{ff} value, and the line density of the grating. For example, the typical energy resolution is ~200 meV for an O 1s spectrum measured with 625 eV photon energy and a 60 µm slit size.

2.1.2 The electron analyzer

When the sample is irradiated with photons photoelectrons are created. A fraction of the ejected photoelectrons are captured by the electron analyzer and their kinetic energies are measured. The analyzer used at the I311 beam line at MAX-lab, was a concentric hemispherical analyzer (CHA) as shown in figure 9. It consists of two hemispherical electrodes. A potential difference is applied between the two electrodes, and a spherical symmetric E-field is created. Since the outer hemisphere is biased negatively with respect to the inner one, the E-field will point away from the inner hemisphere. Only electrons with a kinetic energy equal to the pass energy ($E_p \pm \Delta E_p$), determined by the potential difference between the hemispheres, will follow the trajectory through the gap to reach the detector. Electrons with too high or too low energy will hit the outer or inner hemisphere, respectively, and be lost.

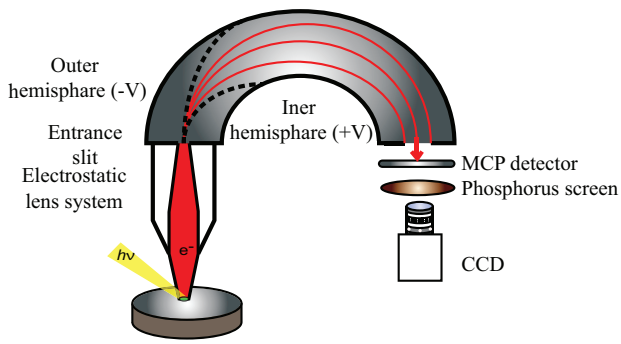

Figure 9: Schematic drawing of the hemispherical electron energy analyzer (see the text for details).

In the detector, the signal is multiplied in the microchannel plate detector (MCP), which consists of a 2D array of channels where each impinging photoelectron is multiplied via secondary emission before reaching the phosphorous screen. The light emitted from the phosphorous screen is recorded by a CCD camera. By keeping the pass energy constant and by varying the acceleration or deceleration voltages, photoelectrons with different kinetic energies can be scanned through the detector window and a plot of the intensity of photoelectrons as a function of their kinetic energy can be obtained. The energy resolution of the electron analyzer (ΔE_{ANA}) is determined by the pass energy E_p, the size of the entrance slit s, and the mean radius of the hemisphere R:

$$\Delta E_{\mathrm{ANA}} = \frac{E_p \cdot s}{2R} \tag{2}$$

The size of R for the I311 analyzer is 200 mm. As an example, for 50 eV of pass energy (E_p), and with an 800 μm slit size the energy resolution of the analyzer used in I311 beamline will be 100 meV [45]. However, increasing the resolution is inversely proportional to the signal intensity and, therefore, a balance between resolution and intensity needs to be chosen during the experiments to achieve the optimum result.

The total energy resolution ΔE will be the sum of the contributions from the energy resolution of photons (ΔE_{MONO}) and energy resolution of the electron analyzer (ΔE_{ANA}):

$$\Delta \mathrm{E} = \sqrt{(\Delta E_{MONO})^2 + (\Delta E_{ANA})^2} \tag{3}$$

2.1.3 Photoemission process

X-ray Photoelectron Spectroscopy (XPS) can be used to study the chemical composition of surfaces. This technique is based on the photoelectric effect, first discovered by Heinrich Hertz in 1887 [46] and later explained theoretically by Albert Einstein [47]. Einstein was awarded the Nobel Prize in 1921 "*for the explanation of the law of photoelectric effect*". For the discoveries and research in the field of X-ray spectroscopy, Manne Siegbahn was awarded the Nobel Prize in Physics in 1925. Later in the 50's Kai Sigbahn (son of Manne Siegbahn) and his collaborators developed the XPS technique, and in 1981 he was awarded the Nobel Prize "*for his contribution to the development of high-resolution electron spectroscopy*" [48].

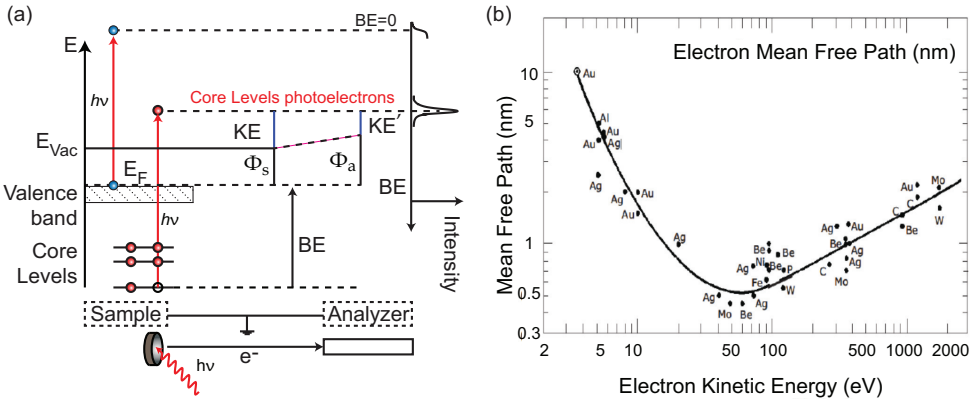

Figure 10: (a) A schematic illustration of core level photoemission process (b) The universal curve for the electron mean free path in solid materials as a function of the kinetic energy of the electrons taken from ref. [49].

Figure 10(a) shows the energy levels in a solid and the electron energy distribution produced by a photon with energy $h\nu$. The sample and the analyzer are in electrical contact and, therefore, their Fermi levels will be aligned. Photoemission spectra are formed by plotting the number of collected photoelectrons as a function of their binding energy. Only the core electrons are localized to specific atoms and therefore their binding energies are element specific. Hence, it is relatively simple to determine the composition of a solid material with XPS. To highlight this, another popular acronym for the technique is ESCA (electron spectroscopy for chemical analysis). As an example oxygen atoms have an O 1s core level with a binding energy around 530 eV while carbon atoms have a C 1s core level with a binding energy around 284 eV.

X-rays can penetrate rather deep into solid materials. In contrast, detected photoelectrons with low kinetic energies originate from the few topmost atomic layers due to the short inelastic mean free path (IMFP) of electrons in solid materials (see figure 10(b)). For this reason, XPS (and all other electron based techniques) is very surface sensitive. As seen from figure 10(b) the shortest IMFP corresponding to maximum surface sensitivity is found for a kinetic energy of the electrons of 50-100 eV. Therefore, we always chose the photon energy such that the kinetic energy of the photoelectrons is between 50-100 eV to achieve maximum surface sensitivity. As an example, the Ir 4f spectra measured with 120 eV photon energy have 60 eV kinetic energy (KE).

2.1.4 Binding energy calculations

The photoemission process is often described with a three-step model. During the first step, a photon is absorbed, and a photoelectron is created. In the second step, this photoelectron travels to the surface. In the last step, the photoelectron is ejected into the vacuum. An energy diagram corresponding to an XPS experiment is shown in figure 10(a). A core electron is excited into the vacuum level by a photon with sufficient energy. The electron is ejected with a kinetic energy into vacuum and an electron analyzer is used to determine its kinetic energy. In other words, the kinetic energy of the photoelectron can be analyzed correctly only when a fixed (well defined) photon energy is used. However, the binding energy (BE) of the core level from which the electron originates is desired rather than the kinetic energy.

The binding energy (BE) of the photoelectrons can be calculated using energy conservation:

$$BE = h\nu - KE - \Phi s \tag{4}$$

Here Φ_s is the work function of the sample and $h\nu$ is the energy of the photon. Since the analyzer also has a work function (Φ_a), the measured kinetic energy (KE′) with respect to the sample vacuum level is different from the kinetic energy (KE) of the photoelectron by Φa - Φs. The measured kinetic energy will be:

$$KE' = h\nu - BE - \Phi s - (\Phi a - \Phi s) = h\nu - BE - \Phi a \tag{5}$$

To exclude the work function Φ_a of the analyzer, a calibration procedure is mandatory to determine the true binding energy of the photoelectrons. As photoelectrons emitted directly from the Fermi level have zero binding energy by definition ($BE = 0$) their kinetic energy will be:

$$KE'' = h\nu - \Phi a \tag{6}$$

By substituting equation (6) into (5) we get:

$$BE = KE' - KE'' \quad (7)$$

From equation (7) it is evident that the difference in the measured kinetic energy of the Fermi level (KE'') and a core level (KE') is equal to the binding energy of the core level (BE).

In the present thesis, the energy of the XP spectra is calibrated by measuring the Fermi level of the sample after each XP spectrum. For the thin cobalt oxide film, there are no states at the Fermi level. Therefore, the XP spectra were calibrated to the known Ir $4f_{7/2}$ or Ag $3d_{5/2}$ binding energies instead for the thin cobalt oxide films.

An overview spectrum from the Ir(111) surface recorded using 1000 eV photon energy is shown in figure 11. The photoelectrons with zero binding energy (BE=0) has the highest kinetic energy are emitted from the Fermi edge (green spectrum in figure 11) while photoelectrons originating from core levels have a lower kinetic energy corresponding to a higher binding energy.
The filling of the core hole created due to the photoemission process happens by an electron from a higher energy level. The energy from this process can be released through fluorescence decay or by sending out a so-called Auger electron. The fluorescence decay is used in X-ray fluorescence spectroscopy, and the Auger electron is used in Auger spectroscopy. The Auger peak can overlap with XPS peaks which can complicate the curve deconvolution process. However, as Auger electrons have fixed kinetic energy, it is possible to shift Auger peaks out of a binding energy window by changing the photon energy.
The tail of photoelectrons towards lower kinetic energy is due to inelastically scattered electrons that often are named *secondary electrons*. These secondary electrons originate from the near surface region but they are not useful for core level spectroscopy, and this is also the main reason that the kinetic energy of the photoelectrons usually is kept above 50 eV in XPS experiments. They are however used for photoemission electron microscopy (PEEM) imaging since imaging requires a very large number of photoelectrons.

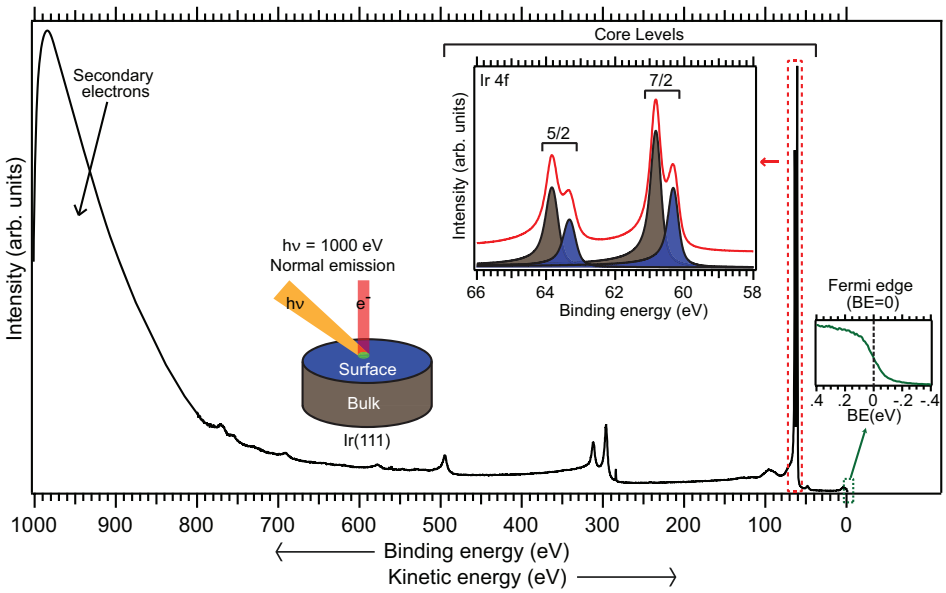

Figure 11: XPS spectrum from an Ir(111) surface measured with 1000 eV photon energy. High resolution Fermi edge and the Ir 4f core level spectra are shown as insets in the figure.

2.1.5 Photoemission Cross Section

The photoemission cross section is defined as the electron transition probability per unit time for exciting a single atom from an initial state $\Psi_i(N)$ to a final state $\Psi_f(N)$ of a system containing N electrons [50, 51]. Fermi's golden rule together with the electric dipole approximation is used to describe the electron transition probability from the initial state to the final state, which is:

$$T_{i\to f} \propto \frac{2\pi}{\hbar}|\langle\Psi_f(N)|D|\Psi_i(N)\rangle|^2\delta(E_f(N-1)+KE-E_i(N)-h\nu) \tag{8}$$

Here D is the dipole operator while the δ function ensures the energy conservation. In a photoemission spectroscopy experiment, partial cross-sections are needed referring to the transition probability from a specific atomic level. In contrast, the total cross-sections are the sum of all possible electron transitions at a chosen photon energy.

Photoionization cross sections for different elements are tabulated. See for example reference [52]. As an example, the cross section for Ir 4f, C 1s, and O 1s are plotted in figure 12.

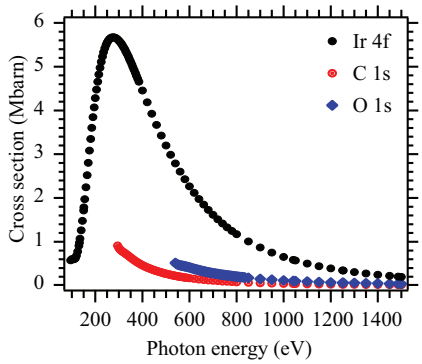

Figure 12: The cross section for Ir 4f, C 1s, and O 1s levels. Plotted based on data in [52, 53].

The tabulated cross-section can be used to optimize the intensity of a particular core level by choosing the photon energy with the highest cross-section.

XPS Approximations

The photoemission process excites one electron to a certain kinetic energy *KE*. The initial state wave function $\Psi i(N)$ will be the product of the wave function of the single emitted electron from any particular orbital ($\Phi_{i,k}$) and the remaining electrons wave function $\Psi_i^k\ (N-1)$ before emission. Similarly, the final state wave function is the product of the wave function of the single emitted electron ($\Phi_{f,k}$) and the remaining electrons wave function $\Psi_f^k\ (N-1)$ after emission. The transition matrix for "one electron approximation" is:

$$\langle \Psi_f(N)|D|\Psi_i(N)\rangle = \langle \Phi_{f,k}|D|\Phi_{i,k}\rangle\langle \Psi_f(N-1)|\Psi_i(N-1)\rangle \quad (9)$$

The emission of an electron from its electronic states to the continuum forms an electron-hole in the orbital from which the electron was emitted. However, according to the *frozen orbital approximation,* the remaining electrons are not affected by the photoemission process. Therefore,

there are no changes in the wave functions of the remaining electrons. The transition matrix element will depend on one-electron wave functions only. The binding energy of the emitted electron is then obtained from the Hartree-Fock orbital energies from which the photoelectron was emitted (see equation (10). This binding energy is called the Koopmans binding energy:

$$BE(k) = \varepsilon k \tag{10}$$

Here k denotes the orbital from which the photoelectron was emitted.

However, the orbitals cannot be frozen after the photoemission process. To minimize the total energy, the remaining electrons in the orbitals readjust themselves. Therefore, the final state wave functions of the remaining electrons are changed. For that reason, the additional final state contributions such as relaxation and correlation effects need to be considered (see equation (11)).

$$BE(k) = \varepsilon k + E_{relaxation} + E_{correlation} \tag{11}$$

In the case of core-level photoelectron spectroscopy, the photoemission process takes place immediately. Therefore, the valence electrons have no time to respond to the created core hole potential. In this case, the “Sudden Approximation” (see equation (12)) allows multiple excited final states with the same core hole [50]. After the photoemission process, the wave function of the remaining (N-1) electrons can be described as a combination of eigenstates, with the corresponding eigenvalues. In other words, the final state has excited states with $\Psi_{f,s}\,(N-1)$ wave functions. The transition matrix element will include a sum over overlap integrals for all possible final states.

$$\langle \Psi_f(N) | D | \Psi_i(N) \rangle = \langle \Phi_{f,k} | D | \Phi_{i,k} \rangle \Sigma_s \langle \Psi_{f,s}(N-1) | \Psi_i(N-1) \rangle \tag{12}$$

The “Sudden Approximation" also explains the appearance of the satellite features at the higher binding energy side in the photoemission spectra. The satellite features are the excitations of electrons from occupied level to unoccupied valence levels resulting in kinetic energy losses. An example of such satellite peaks is shown in figure 13.

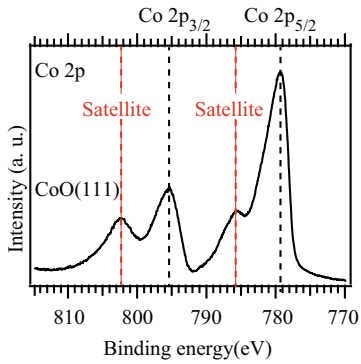

Figure 13: The Co 2p region from CoO(111) grown on Ir(100). The satellites features can be observed in addition to the Co $2p_{3/2}$, and Co $2p_{5/2}$ main peaks.

2.1.6 Line shape decomposition and curve fitting

The core level photoemission spectra consist of the sharp peak (main peak) with some additional features. The instrumental limitations, the core hole lifetime, and vibrational broadening are mainly responsible for the broadening of photoemission line shapes. The core hole lifetime has a Lorentzian distribution and can be explained by Heisenberg's uncertainty principle $\Delta E \times \Delta t \geq \frac{\hbar}{2}$. The lifetime of the excited state is approximately an energy level specific property and due to this, the Lorentzian width does not differ significantly due to the chemical environment of the atom [54]. The instrumental broadening is caused by the energy width of the X-ray source determined by the size of the exit slit and electron analyzer resolution determined by the pass energy and the entrance slit. Typical values for monochromator and analyzer resolutions are 0.05 eV and 0.02 eV, respectively. The experimental broadening are characterized by a Gaussian distribution [55]. The vibrational broadening is also characterized by a Gaussian distribution.

Typically, for metals, the XPS peaks appears asymmetric due to the spectral background. The elastic photoelectrons generate the main line, and the inelastic photoelectrons (secondary electrons) [56] create the background signal (inelastic tail) at the higher binding energy side. Excitation of the core electron leads to the creation of electron-hole pairs at the Fermi level, excitations of plasmons, and other quantized secondary excitations [57] are also responsible for

the creation of the tail on the high binding energy side. Therefore, background subtraction is an important part of XPS analysis. Different background subtraction can be used for this task, such as Shirley, linear, or polynomial backgrounds. Figure 14 shows the Ir 4f, C 1s, and O 1s spectra before (a, b, and c) and after subtraction of a polynomial background (d, e, and f).

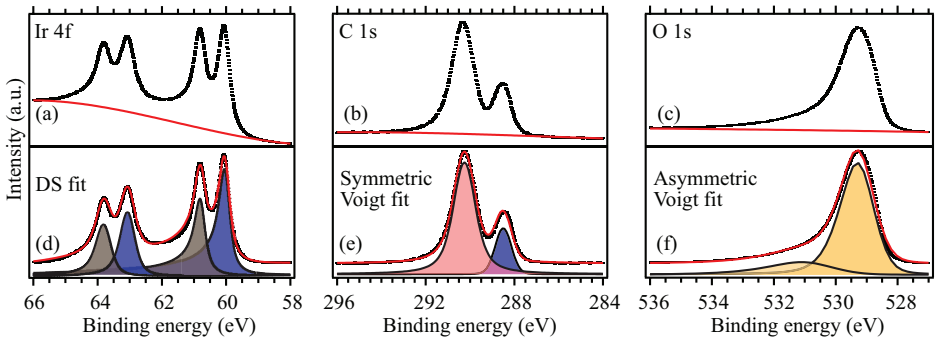

Figure 14: (a, b, and c) Ir 4f, C 1s, and O 1s raw spectra and (d, e, and f) deconvoluted spectra after subtracting a polynomial background. The experimental spectra are shown as black dotted lines while the filled components correspond to different components.

Often each spectrum contains a number of overlapping peaks. These overlapping peaks are usually de-convoluted by fitting the spectrum with a function consisting of different components. The de-convolution determines then the binding energy (BE), area, and width of each component. Several different functions can be used for the components. Doniach-Šunjić (DS) line shapes are often used to fit asymmetric components originating from a metal surface:

$$Y(E) = \frac{\Gamma(1-\propto)}{(\varepsilon^2+\gamma^2)^{\frac{(1-\propto)}{2}}} \cos\left[\frac{\pi \propto}{2} + (1-\propto)\arctan\left(\frac{\varepsilon}{\gamma}\right)\right] \tag{13}$$

Here Γ is the gamma function, and γ is the lifetime broadening of the Lorentzian distribution ($\gamma = 2 \cdot \mathrm{LFWHM}$) [57]. ε is the binding energy of the photoelectrons and α is the asymmetry parameter. Finally, each DS component is convoluted with a Gaussian function to include the experimental broadening. As an example, the Ir 4f XP spectrum is deconvoluted with 4 DS components, shown in figure 14(d). The blue and gray components correspond to the iridium surface and bulk components of Ir $4f_{5/2}$ and Ir $4f_{7/2}$.

Another deconvolution function that often is used is a Voigt function which is a convolution of a Gaussian and a Lorentzian curve shape [58]. Figure 14(b) shows a C 1s raw spectrum after dosing CO_2 onto Co_3O_4(111) with two distinct components. A symmetric line shape of each component is observed after subtracting the polynomial background as shown in figure 14(e). Therefore, we have used a symmetric Voigt function to fit the two components, corresponding to adsorbed CO_3 (blue) and CO_2 (red) species.

However, an asymmetric Voigt function can also be used to fit an asymmetric line shape after removing the background. An asymmetric Voigt function is modeled by combining two half Voigt functions with different widths at their peak point. The asymmetric line shape of the O 1s spectrum of the pristine CoO(111) surface shown in figure 14(c) is fitted with two different components asymmetric Voight functions (see figure 14(f).

2.1.7 Core level shifts

The binding energy of a core electron depends on its chemical environment - *i, e*. the binding energy of a core electron in an atom is sensitive to the chemical surroundings of that atom. The change in binding energy is often referred as "*core level shifts* (CLS)" or "*chemical shift*", and, therefore, the CLS can be used as a fingerprint of the existence of different chemical species on the surface. For example, the surface peak of the Ir 4f core level of Ir atoms in the Ir(100) surface layer is shifted due to the adsorbed oxygen atom as shown in figure 15. The figure compares the Ir $4f_{7/2}$ spectrum before and after dosing O_2 on a clean Ir(100)-(1×1) surface. Upon adsorption of O_2 the Ir surface (Ir_S) component disappears, and a new component develops at higher binding energy. The higher binding energy peak corresponds to the Ir bound to one oxygen atom. The core level shifts are also related to the charge on an atom and in general core level shifts will be higher for positively charged atoms.

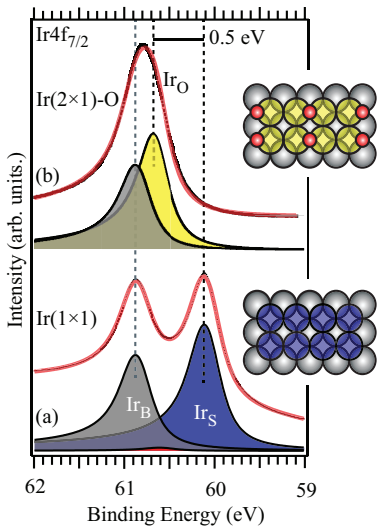

Figure 15: Ir $4f_{7/2}$ of Ir(100)-(1×1) without (a) and with (b) adsorbed oxygen. The gray, blue, yellow, and red spheres correspond to Ir_B, Ir_S, Ir_O, and oxygen atoms.

2.2 Temperature programmed XPS

In temperature programmed XPS (TPXPS) the sample is heated while the evolution of the photoemission spectra is recorded simultaneously. Later, an “all at once” fitting procedure can be used to determine the evolution of the different chemical species and the desorption temperature of the different species signaled by different components can be determined.

As an example, after dosing CO_2 onto $Co_3O_4(111)$, we observed two distinct peaks in the C 1s spectrum as shown in figure 16(a). In order to assign these components, the C 1s region was measured while heating the sample from 85 K to 500 K at a heating rate of 20 K/min. Figure 16(b) shows a 2D image plot of the spectral evolution during the temperature ramp. Figure 16(c) shows the temperature evolution of the intensity of the two components shown in (a) obtained from simultaneous curve fitting the data shown in (b). The intensity of the component at 288.5 eV disappears at 400 K. Due to the binding energy position and the high thermal stability, this feature is assigned to a surface carbonate species. In contrast, the component located at 290.3 eV is fully

removed at around 190 K. Therefore, this feature is assigned to the weakly adsorbed CO_2 on the surface (see Paper III for details).

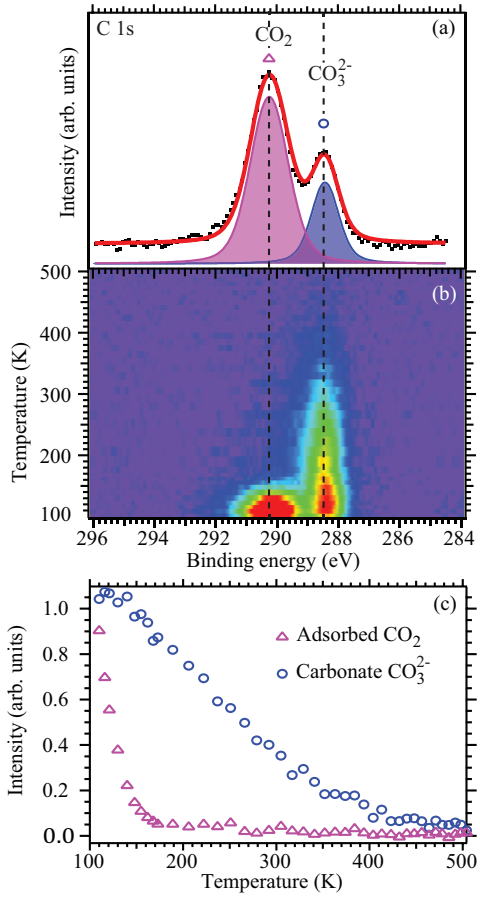

Figure 16: (a) C 1s spectrum acquired after dosing 110 L CO_2 at 85 K onto Co_3O_4(111)/Ir(100). The experimental spectrum is shown with black dots, the fit as a semi-transparent solid red line, and the filled curves represent the components of the fit. (b) 2D image plot showing spectral evolution of the C 1s region during the temperature ramp. (c) Temperature evolution of the intensity of the two components shown in (a) obtained from simultaneous curve fitting the data shown in (b).

2.3 High pressure X-ray photoelectron spectroscopy (HPXPS)

Gas adsorption studies at UHV conditions are essential for a fundamental understanding of gas adsorption, dissociation, and reactions taking place on metal surfaces and surface oxides. Unfortunately, the measurements obtained under UHV conditions cannot always be used to mimic the same processes at real catalytic condition [23]. The surface structure of the metal or oxide surface might have changed in response to the high pressure condition. For this reasons, there can be a significant difference in measuring the catalytic properties of a catalyst at high pressure conditions compared to UHV conditions. This so-called *pressure gap* can, however, partially be overcome by studying the model surfaces with novel high pressure techniques such as high pressure X-ray photoelectron spectroscopy (HPXPS).

The HPXPS experimental setup is designed by considering the low IMFP of photoelectrons in gas as well as the inability of the analyzer to work in high pressure. The IMFP of electrons in gas can be calculated by the combination of the kinetic gas theory with the approximation of a Maxwell-Boltzmann distribution, which gives:

$$\lambda = \frac{k_B T}{\sqrt{2}\pi p d^2} \tag{14}$$

Here k_B is Boltzmann constant, T is the temperature, p is the pressure, and d is the radius of the atom/molecule. The IMFP at good vacuum conditions (10^{-3} to 10^{-7}mbar) is 10 cm to 1 km. In contrast, the IMFP at 10 to 10^{-3} mbar is 0.1 mm to 100 mm and it is, therefore, important to reduce the pressure quickly in the HPXPS setup. This is normally done with a series of differential pumping stages. A schematic illustration of the HPXPS endstation at the SPECIES beamline is shown in figure 17. This setup has the ability to operate both in UHV and at high pressure conditions. The high pressure experiments are performed in a separate high pressure cell, which can be docked to the differentially pumped analyzer [59].

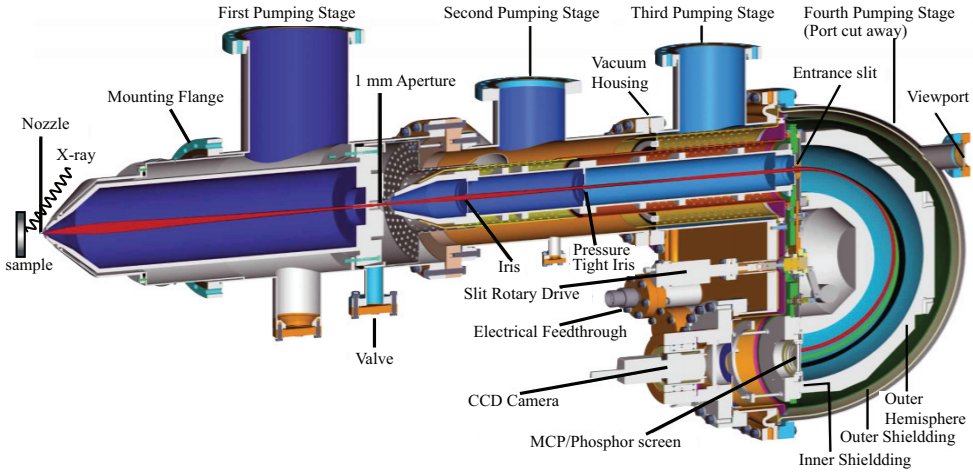

Figure 17: Illustration of the HPXPS setup used at the SPECIES beamline. The image is taken from ref. [60].

The photoelectrons leave the HP cell through a small aperture nozzle (0.3 - 1mm opening) see figure 17. Some amount of gas from the HP cell will also flow through the nozzle, but due to the differential pumps the pressure will be reduce from the mbar regime (HP cell) to $\sim 5 \cdot 10^{-8}$ mbar (at the analyzer). Additionally, the use of electrostatic lenses refocuses the photoelectrons onto the different apertures and hence, the transmission increases. A mass spectrometer is used to record the gas composition of the exhaust gas from the HP cell.

The binding energy of the gas phase peaks are calibrated to the vacuum level of the gas. However, the vacuum level of the gas phase molecules will change with respect to the distance from the sample work function. Therefore, the apparent BE of the gas phase peaks will shift accordingly with the change of the sample work function.

2.4 X-Ray absorption spectroscopy (XAS)

Excitation of a core level electrons are carried out for both X-ray absorption spectroscopy (XAS) and XPS. The main difference between the two techniques is that while the electrons are excited into the vacuum level in XPS, they are excited to the unoccupied states of the sample in XAS. In a typical XAS experiment, the photon energy is scanned across the absorption edge of a core level of an element and the absorption into different unoccupied levels is then measured. Therefore, XAS mainly probes the unoccupied states.

Rather than measuring the absorption signal directly it is much easier to measure a signal related to the filling of the core hole left after the absorption process. This can be carried out in two different ways: Fluorescence decay mode or Auger decay mode. In my work, I exclusively used Auger decay mode as this can be measured directly with the tunable synchrotron light and an electron energy analyzer. In the Auger decay mode, the filling of the core hole is achieved by a valence electron. The energy from this process is used to excite another electron into the vacuum by the Auger process. The number of Auger electrons is then proportional to the number of excited electrons and therefore also proportional to the absorption signal. A schematic illustration of the XAS process in Auger decay mode is shown in figure 18(a).

In the XAS measurement, a kinetic energy window around the kinetic energy of the expected Auger peak is selected, and the intensity of this Auger process is then measured as a function of the photon energy around the absorption edge. In the work discussed in this thesis, the Co 2p (L3) XAS spectra of CoO(111) and Co_3O_4(111) (shown in figure 18(b)) were recorded by varying the photon energy from 775 to 785 eV in Auger decay mode by choosing a fixed Auger peak at 650 eV kinetic energy.

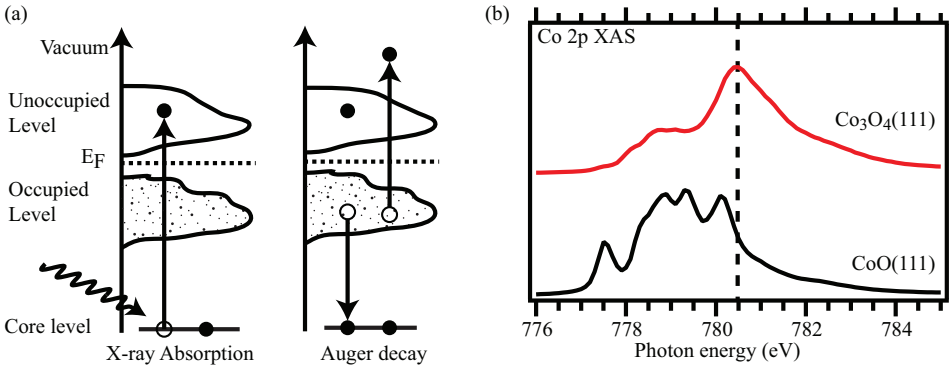

Figure 18: (a) Schematic illustration of the XAS process by Auger decay and (b) Co 2p XAS spectra of CoO(111) and Co_3O_4(111).

XAS spectra are often very sensitive to the oxidation state of metal atoms, and the technique is, therefore, often used to identify different oxide phases. As an example, it is easy to distinguish the Co 2p XAS spectra of the Co_3O_4 and CoO cobalt oxide film as shown in figure 18(b).

2.5 Scanning tunneling microscopy (STM)

Scanning tunneling microscopy (STM) gives a local real space image of the surface morphology convoluted with its electronic structure near the Fermi level. One of the main advantages of the STM is its resolution (below 0.1 Å) which makes local atomic level investigations possible.

Gerd Binnig and Heinrich Rohrer invented the STM in 1982 [61, 62]. Later in 1986, they were awarded the Nobel Prize for their invention [63]. The STM technique is based on quantum tunneling of electrons through a vacuum barrier formed between a tip that is raster scanned very close to a conductive surface. Using a feedback circuit to control the tip height above the surface and thereby keep the current of electrons that tunnel through the vacuum barrier constant it is possible to image the surface by plotting the tip height as a function of the '*x*' and '*y*' raster coordinates.

2.5.1 Working principle

According to classical mechanics, electrons at the Fermi level are unable to penetrate into the vacuum, since they are unable to overcome the work function barrier (see figure 19(a)). However, in quantum mechanics, the Fermi electrons can penetrate into the vacuum as their wave functions decay exponentially into the vacuum region. The probability of finding an electron at position z (inside the vacuum) is:

$$|\Psi(z)|^2 = |\Psi(0)|^2 \cdot e^{\frac{-2\sqrt{2m\Phi}}{h}z} \tag{15}$$

where, m is the electron mass, h is the Planks constant, Ψ is the wavefunction of the electron, and Φ is the work function of the sample surface.

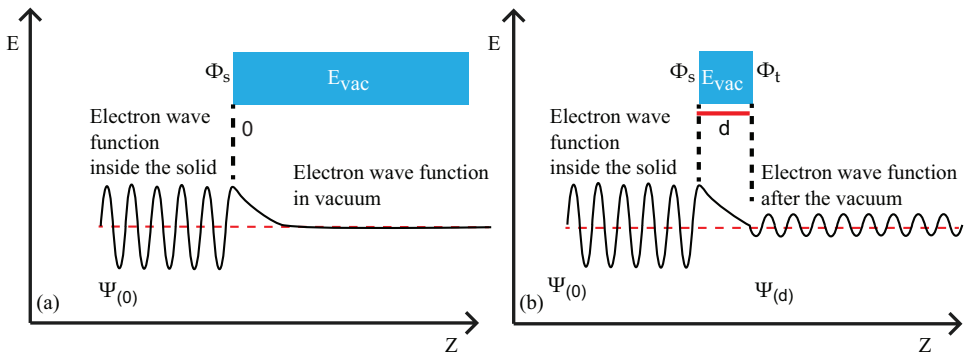

Figure 19: Schematic illustration of (a) an electron tunneling from a sample to the vacuum, and (b) an electron tunneling from a sample to a tip.

Imagine that the vacuum is replaced by another electrode at a distance d, as shown in figure 19(b). The transmission probability T of the square barrier will then be:

$$T = \frac{|\Psi(d)|^2}{|\Psi(0)|^2} = e^{\frac{-2\sqrt{2m\Phi}}{h}d} \tag{16}$$

Equation (16) shows that the tunneling probability decays exponentially with the separation distance d between the sample and the tip.

2.5.2 Tunneling theory

According to the equation (16), the electrons will only tunnel through the vacuum barrier formed between two conductors if the distance is small enough (a few Å). Generally, the Fermi levels of the tip and sample are aligned, and there will be no net tunneling current. Therefore, a bias voltage is needed to facilitate a net electron current. Due to this bias voltage, the Fermi levels of the tip and the sample are shifted, and electrons will tunnel from filled states to empty states of the tip/sample or vice versa depending on the polarity of the bias voltage.

In 1961 [64], Bardeen described electron tunneling through a metal-insulator-metal junction theoretically. He considered two non-interacting electrodes and described the transmission between these electrodes with time-dependent perturbation theory. When a negative voltage V_{bias} is applied to the sample, the electrons will tunnel from the sample to the tip. According to Bardeen, the tunneling current will be:

$$I_{s\to t} = \frac{4\pi e}{\hbar}\int_{-\infty}^{\infty} \rho_t(\varepsilon + eV_{bias}) f_t(\varepsilon + eV_{bias}) |M_{s,t}|^2 \, \rho_s(\varepsilon)[1 - f_s(\varepsilon)] d\varepsilon \tag{17}$$

Here, ρ_s and ρ_t are the local density of states (LDOS) of the sample and tip, respectively. V_{bias} is the applied potential to the sample. The Fermi function $f_{s,t}$, gives the probability of the sample/tip states being populated and $|M_{s,t}|$ is the Matrix element between the sample states Ψ_s and tip states Ψ_t. The matrix element $|M_{s,t}|$ can be expressed (eq. (18)) as a surface integral over a surface that lies in the vacuum barrier region [64].

$$\left|M_{s,t}\right| = \frac{\hbar^2}{2m}\int_s (\Psi_t^* \nabla\Psi_s - \Psi_s \nabla\Psi_t^*) dS \tag{18}$$

Tersoff and Hamann [65] assumed that the tip's wave function is a spherical s-wave with its center a distance r_0 above the sample surface and used the sample's LDOS close to the Fermi level, $LDOS_s(E_F)$, evaluated at the center of the tip. At low temperature and low bias voltage the expression for tunneling current flowing from the tip to the sample is proportional to:

$$I \,\alpha\, V_{bias} LDOS_s(E_F, r_0) \tag{19}$$

Equation (19) clearly shows that the STM does not generate the direct image of the surface topography. Instead, an STM image shows the convolution between the LDOS (evaluated at the tip center) and the geometric features of the surface.

2.5.3 Experimental apparatus

An atomically sharp metal tip is used in the STM. This tip is brought very close to the surface, and a bias voltage is applied between the tip and the sample. An image and a schematic representation of the experimental setup are shown in figure 20.

The main parts of the STM instrument used here are, a conducting sample, a probing tip, and the electronics used to control the STM. The sample is placed in a holder which can move in two dimensions. With the help of a camera, the sample holder is used to move the sample as close as possible to the STM tip without forming a contact between the tip and the sample. Using an automatic approach mechanism, the sample is positioned a few Ångstroms from of the tip, where tunneling can occur. A finer positioning of the tip is achieved with a piezoelectric tripod scanner that controls the motion of the tip. This tripod scanner consists of three piezoelectric scanner rods attached to the tip carrier plate.

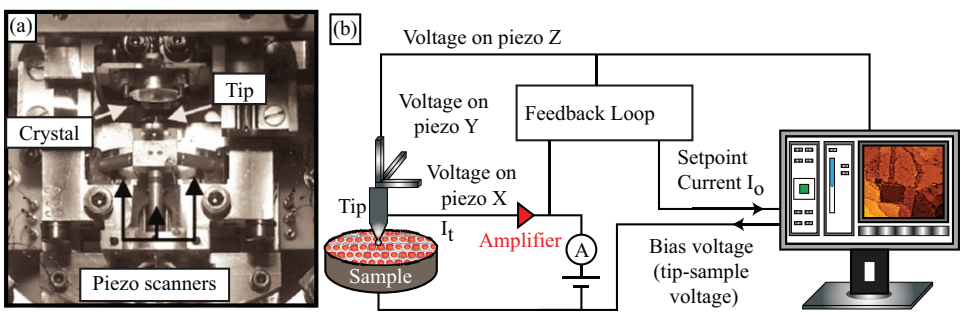

Figure 20: (a) The image shows the primary parts of the STM: Piezo scanners for precise scanning of the tip across the surface. (b) Schematic illustration of the STM setup.

During the STM measurements, the user needs to set the tunnel current and the bias voltage. The tip raster scans the *xy*-plane line by line, and by the help of the electronic feedback loop, the position of the tip height is continuously adjusted keeping the tunnel current constant.

2.6 Low energy electron diffraction (LEED)

In low energy electron diffraction (LEED) electrons are diffracted by a periodic surface structure, and a diffraction pattern is created on a fluorescent screen. This diffraction pattern can then be used to deduce the surface structure. Electron diffraction is based on de Broglie's prediction in 1924 [66], that particles with mass m and a kinetic energy E have a wavelength λ:

$$\lambda = \frac{h}{\sqrt{2mE}} \tag{20}$$

In 1927, a couple of years later, this prediction was confirmed experimentally by observing the diffraction of electrons from a nickel crystal surface by Davisson and Germer [67]. The setup for electron diffraction was improved further by Lander by including spherical grids and a fluorescent screen to observe the electron diffraction pattern. The experimental setup developed by Lander essentially forms the basis for modern LEED setups used today. Today, LEED is used extensively as a quick way to determine the periodicity of two-dimensional crystalline surfaces [68]. LEED can be used in two different ways, qualitatively, and quantitatively. In qualitative LEED the diffraction pattern is recorded and from the position of diffraction spots the surface unit cell can be calculated. In contrast, in quantitative LEED, the intensities of the scattered beams are recorded as a function of electron energy. The comparison of the experimental IV curves with theoretical curves provides information about the exact position of all atoms in the near surface region.

2.6.1 Reciprocal lattice

Three-dimensional Bravais lattices can be expressed mathematically as:

$$\vec{R} = n_1\vec{a}_1 + n_2\vec{a}_2 + n_3\vec{a}_3 \tag{21}$$

where $\vec{R}$ is the position vector for all the lattice points, n_i are integers and $\vec{a}_i$ are the vectors of the primitive unit cell of a real lattice. Similarly, a reciprocal lattice vector can be expressed mathematically as:

$$\vec{K} = n_1\vec{a}_1^* + n_2\vec{a}_2^* + n_3\vec{a}_3^* \tag{22}$$

where $\vec{K}$ is the reciprocal lattice vector of a real lattice in three dimention, k_i are integers and $\vec{a}_j^*$ are the basis vectors of a reciprocal lattice. Primitive vectors ($\vec{a}_j^*$) of a reciprocal lattice can be calculated from the corresponding primitive vectors ($\vec{a}_i$) of the real space lattice as:

$$\vec{a}_1^* = 2\pi\frac{\vec{a}_2\times\vec{a}_3}{\vec{a}_1\cdot(\vec{a}_2\times\vec{a}_3)},\ \vec{a}_2^* = 2\pi\frac{\vec{a}_3\times\vec{a}_1}{\vec{a}_3\cdot(\vec{a}_1\times\vec{a}_2)},\ \vec{a}_3^* = 2\pi\frac{\vec{a}_1\times\vec{a}_2}{\vec{a}_3\cdot(\vec{a}_1\times\vec{a}_2)} \tag{23}$$

From equation (23) it follows that:

$$\vec{a}_j^*\cdot\vec{a}_i = 2\pi\,\delta_{ij} \tag{24}$$

where δ_{ij} is Kronecker delta function.

2.6.2 The diffraction conditions

Von Laue considered a lattice of identical atoms with a separation distance R and assumed that diffraction occurs from an individual atom in all directions. However, sharp spots are only observed when electrons scattered from all lattice points interfere constructively.

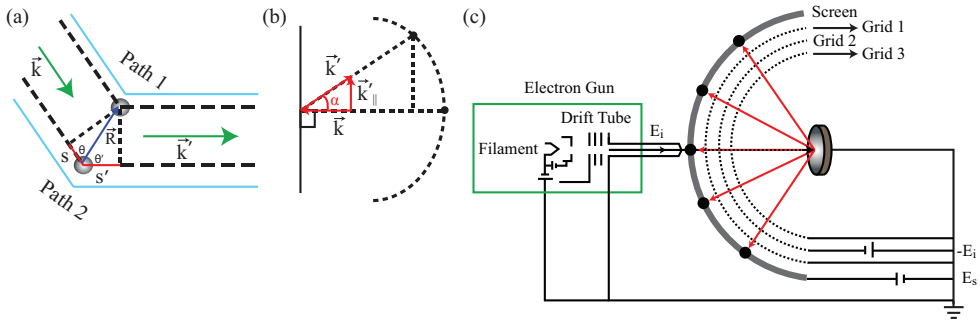

Figure 21: (a) Illustration of a wave scattered from two different atoms separated by a distance R. (b) Electron scattering on a surface at normal incidence. Incident wave and scattered wave are indicated with wave vector $\vec{k}$ and $\overrightarrow{k'}$, respectively. (c) Illustration of LEED apparatus (see text for details).

Consider two atoms separated by a distance R as shown in figure 21. Constructive interference occurs if the path difference (marked with red) is equal to an integer multiple of the wavelength of the incoming wave. Using this requirement, it can be shown that:

$$\vec{R} \cdot \Delta\vec{k} = 2\pi n \tag{25}$$

In all directions where this condition is fulfilled, constructive inference will occur. For a 2D Bravais lattice given by $\vec{R} = n_1\vec{a}_1 + n_2\vec{a}_2$ the incident electron beam with wave vector $\vec{k}$ is perpendicular to the surface and it has therefore no parallel component. It follows then directly from figure 21 that equation (25) can be rewritten to:

$$\vec{R} \cdot \overrightarrow{k'_{||}} = 2\pi n \tag{26}$$

As the form of equation (26) is identical to equation (25) it follows that diffraction spots are observed at positions where $k'_{||}$ is a reciprocal lattice vector of the surface.

2.6.3 Experimental details

The LEED apparatus mainly consists of two elements; an electron gun and a detection system (see figure 21(c) for details). The electron gun produces a parallel and mono-energetic beam of electrons. The electrons are generated by a hot cathode inside a cylinder named as Wehnelt cylinder. Subsequently, the electrons travel through a drift tube. The detection system of the LEED apparatus consists of three hemispherical concentric grids (marked as grid 1, 2, and 3 in figure 21(c)) and a fluorescent screen. Grid (1) is grounded and provides a field free region for the scattered electron to travel from the sample to the fluorescent screen. The second grid (2) is biased with the negative potential ($V = -E_i$) to allow only the elastically scattered electrons to transmit to the fluorescent screen. The third grid (3) is grounded to shield the electric field formed due to the positive potential (E_s = 3 to 6 kilovolts) applied on the fluorescent screen. This positive potential is used to accelerate the elastically scattered electrons onto the screen. The elastically scattered electrons will form a pattern of spots onto the fluorescent screen.

Chapter 3

Gas interaction and structural properties of Ir(100)

This chapter uses the Ir(100) surface to illustrate how XPS, STM, and LEED can be used to characterize a clean and adsorbate covered surface. Chapter 3.1 briefly discuss the different Ir(100) surface reconstructions and their corresponding XP spectra, while Chapter 3.2 discusses the adsorption of H_2, O_2, and CO with the focus on CO adsorption.

3.1 Structural properties of the Ir(100) surface

As discussed previously the surface of clean Ir(100) can be prepared in two different phases: (i) unreconstructed Ir(100)-(1×1) and (ii) reconstructed Ir(100)-(5×1)-hex. Ball models of both phases are shown in figure 22(a) and (b), respectively.

Starting with the Ir $4f_{7/2}$ spectrum of the unreconstructed Ir(100)-(1×1) phase shown in figure 22(d) deconvolution reveals one surface component (Ir_S) and one bulk component (Ir_B) with an intensity ratio of 1.4:1 nicely demonstrating the surface sensitivity of XPS.

The reconstruction of the Ir(100)-(1×1) phase happens upon annealing by the formation of a dense quasi-hexagonal lattice on top of the square bulk lattice [41]. The surface layer of this reconstructed Ir(100)-(5×1)-hex phase consists of six Ir rows arranged in a quasi-hexagonally close-packed structure on top of five rows of the square substrate [69, 70]. Therefore, the surface layer has 20% extra Ir atoms as compared to the subsurface 1×1 layers. The crystallographic structure of this so-called *(5×1)-hex* reconstructed phase has been studied in detail with LEED-IV [71, 72, 73], DFT calculations [74, 75, 76], and STM investigations [41, 77] and a well-accepted structural model is now available. It is for example known that the surface reconstruction leads to displacements of

the subsurface atoms down to as much as the fourth subsurface layer [41]. The Ir $4f_{7/2}$ spectrum of the reconstructed Ir(100)-(5×1)-he*x* phase shown in figure 22(e) can be deconvoluted by four surface components consistent with the four different Ir surface atoms in the unit cell marked with 1, 2, 3, and 4 in figure 22(b). Further deconvolution reveals that the intensity ratio between the surface and bulk components is 1.7:1, fitting nicely with 20% more Ir surface atoms in the (5×1)-hex phase. Further details about the deconvolution of the Ir(100)-(5×1)-hex phase is given in Paper I.

The (5×1)-hex reconstruction can be lifted by chemisorption of gas adsorbates like, O_2 [78, 79], CO [80, 81, 82], NO [83] or by metal adsorption such as Fe [84], or Cu [85]. H_2 adsorption also promotes a lifting of the reconstruction [86] phase at around 200K with the formation of straight monatomic Ir chains formed from the 20% excess atoms in the surface layer. The structural model of the straight Ir chains is shown in figure 22(c). As this phase also has a 5×1 periodicity it is named *deconstructed 5×1-H* phase to distinguish it from the (5×1)-hex phase. The deconvoluted Ir $4f_{7/2}$ spectrum of the deconstructed 5×1-H phase is shown in, and again different types of Ir surface atoms are visible as different components. The deconstructed 5×1-H phase will transform back to the reconstructed 5×1-hex phase, as soon as hydrogen is removed from the surface [Paper I].

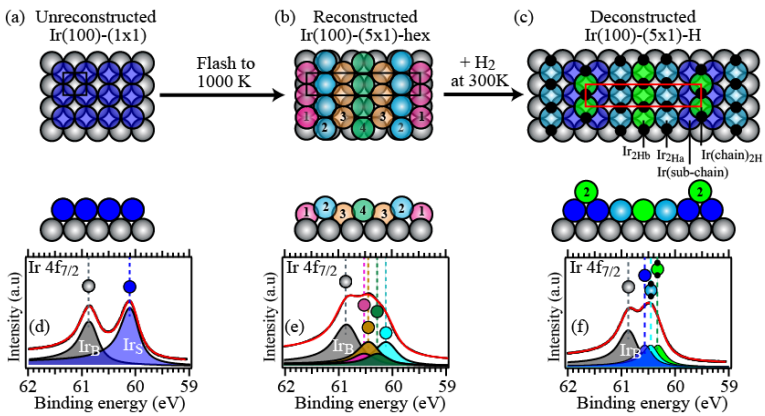

Figure 22: Structural model of (a) unreconstructed Ir(100)-(1×1), and (b) reconstructed Ir(100)-(5×1)-hex, and (c) deconstructed Ir(100)-(5×1)-H. The middle panel of the figure shows a side view of the surfaces.

3.1.1 Adsorption of probe molecules onto unreconstructed Ir(100)-(1×1)

After having discussed the clean Ir(100) phases the adsorption structures of small probe molecules like O_2, H_2, and CO onto the unreconstructed Ir(100)-(1×1) phase is discussed in this section.

In figure 23, the Ir $4f_{7/2}$ spectra of clean, hydrogen and oxygen covered Ir(100)-(1×1) are compared. Starting with the oxygen covered surface, it is known from the literature that a p(2×1)-O phase with oxygen atoms adsorbed in the bridge sites is formed upon oxygen saturation of the surface [78, 87]. As seen from the ball model in panel (b) all surface iridium atoms are chemical equivalent and the spectrum is therefore deconvoluted with one Ir_B and one Ir_O component, while no Ir_S component is observed.

Hydrogen adsorption on the Ir(100)-(1×1) surface is discussed in detail in Paper I. In summary, hydrogen saturation of the Ir(100)-(1×1) surface leads to complete removal of the Ir_S component and two hydrogen induced components Ir_{1H} and Ir_{2H} as seen in figure 23(c). These two components are assigned to Ir surface atoms that bind to one and two hydrogen atoms, respectively. Thus, in contrast to oxygen adsorption that leads to fully chemical equivalent Ir surface atoms, hydrogen adsorption leads to two different components shifted by +0.17 eV (Ir_{1H}) and +0.33 eV (Ir_{2H}), respectively, with respect to the Ir_S component. Following the relative intensity of the Ir_{1H}, Ir_{2H}, and Ir_S components upon heating it is even possible to follow the distribution of hydrogen in less dense hydrogen phases and determine if hydrogen atoms tend to cluster together in islands (H-H attraction) or if it spreads uniformly out on the surface (H-H repulsion). This is discussed in detail in Paper I.

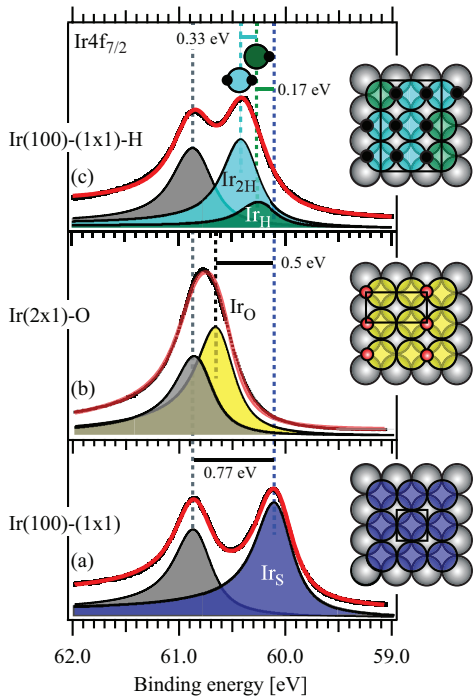

Figure 23: Ir $4f_{7/2}$ XP spectra from (a) clean unreconstructed Ir(100)-(1×1) surface, (b) after dosing O_2, and (c) after dosing H_2. The gray, blue, yellow, green, cyan, black, and red spheres correspond to Ir_B, Ir_S, Ir_O, Ir_{1H}, Ir_{2H}, hydrogen and oxygen atoms.

As a second example, two different CO adsorption structures on Ir(100)-(1×1) are discussed, demonstrating the powerful combination of XPS, STM, and LEED to provide atomic scale models of unknown adsorption structures. Figure 24 shows the experimental XP spectra of Ir $4f_{7/2}$ recorded (a) before CO dosing, after the Ir(100)-(1×1) surface had been exposed to CO at (b) $3 \cdot 10^{-8}$ mbar for 5 min , and (c) $1 \cdot 10^{-5}$ mbar for 15 min at room temperature.

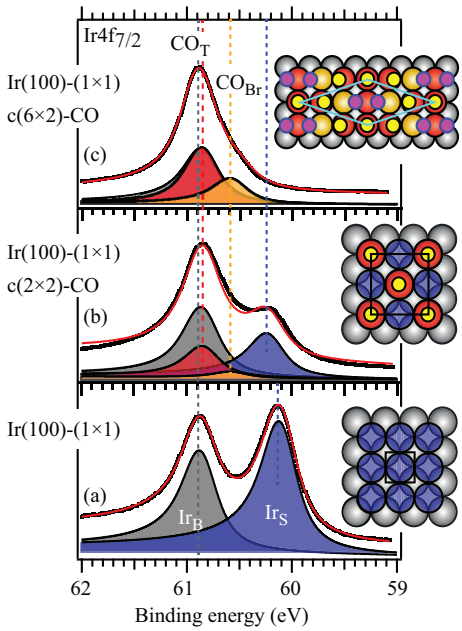

Figure 24: Ir $4f_{7/2}$ XP spectra from (a) clean unconstructed Ir(100)-(1×1) (b) after exposure to CO at $3 \cdot 10^{-8}$ mbar, and (c) CO at $1 \cdot 10^{-5}$ mbar. The gray, blue, red, and golden spheres correspond to Ir_B, Ir_S, Ir_{1CO}(atop)+ Ir_{2CO}(bridge), and Ir_{1CO}(bridge) atoms. The yellow spheres correspond to CO molecules. See page 48 for details about panel (c).

Starting with the adsorption of CO at UHV conditions it was first studied in the late seventies [88] and the structural model proposed by Ghosh *et al.* in 2007 [89] based on DFT calculations showed that CO is adsorbed atop Ir surface atoms in a c(2×2) structure with 0.5 ML coverage. The deconvolution of the Ir $4f_{7/2}$ spectrum in figure 24 is consistent with this as the Ir_S component decreases to 60% of the initial value while a new component overlapping with the bulk component forms upon dosing CO at $3 \cdot 10^{-8}$ mbar for 5 min. This component (CO_T) shifted by +0.70 eV with respect to the Ir_S component is assigned to Ir surface atoms that bind to one CO molecule atop. The last component shifted by +0.50 eV is assigned to a small fraction of bridge site CO adsorption. A similar component has been observed on previously for the c(2×2)-CO phase on the Rh(100) surface [90].

The corresponding O 1s and C 1s spectra acquired for the c(2×2)-CO structure shown in figure 25(a) and (b), respectively. Both spectra are fully consistent with the large majority of the CO molecules being adsorbed in atop site. The two shoulder components CO_{v1} and CO_{v2} are due to C−O vibrations consistent with what has been observed for CO on Pd(111) [91].

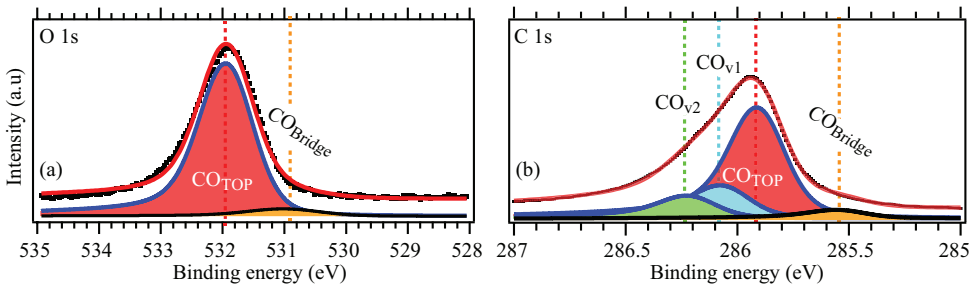

Figure 25: (a) O 1s and (b) C 1s spectra of the c(2×2)-CO structure. The black dotted, and solid red spectra correspond to the experimental, and curve fitted spectra respectively.

Upon 1 mbar of CO dosing for 10min at room temperature a c(6×2) structure forms, which is evident by the LEED and STM images shown in figure 26(a). This CO induced structure on Ir(100)-(1×1) surface has not previously been observed. Assuming that the bright protrusions in the STM image correspond to atop adsorbed CO molecules the structural model in figure 26(b) can be constructed. In the XPS setup, the Ir(100) surface was exposed to CO at $1 \cdot 10^{-5}$ mbar for 15min and the observed LEED image was identical to the inset of figure 26(a).

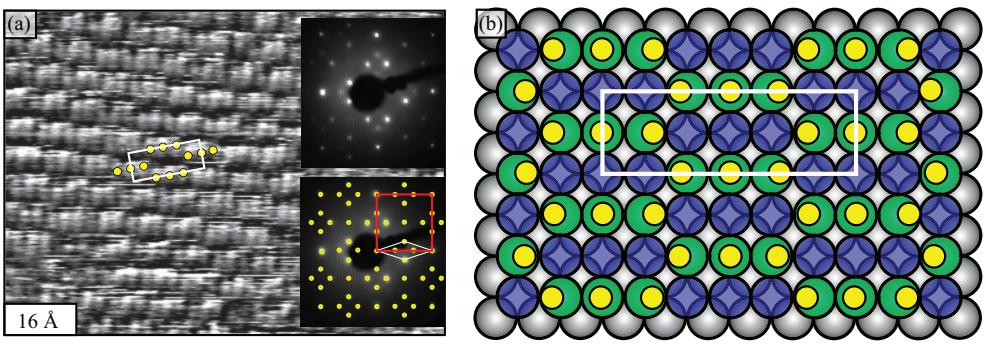

Figure 26: (a) STM image (90 × 35 $Å^2$) of the c(6×2) structure. The c(6×2) unit cell is superimposed onto the STM image. The unit cell consists of 6 CO molecules marked with yellow spheres. The inset in the upper and lower right corner shows the LEED image taken with 88 eV

and c(6×2) reciprocal pattern, respectively. The (1 × 1), and superimposed c(6×2) unit cell is marked with red and white, respectively, (b) Structural Model of the c(6×2)-CO structure. The gray, blue, green, and yellow spheres correspond to Ir_B, Ir_S, Ir_{CO}, and CO atoms and molecules.

According to the proposed structural model as shown in figure 26(b) we expected only one component in the O 1s and C 1s spectra. We also expect to observe the Ir_S component in addition with the Ir_{CO}, and Ir_B components in the Ir $4f_{7/2}$ spectrum. However, both the O 1s and C 1s spectra shows two distinct features assigned to CO in bridge and atop sites, respectively, as shown in figure 27(a) and (b).

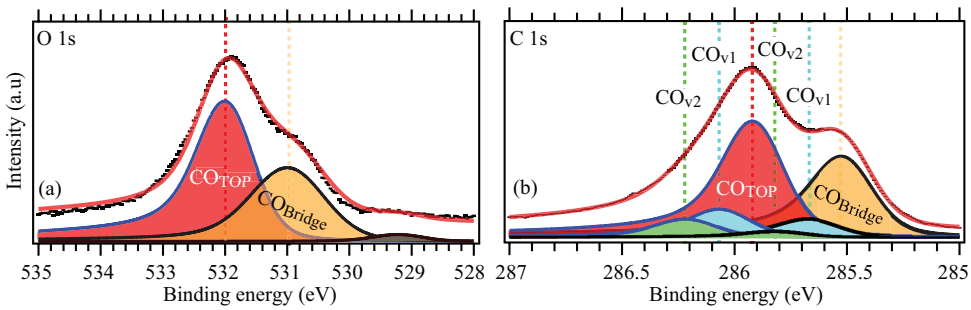

Figure 27: Experimental spectra from c(6×2)-CO of (a) O 1s, and (b) C 1s. The black dotted, and solid red spectra correspond to the experimental, and curve fitted spectra respectively. The filled curves correspond to different surface species.

Further, the Ir_S component disappeared completely in the Ir $4f_{7/2}$ spectrum, see figure 24(c). These observations do not support the proposed structural model in figure 26(b). Therefore, we modified the structural model by adding extra CO molecules in the bridge sites as shown in figure 28(b). These extra CO bridge molecules can explain the complete disappearance of Ir_S in Ir $4f_{7/2}$, and the appearance of two distinct features in C 1s and O 1s spectra (see figure 27(a) and (b)).

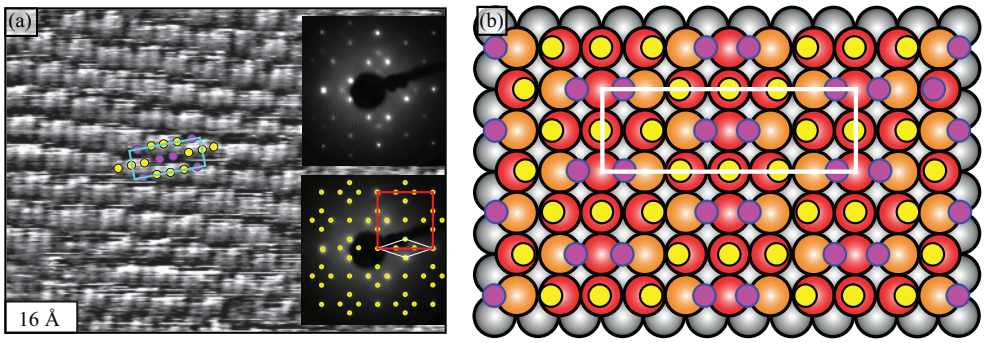

Figure 28: (a) STM image marked with additional bridge bonded CO molecules. (b) c(6×2)-CO structural model with CO bridge molecules. The c(6×2) unit cell consists of ten CO molecules, six bright protrusions (yellow spheres), and four dark spots (purple spheres). The gray, red, and golden spheres correspond to Ir_B, Ir_{1CO}(top)+ Ir_{2CO}(bridge), and Ir_{1CO}(bridge) atoms.

Figure 34 summarize the experimental surface core level shifts (SCLS) determined for the various molecules studied in this chapter nicely demonstrating how the high resolution XPS can be used to identify the nature of the adsorbates and the number of Ir atoms each adsorbate binds to.

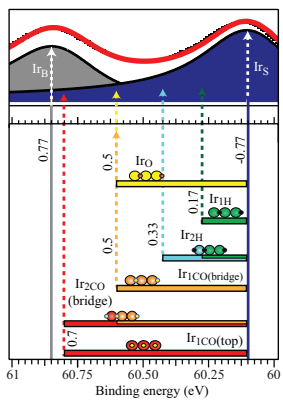

Figure 29: Iridium surface core level shifts due to adsorption of probe molecules.

Chapter 4

Ir(100) supported cobalt oxide films for catalytic applications

In nature, two different types of cobalt oxide bulk phase exist: the spinel structured Co_3O_4 (figure 30(a)) and the rocksalt structure (figure 30(b)). The unit cell of the Co_3O_4 spinel structure consists of 32 oxygen atoms positioned in 8 fcc unit cells. Only half a unit cell is shown in figure 30(a). Within these 8 fcc unit cells there are 16 Co^{3+} ions which occupy half of the octahedral sites and 8 Co^{2+} ions that occupy $\frac{1}{8}$ of the tetrahedral sites [92].

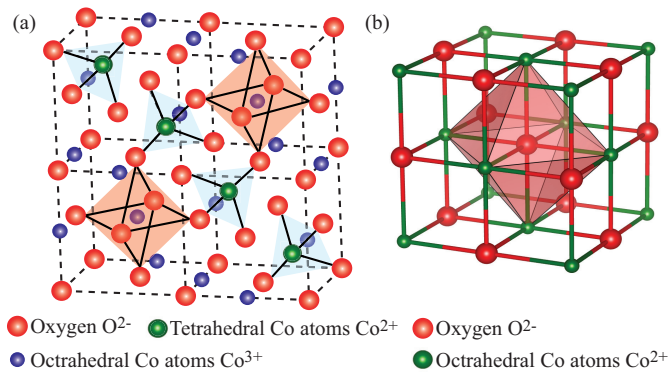

Figure 30: The stable crystal structure of (a) Spinel Co_3O_4 (only the front half of the unit cell is displayed), (b) Rocksalt CoO. These images are taken and modified from ref. [92].

In contrast to the complex spinel structure that contains a mixture of tetrahedral and octahedral cobalt ions, the rocksalt structure is simple, as it is formed by octahedrally coordinated cobalt and oxygen ions with a 1:1 ratio.

As Cobalt oxide crystals have a band gap, they are difficult to study with the electron based techniques such as STM, XPS, and LEED. Instead, I used thin (15 MLE) cobalt oxide films grown on Ir(100)-(1×1) or Ag(100). One MLE is here equivalent to the full monolayer coverage of two dimensional c(8×2) cobalt oxide film grown on Ir(100)-(1×1) surface [93]. These cobalt oxide films are thick enough to have the adsorption properties of the bulk crystals and thin enough to allow a current to pass through the film to compensate the charging. The structures of the Ir(100)-(1×1) and Ag(100) supported cobalt oxide films will be discussed in details below.

4.1 Structure of different cobalt oxide films grown on Ir(100

It is well established that a variety of well-characterized thin [94] and ultra-thin [95, 96, 97, 98] cobalt oxide films can be grown on the Ir(100)-(1×1) surface. Focusing on the thin films previous studies revealed a lattice mismatch between the in-plane Ir(100) (2.715 Å) and Co_3O_4(111) (5.7 Å) of 5% [99]. This significant in-plane lattice mismatch between the Ir(100)-(1×1) substrate and the Co_3O_4(111) film prohibits pseudomorphic growth in (100) orientations. Also, the in-plane lattice mismatch between Ir(100) (2.715 Å) and CoO(111) (3.01 Å) is quite large 10%. It is, however, possible to grow CoO both in the (111) and (100) orientation on the Ir(100)-(1×1) substrate [100]. The growth recipes of the Ir(100) supported Co_3O_4(111), and CoO(111) films are described in detail in Paper II, III, and IV. In short, it consists of reactive deposition of Co and annealing in oxygen and UHV for the Co_3O_4(111) film, while the CoO(111) film can be formed from the Co_3O_4(111) by careful flashing this film in UHV to desorb oxygen partly. The Ir(100) substrate influences, however, the rotation of the films. Due to the square symmetry of the substrates, the cobalt oxide films grows in two orthogonal domains one along the [011] direction and the other along the $[0\bar{1}1]$ direction of the (100) substrate [101].

For the Co_3O_4(111) film six different surface terminations are possible [92] as shown in the structural model of Co_3O_4 (111) in figure 31(a). Comparing experimental and simulated LEED-IV spectra Hammer *et al.* [92] demonstrated that the Ir(100) supported Co_3O_4(111) surface is terminated by Co^{2+} ions, as shown in figure 31(a). On the surface of Co_3O_4(111) film, these Co^{2+} ions are located in the 3-fold hollow sites of the oxygen lattice forming a (2×2) structure, as seen

in figure 31(b) [99]. STM and LEED experiments have shown that the lattice parameter of the $Co_3O_4(111)$ on Ir(100) is the same as in the bulk spinel and the film is therefore fully relaxed [92].

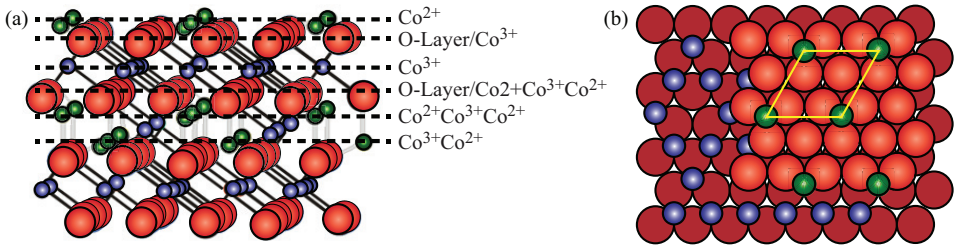

Figure 31: (a) The six different surface terminations are indicated in the structural model of $Co_3O_4(111)$ film. (b) The surface structure of $Co_3O_4(111)$ film. The images are modified from ref. [99]. The (2×2) unit cell is marked with yellow parallelogram. The red, blue, and green spheres correspond to oxygen, Co^{3+}, and Co^{2+} ions, respectively.

In contrast to the $Co_3O_4(111)$ film, no Co ions are located on the surface, and the surface of CoO(111) is terminated by a hexagonal O-layer [94]. The octahedral coordinated Co^{2+} ions are positioned subsurface sandwiched between the top and second layer of oxygen, as shown in figure 32(a), and (b).

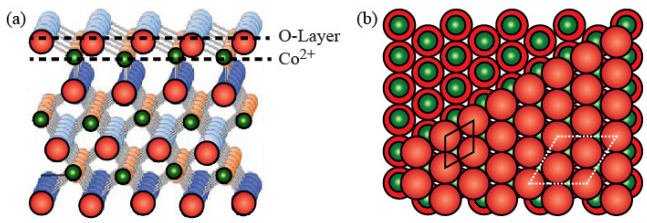

Figure 32: (a) Structural model, and (b) surface structure of CoO(111). The images are modified from ref. [101]. The (1×1), and $\left(\sqrt{3} \times \sqrt{3}\right) R30^{o}$ unit cells are marked with black and white dotted parallelograms. The red and blue spheres correspond to oxygen and cobalt ions, respectively.

However, due to the subsurface reconstruction below 323 K, the Co^{2+} species in the second layer change position from the octahedral threefold hollow sites to tetrahedral sites. Due to this reconstruction, only the first two layers of CoO(111) is converted to a Wurtzite structure, while

the rest of the film maintain the rocksalt structure, as can be seen in figure 32(a) [92]. As a result of the Wurtzite formation, the primitive unit cell of the surface is transformed from a (1×1) to a $\left(\sqrt{3} \times \sqrt{3}\right) R30^o$ unit cell upon cooling to below 320 K [92]. Figure 32(b) shows the surface structure of CoO(111) film and the (1×1), and $\left(\sqrt{3} \times \sqrt{3}\right) R30^o$ unit cells are marked with black solid and white dotted parallelograms. In addition to the Ir(100) supported CoO(111) and Co_3O_4(111) surfaces, we have also studied Co_3O_4(100) film grown on Ag(100) as reported in Paper V and VI.

4.2 Reactivity of spinel and rocksalt cobalt oxide films

The well-characterized Co-oxide films give a unique chance to link catalytic properties to atomic scale structure. In this work, we used small probe molecules like CO, CO_2, and H_2O to study the related surface chemistry of the well-ordered Co_3O_4(111)/Ir(100), CoO(111)/Ir(100), and Co_3O_4(100)/Ag(100) films at a molecular level. The main technique for these studies has been HRXPS and the overall results of the research are discussed in detail in Paper II-VI. As an example, the CO adsorption on the different Co oxide surfaces is discussed below.

4.2.1 CO adsorption properties

In figure 33 the CO saturated C 1s spectra of Co_3O_4(111)/Ir(100), CoO(111)/Ir(100), and Co_3O_4(100)/Ag(100) are compared. CO was here dosed at 85 K. Upon CO dosing three new components are observed at binding energies of 287.0 (red), 288.5 (blue), and 290.9 eV (green) for Co_3O_4(111)/Ir(100) and Co_3O_4(100)/Ag(100) as seen in figure 33(a, c), while very little CO is adsorbed on the CoO(111)/Ir(100) surface. The components at 287.0 eV and 290.9 eV are here assigned to weakly bound CO and its shake-up component, respectively, while the remaining component at 288.5 eV is assigned to a carbonate species [Paper II, III, V]. Clearly, the XPS characterization can be used to identify the nature of the chemical species formed on the surfaces upon adsorption and thereby their catalytic properties. For example, the experiments revealed very similar adsorption of CO on the (100) and (111) surfaces of Co_3O_4 suggesting similar catalytic properties of these two surface terminations. In contrast, we expect very little catalytic activity of the CoO(111) surface as this is inert with respect to CO adsorption.

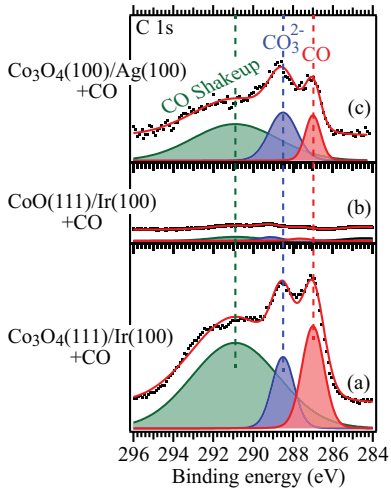

Figure 33: C 1s spectra after dosing CO on (a) Co_3O_4(111)/Ir(100), (b) CoO(111)/Ir(100), and (c) Co_3O_4(100)/Ag(100). The red, blue, and green filled components in C 1s correspond to CO, CO_3, and CO shakeup, respectively.

4.2.2 Transformation between spinel and rocksalt surfaces

Different Co oxide surfaces have very different adsorption properties for CO and therefore also different catalytic properties are expected. The Co oxide surfaces are, however, very dynamic at reaction conditions and as will be shown below they are easy to convert from one phase to another by changing the gas mixture.

The details of the transformation process of the Ag(100) supported cobalt oxide films is discussed in Paper VI. However, the transformation process of the Ir(100) supported cobalt oxide films is not included in any paper and is, therefore, discussed briefly here.

As discussed above the Ir(100) supported CoO(111) film can be formed by flashing the Co_3O_4(111) film to sufficiently high temperature. To increase the amount of oxygen in the CoO(111) film and thereby transform it back to Co_3O_4(111) film, two different methods have been studied: (i) annealing in molecular oxygen and (ii) annealing while exposing the film to oxygen radicals (O_{rad}).

Using LEED, I investigated how molecular oxygen (O_2) and oxygen radical (O_{rad}) exposure onto a CoO(111)/Ir(100) film can be used to convert the film to the Co_3O_4(111)/Ir(100) film. No changes were observed after annealing in O_2 ($1 \cdot 10^{-5}$mabr, 5min) at 550 K (which is significantly below the formation temperature of CoO(111) from Co_3O_4(111)). In other words, it is impossible to transform the CoO(111) film to a Co_3O_4(111) film by O_2 dosing at UHV conditions, at least if the dosing time is kept short.

In the second set of experiments oxygen radicals were exposed onto the CoO(111) film for 2min at $6 \cdot 10^{-6}$ mbar (flux rate of $5 \cdot 10^{15}$ atoms/s) at different temperatures from 300 K to 520 K. From these experiments we found that the CoO(111) film starts to convert to the Co_3O_4(111) film around 400 K, while the film is fully converted to Co_3O_4(111) at 520 K. The LEED image of the transformed Co_3O_4(111) film is shown in the inset of figure 34(c). In the following, the transformed Co_3O_4(111) from CoO(111) film and the freshly grown Co_3O_4(111) film will be called T-Co_3O_4(111) and F-Co_3O_4(111), respectively. In addition to the LEED images, the Co 2p XP spectra for Ir(100) supported F-Co_3O_4(111) film (bottom-red), CoO(111) film (middle-black), and T-Co_3O_4(111) film (top-blue) are also compared in figure 34. Comparing the spectra of the transformed T-Co_3O_4(111) and freshly prepared F-Co_3O_4(111) films it is evident that they are identical and therefore have identical electronic properties.

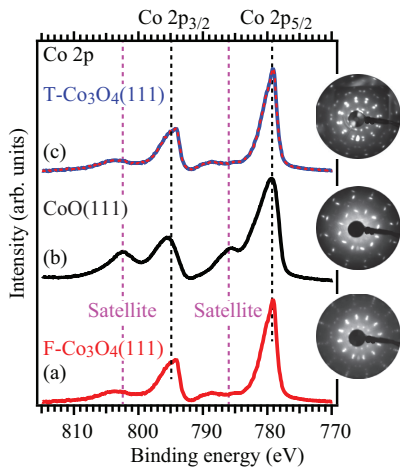

Figure 34: The Co 2p spectra of (a) freshly grown Co_3O_4(111), (b) CoO(111), and (c) transformed Co_3O_4(111) is shown in red, black and blue. The red dotted line from F- Co_3O_4(111) is

superimposed on T-Co_3O_4(111) for direct comparison. Corresponding LEED images are shown in the inset of the figure.

Based on the above observations we suggest that oxygen radicals diffuse easily into the CoO(111) film and transforms it to the Co_3O_4(111) film. In contrast, no evidence of transformation is observed upon molecular oxygen dosing. These observations suggest that the CoO(111) surface is unable to dissociate oxygen, and this prohibit further oxidation of the film. We can, however, not exclude that longer exposure to molecular oxygen or the use of higher pressure could facilitate the transformation if oxygen dissociation takes place on defects on the CoO(111) surface. In this respect, it is interesting to notice that we observed the transformation of Ag(100) supported CoO(100) to Co_3O_4(100) film in high pressure mixtures of CO and O_2 at a total pressure of 1.2 mbar. The transformation of Ag(100) supported CoO(100) to Co_3O_4(100) film and vice versa is discussed in Paper VI.

Summary of papers

Adsorption of probe molecules on Ir(100) surfaces

Paper I: Adsorption of hydrogen on stable and metastable Ir(100) surfaces

This paper present a detailed spectroscopic study for clean and hydrogen covered Ir(100) surfaces: (i) Ir(100)-1×1, (ii) Ir(100)-1×1-H, (iii) Ir(100)-(5×1)-hex, (iv) Ir(100)-(5×1)-hex-H, and (v) deconstructed 5×1-H phase with linear atomic Ir chains on the surface. The experimentally determined core level shifts match very well with density functional theory calculated CLS. The paper demonstrates that the hydrogen coverage and the distribution of hydrogen in different adsorption sites can be tracked by HRXPS at all temperatures. In particular, we find evidence for (1×1)-H islands formation at low temperature for partial hydrogen coverages on the unreconstructed Ir(100)-(1×1) surface.

Adsorption properties of probe molecules on Cobalt oxide surfaces

Paper II: Adsorption and activation of CO on Co_3O_4(111) thin films

This paper reports on the interaction of CO and O_2 with well-ordered Co_3O_4(111) thin films grown on Ir(100)-(1×1) using STM, HRXPS, IRAS, and TPD under UHV conditions. The study reveals two characteristic coverage regimes of CO adsorption on Co_3O_4(111) at 100 K. At low coverage, CO molecules bind to surface Co^{2+} ions, while a compressed phase is formed at higher coverage with additional CO molecules located at sites in between the Co^{2+} ions. Formation of carbonate species was also observed after the completion of the low coverage CO phase. This surface carbonate is believed to be a minority species formed on surface defects such as step edges of terraces or the side facets of the (111) oriented grains. The molecularly adsorbed CO desorbs at temperatures between 100 K and 180 K, whereas the surface carbonate decomposes in a broad temperature range up to 400 K.

Furthermore, pre-adsorbed oxygen on the $Co_3O_4(111)$ surface was shown to block the formation of the high coverage phase of CO, whereas it has little effect on the formation of low coverage CO phase and carbonate formation.

Paper III: Adsorption properties of CO and CO_2 onto CoO(111) and $Co_3O_4(111)$ films studied with core level spectroscopy

In contrast to the Paper II that focused on the CO adsorption properties on the $Co_3O_4(111)$ surface and studied it with the interplay of different techniques, Paper III compares CO and CO_2 adsorption on CoO(111) and $Co_3O_4(111)$ surfaces. The paper gives a detailed and quite a complete picture of CO and CO_2 adsorption on the two surfaces.

First of all the study reveals that the oxygen terminated pristine CoO(111) film is inert for both CO and CO_2 adsorption at UHV conditions, while both molecules easily adsorb onto the Co^{2+} terminated surface of the pristine $Co_3O_4(111)$ surface at ~ 100 K. Secondly, it is shown that the inert CoO(111) surface can be given the adsorption properties of the $Co_3O_4(111)$ surface if the otherwise inert surface is modified by Co_{add} atoms or oxygen vacancies. The surface chemistry of the Co oxide films, therefore, depends much more on the whether accessible Co surface atoms exist than on the Co_3O_4 or CoO nature of the film. Finally, it is demonstrated that adsorption onto Co_{add} atoms or oxygen vacancies can be distinguished using HRXPS.

Paper IV: Water and hydrogen radical adsorption onto CoO(111) and $Co_3O_4(111)$ surfaces studied by photoemission spectroscopy

In this paper we studied the adsorption and dissociation of water on the Ir(100) supported CoO(111) and $Co_3O_4(111)$ films using HRXPS and TPXPS. Similar to CO and CO_2 adsorption discussed in Paper III we find that the CoO(111) is inert with respect to water dissociation, while the $Co_3O_4(111)$ surface readily dissociates water and on this surface, we find evidence for an H_2O-OH network structure. Physisorbed water is observed on both surfaces.

Hydroxylation upon hydrogen radical exposure is also studied in the paper, and clear evidence for increased sticking of physisorbed water on the hydroxylated $Co_3O_4(111)$ is found suggesting that hydrogen bonds between adsorbed water and the OH groups help stabilizing the water film. Finally, we find evidence for the formation of partially reduced structures upon flashing a

hydroxylated CoO(111) film. Altogether, the paper gives a detailed spectroscopic picture of water adsorption and dissociation on the two surfaces.

Paper V: Co_3O_4(100) films grown on Ag(100): Structure and chemical properties

In contrast, to Paper II – IV which focused on the (111) surface of CoO and Co_3O_4 this paper describes how the (100) surface of Co_3O_4 can be grown on the Ag(100). The findings open up for a systematic comparison of the activity and chemistry of (111) and (100) facets of Co_3O_4.
In the paper, the structural and chemical properties of the Co_3O_4(100) film are studied by a combination of STM, LEED, XPS, and XAS. The experiments indicate that the prepared Co_3O_4(100) surface is unreconstructed, in contrast to the identical Fe_3O_4(100) [102]. STM images of the Co_3O_4(100) surface reveals, however, that single subsurface cation vacancies defects are found on the surface similar to the defects found on the Fe_3O_4(100). The CO adsorption properties on Co_3O_4(100)/Ag(100) surface is also studied and found to be similar to the Co_3O_4(111)/Ir(100) surface discussed on Paper II and III.

Paper VI: Transformation between Co_3O_4 and CoO phases under reaction conditions

In this paper, the transformations between CoO and Co_3O_4 films supported by Ag(100) is studied in mbar gas mixtures mainly with HPXPS. It is shown that the Co_3O_4(100) phase is readily formed at temperatures above 400 K in a stoichiometric mixture of CO and O_2 at a total pressure of 1.2 mbar. Only upon complete removal of CO in the gas mixture, the film transforms back to the CoO(100) phase. Carbonates is the only carbon containing species identified on the surface and it is found to be stable in the temperature range between 300 K and 450 K.
Gas phase CO_2 production was also observed for the Co_3O_4(100) film, but since we also observed this on a pure Ag(100) sample at similar gas mixtures, pressures, and temperatures we are unable to correlate the observed CO_2 production with the presence of the Co_3O_4 phase.

Paper VII: Interface Controlled Oxidation States in Layered Cobalt Oxide Nano-Islands on Gold

In this article, we provide an atomic scale characterization of Cobalt oxide nanoislands grown on the Au(111) surface by using STM, XPS, and XAS. Thus, in contrast to Paper II-VI that studied thin Co oxide films that cover the entire substrate, we here studied thin Co oxide nano-islands. The interface of cobalt oxide and gold is of particular interest since gold can act as a strong promoter to cobalt oxides for OER reaction [103, 104].

In the study 3 different types of Co oxide nano-islands were identified: (i) CoO(111) bilayer islands, (ii) CoO(111) double bilayer islands, and (iii) CoO_2 trilayer islands.

The most important take-home message from this paper is that upon Co-O bilayer transformation to an O-Co-O trilayer the charge of the cobalt ions also changed from Co^{2+} to Co^{3+}.

Summary and outlook

Cobalt oxide based nanomaterials are catalytically active for a number of reactions, but the underlying atomic scale processes causing the activity remain unclear. The present thesis, describes my work on well-characterized cobalt oxide *model catalyst surfaces* consisting of CoO and Co_3O_4 thin films with the (111) and (100) terminations supported by Ag(100), Ir(100), and Au(111) single crystal surfaces. These thin films are conductive enough for the use of electron based techniques to study their structure and chemical properties.

Starting with the structural characterization the Ir(100) supported CoO(111) and Co_3O_4(111) films they have been studied extensively by Hammer and Heinz and my work, therefore, rely heavily on the established structural models from their work [92]. In contrast, I have successfully grown and characterized Ag(100) supported CoO(100) and Co_3O_4(100) thin films for the first time by myself. Using HPXPS, I also studied these Ag(100) supported cobalt oxide thin films in mbar reaction mixtures of O_2:CO and shown that phase changes takes place in response to the gas composition. Finally, I also studied the structure of ultra-thin nano islands of CoO and CoO_2 phases supported by Au(111) with HRXPS and XAS, and together with detailed STM work performed by my co-authors this led to structural models.

The chemistry of the cobalt oxide thin films were studied by dosing small *probe molecules* such as CO, CO_2, H_2O, H_2, and hydrogen radicals onto the thin films at UHV conditions and characterizing the adsorbates with HRXPS. This work revealed that the oxygen terminated CoO(111) and CoO(100) films are very inert while Co ions naturally found on the surface of Co_3O_4(111) and Co_3O_4(100) or formed artificially on the inert surfaces makes the surface much more reactive for weakly adsorbed CO and CO_2, the formation of carbonate, and for dissociation of water.

As a side project, to my work of the cobalt oxide chemistry, I also studied the different surface reconstructions of the Ir(100) surface and H, O, and CO adsorption structures formed on them mainly using HRXPS. This work led to a quite complete picture of the photoelectron spectroscopy components formed by the different reconstructions and the adsorbate structures. The work related to the surface reconstructions, and the H adsorption is discussed in Paper I, while the CO adsorption is discussed briefly in this thesis. The CO adsorption data will be written up in a

forthcoming publication. Currently, my co-authors in the group of Lutz Hammer and Alexander Schneider are working on a draft on oxygen adsorption on Ir(100).

The natural continuation of my *model system* work is to measure real activity and to correlate the measured activity with the structure of the cobalt oxide thin films, and the adsorbates found on the surfaces. My preliminary HPXPS work in this direction on Ag(100) and Ir(100) supported cobalt oxide thin films, unfortunately, failed as we mainly measured the catalytic activity of the substrate or sample holder rather than the activity of the metal oxide films. While my work clearly underlines the importance of reference, experiments before observed reactivity can be correlated with surface structures it also calls for improved experimental setups for measuring the reactivity of samples locally. One way to do this is to have very localized heating of the sample using for example laser based heating. The HIPPIE beamline at the MAX IV Laboratory will have such a laser heated reaction cell and it is planned to repeat the HPXPS experiments on the Ag(100) supported CoO and Co_3O_4 phases on this setup.

Another interesting future direction of my work is the structural characterization of the low temperature adsorption of probe molecules on the different surface terminations of the CoO and Co_3O_4 phases. Low temperature STM characterization could potentially be used for this.

The detailed work of the cobalt oxide thin films also opens up for using the cobalt oxide films as support material for particles or even individual atoms and the study of their catalytic properties. In that respect it is interesting that defects on the $Fe_3O_4(001)$ surface [105] similar to the point defects identified in my work on the $Co_3O_4(100)$/Ag(100), previously have been used to stabilize for example Au [106] atoms. Low temperature STM work focused on for example water adsorption onto the point defects on $Co_3O_4(100)$/Ag(100) similar to the extensive work on $TiO_2(110)$ defects [107] would definitely also be interesting.

Finally, model systems closer to real cobalt oxide catalysts would be interesting to study. Using surface X-ray diffraction (SXRD), I started such work and studied the transformation of CoO(111) single crystal surface in high pressures of O_2.

Bibliography

[1] Clark, J. H. **"Green Chemistry: Today (and Tomorrow)"**. *Green Chemistry*. **2006**, *8*, 17.

[2] Berzelius, J. J. **"Annual report on progress in physics and chemistry"**. *Jber. Chem.* **1835**, *15*, 237

[3] Ostwald W. *Phys. Z.* **1902,** *3*, 313; *Ann. Naturphil.* **1910**, *9*, 1

[4] Lewandowski, M.; Groot, I. M. N.; Shaikhutdinov, S.; Freund, H. J. **"Scanning Tunneling Microscopy Evidence for the Mars-van Krevelen Type Mechanism of Low Temperature CO Oxidation on an FeO(111) Film on Pt(111)"**. *Catal. Today.* **2012**, *181*, 52–55.

[5] Xie, X.; Li, Y.; Liu, Z.-Q.; Haruta, M.; Shen, W. **"Low-Temperature Oxidation of CO Catalysed by Co_3O_4 Nanorods"**. *Nature,* **2009**, *458*, 746–749.

[6] Choudhary, T. V.; Banerjee, S.; Choudhary, V. R. **"Catalysts for Combustion of Methane and Lower Alkanes"**. *Applied Catalysis A: General*. **2002**, *234*, 1–23.

[7] Liotta, L. F.; Wu, H.; Pantaleo, G.; Venezia, A. M. **"Co_3O_4 Nanocrystals and Co_3O_4–MOx Binary Oxides for CO, CH_4 and VOC Oxidation at Low Temperatures: A Review"**. *Catal. Sci. Technol.* **2013**, *3*, 3085–3102.

[8] Xiong, S.; Yuan, C.; Zhang, X.; Xi, B.; Qian, Y. **"Controllable Synthesis of Mesoporous Co_3O_4 Nanostructures with Tunable Morphology for Application in Supercapacitors".** *Chem. - A Eur. J.* **2009**, *15*, 5320–5326.

[9] Dau, H.; Limberg, C.; Reier, T.; Risch, M.; Roggan, S.; Strasser, P. **"The Mechanism of Water Oxidation: From Electrolysis via Homogeneous to Biological Catalysis"**. *ChemCatChem*. **2010**, *2*, 724–761.

[10] Liang, Y.; Li, Y.; Wang, H.; Zhou, J.; Wang, J.; Regier, T.; Dai, H. **"Co_3O_4 Nanocrystals on Graphene as a Synergistic Catalyst for Oxygen Reduction Reaction"**. *Nat. Mater.* **2011**, *10*, 780–786.

[11] Jansson, J. **"Low-Temperature CO Oxidation over Co_3O_4/Al_2O_3"**. *J. Catal.* **2000**, *194*, 55–60.

[12] Thormahlen, P. **"Low-Temperature CO Oxidation over Platinum and Cobalt Oxide Catalysts"**. *J. Catal.* **1999**, *188*, 300–310.

[13] Yu, Y.; Takei, T.; Ohashi, H.; He, H.; Zhang, X.; Haruta, M. **"Pretreatments of Co_3O_4 at Moderate Temperature for CO Oxidation at -80 °C"**. *J. Catal.* **2009**, *267*, 121–128.

[14] Zhao, Z.; Lin, X.; Jin, R.; Dai, Y.; Wang, G. **"High Catalytic Activity in CO PROX Reaction of Low Cobalt-Oxide Loading Catalysts Supported on Nano-Particulate CeO_2-ZrO_2 Oxides"**. *Catal. Commun.* **2011**, *12*, 1448–1451.

[15] Finocchio, E.; Busca, G.; Lorenzelli, V.; Escribano, V. S. **"FTIR Studies on the Selective Oxidation and Combustion of Light Hydrocarbons at Metal Oxide Surfaces. Part 2.-Propane and Propene Oxidation on Co_3O_4"**. *J. Chem. Soc. Faraday Trans.* **1996**, *92*, 1587.

[16] Walton, A. S.; Fester, J.; Bajdich, M.; Arman, M. A.; Osiecki, J.; Knudsen, J.; Vojvodic, A.; Lauritsen, J. V. **"Interface Controlled Oxidation States in Layered Cobalt Oxide Nanoislands on Gold"**. *ACS Nano.* **2015**, *9*, 2445–2453.

[17] Liang, Y.; Wang, H.; Diao, P.; Chang, W.; Hong, G.; Li, Y.; Gong, M.; Xie, L.; Zhou, J.; Wang, J.; Regier, T. Z.; Wei, F.; Dai,H. **"Oxygen Reduction Electrocatalyst Based on Strongly Coupled Cobalt Oxide Nanocrystals and Carbon Nanotubes"**. *J. Am. Chem. Soc.* **2012**, *134*, 15849–15857.

[18] The Nobel Prize in Chemistry 2007. /http://www.nobelprize.org; G. Ertl, Reactions at surfaces: from atoms to complexity, Nobel lecture (2007).

[19] https://www.alcf.anl.gov/projects/catalyst-support-interactions browsed on 11/22/2016

[20] Se H. Oh.; Galen B. F.; Joyce E. C.; Goodman, D. W. **"Comparative kinetic studies of CO-O_2 and CO-NO reactions over single crystal and supported rhodium catalysts"**. *J. Catal.* **1986**, *100*, 360-376.

[21] Gao, F.; McClure, S. M.; Cai, Y.; Gath, K. K.; Wang, Y.; Chen, M. S.; Guo, Q. L.; Goodman, D. W. **"CO Oxidation Trends on Pt-Group Metals from Ultrahigh Vacuum to near Atmospheric Pressures: A Combined in Situ PM-IRAS and Reaction Kinetics Study"**. *Surf. Sci.* **2009**, *603*, 65–70.

[22] Gao, F.; Goodman, D. W. **"Reaction Kinetics and Polarization Modulation Infrared Reflection Absorption Spectroscopy Investigations of CO Oxidation over Planar Pt-Group Model Catalysts"**. *Langmuir* **2010**, *26*, 16540–16551.

[23] **Borodin, S.; Vogel, D.; Swaminathan, S.; Rohwerder M.** "Direct In-Situ Investigation of Selective Surface Oxidation During Recrystallization Annealing of a Binary Model Alloy"**, Oxid. Met.** 2016**, *85*, 51-63.**

[24] Hendriksen, B. L. M.; Bobaru, S. C.; Frenken, J. W. M. **"Looking at Heterogeneous Catalysis at Atmospheric Pressure Using Tunnel Vision"**. *Top. Catal.* **2005**, *36*, 43–54.

[25] Anic, K.; Bukhtiyarov, A. V.; Li, H.; Rameshan, C.; Rupprechter, G. **"CO Adsorption on Reconstructed Ir(100) Surfaces from UHV to Mbar Pressure: A LEED, TPD, and PM-IRAS Study"**. *J. Phys. Chem. C.* **2016**, *120*, 10838–10848.

[26] Herbschleb, C. T.; Van Der Tuijn, P. C.; Roobol, S. B.; Navarro, V.; Bakker, J. W.; Liu, Q.; Stoltz, D.; Cañas-Ventura, M. E.; Verdoes, G.; Van Spronsen, M. A.; Bergman, M.; Crama, L.; Taminiau, I.; Ofitserov, A.; van Baarle, GJ.; Frenken, JW. **"The ReactorSTM: Atomically Resolved Scanning Tunneling Microscopy under High-Pressure, High-Temperature Catalytic Reaction Conditions"**. *Rev. Sci. Instrum.* **2014**, *85,* 083703

[27] Schnadt, J.; Knudsen, J.; Andersen, J. N.; Siegbahn, H.; Pietzsch, A.; Hennies, F.; Johansson, N.; Mårtensson, N.; Öhrwall, G.; Bahr, S.; Mähl, S.; Schaff, O. **"The New Ambient-Pressure X-Ray Photoelectron Spectroscopy Instrument at MAX-Lab"**. *J. Synchrotron Radiat.* **2012**, *19*, 701–704.

[28] Balmes, O.; van Rijn, R.; Wermeille, D.; Resta, A.; Petit, L.; Isern, H.; Dufrane, T.; Felici, R. "The ID03 Surface Diffraction Beamline for in-Situ and Real-Time X-Ray Investigations of Catalytic Reactions at Surfaces". *Catal. Today* **2009**, *145*, 220–226.

[29] Sedona, F.; Rizzi, G. A.; Agnoli, S.; Llabres i Xamena, F. X.; Papageorgiou, A.; Ostermann, D.; Sambi, M.; Finetti, P.; Schierbaum, K.; Granozzi, G. **"Ultrathin TiOx Films on Pt(111): A LEED, XPS, and STM Investigation"**. *J. Phys. Chem. B* **2005**, *109*, 24411–24426.

[30] Li, F.; Parteder, G.; Allegretti, F.; Franchini, C.; Podloucky, R.; Surnev, S.; Netzer, F. P. **"Two-Dimensional Manganese Oxide Nanolayers on Pd(100): The Surface Phase Diagram"**. *J. Phys. Condens. Matter* **2009**, *21*, 134008.

[31] Joseph, Y.; Ranke, W.; Weiss, W. **"Water on FeO(111) and Fe_3O_4(111): adsorption behavior on different surface terminations"**. *J. Phys. Chem. B*, 2000, *104*, 3224–3236.

[32] Giovanardi, C.; Hammer, L.; Heinz, K. **"Ultrathin Cobalt Oxide Films on Ir(100)-(1×1)"**. *Physical Review B*, **2006**, *74*, 1–9.

[33] Rodriguez, J. **"Physical and Chemical Properties of Bimetallic Surfaces"**. *Surf. Sci. Rep.* **1996**, *24*, 223–287.

[34] De Santis, M.; Buchsbaum, A.; Varga, P.; Schmid, M. **"Growth of Ultrathin Cobalt Oxide Films on Pt(111)"**. *Phys. Rev. B - Condens. Matter Mater. Phys.* **2011**, *84*, 125430.

[35] Vaz, C. A. F.; Prabhakaran, D.; Altman, E. I.; Henrich, V. E. **"Experimental Study of the Interfacial Cobalt Oxide in Co_3O_4/α- Al_2O_3 (0001) Epitaxial Films"**. *Phys. Rev. B - Condens. Matter Mater. Phys.* **2009**, *80*.

[36] R.Masel, **"Principles of Adsorption and Reaction on Solid Surfaces"**, *Wiley Series in Chemical Engineering* , **1996**.

[37] Lennard-Jones J. E. **"Processes of adsorption and diffusion on solid surfaces"**, *Trans. Faraday Soc.*, **1932**, *28*, 333-359

[38] Scheffler M.; Stampfl C. **"*Theory of Adsorption on Metal Substartes"***, *Handbook of Surface Science*, **2000**, *2*.

[39] Lerch, D.; Klein, A.; Schmidt, A.; Müller, S.; Hammer, L.; Heinz, K.; Weinert, M. **"Unusual Adsorption Site of Hydrogen on the Unreconstructed Ir(100) Surface"**. *Phys. Rev. B.* **2006**, *73*, 075430.

[40] Langmuir, I. **"The Constitution and Fundamental Properties of Solids and Liquids. Part I. Solids"**. *J. Am. Chem. Soc.* **1916**, *252*, 2221–2295.

[41] Schmidt, A.; Meier, W.; Hammer, L.; Heinz, K. **"Deep-Going Reconstruction of Ir(100) - 5×1"**. J. Phys.: Condens. Matter. **2002**, *14*, 12353–12365.

[42]http://photon-science.desy.de/research/studentsteaching/primers/synchrotron_radiation/index_eng.html (Browsed on 10/21/2016)

[43] https://www.maxlab.lu.se/files/gaps1741.pdf (Browsed on 10/21/2016)

[44] Nyholm, R.; Andersen, J. N.; Johansson, U.; Jensen, B. N.; Lindau, I. **"Beamline I311 at MAX-LAB: A VUV/soft X-ray undulator beamline for high resolution electron spectroscopy".** Nucl. Instr. Meth. Phys. Res. A. **2001**, *467–468*, 520–524

[45] https://www.maxlab.lu.se/node/817 Browsed on 11/25/2016

[46] Hertz H. **"Ueber einen einuss des ultravioletten lichtes auf die electrische ent-Ladung (about an inuence of ultraviolet light on the electrische discharge)"**. Ann. Phys.**1887**, 267: 983–1000.

[47] Einstein, A. **"Ueber einen die erzeugung und des verwandlung lichtes betre_enden heuris-tischen gesichtspunkt (over a the production and transformation of light heuristic point of view)"**. Ann. Phys.**1905**, *132*

[48] Siegbahn, K. M. **"Electron Spectroscopy for Atoms, Molecules and Condensed Matter"**. *Nobel Lect.* **1981**, 63–92.

[49] Somorjai, G. **"Chemistry in Two Dimensions, Surfaces"**. Cornell University Press, Ithaca, **1981**.

[50] Hufner S. **"Photoelectron Spectroscopy"**. Springer-Verlag, Berlin Heidelberg, **1995**.

[51] Schattke W.; Van H. M. A. **"Solid-State Photoemission and Related Methods Theory and Experiment"**. Wiley-VCH, Weinheim, **2003**.

[52] Yeh, J. J.; Lindau, I. **"Atomic Data and Nuclear Data Tables"**. **1985**, *32*, 1.

[53] https://vuo.elettra.eu/services/elements/WebElements.html (Browsed on 09/09/2016)

[54] Coville, M.; Thomas, T. D. **"Molecular Effects on Inner-Shell Lifetimes: Possible Test of the One-Center Model of Auger Decay"**. *Phys. Rev. A* **1991**, *43*, 6053–6056.

[55] Briggs D.; Seah M. P. **"Practical Surface Analysis Auger and Xray Photoelectron SpectroscopySecond Edition, volume 1"**. John Wiley and Sons, **1990**.

[56] Tougaard, S.; Jorgensen, B. **"Inelastic Background Intensities in XPS Spectra"**. *Surf. Sci.* **1984**, *143*, 482–494.

[57] Doniach, S.; Sunjic, M. **"Many-Electron Singularity in X-Ray Photoemission and X-Ray Line Spectra from Metals"**. *J. Phys. C Solid State Phys.* **1970**, *3*, 285–291.

[58] Wertheim, G. K.; Butler, M. A.; West, K. W.; Buchanan, D. N. E. **"Determination of the Gaussian and Lorentzian Content of Experimental Line Shapes"**. Rev. Sci. Instrum. **1974**, *45*, 1369–1371.

[59] Schnadt J.; Knudsen J.; Andersen J. N.; Siegbahn H.; Pietzsch A.; Hennies F.; Johansson N.; Mårtensson N.; Öhrwall G.; Bahr S.; Mähld S.; Schaffd O. **"The new ambient-pressure X-ray photoelectron spectroscopy instrument at MAX-lab".** J. Synchrotron Radiat. **2012**, *19*, 701.

[60] SPECS GmbH, PHOIBOS NAP Hemispherical Energy Analyzer Series Near Ambient Pressure Analyzer, 2010. Technical Manual. http://www.specs.de/cms/upload/PDFs/SPECS_Prospekte/2010_11_PHOIBOS_150_NAP_product_brochure_final_web.pdf (Browsed on 11/20/2016)

[61] Binnig, G.; Rohrer, H.; Gerber, C.; Weibel, E. **"Tunneling through a Controllable Vacuum Gap"**. *Appl. Phys. Lett.* **1982**, *40*, 178–180.

[62] Binnig, G.; Rohrer, H.; Gerber, C.; Weibel, E. **"Surface Studies by Scanning Tunneling Microscopy"**. *Phys. Rev. Lett.* **1982**, *49*, 57–61.

[63] Binnig, G.; Rohrer, H. **"Scanning Tunneling Microscopy"**. *IBM J. Res. Dev.* **1986**, *30*, 279–293.

[64] Bardeen J. **"Tunnelling from a many-particle point of view"**. Phys. Rev. Lett. **1961**,6,57-59.

[65] Tersoff J.; Hamann D. R. **"Theory of the scanning tunneling microscope"**. *Phys. Rev. B.* **1985**, *31*, 805–813.

[66] De Broglie L. **"Researches on the quantum theory"**, thesis (paris). **1924**, 3, 22.

[67] Davisson, C.; Germer, L. H. **"Diffraction of Electrons by a Crystal of Nickel"**. *Phys. Rev.* **1927**, *30*, 705–740.

[68] D.E. Sands, Introduction to Crystallography (Dover Books.Publisher: Dover Publications) Publication Date: 1994-01-07

[69] Grant, J. T. **"A LEED Study of the Ir(100) Surface"**. *Surf. Sci.* **1969**, *18*, 228–238.

[70] Rhodin, T. N.; Broden G. **"Preparation and chemisorptive properties of the clean normal and reconstructed surfaces of Ir(100) - role of multiplets"**. Surf. Sci. **1976**, *60*, 466–484.

[71] Van Hove, M. A.; Koestner, R. J.; Stair, P. C.; Biberian, J. P.; Kesmodel, L. L.; Bartos, I.; Somorjai, G. A. **The Surface Reconstructions of the (100) Crystal Faces of Iridium, Platinum and Gold. II. Structural Determination by LEED Intensity Analysis"**. *Surf. Sci.* **1981**, *103*, 218–238.

[72] Lang, E.; Müller, K.; Heinz, K. LEED intensity analysis of the (1 × 5) reconstruction of Ir(100). Surf. Sci. **1983**, *27*, 347–365.

[73] Bickel, N.; Heinz, K. **"Quasidynamical LEED Structure Determination of the Ir(100)-(1×5) Surface Reconstruction"**. *Surf. Sci.* **1985**, *163*, 435–443.

[74] Ge, Q.; King, D. A.; Marzari, N.; Payne, M. C. **"First Principles Calculation of the Energy and Structure of Two Solid Surface Phases on Ir {100}"**. *Surf. Sci.* **1998**, *418*, 529–535.

[75] Spišák, D.; Hafner, J. **"Reconstruction and de-Reconstruction of the Ir(100) Surface and Ultrathin Fe/Ir(100) Films"**. *Surf. Sci*. **2003**, *546*, 27–38.

[76] Lerch, D.; Müller, S.; Hammer, L.; Heinz, K. **"Complex Adsorbate-Substrate Interplay of H on Ir(100)-(5×1)-hex: Density Functional Calculations"**. *Phys. Rev. B* **2006**, *74*, 1–9.

[77] Gilarowski, G.; Méndez, J.; Niehus, H. **"Initial Growth of Cu on Ir(100)-(5×1)"**. *Surf. Sci.* **2000**, *448*, 290–304.

[78] Küppers, J.; Michel, H. **"Preparation of Ir(100)-1 X 1 Surface Structures by Surface Reactions and Its Reconstruction Kinetics as Determined with LEED, UPS and Work Function Measurements"**. *Appl. Surf. Sci.* **1979**, *3*, 179–195.

[79] Ferstl, P.; Schmitt, T.; Schneider, M. A.; Hammer, L.; Michl, A.; Müller, S. **"Structure and Ordering of Oxygen on Unreconstructed Ir(100)"**. *Phys. Rev. B* **2016**, *93*, 235406.

[80] Kisters, G.; Chen, J. G.; Lehwald, S.; Ibach, H. **"Adsorption of CO on the Unreconstructed and Reconstructed Ir(100) Surface"**. *Surf. Sci.* **1991**, *245*, 65–71.

[81] Ali, T.; Klötzer, B.; Walker, A. V.; King, D. A. **"A Molecular Beam Study of Nonlinearity in the CO-Induced Surface Restructuring of Ir100"**. *J. Chem. Phys.* **1998**, *109*, 10996–11009.

[82] Anic, K.; Bukhtiyarov, A. V.; Li, H.; Rameshan, C.; Rupprechter, G. **"CO Adsorption on Reconstructed Ir(100) Surfaces from UHV to Mbar Pressure: A LEED, TPD, and PM-IRAS Study"**. *J. Phys. Chem. C.* **2016**, *120*, 10838–10848.

[83] Khatua, S.; Liu, Z. P.; King, D. A. **"NO Restructuring of Surface Ir and Bond Formation to Preadsorbed O on Ir{100} at 95 K"**. *Surf. Sci.* **2005**, *584*, 214–224.

[84] Hammer, L.; Meier, W.; Schmidt, A.; Heinz, K. **"Submonolayer Iron Film Growth on Reconstructed Ir(100)-(5×1)"**. *Phys. Rev. B.* **2003**, *67*, 125422.

[85] Gilarowski, G.; Méndez, J.; Niehus, H. **"Initial Growth of Cu on Ir(100)-(5×1)"**. *Surf. Sci.* **2000**, *448*, 290–304.

[86] Ali, T.; Walker, A. V; Klo, B.; King, D. A. **"A Molecular Beam Study of the H -Induced Lifting of the Ir {100} - (1×5) Reconstruction"**. *Surf. Sci.* **1998**, *414*, 304–314.

[87] Johnson, K.; Ge, Q.; Titmuss, S.; King, D. A. **"Unusual Bridged Site for Adsorbed Oxygen Adatoms: Theory and Experiment for Ir{100}-(1×2)-O"**. *J. Chem. Phys.* **2000**, *112*, 10460–10466.

[88] Grant, J. T. A. **"LEED Study of the Ir(100) Surface"**. *Surf. Sci.* **1969**, *18*, 228–238.

[89] Ghosh, P.; Narasimhan, S.; Jenkins, S. J.; King, D. A. **"Lifting of Ir{100} Reconstruction by CO Adsorption: An Ab Initio Study"**. *J. Chem. Phys.* **2007**, *126,* 244701.

[90] Strisland, F.; Ramstad, A.; Ramsvik, T.; Borg, A. **"CO Adsorption on the Rh(100) Surface Studied by High Resolution Photoelectron Spectroscopy"**. *Surf. Sci.* **1998**, *415*, 1020–1026.

[91] Martin, N. M.; Van Den Bossche, M.; Grönbeck, H.; Hakanoglu, C.; Zhang, F.; Li, T.; Gustafson, J.; Weaver, J. F.; Lundgren, E. **"CO Adsorption on Clean and Oxidized Pd(111)"**. *J. Phys. Chem. C.* **2014**, *118*, 1118–1128.

[92] Heinz, K.; Hammer, L. **"Epitaxial Cobalt Oxide Films on Ir(100)-the Importance of Crystallographic Analyses"**. *J. Phys. Condens. Matter.* **2013**, *25*, 173001.

[93] Gubo, M.; Ebensperger, C.; Meyer, W.; Hammer, L.; Heinz, K. **"Structural Elements in the Oxidation Process of a Single Cobalt Layer on Ir(100)-(1×1)"**. *Phys. Rev. B - Condens. Matter Mater. Phys.* **2011**, *83*, 1–8.

[94] Biedermann, K.; Gubo, M.; Hammer, L.; Heinz, K. **"Phases and Phase Transitions of Hexagonal Cobalt Oxide Films on Ir(100)-(1×1)"**. *J. Phys. Condens. Matter* **2009**, *21*, 185003.

[95] Ebensperger, C.; Gubo, M.; Meyer, W.; Hammer, L.; Heinz, K. **"Substrate-Induced Structural Modulation of a CoO(111) Bilayer on Ir(100)"**. *Phys. Rev. B - Condens. Matter Mater. Phys.* **2010**, *81,* 235405.

[96] Gubo, M.; Hammer, L.; Heinz, K. **"Laterally Nanostructured Cobalt Oxide Films on Ir(100). *Phys. Rev. B – Condens". Matter Mater. Phys.* 2012**, *85*, 1–4.

[97] Gubo, M.; Ebensperger, C.; Meyer, W.; Hammer, L.; Heinz, K. **"Substoichiometric Cobalt Oxide Monolayer on Ir(100)-(1×1)"**. *J. Phys. Condens. Matter.* **2009**, *21*, 474211.

[98] Giovanardi, C.; Hammer, L.; Heinz, K. **"Ultrathin Cobalt Oxide Films on Ir(100)-(1×1)"**. *Phys. Rev. B.* **2006,** *74*, 125429.

[99] Meyer, W.; Biedermann, K.; Gubo, M.; Hammer, L.; Heinz, K. **"Surface Structure of Polar Co_3O_4(111) Films Grown Epitaxially on Ir(100)-(1×1)"**. *J. Phys. Condens. Matter.* **2008**, *20*, 265011.

[100] Gubo, M.; Ebensperger, C.; Meyer, W.; Hammer, L.; Heinz, K.; Mittendorfer, F.; Redinger, J. **"Tuning the Growth Orientation of Epitaxial Films by Interface Chemistry"**. *Phys. Rev. Lett.* **2012**, *108,* 066101.

[101] Meyer, W.; Hock, D.; Biedermann, K.; Gubo, M.; Muller, S.; Hammer, L.; Heinz, K. **"Coexistence of Rocksalt and Wurtzite Structure in Nanosized CoO Films"**. *Phys. Rev. Lett.* **2008**, *101,* 016103.

[102] Bliem R.; McDermott E.; Pascal F.; Setvin M.; Gamba O.; Pavelec J.; Schneider M. A.; Schmid M.; Diebold U.; Blaha P.; Lutz H.; Parkinson G. S.: **"Subsurface cation vacancy stabilization of the magnetite (001) surface"**. *Science*, 2014, 346, 6214.

[103] Yeo, B. S.; Bell, A. T. **"Enhanced Activity of Gold-Supported Cobalt Oxide for the Electrochemical Evolution of Oxygen"**. *J. Am. Chem. Soc.* **2011**, 133, 5587–5593.

[104] Chun Y. M.; Zhen M.; Jin J. L.; Yong G. J.; Jie C.; Gao Q. L.; Zheng P. H.; Shi Z. Q. **"Mesoporous Co_3O_4 and Au/Co_3O_4 Catalysts for Low-Temperature Oxidation of Trace Ethylene"**, *J. Am. Chem. Soc.,* **2010**, 132, 2608–2613

[105] Bliem, R.; McDermott, E.; Ferstl, P.; Setvin, M.; Gamba, O.; Pavelec, J.; Schneider, M. A.; Schmid, M.; Diebold, U.; Blaha, P.; Hammer, L.; Parkinson, G. S. **"Subsurface Cation Vacancy Stabilization of the Magnetite (001) Surface"**. *Science* **2014**, *346*, 1215–1218.

[106] Novotný, Z.; Argentero, G.; Wang, Z.; Schmid, M.; Diebold, U.; Parkinson, G. S. **"Ordered Array of Single Adatoms with Remarkable Thermal Stability: Au/Fe_3O_4(001)"**. *Phys. Rev. Lett.* **2012**, *108*.

[107] Wendt, S.; Schaub, R.; Matthiesen, J.; Vestergaard, E. K.; Wahlström, E.; Rasmussen, M. D.; Thostrup, P.; Molina, L. M.; Lægsgaard, E.; Stensgaard, I.; Hammer, B.; Besenbacher, F. **"Oxygen Vacancies on TiO_2(1 1 0) and Their Interaction with H_2O and O_2: A Combined High-Resolution STM and DFT Study"**. *Surf. Sci.* **2005**, *598*, 226–245.

Paper I

Surface Science 656 (2017) 66–76

Contents lists available at ScienceDirect

Surface Science

journal homepage: www.elsevier.com/locate/susc

Adsorption of hydrogen on stable and metastable Ir(100) surfaces

Mohammad Alif Arman[a], Andreas Klein[b], Pascal Ferstl[b], Abhilash Valookaran[c], Johan Gustafson[a], Karina Schulte[d], Edvin Lundgren[a], Klaus Heinz[b], Alexander Schneider[b], Florian Mittendorfer[c], Lutz Hammer[b], Jan Knudsen[a,d,*]

[a] Division of Synchrotron Radiation Research, Department of Physics, Lund University, Sweden
[b] Lehrstuhl für Festkörperphysik, Universität Erlangen-Nürnberg, Germany
[c] Institute of Applied Physics and Center for Computational Materials Science, Vienna University of Technology, Austria
[d] MAX IV Laboratory, Lund University, Sweden

ARTICLE INFO

Keywords:
High resolution core level photoemission spectroscopy
Temperature programmed desorption
Density functional theory
Ir(100)
Hydrogen

ABSTRACT

Using the combination of high resolution core level spectroscopy and density functional theory we present a detailed spectroscopic study for all clean and hydrogen covered phases of Ir(100). The results are complemented by an investigation of the hydrogen desorption process from various phases using temperature programmed desorption spectroscopy and scanning tunneling microscopy. In total, all experimentally determined core level shifts match very well with those predicted by density functional theory based on established structural models. In particular, we find for the (bridge site) adsorption on the unreconstructed 1×1 phase that the initial core level shift of surface Ir atoms is altered by +0.17 eV for each Ir–H bond formed. In the submonolayer regime we find evidence for island formation at low temperatures. For the H-induced deconstructed 5×1-H phase we identify four different surface core level shifts with two of them being degenerate. Finally, for the reconstructed 5×1-hex phase also four surface components are identified, which undergo a rather rigid core level shift of +0.15 eV upon hydrogen adsorption suggesting a similarly homogeneous charge transfer to all Ir surface atoms. Thermodesorption experiments for the 5×1-H phase reveal two different binding states for hydrogen independent of the total coverage. We conclude that the surface always separates into patches of fully covered deconstructed and uncovered *re*constructed phases. We could also show by tunneling microscopy that with the desorption of the last hydrogen atom from the *de*constructed unit cell the surface instantaneously reverts into the *re*constructed state. Eventually, we could determine the saturation coverage upon molecular adsorption for all phases to be $\theta_{max}^{1\times1-H} = 1.0$ ML, $\theta_{max}^{5\times1-H} = 0.8$ ML, and $\theta_{max}^{5\times1-hex-H} \geq 1.0$ ML.

1. Introduction

The Ir(100) surface is quite special from a structural point of view because it can be prepared in two modifications: a bulklike terminated, unreconstructed 1×1 surface as well as a 5×1 reconstructed surface. In the reconstructed phase six Ir rows are arranged quasi-hexagonally close-packed on top of five rows of the square substrate [1,2], i.e. the outermost layer hosts 20% more Ir atoms than a bulklike 1×1 layer. The crystallographic structure of this so-called 5×1-hex reconstruction was studied in detail for decades leading to the following well-accepted structural model: the registry between top layer and substrate is defined via the occupation of two bridge sites, which was determined first on the basis of low energy electron diffraction (LEED) intensity analyses [3–6]. Later, this "buckled two-bridge" model was corroborated by density functional theory (DFT) calculations [7–9] and scanning tunneling microscopy (STM) investigations [10,11]. The mismatch between the hexagonal top layer and the square substrate lattice also produces an extended strain field, which induces significant atomic displacements down to the fourth layer [11] and thus stabilizes the reconstruction [7,9].

The driving force for the quasi-hexagonal reconstruction is to reduce the undercoordination of surface atoms. It is therefore not surprising that chemisorption of many adsorbates, partly restoring the truncated bonds of surface atoms, leads to the lifting of the reconstruction (called *deconstruction*), whereby the surplus Ir atoms of the top layer are expelled. This happens instantaneously for the adsorption of reactive gases like O_2 [2,12,13], CO [14–16] or NO [17], but also of metals [10,18]. For the weaker bound hydrogen the energy balance also promotes a lifting of the reconstruction [19,9] but the excess energy is not sufficient to surmount the energy barrier for pulling an Ir atom out

* Corresponding author at: Division of Synchrotron Radiation Research, Department of Physics, Lund University, Sweden.
E-mail address: jan.knudsen@sljus.lu.se (J. Knudsen).

http://dx.doi.org/10.1016/j.susc.2016.10.002
Received 24 August 2016; Accepted 4 October 2016
Available online 07 October 2016
0039-6028/

of the close-packed top layer. Hence, the reconstructed surface can be covered by hydrogen at low temperatures in a meta-stable state called 5×1-hex-H phase [9,20]. However, already at temperatures of about 200 K the H-induced lifting of the reconstruction starts at defect sites like step edges or reconstruction domain boundaries, where the activation barrier is reduced, and proceeds in a zip-like mechanism all over the terraces [21]. This finally results in a bulklike 1×1 top layer which, however, is covered by straight monatomic chains of Ir excess atoms due to the lack of any Ir adatom diffusion [18]. Since the reconstructed phase contained 20% extra atoms, the mutual distance of the monatomic Ir chains will still be fivefold (on average) giving rise to again a 5×1-periodic LEED pattern. This newly formed phase is virtually an unreconstructed surface covered by Ir chains and hydrogen and therefore it will be called in the following the *deconstructed 5×1-H* phase, in order to distinguish it from both the reconstructed 5×1-hex and the unreconstructed 1×1 phases. The persistence of the 5×1 LEED pattern (though with drastically changed spot intensities) upon H adsorption caused the deconstruction of the surface to be overseen for quite a long time and was finally revealed by real space STM investigations [18,21]. With this method it was also possible to prove another reported H-induced "3×1" surface modification [22,23] to be non-existing. Rather, under the given preparation conditions, an alternating 3-fold/7-fold sequence of chain distances occurs, leading to an in total 10×1 periodicity. The particularly intense superstructure spots at 3/10 and 7/10 positions in LEED were, however, misinterpreted as third order diffraction beams.

Nowadays, the crystallographic structures of the reconstructed and the unreconstructed Ir(100) surfaces modifications – both clean and hydrogen covered – as well as the deconstructed H-induced 5×1-H phase are undisputed and known in much detail from the cited LEED, STM, and DFT studies. From the DFT studies also the adsorption sites and binding energies of hydrogen are predicted, which could be proven experimentally only in the case of the unreconstructed 1×1-H phase [19] by quantitative LEED and temperature programmed desorption spectroscopy (TPD) so far. Additionally, for the 5×1-hex-H phase the H coverage and adsorption geometry was inferred indirectly from a comparison of Ir substrate relaxations derived from a LEED intensity analysis with corresponding DFT model calculations [20]. TPD studies for H-adsorption on the reconstructed phase have also been performed [24,22], but the presented data sets deviate substantially from each other. Moreover, without the knowledge of the correct structural model, which was not available at that time, but is a prerequisite for the quantitative analysis of binding energies, the reported values for the desorption energy have to be questioned.

In contrast to the extensive DFT, LEED, STM, and TPD studies on the various clean and H-covered Ir(100) phases very little photoelectron spectroscopy (XPS) work has been performed so far. We are only aware of the early studies by van der Veen et al. [25] and Barrett et al. [26], but these studies only addressed the clean Ir(100) surface modifications. In the present study, we give a detailed spectroscopic picture for all clean and hydrogen covered phases of Ir(100) using the combination of synchrotron based high resolution core level spectroscopy (HRCLS) and DFT calculated core level shifts (CLS). From that we obtain information about the charge transfer to and between surface atoms. Moreover, we will demonstrate that HCRLS is able to quantitatively reveal the relative occupation of adsorption sites by hydrogen, which hardly can be provided by other methods. Therefore, it is also a rather accurate and quantitative tool to determine the hydrogen coverage of a specific surface phase at a given temperature, whereas TPD only probes the phases present at the desorption temperature. We complement this XPS study by an analysis of further series of TPD spectra, which were – in contrast to previous studies – taken for *well-characterized* reconstructed 5×1-hex-H and deconstructed 5×1-H phases as well as by an STM investigation of structural transition states during H-desorption. Both will provide new insights into the energetic balance of *re*constructed and *de*constructed surfaces and the kinetic processes involved in the transitions between each other.

2. Experimental and calculational details

The HRCLS experiments were performed at beamline I311 at the MAX IV Laboratory in Lund, Sweden [27]. The base pressure of the endstation of this beamline was $\sim 1 \cdot 10^{-10}$ mbar during our measurements. The sample temperature was measured with a type K thermocouple spot welded to the side of the Ir crystal. All Ir $4f_{7/2}$ core level (CL) spectra were recorded at a sample temperature of about 100 K and collected in normal emission with a photon energy of 120 eV to maximize the surface sensitivity. The C 1s and the O 1s spectral regions were used to check the cleanliness of all investigated surface preparations and no traces of CO or oxygen were found unless it is specified in the text.

For the fitting of the CL spectra we first subtracted a polynomial background and the remaining spectra were fitted with Doniach-Šunjić functions convoluted with Gaussians. To reduce the number of free parameters in the curve fitting procedure we used for all components one common Lorentzian full width at half maximum (LFWHM) and one common Gaussian full width at half maximum (GFWHM). Further, the asymmetry parameter was varied in a very narrow range (0.13 ± 0.02). For the temperature dependent measurements in Fig. 2 we used "all-at-once" fitting with identical components varying only their relative intensities.

The TPD and STM experiments were performed in the lab in Erlangen. A beetle-type STM was operated at room temperature and an etched tungsten tip was used. The bias voltage was applied to the sample and varied in the range 2–1000 meV. The tunneling current was in the range 2–3 nA. The TPD spectra were collected using a quadrupole mass spectrometer with a Feulner cup [28] to reduce unwanted contributions from the sample holder. The temperature scan was performed with a heating rate of 1 K/s enabled by temperature-controlled electron bombardment of the crystal from the rear and the temperature was measured by a type K thermocouple. At the beginning of the temperature ramp the switch-on of the filament produced a sudden hydrogen gas burst spoiling the low-temperature start of the TPD spectra. For that reason we truncated the part below 200 K in all spectra. All values given for pressure and exposures are based on the uncorrected reading of the ion gauges and might therefore underestimate the true values. Further details of the apparatus are described in our earlier study on H/Ir(100)-1×1 [19].

The preparation of the different phases followed in all experiments well-established recipes, which were developed in the Erlangen lab to produce most homogeneous phases as verified by STM control measurements. The clean Ir(100)-5×1-hex surface was prepared by cycles of room temperature sputtering and oxygen annealing at around 1300 K followed by a flash to 1420 K to remove any residual oxygen. The hydrogen saturated 1×1-H phase resulted from the reconstructed phase by subsequent oxygen and hydrogen exposure. First oxygen was dosed (pressure $\sim 1 \cdot 10^{-7}$ mbar) while the temperature was lowered from 1273 K to room temperature. This procedure leads to a p(2×1)-O superstructure on a perfectly unreconstructed Ir(100) substrate [13]. Finally, oxygen was reduced by dosing hydrogen ($5 \cdot 10^{-8}$ mbar) at 550 K, whereby the produced water desorbs. Subsequent cooling down to 110 K saturated the surface with hydrogen. The clean Ir(100)-1×1 can be obtained simply by flashing the Ir(100)-1×1-H surface to 500 K. The fully deconstructed 5×1-H phase was prepared by dosing about 50 L of hydrogen onto the clean reconstructed 5×1-hex surface at temperatures around 300 K.

In order to increase the hydrogen coverage on the Ir(100)-1×1-H phase we also offered atomic hydrogen instead of molecular H_2. The atomic hydrogen was produced by a commercial EFM-H cracker (Omicron) operated with a heating power of 30 W. Unfortunately, this led to an increase of the chamber pressure to about $5 \cdot 10^{-9}$ mbar during operation, which was mainly caused by CO.

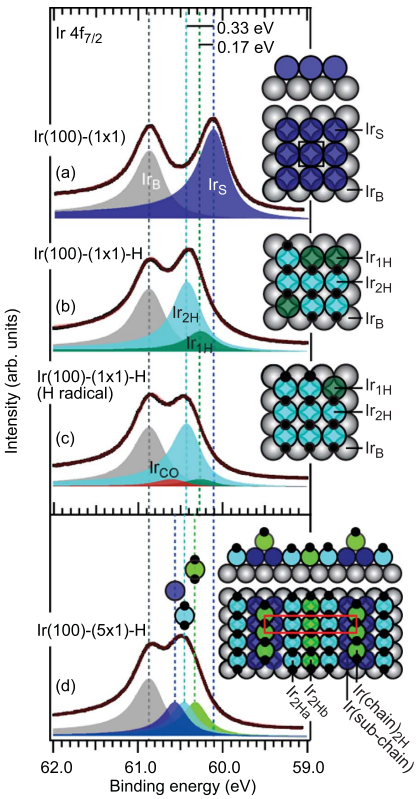

Fig. 1. Ir $4f_{7/2}$ spectra of the following surface phases: (a) clean Ir(100)-(1×1), (b) Ir(100)-(1×1)-H prepared with molecular hydrogen, (c) Ir(100)-(1×1)-H prepared with atomic hydrogen, (d) deconstructed Ir(100)-(5×1)-H. The experimental spectra are shown as black dots, the fits as transparent solid red lines, and the filled curves represent the components of each fit. To the right schematic models of the different phases are displayed. (For interpretation of the references to color in this figure legend, the reader is referred to the web version of this article).

The density functional theory calculations were performed with the the Vienna Ab initio Simulations Package (VASP) [29], using PAW potentials [30] and the PBE exchange-correlation functional [31] and a cutoff energy of 400 eV. The surface was modelled with a 7 layer slab, where the uppermost 4 Ir layers were allowed to relax. The Brillouin zone integration was performed using a (3×15×1) k point mesh for the (5×1) surface cell. The Ir $4f_{7/2}$ core level shifts were evaluated in the initial state approximation.

3. Hydrogen at the unreconstructed Ir(100)-1×1-H surface

Fig. 1 displays the Ir $4f_{7/2}$ spectra recorded for the clean (a) and hydrogen covered (b,c) unreconstructed Ir(100) surfaces (1×1 and 1×1-H phases). For comparison also the deconstructed Ir(100)-5×1-H phase is shown in Fig. 1(d), which will be discussed in detail in the next section. According to accepted structural models from previous studies [19,32], which are sketched to the right of the spectra, hydrogen always adsorbs in bridge sites.

Starting with the simplest phase, i.e. the metastable Ir(100)-1×1, we observe one bulk component, Ir_B, and one surface component, Ir_S, at binding energies of 60.85 eV and 60.08 eV, respectively (Fig. 1(a)). Our deconvolution procedure reveals that the best fit is obtained with LFWHM and GFWHM of 0.30 eV and 0.20 eV, respectively. The LFWHM found here is close to the value that has been used previously for fitting the Ir $4f_{7/2}$ spectra on the Ir(111) surface [33]. Finally, we determine the relative intensity ratio between the Ir_S and Ir_B components to 1.4: 1, i.e. the average probing depth is equal to 1.7 layers at our experimental conditions. The experimentally determined −0.77 eV core level shift (CLS) between Ir_S and Ir_B components is in good agreement with the value of −0.73 eV predicted by our DFT calculations for the Ir(100)-1×1 phase. In addition, our DFT calculations reveal a small +0.10 eV CLS for the first subsurface Ir layer making the agreement even better as the effective probing depth is small.

Our experimentally determined CLS of −0.77 eV is slightly larger than the value of −0.68 eV and −0.55 eV reported by van der Veen et al. [25] and Barrett et al. [26], respectively. This discrepancy – though being quite small – seems to be beyond the error limits of the respective fit procedures. The only explanation we have at the moment is that some residual hydrogen or CO contamination (which leads to a reduction of the CLS as shown below) might have affected the results of the earlier studies. Further we note, that we measure a similar width of the Ir_S and Ir_B components in Fig. 1(a) and we, therefore, find no experimental evidence for a significant different CLS for the 1st subsurface layer with respect to the deeper layers, in contrast to the study of Barrett et al. [26]. As a final observation for the clean Ir(100)-1×1 surface we note that its CLS of the Ir_S component (−0.77 eV) is significantly larger compared to the close-packed Ir(111) surface with a CLS value of the surface component of −0.50 eV [34] and −0.49 eV [25], respectively.

After dosing molecular hydrogen ($5{\cdot}10^{-8}$ mbar) onto the Ir(100)-1×1 surface while cooling the sample from room temperature to 110 K to produce the Ir(100)-1×1-H phase we find that the surface related peak in the Ir $4f_{7/2}$ spectra shifts towards the bulk component, *cf.* Fig. 1(b). This qualitative behavior has already been reported by van der Veen et al. [25], yet not quantitatively evaluated. For the curve fitting of this spectrum (and the following ones) we reduced the number of free parameters by locking the binding energy position of the Ir_B component and the LFWHM and GFWHM of all components to the values obtained for the clean Ir(100)-1×1 spectrum. From the deconvolution we find that the clean surface peak Ir_S has disappeared completely. Instead, two new components are found at 60.25 eV and 60.41 eV, which are included in Fig. 1(b). The intensity ratio between the sum of these two peaks and the Ir_B component is maintained in the fit at 1.4:1 proving that both components have to be assigned to Ir surface atoms. Compared to the former Ir_S peak of the clean surface the first smaller component is shifted by +0.17 eV and the second larger component by +0.33 eV. Hence, we assign them to one-fold and two-fold H-coordinated Ir surface atoms and call them Ir_{1H} and Ir_{2H}, respectively.

By DFT we checked our assignment and calculated the CLS of the Ir_{1H} component from a p(2×1)-H structure with 0.5 monolayer (ML) coverage and the Ir_{2H} component from a p(1×1)-H structure with 1 ML coverage (both calculated for the known bridge site occupation of hydrogen [19]). These calculations revealed CLSs of −0.63 eV and −0.52 eV with respect to the bulk value for the Ir_{1H} and Ir_{2H} components, respectively. Using the DFT value for the Ir_S component (−0.73 eV) for the clean surface we can derive a theoretical prediction for the *H-induced shift* of the surface components, which becomes +0.10 eV (Ir_{1H}) and +0.21 eV (Ir_{2H}). Compared to the corresponding experimentally determined shifts (+0.17 eV and +0.33 eV) our DFT calculations underestimate the H-induced shift, but they confirm nicely the constant CLS *per H-bond* fully consistent with the result of our curve fitting. All experimentally determined and calculated CLS values for the clean and H-covered phases are compiled for comparison in

Table 1
Measured and calculated core levels shifts for Ir surface atoms in the various clean and H-covered phases on Ir(100). All shifts are given with respect to Ir bulk atoms.

Component	Experimental CLS (eV)	Theoretical CLS (eV)
unreconstructed Ir(100)-1×1		
Ir_S	−0.77	−0.73
$Ir_{Subsurface}$	–	+0.10
Ir(100)-1×1-H		
Ir_{1H}	−0.60	−0.63
Ir_{2H}	−0.44	−0.52
Ir_{CO}	−0.25	
deconstructed Ir(100)-5×1-H		
$Ir(chain)_{2H}$	−0.55	−0.58
Ir(sub-chain)	−0.30	−0.32
Ir_{2Ha}	−0.41	−0.47
Ir_{2Hb}	−0.55	−0.56
reconstructed Ir(100)-5×1-hex		
Ir_1	−0.32	−0.34
Ir_2	−0.72	−0.70
Ir_3	−0.40	−0.40
Ir_4	−0.57	−0.55
reconstructed Ir(100)-5×1-hex-H		
Ir_1	−0.17	− 0.37*
Ir_2	−0.57	−0.75 (2)*, −0.68 (2')*
Ir_3	−0.25	−0.49 (3)*, −0.39 (3')*
Ir_4	−0.42	−0.65*

*Calculated values for the model of Ref. [20] with a coverage of 0.6 ML.

Table 1.

Previous TDS and quantitative LEED experiments in combination with DFT calculations have shown that the saturation coverage is close to 1 ML [19]. As we observe two surface components (Ir_{1H}) and (Ir_{2H}) for single and twofold H-coordinated Ir surface atoms, we have to conclude that the 1×1-H structure formed is defective under the chosen experimental conditions. Based on the relative intensities of the Ir_{1H} (0.23) and Ir_{2H} (0.77) components we can calculate the hydrogen coverage as: 0.23·0.5 ML+0.77·1 ML=0.88 ML. The hydrogen coverage calculated from the Ir $4f_{7/2}$ spectrum acquired after exposing the Ir(100)-1×1 surface to ~35 L of H_2 right at room temperature (not shown) yielded a very similar coverage of ~0.9 ML. Therefore, we conclude that the maximum hydrogen coverage within the Ir(100)-1×1-H phase to be achieved in our HRCLS experiments is always ~0.9 ML irrespective of the dosing temperature.

In order to fill the remaining vacancies and further increase the hydrogen coverage we exposed an Ir(100)-1×1 surface to atomic hydrogen. Fig. 1(c) shows the resulting Ir $4f_{7/2}$ spectrum and its deconvolution into different components after saturating the surface with atomic hydrogen. For the deconvolution the binding energy positions as well as the LFWHM and GFWHM of the Ir_B, Ir_{1H}, and Ir_{2H} components were again locked at the values determined before. Apart from the Ir_{1H} and Ir_{2H} components we observe one additional surface component at 60.6 eV (Ir_{CO}) with a relative weight of 10%, which we assign to coadsorbed CO unavoidably released into the chamber when operating the H-cracker. The observed CLS of this Ir_{CO} component (−0.25 eV) fits well with the value of −0.24 eV, which we found for a c(2×2)-CO structure (unpublished data), where CO molecules adsorb in atop positions on the Ir(100)-1×1 surface [35]. Assuming that in the present case the 0.1 ML CO molecules will adsorb at top sites as well and this will most likely block adjacent bridge sites for hydrogen adsorption. Hence, at least some of the Ir atoms next to CO-coordinated one can only be single-coordinated to hydrogen (Ir_{1H}). Lacking any information on the distribution of CO molecules at the surface (dispersed or in compact islands) we cannot really judge on the hydrogen filling of the remaining surface area with hydrogen from our

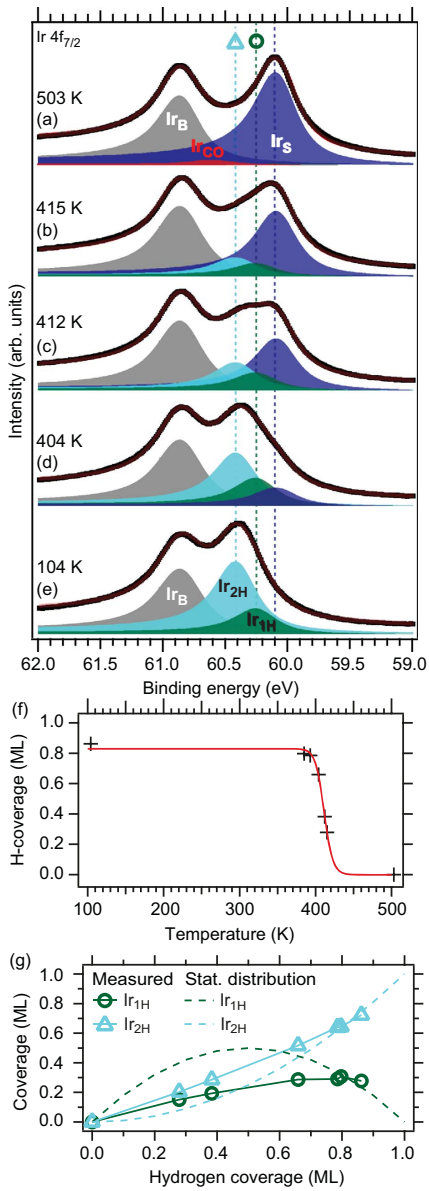

Fig. 2. (a-e) Ir $4f_{7/2}$ spectra of the Ir(100)-1×1-H phase flash-heated to stepwise increased temperatures. Experimental spectra are shown by black dots, the fits as transparent solid lines, and the filled curves represent the components of each fit. (f) Hydrogen coverage calculated from the curve-fitted areas of the Ir_{1H} and Ir_{2H} components shown in panel (a-e) as a function of temperature. (g) Comparison of measured Ir_{1H} and Ir_{2H} proportions with a statistical site distribution (dashed lines, see text for details). (For interpretation of the references to color in this figure legend, the reader is referred to the web version of this article).

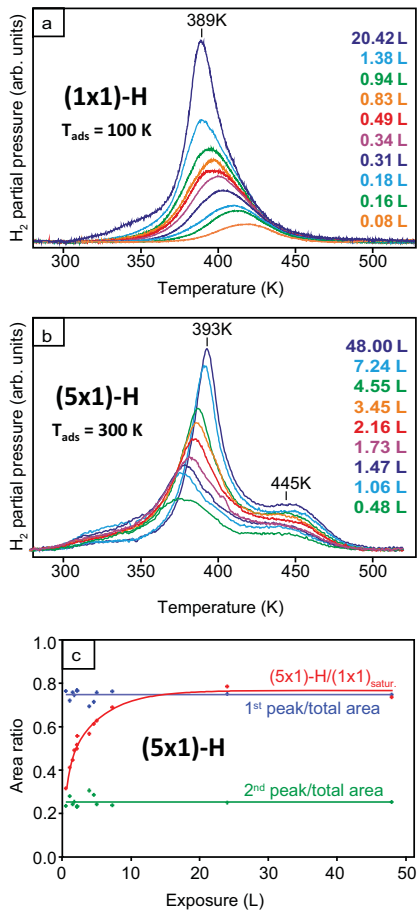

Fig. 3. (a) Series of TPD spectra of hydrogen from the unreconstructed Ir(100)-1×1-H phase for various initial exposures at around 100 K (partly reproduced from Ref. [19]). (b) Series of TPD spectra of hydrogen recorded after various initial hydrogen exposures at the reconstructed Ir(100)-5×1-hex phase at 300 K, which led to a local deconstruction into the 5×1-H phase. (c) Analysis of peak areas from (b). Red curve: Total areas of the TPD curves as a function of exposure and normalized to the area for saturation coverage of the 1×1-H phase taken from (a). Also displayed are the relative area fractions of the lower (blue) and higher temperature peaks (green) in (b). (For interpretation of the references to color in this figure legend, the reader is referred to the web version of this article).

data. The further discussion of the saturation coverage for this and the other hydrogen covered phases is postponed to the last section.

After having identified all spectral components within an Ir $4f_{7/2}$ spectrum of the clean and H-covered unreconstructed Ir(100) surface we take a closer look at less dense hydrogen phases realized by desorbing hydrogen from the saturated surface. Fig. 2(a)–(e) shows a series of Ir $4f_{7/2}$ spectra recorded after flashing the Ir(100)-1×1-H phase to stepwise increasing temperatures and subsequent cool-down to 100 K. The successful fits of the spectra reveal that during the whole desorption sequence the spectra can be reproduced by a mere superposition of the formerly determined Ir_B, Ir_S, Ir_{1H}, and Ir_{2H} components. Only their relative intensities need to be fitted.

In Fig. 2(f) the actual hydrogen coverage calculated from the relative proportions of Ir_{1H} and Ir_{2H} components is plotted as a function of flash temperature. It can be seen that hydrogen desorbs around 400 K in agreement with the TPD results of Lerch et al. [19], *cf.* Fig. 3(a). We further compare in Fig. 2(g) the fitted proportions of Ir_{1H} (open circles) and Ir_{2H} (open triangles), now plotted as a function of hydrogen coverage (determined as above from the relative weights of the Ir_{1H} and Ir_{2H} components), with the expectations for a statistical site occupation (dashed lines). Since for a statistical distribution the occupation probability of each site is just equal to the coverage θ, it follows that the statistical proportions can be calculated as $Ir_{1H} = 2\theta\cdot(1-\theta)$ and $Ir_{2H} = \theta^2$. Already a visual inspection of Fig. 2(g) reveals that the measured Ir_{1H} and Ir_{2H} proportions deviate substantially from the statistical distribution. For all coverages below 0.85 ML there is an increased proportion of the Ir_{2H} component in the experiment (up to a factor of 2) at the expense of the Ir_{1H} component. Moreover, the Ir_{1H} component never surmounts the Ir_{2H} one. This observation suggests that for a partial coverage the adsorbed hydrogen atoms tend to nucleate at low temperature into densely-packed 1×1-H islands rather than spreading out homogeneously on the surface, i.e. there must be an attractive H-H interaction. This conclusion is in line with DFT predictions of previous work by Lerch et al. [19], where an energy gain of some meV per H atom (depending on coverage) was calculated for 1×1-H island formation. Such a small energy gain is consistent with the observation that even at temperatures as low as 100 K in our measurement the island formation still remains incomplete, because otherwise there would be no Ir_{1H} component at all. It also explains why this effect could not be verified by the previous TPD experiments [19], which probe the adsorption site distribution only at the (even much higher) desorption temperature of around 400 K.

4. Hydrogen at the deconstructed Ir(100)-5×1-H surface

By dosing 60 L H_2 onto the Ir(100)-5×1-hex phase at room temperature the surface completely converts into the deconstructed Ir(100)-5×1-H phase with monatomic Ir wires on the otherwise unreconstructed surface [21] as explained in the introduction. A structural model based on the DFT calculations of Ref. [32] is displayed in Fig. 1(d). According to this model hydrogen should assume bridge sites on top of the monatomic rows as well as on the three center substrate rows inbetween leading to a total (theoretical) coverage of 0.8 ML. Inspection of the ball model reveals that Ir surface atoms named Ir_{2Ha} and Ir_{2Hb} have a local binding configuration identical to the Ir_{2H} atoms found for the Ir(100)-1×1-H phase, *cf.* Fig. 1(b),(c). Based on this observation we expect that the DFT calculation for this phase should produce quite similar CLSs for these Ir_{2Ha} and Ir_{2Hb} surface atoms as for the Ir_{2H} component (−0.52 eV) of the 1×1-H phase. This is indeed the case though the calculated energies split up more than expected (± 0.05 eV), resulting in a CLS of −0.47 eV for the Ir_{2Ha} and −0.56 eV for the Ir_{2Hb} component (see also Table 1). This splitting gives an indication of the limits of the local character of this method, i.e. to what extent the environment will affect the CLSs. DFT further reveals that the CLS of the component assigned to the chain atoms ($Ir(chain)_{2H}$), being also two-fold coordinated to hydrogen but strongly undercoordinated with respect to Ir atoms, is (accidently) almost identical to that of the Ir_{2Hb} atoms, which comes as a real surprise. Non surprising, in contrast, is that the calculated CLS for the higher coordinated Ir(sub-chain) atoms lies closer to the bulk value (−0.32 eV) than for any other surface atoms, even when fully H-coordinated.

Since the predicted differences of the CLSs between the various components are quite small, we had to minimize the number of free parameters in the curve fitting procedure as much as possible. So, we again fixed the GFWHM and LFWHM of all components to 0.20 eV and

0.30 eV, respectively. Moreover, triggered by the DFT prediction we assumed an identical CLS for the Ir_{2Hb} and $Ir(chain)_{2H}$ atoms and also did not allow for any vacancies. These restrictions led to only three components ($Ir(chain)_{2H}$+Ir_{2Hb}, Ir_{2Ha}, and Ir(sub-chain)) with equal relative area. As seen from Fig. 1(d) even with these restrictions a nice fit of the experimental Ir $4f_{7/2}$ spectrum could be achieved using CLSs that closely match the DFT prediction, *cf.* Table 1. A final interesting feature of the fit displayed in Fig. 1(d) is that the ratio between the cumulated areas of all surface components ($Ir(chain)_{2H}$+Ir_{2Hb}, Ir_{2Ha}, and Ir(sub-chain)) and the bulk component (Ir_B) has now increased by 21% to 1.7:1 compared to the clean Ir(100)-1×1 phase. This corresponds well with the 20% extra surface atoms in the Ir(100)-5×1-H phase.

Information on the energetics of hydrogen adsorbed in this deconstructed 5×1-H phase can be obtained from temperature programmed desorption spectroscopy. Fig. 3 compares series of TPD spectra for various initial hydrogen exposures recorded for a H-covered 1×1-H phase (Fig. 3(a)) and the H-induced 5×1-H phase (Fig. 3(b)). The series for the 1×1-H phase shows the common behavior for associative (second order) desorption of a weakly interacting adsorbate from a single-site lattice with a rather constant width and a peak maximum shifting slightly towards lower temperatures. These spectra were discussed and evaluated in detail by Lerch et al. [19] yielding a practically coverage-independent binding energy of 460 meV/H-atom for the unreconstructed Ir(100) surface. For the 5×1-H phase, in contrast, the TPD spectra appear significantly different. Even for the smallest exposure we already find two well resolved peaks around 370 K and 440 K. (The small hump in the spectra in the range 300–350 K appears similarly for all H phases and is therefore assigned as an artefact of unwanted H-desorption from either the sample holder or the Feulner cup.) With increasing exposure (and total coverage) both TPD peaks grow strictly in parallel as seen from their constant area fraction with respect to the total desorption spectrum as a function of exposure as displayed in Fig. 3(c). Within the limits of error the lower temperature peak always contains three times as many H-molecules than the higher temperature one pointing towards a 3:1 ratio of corresponding adsorption sites. With increasing coverage the larger peak shifts towards higher temperatures (393 K at saturation coverage) and – most unusual – also narrows significantly. For the second smaller peak no such changes in width and position are found within the accuracy of the measurement. Finally, the total peak area reaches a saturation value of only about 80% of that of the Ir(100)-1×1-H phase (red curve in Fig. 3(c)).

In order to understand this quite peculiar desorption behavior one has to recall the mechanism by which the deconstructed 5×1-H phase is formed from the reconstructed 5×1-hex phase. As discussed in detail in Refs. [18,21] the H-induced deconstruction proceeds in a zip-like process, whereby Ir atoms from the most protruding rows of the quasi-hexagonally top layer are expelled one-by-one while the neighboring surface Ir atoms reorder into the bulklike square arrangement. The process always starts at defect sites, like step edges or domain boundaries of the reconstruction, where the activation energy for expelling single atoms is reduced, and proceeds strictly one-dimensionally across the whole terrace. As a result single deconstructed stripes 4–5 atoms wide develop with a monatomic Ir row on top. The driving force for this process is the strong difference in binding energy for hydrogen on the reconstructed and on the deconstructed surface. According to DFT calculations [9,32] the binding energies of H on top of the single atomic row are higher by about 400 meV than on the most favorite adsorption site of the hexagonally reconstructed surface. Also the bridge sites of the deconstructed area in between these rows are still favorable by about 250 meV. So, there is a large energy gain for hydrogen atoms to reside at the deconstructed patches, which by far exceeds the energetic price for lifting the quasi-hexagonal reconstruction and forming the deconstructed state. From the energetic balance we have to infer that for hydrogen dosages below the saturation value the surface area is always divided into two distinct regimes: fully H-saturated deconstructed stripes are coexisting with completely uncovered 5×1-hex stripes. Increasing the coverage just means an increase of the deconstructed area fraction at the expense of the reconstructed part. As a consequence, the shape of the TPD spectra should not change upon increasing the total hydrogen coverage of the surface. This roughly corresponds to the experimental observation, in particular it explains the appearance of both peaks from the very beginning. According to the accepted model for this 5×1-H phase (*cf.* Fig. 1(d)) we attribute the second peak at around 445 K to more strongly bound hydrogen atoms adsorbed in the bridge sites of the monatomic Ir rows and the lower temperature peak at around 393 K to hydrogen on the unreconstructed regions between the rows. The latter sites are locally identical to those on the 1×1-H phase and correspondingly the desorption peak appears at practically the same temperature, at least for maximum coverage, which corroborates our assignment. The constant ratio of 1:3 between these two peaks is also in line with the DFT prediction that the most stable coverage of the 5×1-H phase hosts exactly four hydrogen atoms within the unit cell (one on the chain and three in-between), i.e. the saturation coverage is expected to be 0.8 ML. The discussion of the absolute coverage of this phase (together with that of the other ones), however, is postponed to the last chapter. Finally, the narrowing of the lower temperature peak and its energy shift with temperature needs to be explained. As demonstrated by a series of STM images displayed in Ref. [21] there is only a small tendency to form islands of the deconstructed 5×1-H phase with significant extension in the direction perpendicular to the monatomic Ir rows, i.e. every single deconstruction stripe grows more or less independently. Hence, it has at both sides a domain boundary towards the reconstructed phase. Subsequently, most of the hydrogen atoms occupy sites right at, or close to, these boundaries and so most probably will have a somewhat modified binding energy. These energetic variances are responsible for the observed broadening of the corresponding desorption peak. Since the deconstruction stripes nucleate only gradually at the surface, the desorption peak will also narrow only gradually and a coverage close to saturation is needed before the domain boundaries will die out substantially and the desorption peak finally sharpens. Under the assumption that the binding energy of hydrogen will be somewhat reduced in the vicinity of domain boundaries (which has not been proven, but appears likely) an shift of the desorption peak maximum as observed experimentally will inevitably result.

As mentioned above, the deconstruction process of the Ir(100) surface upon hydrogen exposure has already been studied by STM in real space [18,21]. Unknown so far is what happens structurally at the surface when hydrogen desorbs. To answer this question we started each single experiment with a fully developed, deconstructed 5×1-H phase and performed identical temperature scans as in the TPD experiments, but only up to a certain temperature where we quenched the sample to room temperature and transferred it to the STM stage. Fig. 4(a)–(f) displays a series of STM images where the sample was heated to successively higher temperatures starting at 393 K with increments of 20 K. The temperatures T_{max}, where the sample was quenched in each case are marked in the corresponding TPD spectrum of Fig. 4(g). It is evident from Fig. 4(a),(b) that practically all hydrogen within the lower temperature desorption peak, i.e. from the unreconstructed areas in between the monatomic Ir chains (displayed as bright lines in the STM images) can desorb without any significant structural change. (Note: hydrogen itself is usually invisible in STM.) However, in parallel to the desorption of the higher temperature peak, i.e. right from the monatomic Ir chains, these chains disappear and the surface transforms back into the reconstructed surface indicated by the typical weak height modulation (imaged dark reddish-brown in Fig. 4(c)–(e)). So, when losing its hydrogen the extra Ir rows are immediately re-incorporated into the surface layer forming locally the denser quasi-hexagonally reconstructed phase. In the re-ordering process all surface

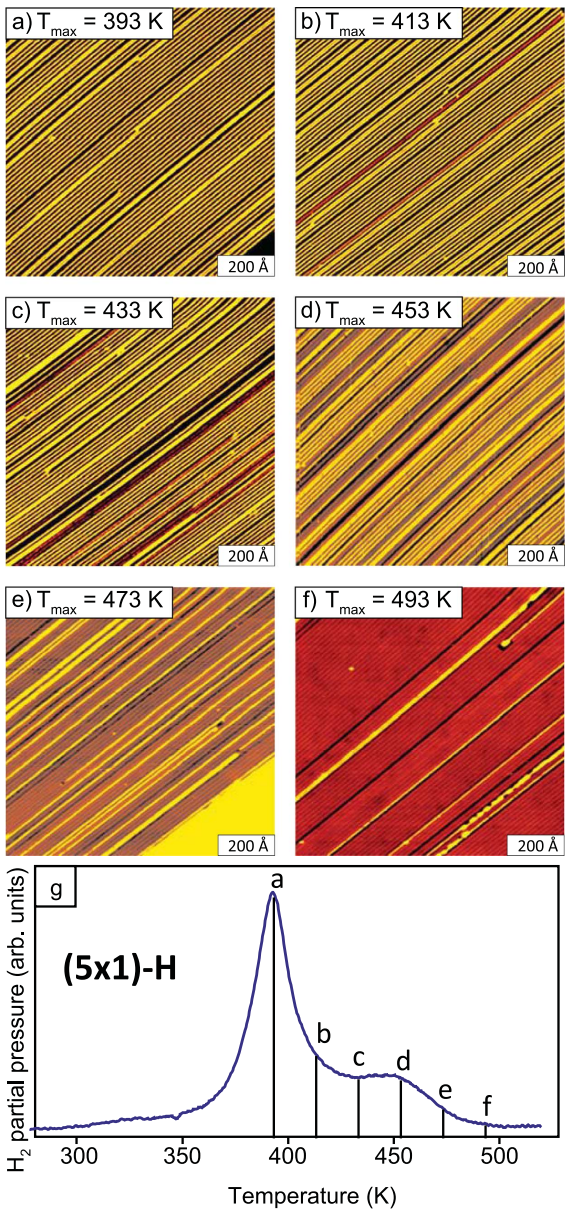

Fig. 4. (a-f) Series of STM images for an initially fully deconstructed Ir(100)-5×1-H phase recorded after successive ramping of the temperature (as in the TPD experiments) to the values T_{max} indicated in the images and the TPD spectrum (g) and subsequent quenching to room temperature before measurement.

Ir atoms have to shift a bit aside in order to find the proper registry towards the underlying lattice. For this there is more than one unique choice and the first reconstructed stripes will act as nucleation centers for that. So, when growing domains of the reconstructions meet each other there might be a registry shift, which leads to either open troughs or remaining single monatomic Ir rows which cannot be incorporated anymore. This is exactly what we observe right after all hydrogen is desorbed (Fig 4(f)). It would require much higher temperatures, when Ir atoms become mobile at the surface, to heal this type of defects.

The fact that one single hydrogen atom per 5×1 unit cell is obviously sufficient to stabilize the deconstructed phase is in agreement with the predictions from DFT [36], where the energetic penalty for having a deconstructed surface against a reconstructed one is found to be just balanced by the energy gain for one single hydrogen atom on top of the Ir rows, compared to occupying the best site on the reconstructed surface. More astonishing, however, is the observation that the surface does not just remain in the metastable deconstructed state after H desorption, i.e. that there is no measurable activation barrier for the incorporation of the Ir rows. This is in clear contrast to the behavior of the unreconstructed 1×1 phase, which converts to the reconstructed state only at temperatures above 800 K [37]. The only difference to the situation here is that the Ir atoms needed to form the 5×1-hex phase are not yet at the right position, but have to be brought from step edges. Hence, the comparably large activation energy of 0.88 eV experimentally determined for the $1 \times 1 \rightarrow 5 \times 1$ structural switch [37] most likely describes nothing else than the barrier for the detachment of Ir atoms from step edges rather than for their incorporation into the topmost surface layer.

5. Hydrogen at the reconstructed Ir(100)-5×1-hex-H surface

After having discussed the hydrogen adsorption on the unreconstructed and the deconstructed Ir(100) surface we finally come to the most complex phase, the 5×1-hex-H. First, however, we have to analyze and understand the clean reconstructed 5×1-hex phase. In Fig. 5(a) the curve fitted Ir $4f_{7/2}$ spectrum for this phase is displayed together with a corresponding ball model. Adopting the common nomenclature [11,9] the unit cell contains 4 types of inequivalent surface Ir atoms marked as (1), (2), (3), and (4). All these atoms differ by their local coordination towards the underlying square substrate lattice and hence also their relative heights differ remarkably leading to a top layer rumpling of about 0.5 Å in total [11]. Due to a mirror plane in the center of the unit cell atoms (2) and (3) appear twice within the cell, while atoms (1) and (4) occur only once. First of all, we notice that Ir surface atoms (2) are located almost atop of second layer Ir atoms. Therefore, they have the lowest coordination (only 7-fold) and since they are also the outermost ones we expect the largest negative CLS for these atoms. Secondly, we notice that two different types of Ir surface atoms located in bridge positions, (1) and (4), exist. Though the coordination number and local adsorption site are the same in both cases, bridge atoms (4) are located above the level of neighboring atoms (3), while bridge atoms (1) are rather confined below the level of the strongly outward displaced atoms (2). Therefore, we expect a larger CLS for the protruding atoms (4) and a smaller CLS for the more confined atoms (1). A similarly low CLS is expected also for the other type of locally confined atoms, which are the type 3 atoms assuming near hollow site positions.

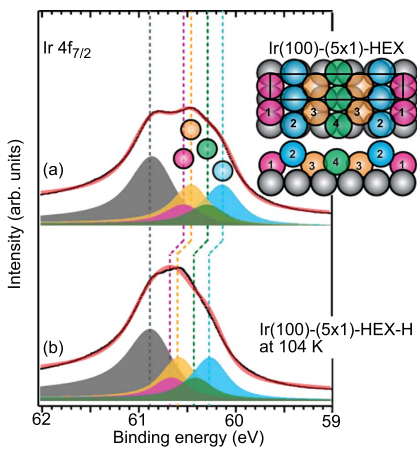

Fig. 5. (a) Ir $4f_{7/2}$ spectra of the clean Ir(100)-(5×1)-hex phase. (b) Ir $4f_{7/2}$ spectra of the Ir(100)-(5×1)-hex phase saturated with hydrogen at 104 K. Experimental spectra are shown as black dots, the fits as transparent solid red lines, and the filled curves represent the components of each fit. (For interpretation of the references to color in this figure legend, the reader is referred to the web version of this article).

These qualitative considerations are fully confirmed by our DFT calculation as can be seen from the CLS values listed in Table 1. Using these DFT calculated CLS's and the relative number of atoms in the unit cell (either 1 or 2, depending on the type) as starting point for the fit, we deconvoluted the Ir $4f_{7/2}$ spectrum into one bulk component Ir_B located at 60.82 eV and four surface components. We note that the bulk component is shifted slightly as compared to the value measured for the metastable Ir(100)-1×1 surface (60.85 eV) most likely because of the higher coordination of first subsurface Ir atoms. As seen from Fig. 5(a) the agreement between the fitted curve and the experimental spectrum is excellent and the resulting CLSs do not deviate by more than 0.02 eV from the predicted DFT values (Table 1). Consistently, the deconvolution of the 5×1-hex spectrum yielded an intensity ratio between the surface and bulk components of 1.7:1, exactly the same as that for the 5×1-H phase. In both cases the surface layer hosts 20% more atoms compared to the bulk-like terminated 1×1 surface, where a peak ratio of 1.4:1 was found.

We finally note that our spectrum for the clean reconstructed surface looks similar to the ones reported by van der Veen et al. [25] and Barrett et al. [26]. In these studies, however, the spectra were fitted quite arbitrarily by two surface components with CLS values of +0.44 eV and +0.75 eV [25] and +0.25 eV and +0.50 eV [26] disregarding the underlying atomic model.

We now turn to the hydrogen covered (5×1)-hex-H phase, for which Fig. 5(b) displays the Ir $4f_{7/2}$ spectrum recorded after an exposure of 77 L of H_2 at 100 K to the reconstructed surface. A visual comparison with the corresponding spectrum for the clean surface (Fig. 5(a)) already reveals that adsorbed hydrogen induces a positive CLS to the broad distribution of surface components as found for the unreconstructed surface. In a previous study by Poon et al. [20] a structural model for this surface with a symmetry-breaking distribution of 3 hydrogen atoms per 5×1 unit cell could be derived from a sophisticated combination of DFT and quantitative LEED analysis. Unfortunately, DFT calculated CLSs for this structural model given in Table 1 turned out to be incompatible with our experimental data. This may be understood by the fact that the rather low hydrogen coverage of θ=0.6 ML found in the study of Poon et al. was traced back to severe electron beam induced desorption in the LEED experiment [20]. As will be shown by our TPD experiments discussed below, the true saturation coverage with no electron beam is substantially higher and of the order of 1 ML. In photoelectron spectroscopy the impact of photo- and secondary electrons – though it cannot be excluded a priori – will certainly be much smaller than that of the intense electron beam of a LEED experiment. Hence we have to expect that the spectrum of Fig. 5(b) corresponds to a significantly higher coverage than 0.6 ML, for which no structural model exists so far. Even worse, as shown by Lerch et al. [9] the total energies of substantially different structural

models involving all types of possible adsorption sites (hollow, bridge and atop) become more and more degenerate with increasing coverage at the meV level. As a consequence, no unique site distribution can be expected at all for finite temperatures. Assuming that the hydrogen atoms will be more or less homogeneously distributed over all surface sites one can further speculate that this would also lead to a rather homogeneous charge transfer to all Ir surface atoms and hence to a homogeneous CLS for all surface components compared to the clean surface. As seen from Fig. 5(b) a common hydrogen induced CLS of +0.15 eV for all the surface components indeed reproduces our experimental spectrum quite well though by no means perfectly. Regarding the drastically different local configurations of surface atoms the model of common charge transfer might just be too simple to fully describe the experimental situation. However, lacking any better model we have to be content with this result, since an unguided fit of six surface components to the spectrum of Fig. 5(b) would only lead to arbitrary results.

TPD experiments for this 5×1-hex-H phase cannot be expected to give further insights into the energetics and occupation of adsorption sites, since the structure unavoidably converts into the deconstructed phase during the temperature scan. Consequently, the series of spectra displayed in Fig. 6 looks identical to those from Fig. 3b in the temperature range beyond 300 K, where the transformation of the surface is completed. For exposures up to about 1 L H_2 there is no further hydrogen desorption in the low temperature regime, i.e. all hydrogen adsorbed at the reconstructed surface at low temperatures will be accommodated within the deconstructed phase as well. For higher exposures (and thus higher initial coverages) at least two more peaks evolve at temperatures around 240 K and 260 K, another one might be hidden in the range below 200 K, which is inaccessible in our experiments. These peaks might originate from excess hydrogen, which does not find an acceptable adsorption site within the deconstructed 5×1-H phase and thus is released in the reordering process. Alternatively, it might also be that we have desorption peaks from still reconstructed surface areas, which can be expected in this temperature range, where the ratio of DFT-based binding energies (discussed in the last section) for the re- and deconstructed surfaces. Further insights might come from an inspection of the absolute peak areas for maximum coverage. Integration over the whole temperature range above 200 K results in a value only 4% below that of the unreconstructed 1×1 surface. That means that the reconstructed 5×1-hex surface definitely is able to host more hydrogen than the deconstructed phase, which can accommodate only about 80% with respect to the 1×1 phase (*cf.* last section). Therefore, severe e-beam assisted desorption must have taken place in the LEED-experiments of Ref. [20], where a coverage of only θ=0.6 ML was inferred. In accordance with that we found that irradiation of the H-saturated 5×1-hex phase with a defocused 500 eV electron beam for about 10 min resulted in the complete disappearance of the low temperature peaks. For the temperature desorption above 300 K, i.e. from the 5×1-H phase, we find an maximum integral value 12% smaller compared to the case where this phase was saturated via room temperature exposure. This difference seems to be beyond experimental error and hence we have to assume either an incompletely filled 5×1-H phase after surface re-ordering or an incompletely re-ordered surface with small uncovered reconstructed patches remaining. Since hydrogen is known to be extremely mobile even at lower temperatures, it is difficult to imagine that it cannot find all available favorable adsorption sites before desorbing from an unfavorable one. So, it is much more likely to assume that desorption from the 5×1-hex phase is indeed a competing process to surface re-ordering. Since both processes are thermally activated, but certainly with rather different kinetics, the relative rates will strongly depend on details of the experimental conditions like heating rate or quality of preparation. This might also explain in part the striking differences of our spectra with those published in earlier work. Ali et al. [24] obtained spectra very similar to ours but less well-resolved due to higher heating rate. In contrast, the spectra published by Moritani et al. [22] exhibit a much more pronounced low-temperature peak, which under certain conditions even exceeds the (unresolved) double peak around 400 K. Since heating rate and principal surface preparation were nominally quite similar to ours we tentatively attribute these differences to a different quality of the initial reconstructed phase, which could not be controlled in real space in the cited study. In any case, due to the lack of the correct model for the deconstructed phase and the knowledge of the quite exceptional re-ordering process, which was not available at that time, both studies cited above inevitably had to come to incorrect conclusions about the energetics and kinetics of the desorption process.

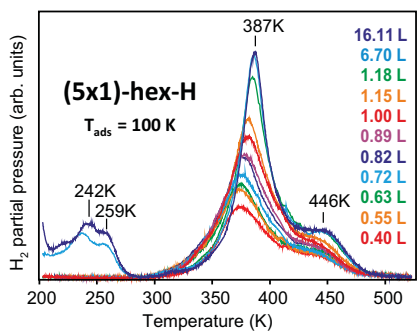

Fig. 6. Series of TPD spectra of hydrogen recorded after various initial exposures onto the reconstructed Ir(100)-5×1-hex phase at around 100 K.

6. Discussion and conclusions

One issue not discussed so far is the saturation coverage of hydrogen for the different surface phases. Both temperature programmed desorption and core level spectroscopy are methods, which are principally well-suited to give quantitative coverage results. While for TPD the determination of *relative coverage* of phases via the mere integration of spectra is a very accurate procedure with errors in the percentage range, there is the problem of calibration. For that an adsorption system with known (or assumed as known) coverage has to be available. This fundamental difficulty is absent for HRCLS, where the known density of surface atoms acts as an internal standard. The accuracy with which the *absolute coverage* at the surface can be revealed is therefore just a matter of the statistical error of the curve fitting procedure and depends on the specific case like the number and energetic separation of the fitted species. However, as for any other electron-based spectroscopy one has to take into account the principal possibility of electron stimulated desorption during data acquisition. In photoemission spectroscopy the dose of photo- and secondary electrons is often regarded as negligible compared to electron beam excited spectroscopies or LEED. However, in cases of extremely high photon fluxes achieved by advanced light sources, as in the present case, this option has to be taken into account as well.

With this in mind we now turn to the puzzling result of the actual (or apparent) inability to completely fill up all available adsorption sites (θ = 1) of the unreconstructed 1×1 phase. A physical explanation would be that with increasing hydrogen coverage at the surface a barrier for H_2 dissociation builds up, preventing a complete filling of sites for exposures manageable under UHV conditions. This behavior is observed for dissociative oxygen adsorption on the Ir(100)-1×1 phase, where only half of energetically favorable sites can be occupied via O_2 dosage [13]. However, by offering atomic species it should be possible to fill *all* available adsorption sites. Unfortunately, the experimentally unavoidable coadsorption of CO in our case prevented a final decision

on the maximum achievable coverage of this phase. An alternative explanation for the incomplete filling of the surface, however, would be electron-stimulated desorption. Due to the identical data acquisition for both molecular and atomic hydrogen exposure experiments the same reduction of the apparent coverage would automatically appear in both cases, which is just what we observe. Such an electron-induced desorption of hydrogen should occur then also for other phases, in particular for the deconstructed 5×1-H phase, where adsorption sites are of the same type. Here, in contrast, the spectra could be excellently fitted perfectly under the assumption of full coverage. However, we have to admit that an incomplete filling of, in particular, the lower energetic Ir_{2Hb} sites would remain vastly hidden since its core level shift almost coincides with that for a single-coordinated Ir_{1H} site, *cf.* Table 1.

In case of TPD the 5×1-H phase could serve as an excellent standard due to its special formation kinetics. In the last section we have proven that hydrogen dissociates readily at the clean reconstructed 5×1-hex phase consistent with Ali et al. who report an initial sticking coefficient of s_0=0.1 [24]. This adsorbed hydrogen, however, instantaneously diffuses towards the developing deconstructed 5×1-H patches, presumably filling all available sites. So dissociation and adsorption sites are spatially separated and hence no dissociation barrier can evolve until practically all surface area has transformed into the 5×1-H phase. The saturation coverage of hydrogen for this phase is predicted by DFT to be $\theta_{max}^{5\times1-H}$ = 0.8 ML, whereby 0.2 ML should be adsorbed on top of the monatomic Ir chains and 0.6 ML inbetween [32]. Any incomplete site filling in an experiment would predominantly affect the occupation of the lower energetic sites between the chains and lead to a deviating ratio 1:3-*x*. Fig. 3c proves that such a deviation is quite negligible and the total coverage in this phase must be very close to 0.8 ML. With this the saturation coverage for the unreconstructed Ir(100)-1×1-H phase follows immediately from the ratio of desorption rate integrals to be nominally $\theta_{max}^{1\times1-H}$ = 1.03 ML, which is consistent with a saturation coverage of 1 ML within the limits of error. Thus, the significantly smaller value of $\theta^{1\times1-H}$ = 0.88 ML measured by HRCLS has to be traced back to electron-stimulated desorption during data acquisition. With the above coverage calibration we can also assign the saturation coverage for the 5×1-hex-H phase to be $\theta_{max}^{5\times1-hex-H} \geq 1.0$ ML depending on whether there are further desorption peaks in the temperature range below 200 K or not.

In conclusion, we have achieved a detailed spectroscopic picture of hydrogen adsorption on the Ir(100) surface by evaluating the Ir $4f_{7/2}$ core level shifts for different clean and H-covered phases. Guided by DFT predictions on the basis of established structural models, available for all but one of these phases, we could unequivocally decompose their spectra into the respective components for every single inequivalent surface or bulk Ir atom. In all cases the experimentally determined values closely match the DFT input, proving in turn the validity of the underlying models. We further demonstrate for submonolayer hydrogen coverages on the unreconstructed 1×1 phase that HRCLS also allows to study correlations within the binding site occupation. This in principle can be done at any temperature accessible to the measurement in contrast to TPD, which probes these sites only at the desorption temperature. However, it turned out that secondary electron induced desorption seems to be relevant even for the present case of an atomic adsorbate. For that purpose complementary TPD measurements were essential to pin down the true saturation coverages for all H-covered phases. Our TPD spectra also provide experimental information on the peculiar and complex kinetics of the H-induced lifting of the surface reconstruction. Finally, also the reverse process, i.e. the immediate re-establishing of the reconstruction when all hydrogen has left the deconstructed phase, could be revealed by means of STM.

Acknowledgement

The authors are grateful for financial support by the Röntgen-Ångström cluster (349-2011-6491) and by the project grant 2012-3850 both financed by the Swedish Research council and by the Austrian Science Fund (FWF SFB-F45). Financial support from Nordforsk is also gratefully acknowledged. The MAX IV Laboratory personnel are acknowledged for support during measurements.

References

[1] J. Grant, A LEED study of the Ir(100) surface, Surf. Sci. 18 (1969) 228. http://dx.doi.org/10.1016/0039-6028(69)90167-8.
[2] T. Rhodin, G. Brodén, Preparation and chemisorptive properties of the clean normal and reconstructed surfaces of Ir(100) – role of multiplets, Surf. Sci. 60 (1976) 466–484. http://dx.doi.org/10.1016/0039-6028(76)90329-0.
[3] M. Van Hove, R. Koestner, P. Stair, J. Biberian, L. Kesmodel, I. Bartos, G. Somorjai, The surface reconstructions of the (100) crystal faces of iridium, platinum and gold. 1. experimental-observations and possible structural models, Surf. Sci. 103 (1981) 189. http://dx.doi.org/10.1016/0039-6028(81)90107-2.
[4] M. Van Hove, R. Koestner, P. Stair, J. Biberian, L. Kesmodel, I. Bartos, G. Somorjai, The surface reconstructions of the (100) crystal faces of iridium, platinum and gold. 2. structural determination by LEED intensity analysis, Surf. Sci. 103 (1981) 218. http://dx.doi.org/10.1016/0039-6028(81)90108-4.
[5] E. Lang, K. Müller, K. Heinz, M. Van Hove, R. Koestner, G. Somorjai, LEED intensity analysis of the (1×5) reconstruction of Ir(100), Surf. Sci. 127 (1983) 347. http://dx.doi.org/10.1016/0039-6028(83)90422-3.
[6] N. Bickel, K. Heinz, L.E.E.D. Quasidynamical, structure determination of the Ir(100)-1×5 surface reconstruction, Surf. Sci. 163 (1985) 435–443. http://dx.doi.org/10.1016/0039-6028(85)91070-2.
[7] Q. Ge, D. King, N. Marzari, M. Payne, First principles calculation of the energy and structure of two solid surface phases on Ir(100), Surf. Sci. 418 (1998) 529–535. http://dx.doi.org/10.1016/S0039-6028(98)00764-X.
[8] D. Spisak, J. Hafner, Reconstruction and de-reconstruction of the Ir(100) surface and ultrathin Fe/Ir(100) films, Surf. Sci. 546 (2003) 27. http://dx.doi.org/10.1016/j.susc.2003.08.052.
[9] D. Lerch, S. Müller, L. Hammer, K. Heinz, Complex adsorbate-substrate interplay of H on Ir(100)-(5×1)-hex: Density functional calculations, Phys. Rev. B 74 (7) (2006) 075426.
[10] G. Gilarowski, J. Mendez, H. Niehus, Initial growth of Cu on Ir(100)-(5×1), Surf. Sci. 448 (2000) 290–304. http://dx.doi.org/10.1016/S0039-6028(99)01255-8.
[11] A. Schmidt, W. Meier, L. Hammer, K. Heinz, Deep-going reconstruction of Ir(100)-5×1, J. Phys.: Condens. Matt. 14 (2002) 12353–12365. http://dx.doi.org/10.1088/0953-8984/14/47/310.
[12] J. Küppers, H. Michel, Preparation of Ir(100)-1×1 surface structures by surface reactions and its reconstruction kinetics as determined with LEED, ups and work function measurements, Appl. Surf. Sci. 2 (1979) 179–195. http://dx.doi.org/10.1016/0378-5963(79)90018-7.
[13] P. Ferstl, T. Schmitt, M.A. Schneider, L. Hammer, A. Michl, S. Müller, Structure and ordering of oxygen on unreconstructed Ir(100), Phys. Rev. B 93 (2016) 235406. http://dx.doi.org/10.1103/PhysRevB.93.235406.
[14] G. Kisters, J. Chen, S. Lehwald, H. Ibach, Adsorption of CO on the unreconstructed and reconstructed Ir(100) surface, Surf. Sci. 245 (1991) 65–71. http://dx.doi.org/10.1016/0039-6028(91)90468-8.
[15] T. Ali, B. Klötzer, A. Walker, D. King, A molecular beam study of nonlinearity in the CO-induced surface restructuring of Ir(100), J. Chem. Phys. 109 (24) (1998) 10996–11009. http://dx.doi.org/10.1063/1.477738.
[16] K. Anic, A. Bukhtiyarov, H. Li, C. Rameshan, G. Rupprechter, CO adsorption on reconstructed Ir(100) surfaces from UHV to mbar pressure: a LEED, TPD, and PM-IRAS study, J. Phys. Chem. C 120 (2016) 10838–10848. http://dx.doi.org/10.1021/acs.jpcc.5b12494.
[17] S. Khatua, Z. Liu, D. King, NO restructuring of surface Ir and bond formation to preadsorbed O on Ir{100} at 95 K, Surf. Sci. 584 (2–3) (2005) 214–224. http://dx.doi.org/10.1016/j.susc.2005.04.002.
[18] L. Hammer, W. Meier, A. Schmidt, K. Heinz, Submonolayer iron film growth on reconstructed Ir(100)-(5×1), Phys. Rev. B 67 (2003) 125422. http://dx.doi.org/10.1103/PhysRevB.67.125422.
[19] D. Lerch, A. Klein, A. Schmidt, S. Müller, L. Hammer, K. Heinz, M. Weinert, Unusual adsorption site of hydrogen on the unreconstructed Ir(100) surface, Phys. Rev. B 73 (2006) 075430. http://dx.doi.org/10.1103/PhysRevB.73.075430.
[20] H. Poon, D. Saldin, D. Lerch, W. Meier, A. Schmidt, A. Klein, S. Müller, L. Hammer, K. Heinz, Spontaneous symmetry breaking of the Ir(100)-(5×1)-hex surface induced by hydrogen adsorption, Phys. Rev. B 74 (2006) 125413. http://dx.doi.org/10.1103/PhysRevB.74.125413.
[21] K. Heinz, L. Hammer, Hydrogen-Induced and Defect-Mediated Structural Transition (5×1)-hex→(5×1)-H on Ir(100), Z. Phys. Chem. 218 (2004) 997. http://dx.doi.org/10.1524/zpch.218.8.997.35979.
[22] K. Moritani, M. Okada, T. Kasai, Y. Murata, Hydrogen adsorption and reaction on the Ir{100}-(1 ×5) surface, Surf. Sci 445 (2000) 315. http://dx.doi.org/10.1016/S0039-6028(99)01072-9.
[23] B. Sauerhammer, K. Johnson, C. Greenwood, W. Braun, G. Held, D. King, Ir{100}-(1 ×3)-H, an intermediate phase between the (1×1) and the (1×5) phases of

Ir{100}, Surf. Sci. 488 (2001) 154–163. http://dx.doi.org/10.1016/S0039-6028(01)01134-7.
[24] T. Ali, A. Walker, B. Klötzer, D. King, A molecular beam study of the H_2-induced lifting of the Ir(100)-(1×5)reconstruction, Surf. Sci. 414 (1998) 304–314. http://dx.doi.org/10.1016/S0039-6028(98)00538-X.
[25] J. Vanderveen, F. Himpsel, D. Eastman, Structure-dependent 4f-Core-level binding-energies for Surface Atoms on Ir(111), Ir(100)-(5×1), and metastable Ir(100)-(1×1), Phys. Rev. Lett. 44 (3) (1980) 189–192. http://dx.doi.org/10.1103/PhysRevLett.44.189.
[26] N. Barrett, C. Guillot, B. Villette, G. Treglia, B. Legrand, Inversion of the core level shift between surface and subsurface atoms of the iridium(100)(1×1) and (100)(5×1) surfaces, Surf. Sci. 251 (1991) 717–721. http://dx.doi.org/10.1016/0039-6028(91)91085-C.
[27] R. Nyholm, J. Andersen, U. Johansson, B. Jensen, I. Lindau, Beamline I311 at MAX-LAB: a VUV/soft X-ray undulator beamline for high resolution electron spectroscopy, Nucl. Instrum. Methhods A 467 (2001) 520. http://dx.doi.org/10.1016/S0168-9002.
[28] P. Feulner, D. Menzel, Simple ways to improve flash desorption measurements from single crystal surfaces, J. Vac. Sci. Technol. 467 (1980) 662–663. http://dx.doi.org/10.1116/1.570537.
[29] G. Kresse, J. Furthmüller, Efficient iterative schemes for ab initio total-energy calculations using a plane-wave basis set, Phys. Rev. B 54 (16) (1996) 11169–11186. http://dx.doi.org/10.1103/PhysRevB.54.11169.
[30] G. Kresse, D. Joubert, From ultrasoft pseudopotentials to the projector augmented-wave method, Phys. Rev. B59 (3) (1999) 1758–1775. http://dx.doi.org/10.1103/PhysRevB.59.1758.
[31] J. Perdew, K. Burke, M. Ernzerhof, Generalized gradient approximation made simple, Phys. Rev. Lett. 77 (18) (1996) 3865–3868. http://dx.doi.org/10.1103/PhysRevLett.77.3865.
[32] D. Lerch, O. Wieckhorst, L. Hammer, K. Heinz, S. Müller, Adsorbate cluster expansion for an arbitrary number of inequivalent sites, Phys. Rev. B 78 (2008) 121405. http://dx.doi.org/10.1103/PhysRevB.78.121405 R.
[33] M. Bianchi, D. Cassese, A. Cavallin, R. Comin, F. Orlando, L. Postregna, E. Golfetto, S. Lizzit, A. Baraldi, Surface core level shifts of clean and oxygen covered Ir(111), New J. Phys. 11 (2009) 063002. http://dx.doi.org/10.1088//1367-2630/11/6/063002.
[34] E. Grånäs, J. Knudsen, U. Schröder, T. Gerber, C. Busse, M. Arman, K. Schulte, J. Andersen, T. Michely, Oxygen Intercalation under Graphene on Ir(111): energetics kinetics, and the role of graphene edges, ACS Nano 6 (2012) 9951. http://dx.doi.org/10.1103/PhysRevB.74.125413.
[35] S. Titmuss, K. Johnson, Q. Ge, D. King, Structure, bonding, and anharmonic librational motion of CO on Ir(100), J. Chem Phys. (2002) 8097. http://dx.doi.org/10.1063/1.1469598.
[36] D. Lerch, Clusterentwicklungen zur Lösung des Grundzustandsproblems für beliebige Gittertypen, Verlag Dr. Hut München (2009) 1–194.
[37] K. Heinz, G. Schmidt, L. Hammer, K. Müller, Dynamics of the reconstruction process Ir(100) $1 \times 1 \rightarrow 1 \times 5$, Phys. Rev. B 32 (1985) 6214–6221. http://dx.doi.org/10.1103/PhysRevB.32.6214.

Paper II

THE JOURNAL OF PHYSICAL CHEMISTRY C

Article

pubs.acs.org/JPCC

Adsorption and Activation of CO on Co_3O_4(111) Thin Films

P. Ferstl,[†] S. Mehl,[‡] M. A. Arman,[§] M. Schuler,[†] A. Toghan,[‡,∥] B. Laszlo,[⊥] Y. Lykhach,[‡] O. Brummel,[‡] E. Lundgren,[§] J. Knudsen,[§,#] L. Hammer,[†] M. A. Schneider,*[,†] and J. Libuda*[,‡,○]

[†]Lehrstuhl für Festkörperphysik, Friedrich-Alexander-Universität Erlangen-Nürnberg, Staudtstrasse 7, 91058 Erlangen, Germany

[‡]Lehrstuhl für Physikalische Chemie II and [○]Erlangen Catalysis Resource Center, Friedrich-Alexander-Universität Erlangen-Nürnberg, Egerlandstrasse 3, 91058 Erlangen, Germany

[§]Division of Synchrotron Radiation Research and [#]MAX IV Laboratory, Lund University Box 118, 22100 Lund, Sweden

[∥]Chemistry Department, Faculty of Science, South Valley University, 83523 Qena, Egypt

[⊥]Department of Physical Chemistry and Materials Science, University of Szeged, H-6720 Szeged, Aradi vértanúk tere 1, Hungary

Supporting Information

ABSTRACT: To explore the catalytic properties of cobalt oxide at the atomic level, we have studied the interaction of CO and O_2 with well-ordered Co_3O_4(111) thin films using scanning tunneling microscopy (STM), high-resolution X-ray photoelectron spectroscopy (HR-XPS), infrared reflection absorption spectroscopy (IRAS), and temperature-programmed desorption spectroscopy (TPD) under ultrahigh vacuum (UHV) conditions. At low coverage and temperature, CO binds to surface Co^{2+} ions on the (111) facets. At larger exposure, a compressed phase is formed in which additional CO is located at sites in between the Co^{2+} ions. In addition, a bridging carbonate species forms that is associated with defects such as step edges of Co_3O_4(111) terraces or the side facets of the (111) oriented grains. Preadsorbed oxygen neither affects CO adsorption at low coverage nor the formation of the surface carbonate, but it blocks formation of the high coverage CO phase. Desorption of the molecularly bound CO occurs up to 180 K, whereas the surface carbonate decomposes in a broad temperature range up to 400 K under the release of CO and, to a lesser extent, of CO_2. Upon strong loss of crystalline oxygen, the Co_3O_4 grains eventually switch to the CoO rocksalt structure.

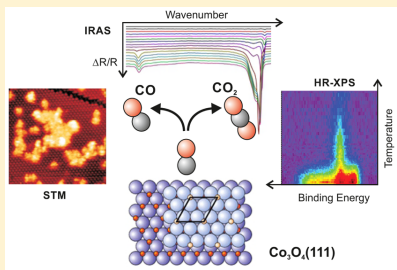

1. INTRODUCTION

Cobalt oxide nanomaterials have recently attracted attention because of their application potential in the fields of heterogeneous catalysis,[1−4] energy-related materials,[5] catalysis,[6−8] and electrocatalysis.[9−11] Among the specific applications are, for example, the production of hydrogen by reforming of hydrocarbon oxygenates such as ethanol,[7,8,12] the low temperature CO oxidation,[1,3,13−20] and the selective oxidation of CO (PROX, for removal of CO from the hydrogen feed of fuel cells),[6] the oxidation of methane and volatile organic compounds (VOC),[2,21−27] and both the oxygen reduction reaction (ORR) and the oxygen evolution reaction (OER) in electrocatalysis.[9,10,28] It is noteworthy that in these applications cobalt oxide often replaces noble metals, such as platinum. With an abundance in the earth crust that is about 5000× higher than that of platinum, this holds the potential of providing low-cost alternatives to noble metal catalysts in the above-mentioned processes.

In various respects the catalytic behavior of cobalt oxide is, however, very different from its noble metal counterparts. One of the unique features is the outstanding structure dependency of the activity of nanostructured cobalt oxide.[4] For example, it has been recognized early that the spinel-type Co_3O_4 shows high activity for the low-temperature CO oxidation, in contrast to the rocksalt-type CoO.[13] Further, Haruta and co-workers demonstrated recently very high activity of Co_3O_4 nanorods for CO oxidation at temperatures as low as 196 K.[1] These nanorods exposed a large fraction of (110) facets. Different reaction pathways have been proposed that could be responsible for the catalytic activity. Among these pathways are (i) the reaction of CO, adsorbed at a Co^{3+} center, with a down coordinated lattice oxygen,[1] (ii) the activation of molecular oxygen at 2-fold coordinated oxygen vacancy sites, followed by reaction with a coadsorbed CO,[17] and (iii) the reaction of CO with 2-fold coordinated lattice oxygen, followed by vacancy diffusion and oxygen dissociation at double vacancies.[29] Quite naturally, even less is known on the microscopic reaction mechanisms for more complex reactions such as those that involve larger hydrocarbons and hydrocarbon oxygenates. Different active sites and structural features have

Received: April 30, 2015
Revised: June 24, 2015
Published: June 30, 2015

DOI: 10.1021/acs.jpcc.5b04145
J. Phys. Chem. C 2015, 119, 16688−16699

been suggested to play a role.[4] For example, Co_3O_4 nanosheets with predominately (112) facets were shown to be particularly active for CH_4 oxidation.[30,31] Here, oxygen activation in the presence of oxygen vacancies and surface Co^{2+} ions were related to the high activity for methane activation and VOC oxidation.

In the above-mentioned catalytic studies on nanomaterials there are two principal problems that complicate the interpretation of structure−reactivity correlations. First, the atomic structure of the nanomaterial facets under reaction conditions is generally unknown, even if their shape is well-controlled. In fact, for complex oxides of a given surface orientation, a variety of bulk terminations are conceivable. Therefore, apart from the complications arising from possible surface reconstructions, the choice of a specific bulk termination (to facilitate comparison with theoretical calculations) may produce misleading results. Second, coadsorbates may be present at the surface, in particular, at low reaction temperatures. These coadsorbates may modify the adsorption energetics and the reaction pathways.

In the present work we follow a model catalysis approach to the cobalt oxide surface chemistry.[32,33] We aim to study structure−reactivity relations on atomically defined cobalt oxide surfaces under well-controlled conditions in ultrahigh vacuum (UHV). We take advantage of the fact that a variety of well-ordered Co_3O_4 and CoO films can be grown on Ir(100).[34−38] In a unique fashion, these films allow to vary the stoichiometry, the surface orientation, the film thickness, and the defect density. Over the last years, many of these structures have been characterized in great detail using low energy electron diffraction (LEED) $I-V$ analysis and scanning tunneling microscopy (STM). In the present work, we start from a well-ordered and well-characterized $Co_3O_4(111)$ film[34,35] and explore its interaction with CO and O_2. We identify the adsorption sites, interaction mechanisms, and possible activation mechanisms for oxidation of CO. The present work will serve as a starting point for future studies that aim at the controlled modification of the $Co_3O_4(111)$ surface to design atomically controlled sites for CO, hydrocarbon, and oxygen activation.

2. EXPERIMENTAL SECTION

The experiments were performed in three different UHV systems. IRAS, TPD, and STM measurements were performed in two separate laboratories at the Universität Erlangen-Nürnberg, Germany, and HR-XPS was performed at the beamline I311 at the MAX IV Laboratory (Lund, Sweden).

IRAS Experiments. The IRAS experiments were performed in a UHV system with a base pressure of $p = 2 \times 10^{-10}$ mbar, containing standard preparation characterization methods (low energy electron diffraction, Auger electron spectroscopy, temperature-programmed desorption). The infrared (IR) measurements were performed with a vacuum Fourier-Transform infrared spectrometer (Bruker VERTEX 80v) equipped with a liquid-nitrogen cooled narrow-band mercury cadmium telluride detector. The spectrometer is coupled via differentially pumped KBr windows to the UHV system. The present measurements were performed in a remote-controlled mode (National Instruments (NI) and LabView (NI) interface) by dosing pulses of CO via a gas doser equipped with an electromagnetic valve and subsequent acquisition of the IR spectra. The low pressure reservoir of the doser was filled with CO (Messer, 4.7) that was further purified using a liquid nitrogen cold trap to remove possible traces of volatile carbonyls. Before the experiment, a background spectrum was taken (200 scans, sampling rate 10 kHz, resolution 4 cm^{-1}, 110 s). For each experiment, 15 pulses of CO corresponding to exponentially increasing gas doses were admitted. After each CO pulse, a spectrum was taken (200 scans, sampling rate 10 kHz, resolution 4 cm^{-1}, 110 s).

STM and TPD Experiments. STM and TPD experiments were conducted in a second UHV chamber at a base pressure of 2×10^{-11} mbar. Sample preparation, LEED, TPD, and STM were performed in situ. LEED and TPD were performed on a liquid-nitrogen-cooled manipulator. The TPD spectra were taken with a quadrupole mass spectrometer (QMS) equipped with Feulner cup,[39] the entrance of the nozzle was placed ∼0.5 mm in front of the sample surface, and only gases desorbing from the area of the Ir crystal could enter the QMS. To calibrate the amount of CO desorbed from the sample, the desorption of CO from the well-known Ir(100)-c(2 × 2)-CO structure[40] was measured using exactly the same geometry. Due to the small heating power needed at temperatures below 100 K, the employed temperature ramp was nonlinear. The TPD spectra shown are plotted against time and the axis was relabeled using the temperature at the given instance. For STM experiments (at 300 K), the sample was transferred to a separate part of the UHV chamber and electrochemically etched tungsten tips were used.

HR-XPS Experiments. The HR-XPS experiments were conducted at the high resolution X-ray photoemission spectroscopy endstation at beamline I311[41] at the MAX IV Laboratory. All spectra are collected in normal emission with photon energies of 380 eV (C 1s) and 625 eV (O 1s), respectively. During measurements, the sample was moved across the X-ray beam at a speed of 5 μm/s. This velocity ensured that spectra taken were not affected by beam-induced desorption or reactions as judged from the time independence of spectra at constant temperature. For the curve fitting, we used symmetric Voigt components after subtracting a polynomial background.

Sample Preparation. The preparation of the $Co_3O_4(111)$ films on Ir(100) was previously described in the literature.[34,35] We employed here a slightly modified procedure that could be carried out in all used UHV systems with utmost control of the relevant process parameters like substrate cleanliness and structure, Co amount, temperature, and O_2 partial pressure. In all setups, the sample was mounted according to the respective needs of the experiment such that heating to 1500 K and cooling to 100 K or below with liquid nitrogen could be achieved. First, the Ir(100) crystal was cleaned by several cycles of ion bombardment (2 keV, 10 μA) for 60 min with Ar (Linde 6.0, Air Liquide 4.8) followed by annealing for 3 min to 1273 K. This procedure was repeated until the crystal showed a high-quality Ir(100)-(5 × 1) reconstruction as judged by LEED at room temperature or below. Subsequently, the (5 × 1) reconstruction was lifted by producing the Ir(100)-(2 × 1)-O structure by cooling down the sample from 1200 K to room temperature in 10^{-8} mbar oxygen (Linde 5.0, AGA 5.0). The eventual preparation of the Co_3O_4 film involved the use of a O_2 gas doser aiming at the surface at the same time as the Co source, a commercial electron-beam evaporator (Focus EFM3, 2 mm Co rod, Alfa Aesar 99,995%, Good fellow 99.99%). This allowed the local oxygen pressure at the surface to be well above 5×10^{-6} mbar during growth. The evaporation rate of the Co source was calibrated using a quartz microbalance and

DOI: 10.1021/acs.jpcc.5b04145
J. Phys. Chem. C 2015, 119, 16688−16699

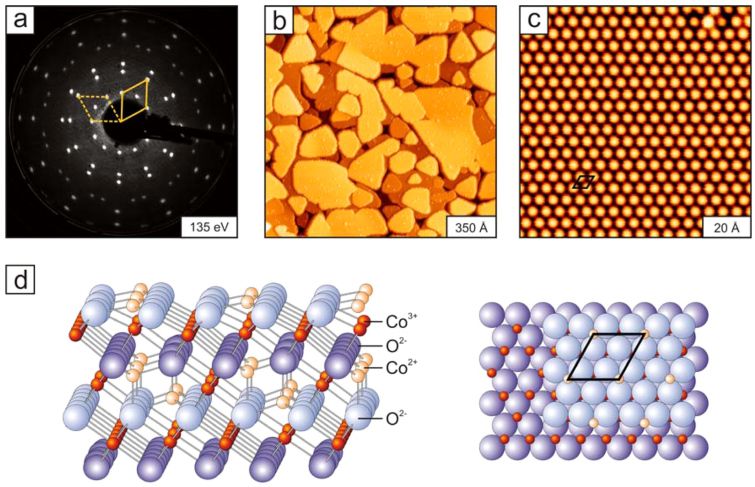

Figure 1. (a) LEED pattern showing the $Co_3O_4(111)$ film on Ir(100); (b) large-scale STM image showing the morphology of the as-prepared $Co_3O_4(111)$ film; (c) atomically resolved STM image of a single terrace on the $Co_3O_4(111)$ film; (d) structural model of the $Co_3O_4(111)$ film on Ir(100) (see text for details).

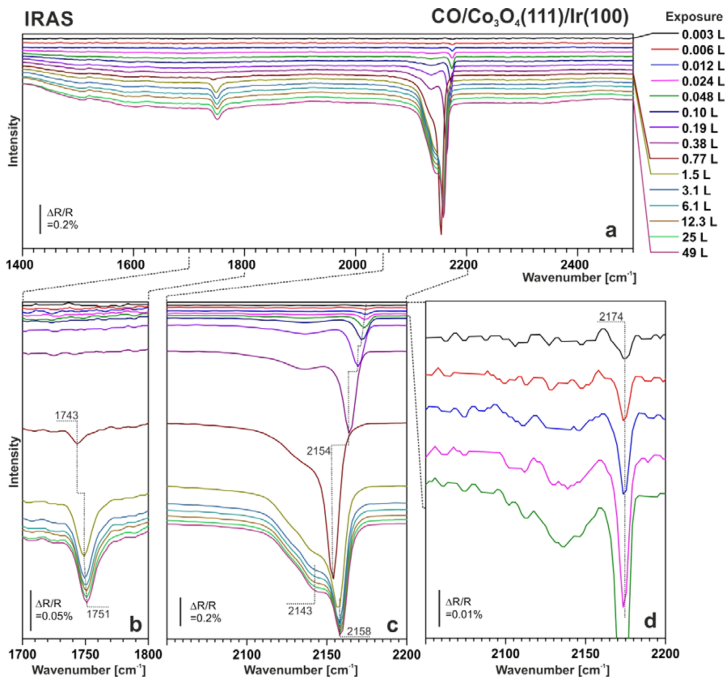

Figure 2. (a) IRAS taken after exposure of $Co_3O_4(111)$/Ir(100) to different doses of CO at 100 K; (b, c) zoom into selected spectral regions; (d) CO stretching frequency region in the limit of very low CO exposures.

DOI: 10.1021/acs.jpcc.5b04145
J. Phys. Chem. C 2015, 119, 16688−16699

by producing other two-dimensional cobalt oxide structures that require exact amounts of Co expressed in monolayer equivalents (MLEs).[36] One MLE corresponds to a full monolayer coverage of the Ir(100) surface. For obtaining the $Co_3O_4(111)$ films, 15 MLE of Co were evaporated under steady oxygen flow with a rate of 1 ML/min at 300 K sample temperature. Subsequently, the roughly 5 nm thick films were annealed keeping the same oxygen flux for 2 min at 523 K and finally briefly heated in UHV to 673 K to improve the degree of ordering.

3. RESULTS AND DISCUSSION

3.1. Structure and Defects of $Co_3O_4(111)$/Ir(100) Films. Figure 1 shows a summary of structural features of the films that are most relevant for the following discussion. LEED images (Figure 1a) taken at 80 K after the preparation of the $Co_3O_4(111)$ films reveal a high degree of structural homogeneity and long-range order without contributions of the underlying Ir(100) substrate. From the previous structural analysis[34] it is known that the surface of the spinel $Co_3O_4(111)$ films is terminated by Co atoms that would nominally correspond to the Co^{2+} ions of the bulk crystal (see structure model in Figure 1d). The distance between Co atoms in the surface layer is 5.72 Å, identical to the corresponding distance in the bulk crystal. The surface unit cell (indicated in the LEED pattern in Figure 1a and in the structure model in Figure 1d has an area of 28.3 $Å^2$. One of the base vectors of the hexagonal Co_3O_4 cell is aligned along [011] of the Ir substrate and the film grows in twins of two orthogonal domains on Ir(100). Large scale STM images like the one shown in Figure 1b reveal that the film consists of large grains with a diameter of up to 500−1000 Å interspersed with some smaller ones. There are steps between (111) terraces of the same grain with a step height of mainly 4.7 Å (single repeat unit). The latter value corresponds to a single repetition unit of the spinel structure. Figure 1c shows an atomically resolved STM topography. We interpret this image to represent the Co lattice at the surface. From many such images, we conclude that the grains exhibit almost perfect surfaces with total point defect density of less than one percent of the Co sites on the (111) terraces. Most of the point defects are adsorbates or missing Co atoms. We infer from the STM images that the thickness variation of the grains is 2−3 repeat units and from the missing beams of the Ir substrate in the LEED image we conclude that the Ir surface is completely covered by Co_3O_4 even between the grains. However, due to the geometry of the STM tip the depth and structure of the grain boundaries cannot be determined with certainty. As a consequence the surface area at the steps and side facets of the Co_3O_4 grains may be up to 20% of the surface area of the top faces and the side facets may be rich in defect sites.

3.2. Adsorption of CO with and without Preadsorption of Oxygen at 100 K. We have probed the interaction of CO with the pristine $Co_3O_4(111)$ film using IRAS, HR-XPS, and TPD. The IRAS spectra taken during CO exposure at a substrate temperature of 100 K are displayed in Figure 2. A remote-controlled doser device was used to obtain reproducible CO exposures over a large range (see Experimental Section). After taking the reference spectrum, the sample was exposed to a preprogrammed series of exponentially increasing doses of CO and IR spectra were automatically acquired after each dose. Thus, an exposure range of more than 4 orders of magnitude could be covered, ranging from 0.003 to 49 L (1 L (Langmuir) = 1×10^{-6} Torr·s).

Overview spectra are shown in Figure 2a. The main bands appear in the spectral region between 2100 and 2200 cm^{-1}. In addition, a weak band appears at around 1750 cm^{-1} at CO doses exceeding 1 L (Figure 2b). Figure 2c shows the development of the main bands over the full coverage range. The spectra in the limit of very low coverage are scaled up in Figure 2d. It is noteworthy that the excellent signal/noise ratio which could be reached with the present experimental setup allows us to identify adsorbed CO down to coverages of about 0.1% of a monolayer (ML). At a CO exposure of 0.003 L we observe a band at 2174 cm^{-1} ($\Delta R/R \sim 0.005\%$), which undergoes a redshift to 2154 cm^{-1} with increasing coverage. The main peak is accompanied by a weak shoulder at 2140 cm^{-1}. At exposures exceeding 1 L, this shoulder (2143 cm^{-1}) drastically increases in intensity, while the main peak undergoes a slight blue shift to 2158 cm^{-1}. At exposures exceeding 3 L, no further change in the spectra is observed. Interestingly, formation of the shoulder at 2143 cm^{-1} is accompanied by the appearance of a weak peak at 1743 cm^{-1}, which grows in intensity and undergoes a slight blue shift to 1751 cm^{-1} up to exposures of 3 L. Similarly, as observed for the main peak, this feature also does not change at exposures exceeding 3 L.

The bands around 2150 cm^{-1} can be attributed to weakly adsorbed molecular CO species on the Co_3O_4 surface. Surprisingly, rather few studies are available in the literature that provide high quality IR spectra of weakly adsorbed CO on ordered oxide surfaces. The best studied systems are CO/MgO(100)[42−45] and CO/Fe_3O_4(111)/Pt(111),[46] with the latter oxide film being closely related to $Co_3O_4(111)$/Ir(100) from the structural point of view.

CO adsorption on MgO(100) was initially investigated by Heidberg and co-workers[42] using vacuum-cleaved single crystal surfaces and later on studied on well-shaped nanoparticles by Zecchina and co-workers.[43−45] On MgO(100) CO adsorbs in a perpendicular geometry at Mg^{2+} sites up to coverages of $\theta < 0.25$.[42] With increasing coverage, the CO stretching band shows a red shift of 9 cm^{-1} from 2157 to 2148 cm^{-1}, arising from a combination of static and dynamic coupling effects.[45] The evolution of the spectral shape of the CO bands on MgO(100) is similar to our spectra on $Co_3O_4(111)$. We observe, however, a higher CO frequency in the low coverage limit and a larger coverage dependent red-shift ($\Delta = 20$ cm^{-1}, from 2174 to 2154 cm^{-1}) than on MgO. Interestingly, the CO density on MgO(100) at $\theta = 0.25$ is 2.8×10^{14} cm^{-2}.[43] This value is about 20% smaller than the density of surface Co^{2+} ions in $Co_3O_4(111)$, which amounts to 3.5×10^{14} cm^{-2}.[35] Based on this comparison, we suggest that in the low coverage regime (0−0.77 L) CO is adsorbed at the surface Co^{2+} sites. The stronger blue shift of the CO stretching band in comparison to MgO(100) can in part be rationalized in terms of a different Stark shift.[43] The Stark shift leads to a blue shift that depends on the strength of the local electric field at the cation site. On $Co_3O_4(111)$, the Co^{2+} ions are positioned 0.32 Å above the O^{2-} ions,[34] in contrast to the MgO(100) surface where cations and anions are coplanar. The situation is to some extent comparable to the more exposed Mg^{2+} ions at nanoparticle edges and corners, which also give rise to stronger blue-shifted bands appearing at 2170 and 2203 cm^{-1}.[43,44] The larger coverage dependence is associated with a stronger dipole

DOI: 10.1021/acs.jpcc.5b04145
J. Phys. Chem. C 2015, 119, 16688−16699

coupling which besides other effects arises from the higher CO density on $Co_3O_4(111)$.

The above assignment is consistent with the work of Lemire et al. who studied CO adsorption on $Fe_3O_4(111)/Pt(111)$.[46] Interestingly, the $Fe_3O_4(111)$ film shows a surface structure and unit cell that is very similar to the $Co_3O_4(111)$. In contrast to Co_3O_4, however, Fe_3O_4 has inverse spinel structure, that is, Fe^{3+} occupy both octahedral and tetrahedral sites. Lemire et al. identified three adsorption sites on $Fe_3O_4(111)$ giving rise to IR bands at 2214−2210, 2154, and 2098−2080 cm^{-1} (low CO coverage−high coverage). On the basis of the rather low vibrational frequency, the authors assigned the principle peak at 2098 cm^{-1} to CO at Fe^{2+} sites and concluded that the $Fe_3O_4(111)$ film is terminated by Fe^{2+} ions and not by Fe^{3+} ions as the bulk structure would suggest. Further, the weaker high frequency band at 2214−2210 cm^{-1} was assigned to CO at Fe^{3+} ions located at structural defect sites. In our case, the principal band at 2174−2154 cm^{-1} is in between the bands assigned to Fe^{2+} and Fe^{3+} and close to CO adsorbed on Mg^{2+}. Our assignment of the principal band at 2174−2154 cm^{-1} to CO adsorbed at Co^{2+} sites appears reasonable, as it agrees with a bulk termination of the film and is consistent with previous structural analysis.[34]

At larger exposure, the CO adsorption behavior on $Co_3O_4(111)$ is rather different from that on $Fe_3O_4(111)$.[46] On the latter surface, only weak bands were observed in addition to the band at 2098−2080 cm^{-1}. These were assigned to CO adsorption at Fe^{3+} defect sites (2210 cm^{-1}) and weak adsorption on the terraces (2154 cm^{-1}). In contrast, the coverage dependence of the spectra on MgO is quite similar to that observed on $Co_3O_4(111)$.[43−45] At higher coverage ($\theta > 0.25$), the peak around 2150 cm^{-1} broadens and develops additional features at lower frequency. These changes are associated with a new adsorbate structure on MgO(100) in which energetically inequivalent sites are occupied. In addition, the CO adopts a slightly tilted orientation. Similar spectral changes are observed on Co_3O_4 at exposures exceeding 0.77 L. Therefore, we suggest the formation of a high coverage phase in which weakly adsorbed CO is adsorbed in between the Co^{2+} sites. The local adsorption site cannot be clearly determined from the present data. One possibility would be a surface dicarbonyl.[47,48] Such a species should, however, be characterized by a symmetric and an asymmetric mode with very different intensities in IRAS. A second possibility would be the occupation of interstitial sites in between the surface Co ions, that is, at sites above the Co^{3+} centers located below the topmost oxygen layer.[34] It should be pointed out that the situation is complicated by the fact that the surface electronic structure of the $Co_3O_4(111)$ film is not entirely clear. Assuming bulk termination and the structure model from the LEED structure analysis,[34] a polar surface is created, and the electrostatic stabilization mechanism has not been established yet.

Finally, we consider the origin of the band around 1750 cm^{-1}. This band has no counterpart, neither on MgO(100) nor on $Fe_3O_4(111)$. Its low intensity suggests that it is not related to a species formed on the regular $Co_3O_4(111)$ facets. We rather associate it with a defect site of the film. The vibrational frequency is within the region of surface carbonates, however, it is close to its upper frequency limit.[49,50] To the best knowledge of the authors carbonate bands above 1700 cm^{-1} have not been reported on cobalt oxide so far. However, bands in this region have been identified on other oxides. On MgO powders bands above 1700 cm^{-1} have been assigned to bidentate carbonates.[50] Recently, Vayssilov et al. performed an extensive theoretical and experimental investigation of surface carbonates on CeO_2.[49] The authors also assigned the highest frequency features between 1720 and 1730 cm^{-1} to the formation of surface bidentates. Note that the formation of weakly bound surface carbonates upon CO exposure at low temperature has previously been observed on other oxide surfaces as well.[51] Based on these considerations, we attribute the feature at 1750 cm^{-1} to a weakly bound bidentate carbonate which is formed at a defect site. A possible type of defect identified in the structural characterization (see section 3.1) are the side facets of the grains and steps between $Co_3O_4(111)$ terraces. The weakly bound carbonate could be formed by binding of CO to two oxygen centers at such step edges.

In the next step we explore the influence of coadsorbed O_2 on the adsorption of CO. In Figure 3 we show the IRAS spectra

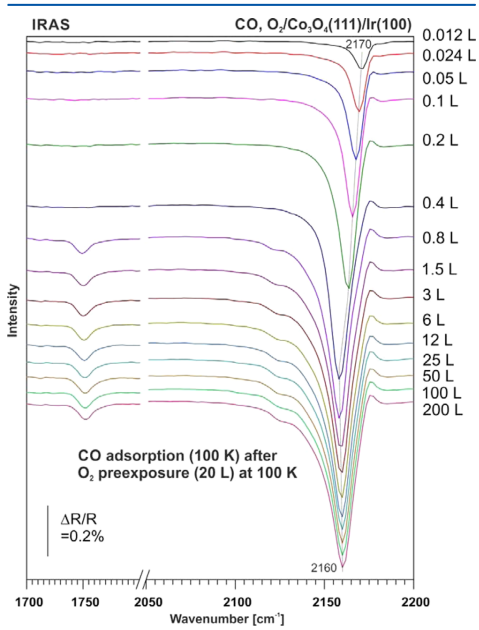

Figure 3. IRAS taken after pre-exposure of $Co_3O_4(111)/Ir(100)$ to 20 L of O_2 at 100 K and subsequent exposure to different doses of CO at 100 K.

obtained after exposure of the $Co_3O_4(111)$ film to 20 L of O_2 at 100 K, followed by successive dosing of CO at 100 K. Apart from the O_2 pre-exposure, the experimental procedure was similar to the one used for adsorption of CO only (see Figure 2). In the limit of small exposure, we observe the appearance of a band at 2171 cm^{-1}, which increases in intensity with increasing CO exposure and undergoes a red-shift to 2160 cm^{-1}. At exposures exceeding 1 L, the band develops a weak shoulder around 2130 cm^{-1}, but the formation of the strong high coverage band at 2140 cm^{-1}, assigned to the compressed CO layer formed on the oxygen-free surface, is completely suppressed. Interestingly, the weak carbonate band

DOI: 10.1021/acs.jpcc.5b04145
J. Phys. Chem. C 2015, 119, 16688−16699

at 1750 cm^{-1} is not influenced by O_2 pre-exposure. Both frequency and intensity are practically identical to the oxygen-free surface.

The different effect of preadsorbed oxygen on the three bands at 2170, 2140, and 1750 cm^{-1} supports the interpretation that the related species are located at different sites, i.e. at Co^{2+} sites on terraces (2170 cm^{-1}), at interstitial sites on terraces (2140 cm^{-1}) and at defects (1750 cm^{-1}) (side facets and steps) of the Co_3O_4 grains. Based on the above observations we suggest that the preadsorbed oxygen blocks CO adsorption at the weakly binding interstitial sites in between the surface Co^{2+} ions. CO adsorption at the more strongly binding Co^{2+} sites is not affected by preadsorbed oxygen. Also, the preadsorbed oxygen has no effect on the carbonate formation at the terrace edges. This observation is in line with the expectation that the interaction of molecular oxygen with the oxygen ions at the terrace edges should be rather weak.

3.3. Monitoring the Thermal Evolution and Desorption of CO by TPD and HR-XPS. To further identify the nature of the adsorbed CO, we have performed HR-XPS after adsorption of CO and during subsequent heating of the sample. Figure 4a shows the C 1s spectrum after exposure to 10 L CO at 85 K.

The experimental spectrum can be fitted with three different components located at binding energies (BEs) of 287.0 (red), 288.5 (blue), and 290.9 eV (green) and having relative intensities of 20, 17, and 63%, respectively (see Figure 4a). The full width at half-maximum (fwhm) of the two components with lowest binding energy are all ~1 eV in contrast to the component at 290.6 eV that is very broad, with a fwhm of 4.6 eV.

To help with the assignment of the different C 1s components we performed temperature-programmed XPS experiments to study their temperature evolution. After dosing 10 L CO at 85 K, we recorded the C 1s energy region while the sample was heated from 85 to 500 K at a heating rate of 20 K/min and while the sample was scanned at a speed of 5 μm/s through the X-ray beam. An image plot showing the evolution of the C 1s region is shown in Figure 4b, while the intensities of the three components (all normalized to 1 at 96 K) are plotted in Figure 4c.

We observe that the intensities of the components at 287.0 eV and at 290.9 eV decrease nearly simultaneously and both components are fully removed at 230 K. In the IRAS data discussed above two different CO adsorption sites were identified: (i) weakly adsorbed CO above surface Co^{2+} ions at small exposures and (ii) even more weakly adsorbed CO above interstitial sites at larger exposures. Concerning the origin of the two features 287.0 and 290.9 eV, one could be tempted to associate these to the two CO species identified in IRAS. However, neither the difference in binding energy nor the different energetic widths of the XPS signature support such an interpretation for a weakly adsorbed CO. The fact that the two features disappear in parallel when the temperature is increased rather suggests that they both originate from the same species. Therefore, we tentatively assign the peaks at 287.0 and 290.9 eV to the main photoemission line and a giant shakeup transition, respectively, originating from weakly bound CO. The binding energy difference between the shakeup transition and the main line (3.9 eV) fits well to what previously has been observed for CO adsorbed on Ni(110), 2.1 eV, Cu(100), 2.5 eV, and Ag(110), 4.2 eV; the shakeup feature may become dominant in weakly bound systems.[52−56]

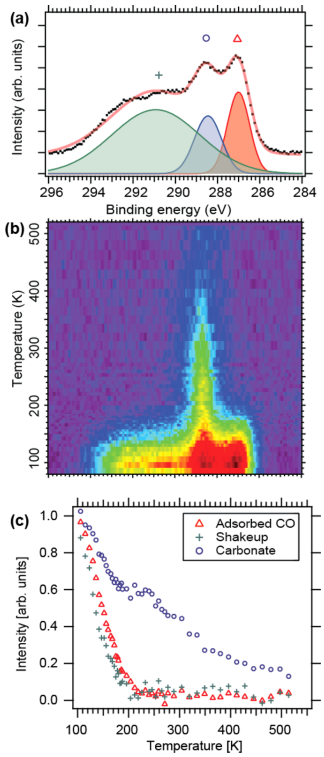

Figure 4. (a) C 1s spectrum after dosing 10 L CO at 85 K onto $Co_3O_4(111)$/Ir(100). The experimental spectrum is shown with black dots, the fit as a solid line, and the filled curves represent the components of the fit. (b) Image plot of the evolution of the C 1s spectrum as a function of temperature after removal of a polynomial background. (c) Temperature evolution of the intensity of the different components shown in (a) obtained from simultaneous curve fitting the data shown in (b).

In contrast to the components at 287.0 and 290.9 eV that are fully desorbed at 230 K, the component at 288.5 eV decays over a very broad temperature range and remains present on the surface up to 400 K. Based on the higher thermal stability, we associate this feature with the surface carbonate species previously identified in IRAS. The binding energy of 288.5 eV is consistent with those observed for surface carbonates previously, for example on cerium oxide[51] and on oxidized Ag surfaces 287.7−289 eV.[57] Also, the broad temperature range for carbonate decomposition is not unusual for these species on oxides.[49,57]

In the bottom part of Figure 5a we compare the O 1s spectra before (violet) and after (red) dosing of 16 L of CO at 90 K. Before CO dosing, the main peak was located at 529.30 eV and a small shoulder peak component at 528.55 eV. Upon CO dosing they both shift by +0.20 eV, and we assign this effect to an electrostatic shift, which is often observed for adsorption on thin metal oxide films.[58] If we shift the spectrum accordingly (see top part of Figure 5a), it becomes clear that the shape of

DOI: 10.1021/acs.jpcc.5b04145
J. Phys. Chem. C 2015, 119, 16688−16699

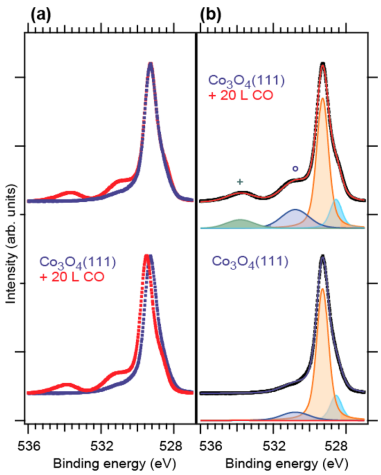

Figure 5. (a) O 1s of $Co_3O_4(111)$ before (blue) and after (red) adsorption of 20 L of CO at 90 K. Spectra calibrated to the Ir bulk peak are shown in the bottom part. The top part the blue spectrum is shifted −0.20 eV otherwise it is identical to the bottom part. (b) Curve fitting of the O 1s region of $Co_3O_4(111)$ before (bottom) and after (top) adsorption of CO.

the main peak remains practically unchanged, while the relative intensity of the shoulder component increases from 0.19 before CO dosing to 0.22 after CO dosing.

In addition to the main peak originating from the $Co_3O_4(111)$ film itself, we observe two new components upon CO dosing shifted by +1.5 and +4.5 eV with respect to the main line (see Figure 5b). To help with the assignment of these two components the O 1s region was followed in situ while heating the sample to 540 K. Figure 6 displays the TP-XPS data from this experiment, and it is evident that the component shifted by +4.5 eV from the main line disappears in the temperature interval between 90 and 250 K. In the same temperature interval, the binding energy of the Co_3O_4 (111) main peak shifts from 529.5 to 529.35 eV. Since the C 1s components at 287.0 and 290.9 eV assigned to weakly adsorbed CO disappear in the same temperature interval we conclude that the O 1s component shifted by +4.5 eV can also be assigned to the weakly adsorbed CO. Further, we note that the disappearance of the shift of the main O 1s peak correlates nicely with the disappearance of the weakly adsorbed CO (see Figure 6c), suggesting that it is mainly this species which is responsible for the shift.

The remaining O 1s component with a BE shift of +1.5 eV should then contain the contribution from the carbonate species observed in the C 1s and IR spectra. Its temperature dependence is, however, relatively complex. The reason is a minority reaction channel to CO_2 that leads to the formation of oxygen vacancies. This will be discussed in section 3.4.

To obtain further insight into the energetics of CO desorption, we have performed TPD experiments as a function of CO exposure. Selected spectra are displayed in Figure 7. Two main features are identified in the temperature region below 300 K. At low exposure a more strongly bound state is populated which gives rise to a desorption maximum close to

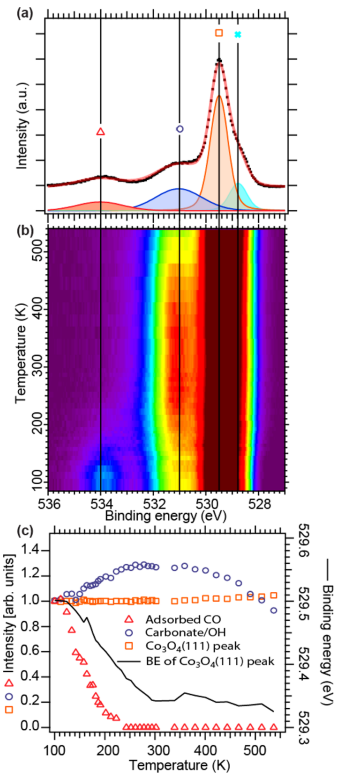

Figure 6. (a) Initial O 1s spectrum after dosing 16 L of CO at 90 K acquired before the heating cycle was started. (b) Image plot showing the development of the O 1s region while heating from 90 to 540 K. (c) Temperature evolution of the intensity of the different components (left *y* axis) shown in (a) obtained from simultaneous curve fitting the data shown in (b). The right *y* axis shows the binding energy of the $Co_3O_4(111)$ main line as a function of temperature.

180 K. With increasing exposure, this feature shifts to lower temperatures. Finally at saturation coverage (top curve in Figure 7), it develops into a shoulder (around 150 K) of a second desorption feature that appears close to 100 K. The low-temperature desorption peak increases with CO exposure. It should be noted, however, that desorption already starts at the lowest adsorption temperatures that could be reached, which implies that the low-temperature state cannot be fully saturated. We note also that, at a temperature above 200 K, a broad and weak CO desorption feature may be discerned that extends up to temperatures around 400 K.

On the basis of the IRAS and the HR-XPS data, we associate the peak between 150 and 180 K with the more strongly adsorbed CO at the Co^{2+} sites, whereas the low temperature desorption peak between 90 and 110 K is caused by the additional CO adsorbed in the compressed adsorbate structure formed at larger exposure. From a simple Redhead analysis, assuming a constant heating rate of 15 $K{\cdot}s^{-1}$, first order desorption, and a pre-exponential factor of 10^{13} s^{-1}, this value

DOI: 10.1021/acs.jpcc.5b04145
J. Phys. Chem. C 2015, 119, 16688−16699

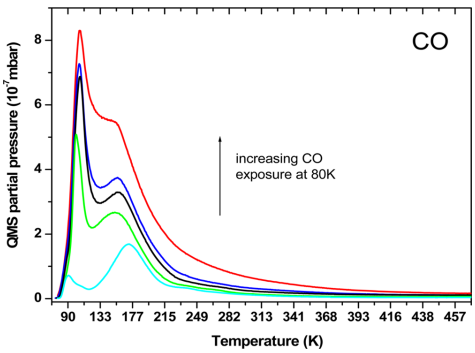

Figure 7. TPD spectra of CO (m/e = 28) on Co_3O_4(111)/Ir(100) recorded as a function of CO coverage after CO adsorbed at 80 K.

corresponds to desorption activation energies of 36−43 kJ·mol^{-1} for the more strongly bound CO and to an upper limit of 21−26 kJ·mol^{-1} for the weakly bound species (for which desorption starts already at 90 K). We note that the total amount of CO desorbing from the fully saturated Co_3O_4 surface is about twice as high as that from the Ir(100)-c(2 × 1)CO structure that was used for comparison.[40] This would roughly correspond to four CO molecules per Co_3O_4(111) unit cell if the film were perfectly flat and single crystalline. The observation is in agreement with the formation of a compressed structure with more than one CO molecule stabilized per surface unit cell. However, the true CO density is certainly lower than four molecules per regular unit cell due to adsorption at the side facets of the Co_3O_4(111) grains. The broad desorption intensity extending up to higher temperature may at least in part be associated with the surface carbonate formed at irregular sites of the oxide film.

3.4. Reactivity. Next we turn to the reactivity of the Co_3O_4 model surface toward CO. We have explored the reactivity by repeated CO adsorption (100 K) and annealing experiments. A comparison of the IR spectra before and after annealing is displayed in Figure 8 and HR-XPS of the O 1s region before and after repeated annealing is shown in Figure 9. Corresponding TPD and STM data is displayed in Figure 10.

Comparison of the IR spectra of adsorbed CO (see Figure 8) reveals that only minor changes occur upon a single CO adsorption and annealing cycle. All three characteristic CO-induced bands reappear in the second CO experiment with small changes in the band shapes only (the small positive contribution in the IR signals is due to traces of CO adsorbing from the background gas during cooling and before acquisition of the reference spectrum). This observation shows that the majority of CO desorbs molecularly without reacting with the oxide lattice. The TPD spectra (Figure 10a) confirm this conclusion, but also indicate a small fraction of CO oxidation, as a weak and broad CO_2 desorption feature is observed between 200 and 400 K. Note that in this temperature regime the surface carbonate is the only CO-derived species that persists on the surface. We may conclude that the majority of the surface carbonate desorbs as CO, but a small fraction is also converted to CO_2.

We also investigated the changes in the O 1s region upon repeated CO adsorption and annealing cycles by HR-XPS. In

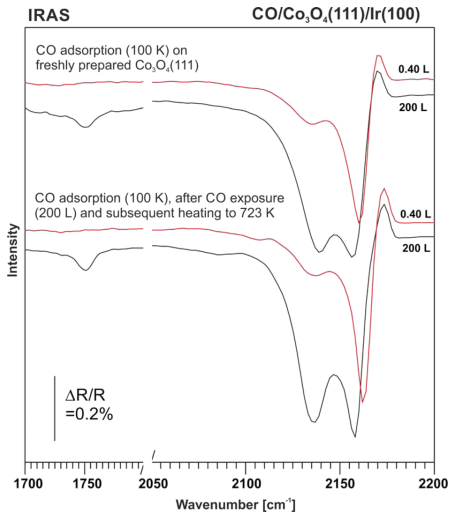

Figure 8. Comparison of IRAS spectra of CO on Co_3O_4(111)/Ir(100) in the low coverage regime (0.4 L) and in the high coverage regime (200 L) at 100 K; (top) pristine Co_3O_4(111)/Ir(100) after preparation; (bottom) after CO exposure (200 L at 100 K) and subsequent annealing to 723 K.

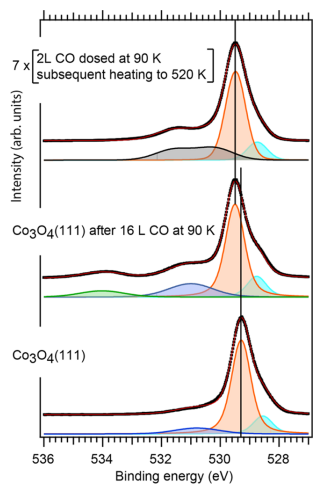

Figure 9. Comparison of O 1s spectra recorded on pristine Co_3O_4(111) (bottom), after adsorption adsorption of 16 L CO (middle), and after 7 adsorption (2 L CO)/desorption cycles to 520 K (top).

Figure 9 we compare the spectra recorded on the pristine film, after CO adsorption and after repeated adsorption/desorption cycles to 520 K. As discussed in section 3.3, the spectrum of the pristine film is dominated by an intense single feature at a BE of 529.3 eV (Figure 9, bottom spectra). Upon CO adsorption the

DOI: 10.1021/acs.jpcc.5b04145
J. Phys. Chem. C 2015, 119, 16688−16699

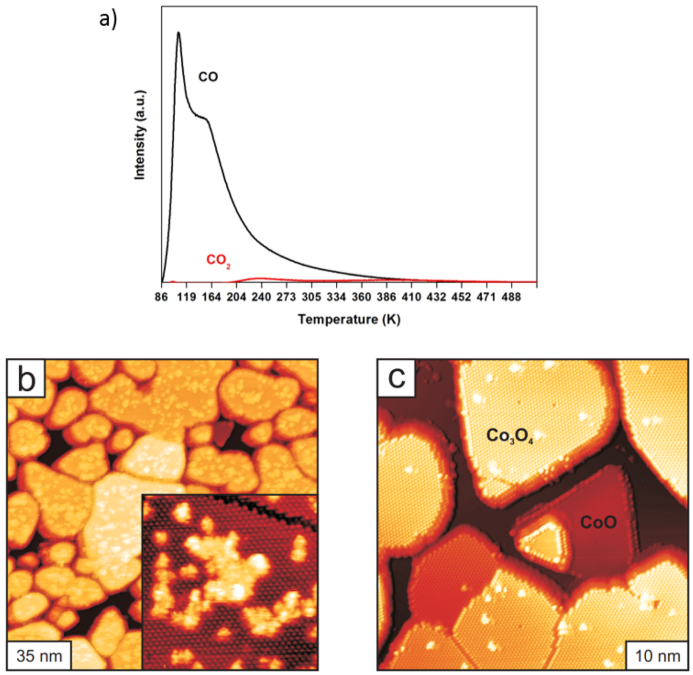

Figure 10. (a) TPD spectrum comparing the CO desorption (m/e = 28) and CO_2 production (m/e = 44) from a fully CO-saturated Co_3O_4(111) film; (b) STM image after four cycles of repeated CO adsorption and desorption up to a maximum temperature of 640 K; insert: close-up of the surface aggregates with perfect surrounding atomic lattice. (c) after annealing the film prepared in (b) to 740 K.

main component shifts by +0.2 eV and the two characteristic O 1s features shifted by +1.5 eV and +4.5 eV appear as discussed in section 3.3. After 7 cycles of CO adsorption and subsequent heating to 520 K, the main component also shifts by +0.2 eV, but now a new broad shoulder appears at the high binding energy side of the main peak. Curve fitting reveals that it is impossible to fit this shoulder component with one single component and we therefore used two components shifted by +0.7 eV (BE 530.0 eV) and +2.1 eV (BE 531.4 eV) for the curve fitting of this component. Further we note that the C 1s spectrum after repeated CO adsorption/desorption cycles (see Supporting Information) only reveals a very small carbonate component consistent with Figure 4c that showed that the large majority of carbonate disappeared at 520 K. Since we do not observe any significant amount of carbonate or any other carbon containing species on the Co_3O_4(111) surface after the repeated CO adsorption/desorption, it is evident that the broad O 1s shoulder at +0.7 to +2.1 eV must originate from the Co oxide film itself. A BE shoulder in this region has previously been assigned to oxygen vacancies in reducible oxides (see ref 59 and references therein). Further, the +0.2 eV shift of the O 1s main peak has been observed for reducible oxide films and again reflect a change of the electrostatic potential at the surface (see, e.g., refs 60−62). The assignment of the O 1s shoulder at +0.7 to +2.1 eV to oxygen vacancies can furthermore partly explain why the temperature development of the shoulder component in O 1s TPXPS experiments (Figure 6c) looks so complex, since this component is assigned to both carbonate and oxygen vacancies. We conclude that the process of CO_2 formation via carbonate decomposition involves the consumption of a small amount of lattice oxygen upon annealing.

This structural reorganization of the crystal in response to the loss of oxygen or equivalently the surplus of cobalt can be monitored by STM at the microscopic scale. After repeated cycles of CO adsorption and heating to 640 K we observe changes represented by the STM topography in Figure 10b. Whereas the overall morphology of the Co_3O_4 film does not change, we observe a high density of protrusions or flat clusters on the terraces (Figure 10b). Similar structures appear in the STM images also when evaporating small amounts of metallic Co onto the Co_3O_4 films. Therefore, we tentatively assign the clusters to cobalt-rich oxide aggregates at or right below the surface, which are formed as a reaction to the loss of lattice oxygen. We observe that the aggregates dissolve again in the Co_3O_4 crystallites if the oxide films are annealed to an even higher temperature of 740 K (Figure 10c). Eventually, the excess of Co (or loss of O) causes the complete crystallite to switch to rocksalt CoO(111), as observed especially for small crystallites (see Figure 10c). CoO(111) crystallites are readily identified by STM and also as faint diffraction spots in LEED.[35] According to the above discussion and by observing an essentially unchanged film morphology in STM, CO_2 formation and reduction of the Co_3O_4 films occurs exclusively via

DOI: 10.1021/acs.jpcc.5b04145
J. Phys. Chem. C 2015, 119, 16688−16699

formation of surface carbonates that are bound to defects such as step edges or side facets.

4. CONCLUSIONS

We have studied the interaction of CO and O_2 with well-ordered $Co_3O_4(111)$ films grown on Ir(100) using STM, TDS, HR-XPS, and IRAS under UHV conditions. The findings can be summarized as follows:

1. CO adsorbs on $Co_3O_4(111)$ at 100 K in two coverage regimes. At exposures below 1 L, a low coverage phase is formed in which the CO adsorbs on the topmost layer of Co^{2+} ions. This phase is characterized by a CO stretching mode with a singleton frequency at 2174 cm^{-1} ($\theta < 0.01$). With increasing coverage the CO stretching band undergoes a redshift ($\Delta = -20$ cm^{-1}) to 2154 cm^{-1} at full coverage of the surface Co^{2+} ions (3.5×10^{14} molecules·cm^{-2}). At larger exposures, a compressed high coverage phase is formed, in which the CO is weakly adsorbed in between the Co^{2+} sites.
2. The weakly adsorbed molecular CO exhibits a complex C 1s spectrum which is associated with a strong charge transfer satellite structure. The C 1s main peak of this molecular CO is found at binding energy of 287.0 eV. Desorption of the molecularly adsorbed CO species gives rise to two desorption features in TDS at temperatures between 90 and 110 K and between 140 and 180 K, respectively. Repeated CO adsorption and desorption experiments show that the molecular CO species are adsorbed and desorbed reversibly.
3. In addition to the molecularly adsorbed CO, a bridging carbonate species is formed once the CO exposure exceeds a value of 1 L. This surface carbonate species is a minority species and forms at defects of the film most likely at steps and defect sites at the side facets of the (111) oriented grains. In contrast to the molecularly adsorbed CO, the surface carbonate species remains on the surface up to higher temperature. It desorbs in a broad temperature range between 200 and 400 K, indicating stronger binding and a substantial activation barrier for formation and desorption. Its IRAS signature is found at 1743−1751 cm^{-1} and the C 1s binding energy at 288.5 eV.
4. O_2 coadsorption does neither influence CO adsorption in the low coverage CO phase nor formation of the surface carbonate species. However, preadsorbed O_2 blocks the formation of the compressed high coverage CO phase.
5. Upon annealing, the surface carbonate decomposes mainly under formation of CO and to a very small extent under formation of CO_2. The latter process consumes lattice oxygen. The loss of oxygen is compensated by producing Co interstitials that segregate and form partially reduced oxide clusters at the surface. If a crystallite has lost too much lattice oxygen, it recrystallizes as a CoO grain.

■ ASSOCIATED CONTENT

Supporting Information

C 1s spectrum after repeated cycles of dosing CO and heating on $Co_3O_4(111)$/Ir(100). The Supporting Information is available free of charge on the ACS Publications website at DOI: 10.1021/acs.jpcc.5b04145.

■ AUTHOR INFORMATION

Corresponding Authors

*E-mail: alexander.schneider@fau.de. Phone: +49 9131 8528405. Fax: +49 9131 8528400.

*E-mail: joerg.libuda@fau.de. Phone: +49 9131 8527308. Fax: +49 9131 8528867.

Notes

The authors declare no competing financial interest.

■ ACKNOWLEDGMENTS

The authors gratefully acknowledge financial support by the Deutsche Forschungsgemeinschaft (DFG) within the DACH Project "COMCAT" and the DFG Research Unit 1878 "funCOS". The work was additionally supported within the Excellence Cluster "Engineering of Advanced Materials" in the framework of the Excellence Initiative and the Clariant AG. Further financial support by the European Commission ("chipCAT", FP7-NMP-2012-SMALL-6, Grant Agreement No. 310191), by COST Action CM1104 "Reducible oxide chemistry, structure and functions", and travel support by the DAAD is gratefully acknowledged. This work was also supported by the Röntgen-Ångström cluster "Catalysis on the atomic scale" (Project No. 349-2011-6491) and by the Project Grant 2012-3850 both financed by the Swedish research council. The MAX IV Laboratory personnel are acknowledged for support during measurements. The authors are grateful for the support of the Alexander von Humboldt Foundation within the Research Group Linkage Program.

■ REFERENCES

(1) Xie, X.; Li, Y.; Liu, Z.-Q.; Haruta, M.; Shen, W. Low-Temperature Oxidation of CO Catalysed by Co_3O_4 Nanorods. *Nature* **2009**, *458*, 746−749.

(2) Choudhary, T. V.; Banerjee, S.; Choudhary, V. R. Catalysts for Combustion of Methane and Lower Alkanes. *Appl. Catal., A* **2002**, *234*, 1−23.

(3) Jansson, J.; Palmqvist, A. E. C.; Fridell, E.; Skoglundh, M.; Osterlund, L.; Thormahlen, P.; Langer, V. On the Catalytic Activity of Co_3O_4 in Low-Temperature CO Oxidation. *J. Catal.* **2002**, *211*, 387−397.

(4) Liotta, L. F.; Wu, H.; Pantaleo, G.; Venezia, A. M. Co_3O_4 Nanocrystals and Co_3O_4-MO_x Binary Oxides for CO, CH_4 and VOC Oxidation at Low Temperatures: A Review. *Catal. Sci. Technol.* **2013**, *3*, 3085−3102.

(5) Xiong, S.; Yuan, C.; Zhang, M.; Xi, B.; Qian, Y. Controllable Synthesis of Mesoporous Co_3O_4 Nanostructures with Tunable Morphology for Application in Supercapacitors. *Chem. - Eur. J.* **2009**, *15*, 5320−5326.

(6) Zhao, Z.; Lin, X.; Jin, R.; Dai, Y.; Wang, G. High Catalytic Activity in CO Prox Reaction of Low Cobalt-Oxide Loading Catalysts Supported on Nano-Particulate CeO_2-ZrO_2 Oxides. *Catal. Commun.* **2011**, *12*, 1448−1451.

(7) Tuti, S.; Pepe, F. On the Catalytic Activity of Cobalt Oxide for the Steam Reforming of Ethanol. *Catal. Lett.* **2008**, *122*, 196−203.

(8) Wang, C.-B.; Lee, C.-C.; Bi, J.-L.; Siang, J.-Y.; Liu, J.-Y.; Yeh, C.-T. Study on the Steam Reforming of Ethanol over Cobalt Oxides. *Catal. Today* **2009**, *146*, 76−81.

(9) Dau, H.; Limberg, C.; Reier, T.; Risch, M.; Roggan, S.; Strasser, P. The Mechanism of Water Oxidation: From Electrolysis Via Homogeneous to Biological Catalysis. *ChemCatChem* **2010**, *2*, 724−761.

(10) Liang, Y.; Li, Y.; Wang, H.; Zhou, J.; Wang, J.; Regier, T.; Dai, H. Co_3O_4 Nanocrystals on Graphene as a Synergistic Catalyst for Oxygen Reduction Reaction. *Nat. Mater.* **2011**, *10*, 780−786.

(11) Xu, C.; Tian, Z.; Shen, P.; Jiang, S. P. Oxide (CeO_2, NiO, Co_3O_4 and Mn_3O_4-Promoted Pd/C Electrocatalysts for Alcohol Electrooxidation in Alkaline Media. *Electrochim. Acta* **2008**, *53*, 2610−2618.
(12) Vargas, J. C.; Libs, S.; Roger, A. C.; Kiennemann, A. Study of Ce-Zr-Co Fluorite-Type Oxide as Catalysts for Hydrogen Production by Steam Reforming of Bioethanol. *Catal. Today* **2005**, *107*−*08*, 417−425.
(13) Yao, Y. Y. Oxidation of Hydrocarbons and CO over Metal-Oxides 0.3. Co_3O_4. *J. Catal.* **1974**, *33*, 108−122.
(14) Jansson, J. Low-Temperature CO Oxidation over Co_3O_4/Al_2O_3. *J. Catal.* **2000**, *194*, 55−60.
(15) Thormahlen, P.; Skoglundh, M.; Fridell, E.; Andersson, B. Low-Temperature CO Oxidation over Platinum and Cobalt Oxide Catalysts. *J. Catal.* **1999**, *188*, 300−310.
(16) Royer, S.; Duprez, D. Catalytic Oxidation of Carbon Monoxide over Transition Metal Oxides. *ChemCatChem* **2011**, *3*, 24−65.
(17) Yu, Y.; Takei, T.; Ohashi, H.; He, H.; Zhang, X.; Haruta, M. Pretreatments of Co_3O_4 at Moderate Temperature for CO Oxidation at −80 °C. *J. Catal.* **2009**, *267*, 121−128.
(18) Tang, C.-W.; Hsu, L.-C.; Yu, S.-W.; Wang, C.-B.; Chien, S.-H. In Situ FT-IR and TPD-MS Study of Carbon Monoxide Oxidation over a CeO_2/Co_3O_4 Catalyst. *Vib. Spectrosc.* **2013**, *65*, 110−115.
(19) Hu, L.; Sun, K.; Peng, Q.; Xu, B.; Li, Y. Surface Active Sites on Co_3O_4 Nanobelt and Nanocube Model Catalysts for CO Oxidation. *Nano Res.* **2010**, *3*, 363−368.
(20) Pollard, M. J.; Weinstock, B. A.; Bitterwolf, T. E.; Griffiths, P. R.; Newbery, A. P.; Paine, J. B., III. A Mechanistic Study of the Low-Temperature Conversion of Carbon Monoxide to Carbon Dioxide over a Cobalt Oxide Catalyst. *J. Catal.* **2008**, *254*, 218−225.
(21) Ma, C.; Wang, D.; Xue, W.; Dou, B.; Wang, H.; Hao, Z. Investigation of Formaldehyde Oxidation over Co_3O_4-CeO_2 and Au/Co_3O_4-CeO_2 Catalysts at Room Temperature: Effective Removal and Determination of Reaction Mechanism. *Environ. Sci. Technol.* **2011**, *45*, 3628−3634.
(22) Ma, C. Y.; Mu, Z.; Li, J. J.; Jin, Y. G.; Cheng, J.; Lu, G. Q.; Hao, Z. P.; Qiao, S. Z. Mesoporous Co_3O_4 and Au/Co_3O_4 Catalysts for Low-Temperature Oxidation of Trace Ethylene. *J. Am. Chem. Soc.* **2010**, *132*, 2608−2613.
(23) Cunningham, D. A. H.; Kobayashi, T.; Kamijo, N.; Haruta, M. Influence of Dry Operating-Conditions - Observation of Oscillations and Low-Temperature CO Oxidation over Co_3O_4 and Au/Co_3O_4 Catalysts. *Catal. Lett.* **1994**, *25*, 257−264.
(24) Luo, J.-Y.; Meng, M.; Li, X.; Li, X.-G.; Zha, Y.-Q.; Hu, T.-D.; Xie, Y.-N.; Zhang, J. Mesoporous Co_3O_4-CeO_4 and Pd/Co_3O_4-CeO_2 Catalysts: Synthesis, Characterization and Mechanistic Study of Their Catalytic Properties for Low-Temperature CO Oxidation. *J. Catal.* **2008**, *254*, 310−324.
(25) Finocchio, E.; Busca, G.; Lerenzelli, V.; Escribano, V. S. FTIR Studies on the Selective Oxidation and Combustion of Light Hydrocarbons at Metal Oxide Surfaces Part 2. Propane and Propene Oxidation on Co_3O_4. *J. Chem. Soc., Faraday Trans.* **1996**, *92*, 1587−1593.
(26) Finocchio, E.; Willey, R. J.; Busca, G.; Lorenzelli, V. FTIR Studies on the Selective Oxidation and Combustion of Light Hydrocarbons at Metal Oxide Surfaces Part 3. Comparison of the Oxidation of C-3 Organic Compounds over Co_3O_4, $MgCr_2O_4$ and CuO. *J. Chem. Soc., Faraday Trans.* **1997**, *93*, 175−180.
(27) Busca, G.; Daturi, M.; Finocchio, E.; Lorenzelli, V.; Ramis, G.; Willey, R. J. Transition Metal Mixed Oxides as Combustion Catalysts: Preparation, Characterization and Activity Mechanisms. *Catal. Today* **1997**, *33*, 239−249.
(28) Liang, Y.; et al. Oxygen Reduction Electrocatalyst Based on Strongly Coupled Cobalt Oxide Nanocrystals and Carbon Nanotubes. *J. Am. Chem. Soc.* **2012**, *134*, 15849−15857.
(29) Jiang, D.-e.; Dai, S. The Role of Low-Coordinate Oxygen on Co_3O_4(110) in Catalytic CO Oxidation. *Phys. Chem. Chem. Phys.* **2011**, *13*, 978−984.
(30) Hu, L.; Peng, Q.; Li, Y. Selective Synthesis of Co_3O_4 Nanocrystal with Different Shape and Crystal Plane Effect on Catalytic Property for Methane Combustion. *J. Am. Chem. Soc.* **2008**, *130*, 16136−16137.
(31) Fei, Z.; He, S.; Li, L.; Ji, W.; Au, C.-T. Morphology-Directed Synthesis of Co_3O_4 Nanotubes Based on Modified Kirkendall Effect and Its Application in CH_4 Combustion. *Chem. Commun.* **2012**, *48*, 853−855.
(32) Kuhlenbeck, H.; Shaikhutdinov, S.; Freund, H.-J. Well-Ordered Transition Metal Oxide Layers in Model Catalysis - a Series of Case Studies. *Chem. Rev.* **2013**, *113*, 3986−4034.
(33) Libuda, J.; Freund, H. J. Molecular Beam Experiments on Model Catalysts. *Surf. Sci. Rep.* **2005**, *57*, 157−298.
(34) Meyer, W.; Biedermann, K.; Gubo, M.; Hammer, L.; Heinz, K. Surface Structure of Polar Co_3O_4(111) Films Grown Epitaxially on Ir(100)-(1 × 1). *J. Phys.: Condens. Matter* **2008**, *20*, 265011.
(35) Biedermann, K.; Gubo, M.; Hammer, L.; Heinz, K. Phases and Phase Transitions of Hexagonal Cobalt Oxide Films on Ir(100)-(1 × 1). *J. Phys.: Condens. Matter* **2009**, *21*, 185003.
(36) Gubo, M.; Ebensperger, C.; Meyer, W.; Hammer, L.; Heinz, K. Structural Elements in the Oxidation Process of a Single Cobalt Layer on Ir(100)-(1 × 1). *Phys. Rev. B* **2011**, *83*, 075435.
(37) Gubo, M.; Ebensperger, C.; Meyer, W.; Hammer, L.; Heinz, K.; Mittendorfer, F.; Redinger, J. Tuning the Growth Orientation of Epitaxial Films by Interface Chemistry. *Phys. Rev. Lett.* **2012**, *108*, 066101.
(38) Heinz, K.; Hammer, L. Epitaxial Cobalt Oxide Films on Ir(100)-the Importance of Crystallographic Analyses. *J. Phys.: Condens. Matter* **2013**, *25*, 173001.
(39) Feulner, P.; Menzel, D. Simple Ways to Improve Flash Desorption Measurements from Single-Crystal Surfaces. *J. Vac. Sci. Technol.* **1980**, *17*, 662−663.
(40) Ghosh, P.; Narasimhan, S.; Jenkins, S. J.; King, D. A. Lifting of Ir{100} Reconstruction by CO Adsorption: An Ab Initio Study. *J. Chem. Phys.* **2007**, *126*, 244701.
(41) Nyholm, R.; Andersen, J. N.; Johansson, U.; Jensen, B. N.; Lindau, I. Beamline I311 at Max-Lab: A Vuv/Soft X-ray Undulator Beamline for High Resolution Electron Spectroscopy. *Nucl. Instrum. Methods Phys. Res., Sect. A* **2001**, *467*, 520−524.
(42) Heidberg, J.; Kandel, M.; Meine, D.; Wildt, U. The Monolayer CO Adsorbed on MgO(100) Detected by Polarization Infrared-Spectroscopy. *Surf. Sci.* **1995**, *331*, 1467−1472.
(43) Spoto, G.; Gribov, E. N.; Ricchiardi, G.; Damin, A.; Scarano, D.; Bordiga, S.; Lamberti, C.; Zecchina, A. Carbon Monoxide MgO from Dispersed Solids to Single Crystals: A Review and New Advances. *Prog. Surf. Sci.* **2004**, *76*, 71−146.
(44) Spoto, G.; Gribov, E.; Damin, A.; Ricchiardi, G.; Zecchina, A. The IR Spectra of Mg-$5c^{2+}$(CO) Complexes on the (001) Surfaces of Polycrystalline and Single Crystal MgO. *Surf. Sci.* **2003**, *540*, L605−L610.
(45) Zecchina, A.; Scarano, D.; Bordiga, S.; Ricchiardi, G.; Spoto, G.; Geobaldo, F. IR Studies of CO and NO Adsorbed on Well Characterized Oxide Single Microcrystals. *Catal. Today* **1996**, *27*, 403−435.
(46) Lemire, C.; Meyer, R.; Henrich, V. E.; Shaikhutdinov, S.; Freund, H. J. The Surface Structure of Fe_3O_4(111) Films as Studied by CO Adsorption. *Surf. Sci.* **2004**, *572*, 103−114.
(47) Solymosi, F.; Knozinger, H. Infrared Study on the Interaction of CO with Alumina-Supported Rhodium. *J. Chem. Soc., Faraday Trans.* **1990**, *86*, 389−395.
(48) Frank, M.; Kuhnemuth, R.; Baumer, M.; Freund, H. J. Vibrational Spectroscopy of CO Adsorbed on Supported Ultra-Small Transition Metal Particles and Single Metal Atoms. *Surf. Sci.* **2000**, *454*, 968−973.
(49) Vayssilov, G. N.; Mihaylov, M.; St. Petkov, P.; Hadjiivanov, K. I.; Neyman, K. M. Reassignment of the Vibrational Spectra of Carbonates, Formates, and Related Surface Species on Ceria: A Combined Density Functional and Infrared Spectroscopy Investigation. *J. Phys. Chem. C* **2011**, *115*, 23435−23454.

DOI: 10.1021/acs.jpcc.5b04145
J. Phys. Chem. C 2015, 119, 16688−16699

(50) Yanagisawa, Y.; Takaoka, K.; Yamabe, S.; Ito, T. Interaction of CO_2 with Magnesium-Oxide Surfaces - a TPD, FTIR, and Cluster-Model Calculation Study. *J. Phys. Chem.* **1995**, *99*, 3704−3710.
(51) Neitzel, A.; Lykhach, Y.; Skala, T.; Tsud, N.; Vorokhta, M.; Mazur, D.; Prince, K. C.; Matolin, V.; Libuda, J. Surface Sites on Pt-CeO_2 Mixed Oxide Catalysts Probed by CO Adsorption: A Synchrotron Radiation Photoelectron Spectroscopy Study. *Phys. Chem. Chem. Phys.* **2014**, *16*, 24747−24754.
(52) Fuggle, J. C.; Umbach, E.; Menzel, D.; Wandelt, K.; Brundle, C. R. Adsorbate Line-Shapes and Multiple Lines in XPS - Comparison of Theory and Experiment. *Solid State Commun.* **1978**, *27*, 65−69.
(53) Tillborg, H.; Nilsson, A.; Martensson, N. Shake-up and Shake-Off Structures in Core-Level Photoemission Spectra from Adsorbates. *J. Electron Spectrosc. Relat. Phenom.* **1993**, *62*, 73−93.
(54) Cappus, D.; et al. Electronic and Geometric Structure of Adsorbates on Oxide Surfaces. *J. Electron Spectrosc. Relat. Phenom.* **1994**, *68*, 347−355.
(55) Sandell, A.; Bennich, P.; Nilsson, A.; Hernnas, B.; Bjorneholm, O.; Martensson, N. Chemisorption of CO on Cu(100), Ag(110) and Au(110). *Surf. Sci.* **1994**, *310*, 16−26.
(56) Haeming, M.; Schoell, A.; Umbach, E.; Reinert, F. Adsorbate-Substrate Charge Transfer and Electron-Hole Correlation at Adsorbate/Metal Interfaces. *Phys. Rev. B* **2012**, *85*, 235132.
(57) Knudsen, J.; Martin, N. M.; Gråsäs, E.; Blomberg, S.; Gustafson, J.; Andersen, J. N.; Lundgren, E.; Klacar, S.; Hellman, A.; Gronbeck, H. Carbonate Formation on p(4 × 4)-O/Ag(111). *Phys. Rev. B* **2011**, *84*, 115430.
(58) Andersson, S.; et al. Metal-Oxide Interaction for Metal Clusters on a Metal-Supported Thin Alumina Film. *Surf. Sci.* **1999**, *442*, L964−L970.
(59) Lykhach, Y.; et al. Water Chemistry on Model Ceria and Pt/Ceria Catalysts. *J. Phys. Chem. C* **2012**, *116*, 12103−12113.
(60) Lykhach, Y.; Happel, M.; Johanek, V.; Skala, T.; Kollhoff, F.; Tsud, N.; Dvorak, F.; Prince, K. C.; Matolin, V.; Libuda, J. Adsorption and Decomposition of Formic Acid on Model Ceria and Pt/Ceria Catalysts. *J. Phys. Chem. C* **2013**, *117*, 12483−12494.
(61) Chen, T. L.; Mullins, D. R. Adsorption and Reaction of Acetaldehyde over CeO_x(111) Thin Films. *J. Phys. Chem. C* **2011**, *115*, 3385−3392.
(62) Mullins, D. R.; Robbins, M. D.; Zhou, J. Adsorption and Reaction of Methanol on Thin-Film Cerium Oxide. *Surf. Sci.* **2006**, *600*, 1547−1558.

DOI: 10.1021/acs.jpcc.5b04145
J. Phys. Chem. C 2015, 119, 16688−16699

Paper III

Adsorption properties of CO and CO_2 onto CoO(111) and Co_3O_4(111) films studied with core level spectroscopy

Mohammad Alif Arman,[†] Pascal Ferstl,[‡] M. Alexander Schneider,[‡] Edvin Lundgren,[†] Lutz Hammer,[‡] and Jan Knudsen[*,†,¶]

Division of Synchrotron Radiation Research, Department of Physics, Lund University, Sweden, and Lehrstuhl für Festkörperphysik, Universität Erlangen-Nürnberg, Germany

E-mail: jan.knudsen@sljus.lu.se

[*]To whom correspondence should be addressed
[†]Division of Synchrotron Radiation Research, Department of Physics, Lund University, Sweden
[‡]Lehrstuhl für Festkörperphysik, Universität Erlangen-Nürnberg, Germany
[¶]MAX IV Laboratory, Lund University, Box 118, 221 00 Lund, Sweden

Abstract

Using high resolution photoemission spectroscopy we give a detailed picture of CO and CO_2 adsorption onto thin films of $Co_3O_4(111)$ and CoO(111) surfaces grown on the Ir(100)-(1×1) surface. The pristine CoO(111) film without Co surface atoms is almost fully inert with respect to CO and CO_2 adsorption at 90 K, while carbonate species, weakly adsorbed CO, and CO_2 are identified on the pristine $Co_3O_4(111)$ surface having Co surface atoms. The CoO(111) surface can, however, be given the adsorption properties of the $Co_3O_4(111)$ surface without changing its electronic properties, if accessible Co atoms are formed artificially on the surface either by introducing oxygen vacancies or by adding Co add atoms. Based on this finding we conclude that it is the surface Co atoms that govern the CO and CO_2 adsorption properties and most likely also the catalytic activity of the film rather than the electronic and structural properties of $Co_3O_4(111)$ and CoO(111) films. Finally, we also demonstrate that it is possible to distinguish CO molecules adsorbed in oxygen vacancies from CO molecules adsorbed on Co_{add} atoms.

Keywords: cobalt oxide, model catalysis, photoelectron spectroscopy, CO, CO_2

Introduction

Cobalt oxide materials have been and are studied extensively because of their potential use as future catalysts for: the low temperature CO oxidation reaction,[1–3] the preferential oxidation of CO in hydrogen (PROX),[4] the oxygen evolution reaction (OER),[5,6] the oxygen reduction reaction (ORR),[7] and the methane oxidation reaction,[8,9] just to mention a few of the relevant reactions where catalytic activity has been demonstrated. An atomic scale understanding of these reactions on Co oxide based catalysts is, however, lacking and this has inspired work where Co-oxide model catalysts grown in-situ at ultrahigh vacuum (UHV) conditions are used.

On the Ir(100) surface a large variety of Co oxide phases has been grown and characterized in detail primarily by quantitative low energy electron diffraction (LEED) I-V analysis and scanning tunneling microscopy (STM) and detailed structural models of these Co-oxide phases exist today.[10] Well-ordered Co oxide films and islands can, however, also be grown on other substrates such as Pd(100),[11] Pt(111),[12,13] Ag(100),[14,15] Ag(111),[13] and Au(111).[13,16]

Focusing on the thick $Co_3O_4(111)$[17] surfaces grown on Ir(100) the previous reported structural characterization showed that its surface is terminated by Co^{2+} ions with a (2×2) periodicity atop the hexagonal oxygen layer. Overview and atomically resolved STM images are shown in figure 1(a-d) together with the LEED image and a simplified structure model. The lattice distance between the surface Co atoms is 5.72 Å, which is identical to the corresponding lattice distance in the bulk crystal. The CoO(111) structure[18] is terminated by O atoms with an in-plane lattice parameter of 3.012 Å.[19] The oxygen atoms form a closed hexagonal layer atop of the octahedraly coordinated Co^{2+} ions (see figure 1(h)). Due to the square symmetry of the Ir(100), the $Co_3O_4(111)$ and CoO(111) films grow in two orthogonal domains one along the [011] and the other in the [011] direction of the Ir(100) substrate.[17,18]

In contrast to the profound knowledge of the structure of Co oxide thin and thick films relatively little is known about the chemical properties of these surfaces. In two recent studies from 2015[20,21] the CO adsorption properties on the pristine $Co_3O_4(111)$ surface was compared with surfaces preexposed to oxygen or metallic Co atoms. In the study by Ferstl *et al.*[20] CO adsorption onto the $Co_3O_4(111)$ film supported by Ir(100) was studied with high resoltion photoemission spectroscopy (HRPES) in combination with infrared reflection absorption spectroscopy (IRAS), scanning tunneling microscopy (STM), and temperature programmed desorption (TPD).[20] One of the main findings in this study was that CO adsorbs weakly with complete desorption at temperatures above 230 K. This weakly adsorbed CO is located both on Co^{2+} ions on the $Co_3O_4(111)$ surface at low coverage and in between the ions at higher coverages. Another take home message from this study was the fact that we observed carbonate formation upon CO exposures above 1 L most likely adsorbed on steps, defect sites, or side facets of the $Co_3O_4(111)$ islands. This carbonate was observed to desorb in a broad temperature interval between 200 and 400 K. In the second study[21] it was demonstrated that predeposition of metallic Co at room temperature onto the $Co_3O_4(111)$ surface before CO adsorption results in a single adsorption site assigned to CO bound to Co ions on the surface and no carbonate formation. Annealing of the $Co_3O_4(111)$ surface preexposed to Co atoms to 500 K resulted in $Co_3O_4(111)$ supported CoO islands with Co atoms located on the surface. The CO adsorption properties of these CoO islands with Co atoms atop was found to be quite similar to the $Co_3O_4(111)$ surface exposed to Co atoms discussed above.

In a very recent operando x-ray absorption spectroscopy and high pressure PES study published by Lukashuk *et al.* in 2016 CO oxidation, H_2, and preferential CO oxidation in H_2 on the supported spinel particles was investigated. The CO oxidation experiments in this work showed that reduction of the Co_3O_4 particles sets in already at room temperature in 0.15 mbar of pure CO, at 523 K the particles are fully converted to CoO, and at 573 K metallic Co is observed. In the corresponding C 1s spectra carbonates (288.2 eV), CO or

C-OH species (286.1 eV), and elementary carbon (284.7 eV) were detected.

Clearly, the three recent articles cited above underlines that that Co oxide model systems currently are studied extensively. In contrast to the extensive body of structural work on the Ir(100) supported Co_3O_4(111) and CoO(111) films, adsorption studies on these films have only recently been initiated. In our present work we give a detailed picture of CO and CO_2 adsorption and desorption on well-characterized Ir(100) supported pristine and defective Co_3O_4(111) and CoO(111) films at well controlled ultra high vacuum condition using HRPES. Our study demonstrates that the aces to free Co atoms on the Co oxide surfaces is essential for CO and CO_2 adsorption and the formation of carbonates. Both molecules adsorb and form carbonates on the Co_3O_4(111) surface and defective CoO(111) surfaces both with accessible Co atoms, while no adsorption or carbonate formation is observed on the pristine CoO(111) surface terminated by oxygen.

Experimental details

The HRPES experiments were performed at beamline I311 at the MAX IV Laboratory (Lund, Sweden).[22] The base pressure of the spectroscopy endstation of this beamline was $\sim 10^{-10}$mbar. Spectra were collected in normal emission with photon energies of 120 eV (Ir 4f), 380 eV (C 1s), 625 eV (O 1s), and 1000 eV (Co 2p). During measurements the sample was scanned in the x-ray beam at a speed of 5μm/s to avoid beam damage. The binding energies (BEs) of C 1s, O 1s, and Co 2p spectra were calibrated by measuring the Ir 4f region directly after the spectra of interest without changing the photon energy and by assuming fixed binding energy of Ir 4f of 60.85 eV. For the curve fitting we used symmetric Voigt components and polynomial backgrounds. The intensity of the O 1s spectra were normalized by setting the integral value of the main component equal to one. The intensity of the C 1s spectra were normalized to the Ir $4f_{7/2}$ peak measured with the same photon energy.

The Ir(100) crystal was cleaned by several cycles of Argon sputtering at room temperature and subsequent O_2 annealing at 1000 K, followed by vacuum annealing at 1273 K. Cleanness of the Ir(100) was confirmed with XPS and (LEED). Upon vacuum annealing at 1273 K, the crystal showed a high-quality Ir(100)-(5×1)-hex reconstruction in LEED at room temperature and below. An homebuild O_2 gas doser and an Omicron EFM-3 Co evaporator were mounted such that O_2 and Co could be dosed simultaneously. The O_2 gas doser allowed the local oxygen pressure at the surface to be well above $5{\cdot}10^{-6}$ mbar during growth. The Co evaporation rate was calibrated by producing two-dimensional cobalt oxide structures that require exact amounts of Co expressed in monolayer equivalents (MLEs).[23] One MLE is here equivalent to the full monolayer coverage of two dimensional c(8×2) cobalt oxide film grown on Ir(100)-(1×1) surface.

The starting point for the preparation of the Co_3O_4(111) film is the Ir(100)-(2×1)-O structure which we formed by cooling down the Ir(100)-(5×1)-hex from 1200 K to room temperature in $1{\cdot}10^{-8}$ mbar oxygen. Subsequently, 15 MLE (1MLE/min) of Co was deposited in $5{\cdot}10^{-7}$ mbar of O_2 at 300 K sample temperature. Finally, the 5 nm thick film was annealed at 523 K in $5{\cdot}10^{-7}$ mbar of O_2 for 2 min followed by vacuum flashing to 673 K to improve the ordering of the films. The CoO(111) film was formed from the Co_3O_4(111) film by flashing it to 900 K in ultra high vacuum (UHV).[10] The ordering of both Co_3O_4(111) and CoO(111) was checked by LEED.

Results and discussion

CO adsorption on Co_3O_4(111) and CoO(111) films

In figure 2 we compare the C 1s spectra of Co_3O_4(111) and CoO(111) before and after exposure to 10 L CO at 85 K, while the corresponding O 1s spectra are shown in figure 3. In reference 20 we discussed the curve fitting and peak assignment of the CO exposed Co_3O_4(111) surface in detail and a summary of these results will therefore only be given

here.

Starting with the C 1s spectrum of the $Co_3O_4(111)$ film before exposure to CO we observe a small component at 288.5 eV. After CO exposure three intense components are observed at binding energies of 287.0 (red), 288.5 (blue), and 290.9 eV (green) as seen in figure 2(b). Using temperature programmed XPS (TPXPS) we previously showed that the intensities of the components at 287.0 eV and 290.9 eV decrease simultaneously and are fully removed at 230 K. Based on this finding and the binding energies difference, these components were assigned to weakly bound CO and its shake-up peak, respectively.[20] The remaining component at 288.5 eV desorbs around 400 K,[20] and based on its higher thermal stability and its binding energy, this component was assigned to carbonate species.

In contrast to the observation of adsorbed CO and carbonate species on the $Co_3O_4(111)$ surface, the C 1s spectrum of the CO exposed CoO(111) surface reveals that carbon containing species essentially are absent after CO exposure. Only extremely weak components close to our detection limit are observed after CO exposure at 284.3 (grey), 287.3 (red), 289.15 (blue), and 291.2 (green).

In figure 3 the O 1s spectra corresponding to the C 1s spectra shown in figure 2 are shown. Starting with the pristine $Co_3O_4(111)$ film our curve fitting reveals a main component located at 529.30 eV (figure 3(a)). In addition, two small shoulder components are located at 528.55 eV (denoted as O_a), and at 530.80 eV (denoted as O_b). As we always observed all three components in our XPS experiments also when the surface is free of carbon, these components should be assigned to the pristine $Co_3O_4(111)$ surface. In our previous work we have shown that the intensity of the O_a component increase substantially by repeated CO adsorption and desorption cycles and this component was therefore assigned to defects.[20] Upon dosing CO two new components shifted by +1.5 eV (O2) and +4.5 eV (O3), respectively, developed in the O 1s spectra. Our previous TPXPS study[20] showed that the O3 component shifted by +4.5 eV from the main component desorbed at 230 K and this component is therefore assigned to weakly adsorbed CO. The remaining O2 component is then assigned to carbonate species.

We note that the BE of the O 1s carbonate component (O1) is identical to the BE of the defect component (O_a) and only by a combination of C 1s and O 1s spectra it is possible to estimate the defect and carbonate coverage.

The O 1s spectra of the CoO(111) film before and after CO exposure are essentially identical and can be fitted with a main component also located at 529.30 eV and a shoulder component (O_a) shifted by +1.8 eV. The absence of CO induced components both in the C 1s and O 1s spectra is clear evidence that the CoO(111) film in contrast to the Co_3O_4(111) surface is almost fully inert with respect to CO adsorption.

The similar FeO(111) and Fe_3O_4(111) films have been studied extensively and the adsorption properties of CO onto them is well described. Ultrathin FeO(111) films which are analog to the CoO(111) surface, are terminated by a hexagonal oxygen layer and CO adsorption is, therefore, fully absent after CO exposure at 100 K.[24] In contrast, CO adsorb easily onto the inverse spinel Fe_3O_4(111) film[25] with CO adsorbed strongly onto Fe^{3+} defect sites located on step edges, less strongly onto Fe^{2+} surface sites, and weakly and mobile CO on the surface.

Comparing the CO adsorption properties of Co_3O_4(111) and CoO(111) surfaces with the related FeO(111) and Fe_3O_4(111) surfaces discussed above, we conclude the following: (i) CO adsorption is inhibited on the oxygen terminated CoO(111) and on FeO(111) surfaces. (ii) On the Co_3O_4(111) and Fe_3O_4(111) surfaces terminated by a 2×2 structure of Co and Fe ions, respectively, CO molecules adsorb on the surface metal ions and weakly in between these ions. Inspired by these conclusions we went one step further and investigated if a CoO(111) can be modified in such a way that it obtains adsorption properties similar to the adsorption properties of the Co_3O_4(111) surface while it maintaining the spectroscopic fingerprints of a CoO(111) film. Before reporting on how the CoO(111) surface can be modified, we investigate the spectroscopic fingerprints of the CoO(111) and Co_3O_4(111) films focusing on the Co 2p core level.

In figure 4(a) and (b) we compare the Co 2p spectra of the Co_3O_4(111) and CoO(111)

surface. Starting with the $Co_3O_4(111)$ surface its Co $2p_{5/2}$ peak consist of two overlapping components located at binding energies of 779 eV and 780.5 eV, respectively, and a broad relatively weak satellite structure extending to binding energies of 790 eV consistent with previous published date acquired on Co_3O_4 powder samples.[26]

For the CoO(111) surface the Co $2p_{5/2}$ peak maximum is located at 780 eV corresponding to a +0.5 eV shift with respect to the $Co_3O_4(111)$ surface. Another clear difference with respect to the $Co_3O_4(111)$ surface is that the full width at half maximum (FWHM) of the main peak is significantly larger (5.2 eV) than what is observed for the $Co_3O_4(111)$ surface (3.0 eV). A final difference is that the satellite peak located at 786 eV is much more intense for the CoO(111) surface than the satellite structure observed for the $Co_3O_4(111)$ surface. This final observation was indeed expected since the intensity of the Co 2p satellite peak often is used as a fingerprint of the CoO rocksalt structure.[26] To summarize the clear differences in the Co 2p spectra facilitates their use as fingerprints of the $Co_3O_4(111)$ and CoO(111) phases.

As discussed above, the access to free Co and Fe ions seems to be essential for the CO adsorption on Co and Fe oxide surfaces. Inspired by this finding we used two different methods to create free Co ions on the surface of the inert CoO(111) surface: (i) By depositing a small amount of Co atoms onto the CoO(111) surface at 90 K we created free Co atoms on the surface. (ii) By exposing the CoO(111) surface to hydrogen radicals at 90 K we formed hydroxyl groups that we subsequently removed in the form in H_2O by flashing to 623 K resulting in the formation of oxygen vacancies providing access to the underlying Co atoms on the surface. The spectra of these modified CoO(111) surfaces are shown in figure 4(c) and (d), respectively. Clearly, the Co 2p fingerprints of the CoO(111) surfaces with Co_{add} atoms or O vacancies is close to identical to the pristine CoO(111) film.

Also the Co 2p (L3) XAS spectra displayed in figure 5 clearly demonstrate that the electronic structure of the CoO(111) film modified by Co_{add} atoms or O vacancies are indistinguishable from the pristine CoO(111) film. In contrast, the XAS spectrum of the

$Co_3O_4(111)$ surface is easy to distinguish from the CoO(111) with and without Co_{add} atoms or O vacancies. To conclude, both the Co 2p XPS and XAS spectra clearly demonstrate that the electronic structure of the CoO(111) film remains intact once it is modified by Co_{add} atoms or O vacancies and based on our PES analysis it should be characterized as a rocksalt like film. As a consequence it is unexpected that CO molecules adsorb on the modified CoO(111) films as we found no CO adsorption on the pristine CoO(111) films.

CO adsorption experiments on the modified CoO(111) films demonstrates, however, that this prediction is wrong as the adsorption behavior is changed dramatically both by Co_{add} atoms or O vacancies. This is easily seen from figure 6 where the C 1s spectra acquired before and after CO saturation at 85 K of the modified CoO(111) films are compared to spectra before and after CO saturation of the $Co_3O_4(111)$ surface. Inspection of this figures reveal that similar C 1s components develop upon CO saturation of the defective CoO(111) films as on the CO saturated $Co_3O_4(111)$ film suggesting that carbonate and weakly adsorbed CO is formed on the defective CoO(111) surfaces.

There are, however, small changes of the positions of the different components observed for the defective CoO(111) surfaces with respect to the $Co_3O_4(111)$ surface. Starting with the blue C 1s component assigned to carbonates we observe a +0.5 eV core level shift (CLS) for both types of defective CoO(111) surfaces with respect to the BE position found for carbonates on the $Co_3O_4(111)$ surface. This is expected as the carbonate adsorbates are adsorbed at quite different $Co_3O_4(111)$ and CoO(111) like surfaces. However, the identical shift observed for CoO(111) films with Co_{add} atoms and O vacancies, respectively, suggests that carbonates are formed in similar sites on both defective surfaces. In contrast, the two components assigned to weakly adsorbed CO have different CLS on the two CoO(111) surfaces modified by Co_{add} atoms and O vacancies, respectively. For the CoO(111) film modified by Co_{add} atoms our curve fitting (see figure 6(d)) reveals binding energy positions of 287.0 eV (red component) and 290.9 eV (green component) identical to the positions observed for the $Co_3O_4(111)$ film. In contrast, we observe a +0.3 eV shift for both components when the

CoO(111) surface is modified by O vacancies. These observations suggest weakly adsorbed CO in similar sites on the CoO(111) surface with Co_{add} atoms and on the Co_3O_4(111) surface, which makes very much sense, as both surfaces contains free Co_{add} atoms atop a hexagonal O-layer. On the CoO(111) surfaces containing O vacancies we expect CO molecules to adsorb in the vacancies and since these sites are quite different from the free Co_{add} atoms sites we expect a different CLS fully consistent with what we observed.

In figure 7 we compare the O 1s spectra of the two defective CoO(111) surfaces with the the Co_3O_4(111) surface before and after CO saturation at 85 K. Before CO exposure both defective CoO(111) films (figure 7(c) and (e)) can be fitted with a main peak and shoulder component (O_a) shifted +1.8 eV identical to what we observed for the pristine CoO(111) film (see also figure 2(c)). Thus, similar to what we observed in the Co 2p XPS and XAS spectra the small amount of Co_{add} atoms and O vacancies are also invisible in the O 1s spectra before CO adsorption.

Consistent with the C 1s spectra the O 1s spectra of the defective CoO(111) films acquired after CO exposure look quite similar to the spectrum of the CO exposed Co_3O_4(111) surface. Two new components named O2 and O3 in figure 7(d, f) develops upon CO exposure. The O2 component shifted by +1.8 eV with respect to the main peak is assigned to carbonate consistent with our assignment of carbonates adsorbed on the Co_3O_4(111) surface. The CLS of +1.8 eV observed both defective CoO(111) surfaces is slightly larger than the 1.5 eV shift observed for carbonates on the Co_3O_4(111) surface consistent with +0.5 eV difference observed in the C 1s spectra of figure 6. The components assigned to weakly adsorbed CO (red and green) are found to have very similar CLS's for CO adsorbed on the Co_3O_4(111) and CoO(111) surface modified by Co_{add} atoms, while a +0.7 eV higher CLS is observed on the CoO(111) surface with O vacancies. This observation gives further support for the adsorption of weakly bound CO in different sites on CoO(111) surfaces modified by Co_{add} atoms and O vacancies, respectively, as the C 1s spectra also suggested.

To summarize the CO adsorption experiments on the pristine Co_3O_4(111) and CoO(111)

films we demonstrated that the closed oxygen layer of the CoO(111) surface blocks CO adsorption at 85 K, while CO easily adsorb at the same temperature on the Co_3O_4(111) surface covered by free Co ions. Both weakly adsorbed CO and and carbonate species are detected on the Co_3O_4(111) surface upon CO adsorption. It is, however, possible to modify the CoO(111) surface by Co_{add} atoms or O vacancies and thereby give the otherwise inert surface the same adsorption properties as the Co_3O_4(111) surface. It is even possible to distinguish CO molecules adsorbed in O vacancies from CO molecules adsorbed at Co_{add} atoms as the O 1s and C 1s components originating from CO molecule signals its adsorption site. Interestingly, the both the Co 2p XPS and XAS spectra as well as the O 1s spectra assigned to the modified CoO(111) films are indistinguishable from the pristine CoO(111) film. Therefore, the free access to the Co ions on the surface governs the CO adsorption properties rather than the electronic structure of the film.

CO_2 adsorption on Co_3O_4(111) and CoO(111) films

After having compared the CO adsorption properties of the Co_3O_4(111) and CoO(111) films we discuss their CO_2 adsorption properties. Starting with the C 1s spectrum of the Co_3O_4(111) film acquired after an exposure of 110 L of CO_2 at 85 K shown in figure 8(a) it can be deconvoluted by two different components positioned at 288.5 eV (blue), and 290.3 eV (pink) with relative intensities of 67 %, and 33 %, respectively. To assign these two components the C 1s and O 1s spectra were measured simultaneously while the sample was heated from from 85 K to 500 K (20 K/min). Figure 8(b) shows an image plot of the temperature evolution of the C 1s region, while the curve fitted intensity evolution of the two components are plotted in panel (c). Inspection of panel (c) reveals that the component at 288.5 eV disappears upon heating to 400 K. As the binding energy position and the desorption temperature are identical to what we previously observed for carbonates on Co_3O_4(111) upon CO dosing,[20] we assign this component to carbonates formed upon the CO_2 dosing. The second component at 290.3 eV fully disappeared upon heating to 170 K. Similar desorption

temperatures has been reported for weakly adsorbed carbon dioxide on TiO_2(110) (TDS desorption peaks at 134 K and 176 K) and ZnO(0001) (TDS desorption peaks at 122-135 K and 170 K).[27,28] Also the 1.8 eV binding energy difference between this component and the carbonate component fits quite well with what has been observed for CO_2 and carbonate on the Cr_2O_3(111) surface.[29] Therefore, the pink component observed at 290.3 eV is assigned to weakly adsorbed CO_2.

Figure 9 shows the O 1s spectrum after 110 L of CO_2 exposure (a), an image plot of the TPXPS data (b), and the temperature evolution of the different components (c) analog to C 1s data presented in figure 8. All the data presented in figure 9 were recorded on the same sample and simultaneously with the data presented in figure 8. Starting with panel (a) two distinct components shifted by +1.5 eV (blue) and +4.5 eV (pink) with respect to the main line developed upon CO_2 exposure. In panel (b-c) the TPXPS data reveals that the component shifted by +4.5 eV is fully desorbed upon heating to 170 K. As the exact same temperature development was observed for the C 1s component of weakly adsorbed CO_2 we also assign the pink O 1s component to weakly adsorbed CO_2. The other CO_2 induced O 1s component shifted by +1.5 eV is assigned to carbonates as it disappears upon heating to 400 K and the overall temperature development is analog to what is observed for the C 1s carbonate component in figure 8.

Comparing the CO and CO_2 exposed Co_3O_4(111) surfaces of figure 1, 2, 8, and 9 we observe the following similarities and differences: (i) Carbonate is formed on the Co_3O_4(111) surface both upon CO and CO_2 exposure. The carbonate is signaled by a C 1s component at 288.5 eV and a O 1s component shifted by +1.5 eV with respect to the Co_3O_4(111) main component. (ii) Weakly adsorbed CO and CO_2 are also observed upon dosing the respective gases. From the O 1s spectra it is difficult to distinguish weakly adsorbed CO and CO_2 as both adsorbed species are signaled by a component shifted by +4.5 eV. In contrast, it is easy to distinguish the two adsorbed species from each other in the C 1s spectrum, as weakly adsorbed CO is signaled by two components positioned at 287.0 eV (main peak) and a broad

shake-up component at 290.9 eV, while weakly adsorbed CO_2 is signaled by one component positioned at 290.3 eV.

After the CO and CO_2 adsorption onto the $Co_3O_4(111)$ surface has been discussed we now compare CO_2 adsorption onto different Co oxide surfaces: $Co_3O_4(111)$, pristine CoO(111) , and CoO(111) with oxygen vacancies. In figure 10 and 11, C 1s and O 1s spectra acquired before and after dosing CO_2 at $\sim$ 85 K are compared for the different Co oxide surfaces. Starting with the C 1s spectra of CO_2 exposed CoO(111) without (figure 10(d)) and with (figure 10(f)) O vacancies we observe two components positioned at 289.15 eV (blue), and 291.25 eV (pink). With respect to the blue carbonate component and pink CO_2 component observed on the CO_2 exposed $Co_3O_4(111)$ surface (cf. figure 10(b)), these two components are shifted by +0.65 eV and +0.95 eV, respectively. The shift of +0.65 eV is close to the +0.5 eV shift we observed between carbonates on the $Co_3O_4(111)$ surface and the CoO(111) surface with O vacancies upon CO exposure (cf. figure 6). Therefore, the blue components in figure 10 are assigned to carbonate and the +0.65 eV shift is ascribed to carbonate adsorbed on quite different $Co_3O_4(111)$ and CoO(111) like surfaces similar to what we concluded for carbonates formed upon CO exposure. The slightly larger shift between carbonate components on CoO(111) and $Co_3O_4(111)$ like surfaces, respectively, observed when carbonate is formed from CO_2 rather than CO could be caused by the co-existing CO_2 molecules. The pink component is then assigned to weakly adsorbed CO_2 on $Co_3O_4(111)$ (b) and CoO(111) like surfaces (d,f). In this case, the binding energy difference of weakly adsorbed CO_2 on the two surfaces is +0.95 eV, which is significant larger than what we observed for CO (+0.3 eV) and carbonate (+0.65 eV).

As it is difficult to determine the coverage of carbonate and weakly adsorbed CO_2 from the absolute C 1s intensities we instead inspect the corresponding O 1s spectra displayed in figure 11 normalized to the O 1s main peak intensity. Inspection of panel (a-d) reveals that the carbonate component (blue) and CO_2 component (pink) on the CoO(111) surface upon CO_2 dosing is almost invisible and much smaller than the components observed for the

$Co_3O_4(111)$ surface. The pristine CoO(111) surface is, therefore, fully inert towards CO_2 adsorption and carbonate formation just like it was found to be fully inert towards CO. The presence of O vacancies in the CoO(111) film increase, however, the coverage of both carbonate and weakly adsorbed CO_2 substantially, as panel (e,f) clearly demonstrate. The relative CLS of the carbonate component observed in figure 11 is +1.5 eV ($Co_3O_4(111)$) and +1.8 eV (CoO(111) with O vacancies) identical to what we observed for carbonates formed from CO dosing (c.f. figure 6). For the pink component assigned to weakly adsorbed CO_2 we observe relative CLS of +4.5 eV ($Co_3O_4(111)$) and +5.4 eV (CoO(111) with O vacancies), i.e. a relative CLS for CO_2 observed on the two different surfaces of +0.9 eV matching the +0.95 eV found for the corresponding pink C 1s component of figure 10 relatively well.

To summarize the comparison of CO_2 adsorption onto $Co_3O_4(111)$, pristine CoO(111) , and CoO(111) with oxygen vacancies we found that: (i) The pristine CoO(111) surface is almost fully inert with respect to CO_2 adsorption similar to what we found for CO adsorption. (ii) The adsorption properties of the CoO(111) surface are, however, changed dramatically once oxygen vacancies are present on the surface. On the CoO(111) surface with oxygen vacancies we observe carbonate formation and weakly adsorbed CO_2 with C 1s and O 1s components with slightly BE with respect to the components observed on the $Co_3O_4(111)$ surface.

Conclusions

First of all, we demonstrated that both CO and CO_2 easily adsorbs onto the $Co_3O_4(111)$ surface with accessible Co surface ions. Upon adsorption carbonate is formed and co-exists with CO or CO_2, depending on the type of gas dosed. In contrast, we demonstrated that the closed oxygen layer of the CoO(111) surface efficiently block both for CO and CO_2 adsorption at $\sim$ 85 K. The inert CoO(111) surface can, however, be given similar adsorption properties as the $Co_3O_4(111)$ surface, if accessible Co atoms are formed artificially on the

surface either by introducing oxygen vacancies or by adding Co add atoms. Interestingly, these surface defects does not change the electronic properties of the surface and Co 2p and O 1s spectra as well as Co 2p XAS spectra of both types of defective CoO(111) surfaces are essentially indistinguishable from the pristine CoO(111) surface. The surface chemistry, therefore, depends much more on the whether accessible Co surface atoms exist than on the Co_3O_4(111) or CoO(111) nature of the surface. Secondly, we demonstrated that it is possible to distinguish whether CO and CO_2 are adsorbed onto (a) free Co atoms on the pristine Co_3O_4(111) surface or on artificially created Co_{add} atoms on the CoO(111) surface or (b) in an oxygen vacancy site. For example, a shift of +0.3 eV in C 1s and +0.7 eV in O 1s spectra are observed for weakly adsorbed CO in an oxygen vacancy site with respect to the adsorption onto free Co atoms.

Acknowledgement

The authors are grateful for financial support by the Röntgen-Ångström cluster (349-2011-6491) and by the project grant 2012-3850 both financed by the Swedish research council and by the Austrian Science Fund (FWF SFB-F45). Financial support from Nordforsk is also gratefully acknowledged. The MAX IV Laboratory personnel are acknowledged for support during measurements.

References

(1) Jansson, J.; Palmqvist, A.; Fridell, E.; Skoglundh, M.; Österlund, L.; Thormahlen, P.; Langer, V. On the catalytic activity of Co_3O_4 in low-temperature CO oxidation. *J. Catal.* **2002**, *211*, 387–397.

(2) Jansson, J. Low-temperature CO oxidation over Co_3O_4/Al_2O_3. *J. Catal.* **2000**, *194*, 55–60.

(3) Xie, X.; Li, Y.; Liu, Z.-Q.; Haruta, M.; Shen, W. Low-temperature oxidation of CO catalysed by Co_3O_4 nanorods. *Nature* **2009**, *458*, 746–749.

(4) Zhao, Z.; Lin, X.; Jin, R.; Dai, Y.; Wang, G. High catalytic activity in CO PROX reaction of low cobalt-oxide loading catalysts supported on nano-particulate CeO_2-ZrO_2 oxides. *Cat. Comm.* **2011**, *12*, 1448–1451.

(5) Zhang, P.; Dong, Y.; Kou, Y.; Yang, Z.; Li, Y.; Sun, X. First-Principles Study of Oxygen Evolution Reaction on the Oxygen-Containing Species Covered Co-II-Exposing Co_3O_4(100) Surface. *Catal. Lett.* **2015**, *145*, 1169–1176.

(6) Chen, Z.; Kronawitter, C. X.; Koel, B. E. Facet-dependent activity and stability of Co_3O_4 nanocrystals towards the oxygen evolution reaction. *Phys. Chem. Chem. Phys.* **2015**, *17*, 29387–29393.

(7) Xiao, J.; Kuang, Q.; Yang, S.; Xiao, F.; Wang, S.; Guo, L. Surface Structure Dependent Electrocatalytic Activity of Co_3O_4 Anchored on Graphene Sheets toward Oxygen Reduction Reaction. *Sci. Rep.* **2013**, *3*, 2300.

(8) Fei, Z.; He, S.; Li, L.; Ji, W.; Au, C.-T. Morphology-directed synthesis of Co_3O_4 nanotubes based on modified Kirkendall effect and its application in CH_4 combustion. *Chem. Commun.* **2012**, *48*, 853–855.

(9) Hu, L.; Peng, Q.; Li, Y. Selective Synthesis of Co_3O_4 Nanocrystal with Different Shape and Crystal Plane Effect on Catalytic Property for Methane Combustion. *J. Am. Chem. Soc.* **2008**, *130*, 16136–16137.

(10) Heinz, K.; Hammer, L. Epitaxial cobalt oxide films on Ir(100)-the importance of crystallographic analyses. *J. phys. cond. matt.* **2013**, *25*.

(11) Gragnaniello, L.; Agnoli, S.; Parteder, G.; Barolo, A.; Bondino, F.; Allegretti, F.;

Surnev, S.; Granozzi, G.; Netzer, F. P. Cobalt oxide nanolayers on Pd(100): The thickness-dependent structural evolution. *Surf. Sci.* **2010**, *604*, 2002–2011.

(12) De Santis, M.; Buchsbaum, A.; Varga, P.; Schmid, M. Growth of ultrathin cobalt oxide films on Pt(111). *Phys. Rev. B* **2011**, *84*.

(13) Fester, J.; Bajdich, M.; Walton, A. S.; Sun, Z.; ; Plessow, P. N.; Vojvodic, A.; Lauritsen, J. V. Comparative Analysis of Cobalt Oxide Nanoisland Stability and Edge Structures on Three Related Noble Metal Surfaces: Au(111), Pt(111) and Ag(111). *Top. Cat.* **2016**, 1–10.

(14) Sebastian, I.; Neddermeyer, H. Scanning tunneling microscopy on the atomic and electronic structure of CoO thin films on Ag(100). *Surf. Sci.* **2000**, *454*, 771–777.

(15) Arman, M. A.; Merte, L. R.; Lundgren, E.; Knudsen, J. Co_3O_4(100) films grown on Ag(100): Structure and chemical properties. *Accepted in Surf. Sci.*

(16) Walton, A. S.; Fester, J.; Bajdich, M.; Arman, M. A.; Osiecki, J.; Knudsen, J.; Vojvodic, A.; Lauritsen, J. V. Interface Controlled Oxidation States in Layered Cobalt Oxide Nanoislands on Gold. *ACS Nano* **2015**, *9*, 2445–2453.

(17) Meyer, W.; Biedermann, K.; Gubo, M.; Hammer, L.; Heinz, K. Surface structure of polar Co_3O_4(111) films grown epitaxially on Ir(100)-(1×1). *J. phys. cond. matt.* **2008**, *20*.

(18) Meyer, W.; Hock, D.; BiedermannBiedermann, K.; Gubo, M.; Mueller, S.; Hammer, L.; Heinz, K. Coexistence of rocksalt and wurtzite structure in nanosized CoO films. *Phys. Rev. Lett.* **2008**, *101*.

(19) Biedermann, K.; Gubo, M.; Hammer, L.; Heinz, K. Phases and phase transitions of hexagonal cobalt oxide films on Ir(100)-(1×1). *J. Phys. Cond. Matt.* **2009**, *21*.

(20) Ferstl, P.; Mehl, S.; Arman, M. A.; Schuler, M.; Toghan, A.; Laszlo, B.; Lykhach, Y.; Brummel, O.; Lundgren, E.; Knudsen, J. et al. Adsorption and Activation of CO on Co_3O_4(111) Thin Films. *J. Phys. Chem. C* **2015**, *119*, 16688.

(21) Mehl, S.; Ferstl, P.; Schuler, M.; Toghan, A.; Brummel, O.; Hammer, L.; Schneider, M. A.; Libuda, J. Thermal evolution of cobalt deposits on Co_3O_4(111): atomically dispersed cobalt, two-dimensional CoO islands, and metallic Co nanoparticles. *Phys Chem Chem Phys* **2015**, *17*, 23538–23546.

(22) Nyholm, R.; Andersen, J.; Johansson, U.; Jensen, B.; Lindau, I. Beamline I311 at MAX-LAB: a VUV/soft X-ray undulator beamline for high resolution electron spectroscopy. *Nucl. Instrum. Meth. A* **2001**, *467*, 520.

(23) Gubo, M.; Ebensperger, C.; Meyer, W.; Hammer, L.; Heinz, K. Structural elements in the oxidation process of a single cobalt layer on Ir(100)-(1×1). *Phys. Rev. B* **2011**, *83*.

(24) Meyer, R.; Lahav, D.; Schalow, T.; Laurin, M.; Brandt, B.; Schauermann, S.; Guimond, S.; Kluner, T.; Kuhlenbeck, H.; Libuda, J. et al. CO adsorption and thermal stability of Pd deposited on a thin FeO(111) film. *Surf. Sci.* **2005**, *586*, 174–182.

(25) Lemire, C.; Meyer, R.; Henrich, V.; Shaikhutdinov, S.; Freund, H. The surface structure of Fe3O4(111) films as studied by CO adsorption. *Surf. Sci.* **2004**, *572*, 103–114.

(26) Hagelin-Weaver, A.; Hoflund, G.; Minahan, D.; Salaita, G. Electron energy loss spectroscopic investigation of Co metal, CoO, and Co_3O_4 before and after Ar^+ bombardment. *App. Surf. Sci.* **2004**, *235*, 420–448.

(27) Funk, S.; Burghaus, U. Adsorption of CO_2 on oxidized, defected, hydrogen and oxygen covered rutile (1×1)-TiO_2(110). *Phys. Chem. Chem. Phys.* **2006**, *8*, 4805–4813.

(28) Wang, J.; Hokkanen, B.; Burghaus, U. Adsorption of CO_2 on pristine Zn-ZnO(0001)

and defected Zn-ZnO(0001): A thermal desorption spectroscopy study. *Surf. Sci.* **2005**, *577*, 158–166.

(29) Kuhlenbeck, H.; XU, C.; Dillmann, B.; Hassel, M.; Adam, B.; Ehrlich, D.; Wohlrab, S.; Freund, H.; Ditzinger, U.; Neddermeyer, H. et al. Adsorption and reaction on oxide surfaces - CO and CO_2 on Cr_2O_3(111). *Ber. Bunsen-Ges. Phys. Chem* **1992**, *96*, 15–27.

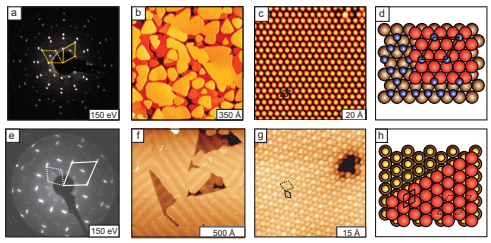

Figure 1: (a) LEED image, (b,c) STM images, and (d) structural model of the $Co_3O_4(111)$ surface. Co atoms are shown as blue spheres, while oxygen atoms are shown as red and brown spheres. (e) LEED image, (f,g) STM images, and (g) structural model of the CoO(111) surface. Co atoms are shown as yellow spheres, while oxygen atoms are shown as red and brown spheres.

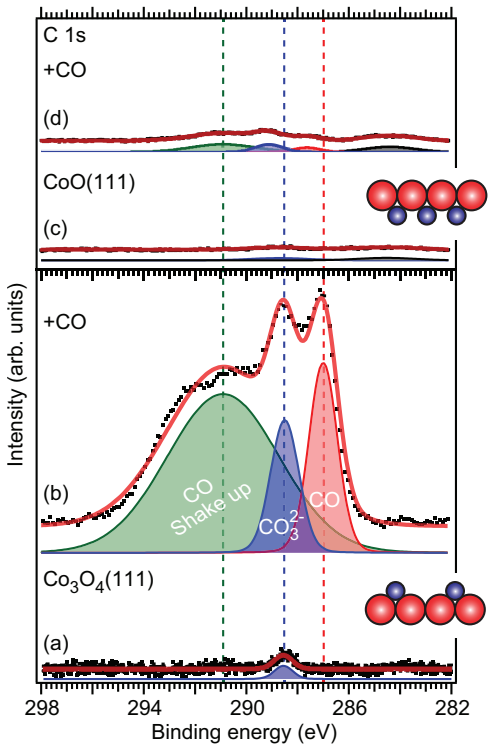

Figure 2: (a) and (b) C 1s spectra of $Co_3O_4(111)$ before and after exposure to 10 L CO, respectively. (c) and (d) C 1s spectra of CoO(111) before and after exposure to 10 L CO. The experimental C 1s spectra are shown with black dots, the fits as solid red lines, and the filled curves represent the components of the fits. Red and blue spheres in the ball models indicate O and Co atoms, respectively.

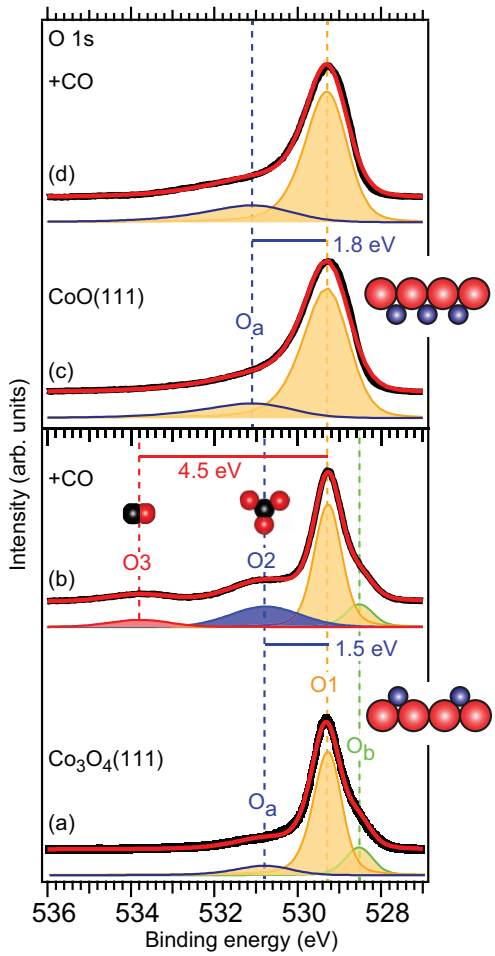

Figure 3: (a) and (b) O 1s spectra of $Co_3O_4(111)$ before and after exposure to 10 L CO, respectively. (c) and (d) C 1s spectra of CoO(111) before and after exposure to 10 L CO. Red and blue spheres in the ball models indicate O and Co atoms, respectively.

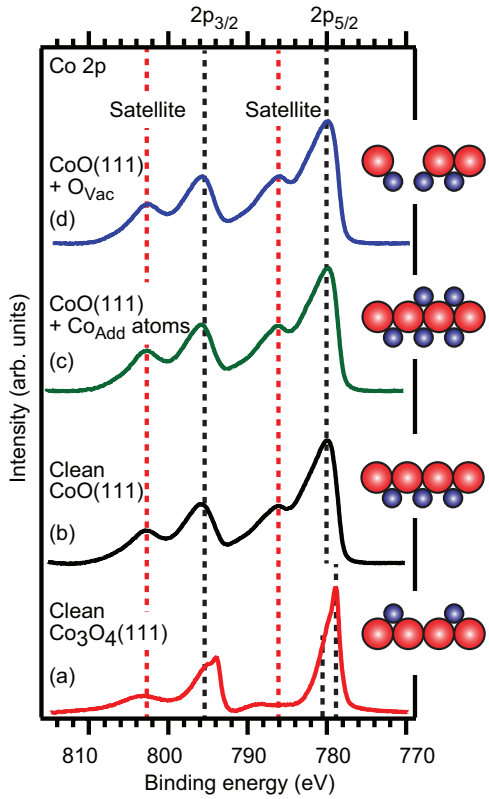

Figure 4: Co 2p spectra of (a) $Co_3O_4(111)$, (b) CoO(111) , (c) CoO(111) with Co_{Add} atoms, and (d) CoO(111) with oxygen vacancies. Red and blue spheres in the ball models indicate O and Co atoms, respectively.

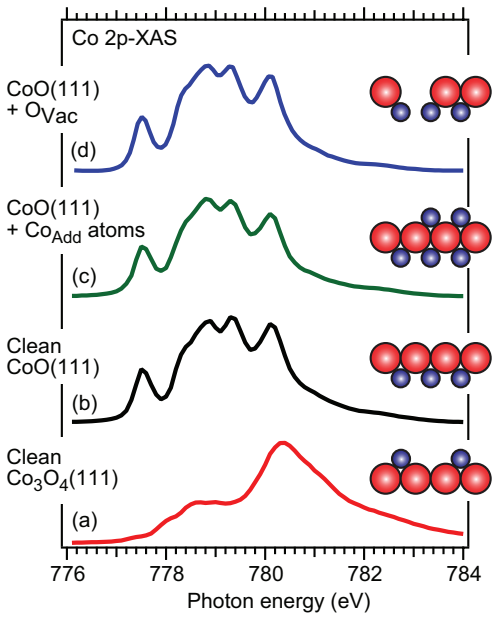

Figure 5: Co 2p (L3) XAS spectra of (a) $Co_3O_4(111)$, (b) CoO(111) , (c) CoO(111) with Co_{Add} atoms, and (d) CoO(111) with oxygen vacancies. Red and blue spheres in the ball models indicate O and Co atoms, respectively.

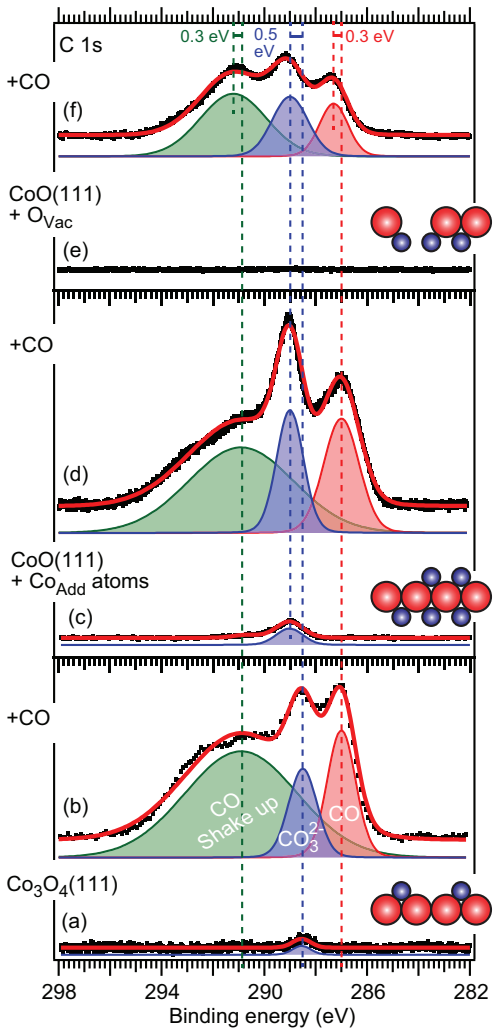

Figure 6: Deconvoluted C 1s spectra acquired before and after dosing 10 L CO at 85 K onto a: (a,b) $Co_3O_4(111)$ film, (c,d) CoO(111) film with Co_{add} atoms, and (e,f) CoO(111) film with O vacancies. Red and blue spheres in the ball models indicate O and Co atoms, respectively.

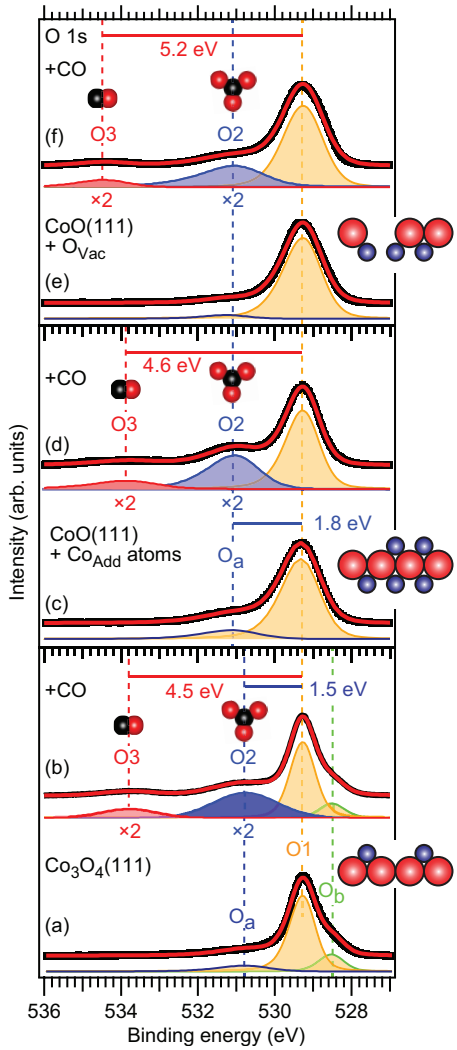

Figure 7: Deconvoluted O 1s spectra acquired before and after dosing 10 L CO at 85 K onto: (a, b) a $Co_3O_4(111)$ film, (c, d) a CoO(111) film with Co_{add} atoms, and a (e, f) a CoO(111) film with O vacancies. Red and blue spheres in the ball models indicate O and Co atoms, respectively.

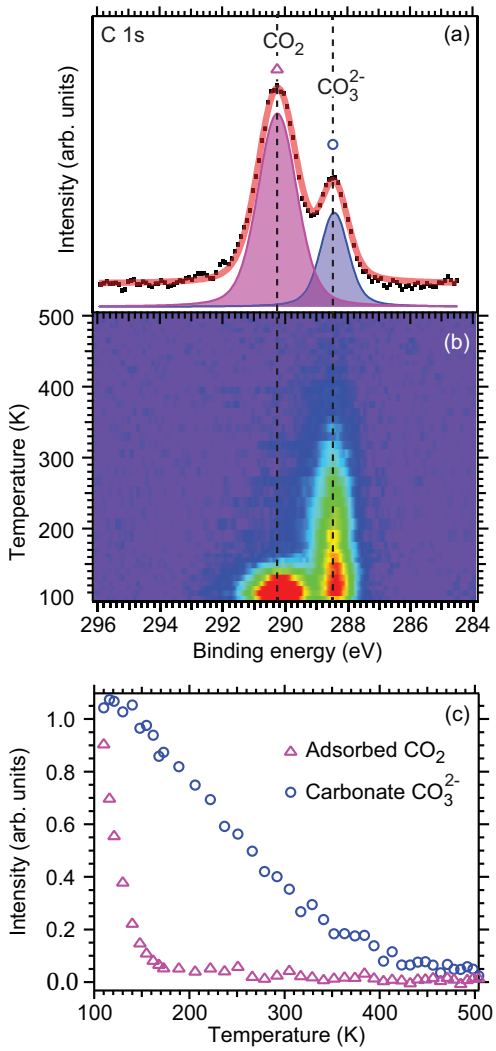

Figure 8: C 1s spectrum after dosing 110 L CO_2 at 85 K onto the $Co_3O_4(111)$ surface. The experimental spectrum is shown with black dots, the fit as a transparent red line, and the filled curves represent the components of the fit. (b) Image plot of the evolution of the C 1s spectrum as a function of temperature. (c) Temperature evolution of the intensity of the two components shown in (a) obtained from simultaneous curve fitting the data shown in (b)

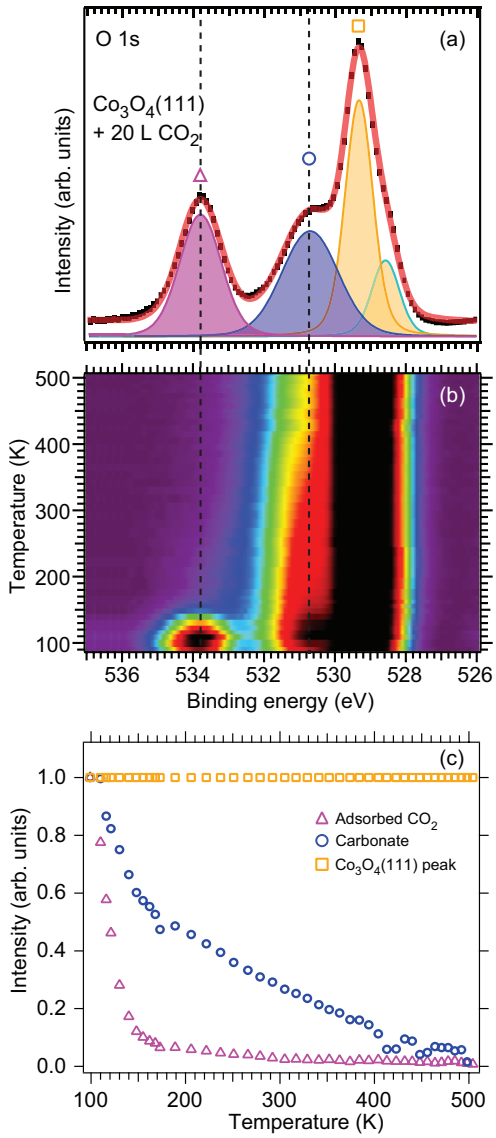

Figure 9: O 1s spectrum after dosing 110 L CO_2 at 85 K onto the Co_3O_4(111) surface. The experimental spectrum is shown with black dots, the fit as a transparent red line, and the filled curves represent the components of the fit. (b) Image plot of the evolution of the O 1s spectrum as a function of temperature. (c) Temperature evolution of the intensity of the different components shown in (a) obtained from simultaneous curve fitting the data shown in (b)

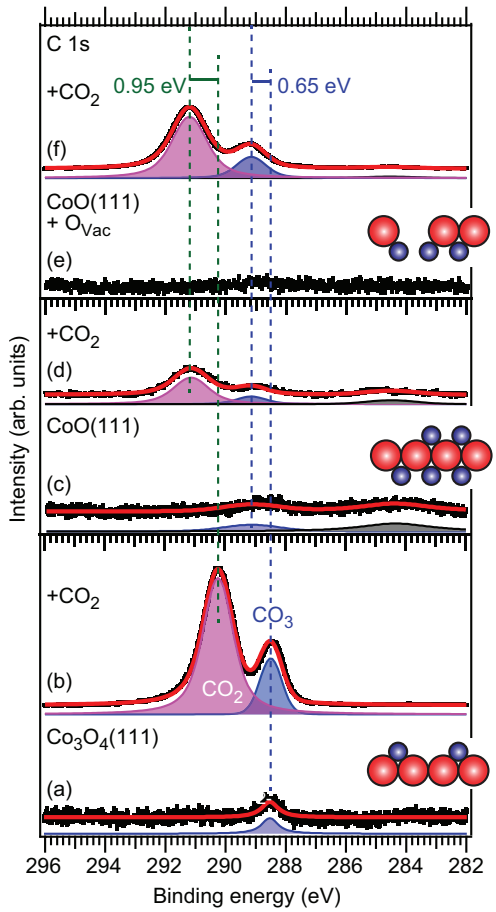

Figure 10: Deconvoluted C 1s spectra acquired before and after dosing CO_2 at 85 K onto a: (a,b) $Co_3O_4(111)$ film, (c,d) CoO(111) film, and (e,f) CoO(111) film with O vacancies. Red and blue spheres in the ball models indicate O and Co atoms, respectively.

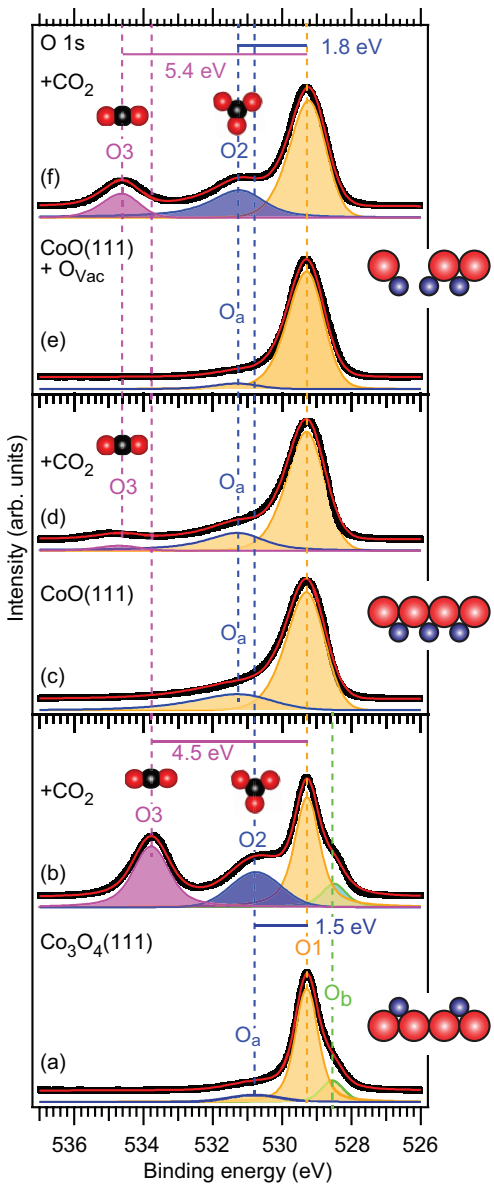

Figure 11: Deconvoluted O 1s spectra acquired before and after dosing CO_2 at 85 K onto a: (a,b) $Co_3O_4(111)$ film, (c,d) CoO(111) film, and (e,f) CoO(111) film with O vacancies. Red and blue spheres in the ball models indicate O and Co atoms, respectively.

Paper IV

Water and hydrogen radical adsorption onto CoO(111) and Co_3O_4(111) surfaces studied by photoemission spectroscopy

M. A. Arman[1], P. Ferstl[2], M. A. Schneider[2], L. Hammer[2], E. Lundgren[1], and J. Knudsen[1,3]

[1]Division of Synchrotron Radiation Research, Lund University, Box 118, 22100 Lund, Sweden

[2]Lehrstuhl für Festkörperphysik, Friedrich-Alexander-Universität Erlangen-Nürnberg, Staudtstrasse 7, 91058 Erlangen, Germany

[3]MAX IV Laboratory, Lund University, Box 118, 22100 Lund, Sweden

Abstract

Water and hydrogen radical exposed CoO(111) and Co_3O_4(111) films epitaxially grown on the Ir(100)-(1×1) surfaces are studied using x-ray photoelectron spectroscopy. We demonstrate that water dissociation at 90 K only takes place on the Co_3O_4(111) surface and find evidence for a H_2O-OH network structure on this surface. Once hydroxylated the Co_3O_4(111) surface binds water very efficiently and H_2O films build up fast even at ultra-high vacuum conditions. Hydroxylation of both the CoO(111) and Co_3O_4(111) surfaces can be achieved by exposing them to hydrogen radicals. After subsequent flashing of the hydroxylated CoO(111) film we observed a changed electronic structure with respect to the pristine film suggesting partial reduction.

Keywords: cobalt oxide, model catalysis, photoelectron spectroscopy, water, Ir(100)

1. Introduction

Water adsorption and dissociation on metal oxide surfaces are probably some of the best-studied surface related processes [1]. For example, water adsorption onto iron oxide surfaces has been studied extensively [2], in particular the well-characterized iron oxide films grown on Pt(111) such as thin FeO(111) [3, 4], partly reduced FeO(111) [5], FeO_2 [6,7], and Fe_3O_4(111) [3, 8, 9]. Today, we, therefore, have a significant understanding on of iron oxide thin films and their water chemistry.

Similar to iron oxide thin films, it is also possible to grow a large variety of structural analog cobalt oxide films. In particular, the structure of Ir(100) supported cobalt oxide films has been studied extensively with scanning tunneling microscopy and low energy electron diffraction (LEED) IV analysis [10]. Recently the surface science community showed renewed interest in cobalt oxide films, and cobalt oxide films have now also been grown and characterized on other substrates such as Pd(100) [11], Pt(111) [12,13], Ag(100) [14,15], Ag(111) [13], and Au(111) [13,16]. In contrast, to the knowledge of iron oxide films water chemistry, very little is known about water adsorption on the Co oxide films. This is somewhat surprising as the extensive structural characterization gives a unique opportunity for determining adsorption sites, dissociation pathways, etc.

In this paper, we take the first steps towards achieving a better understanding of water chemistry of cobalt oxide films. Using photoemission spectroscopy we study water and hydrogen radical adsorption on Ir(100) supported rocksalt CoO(111) and Co_3O_4(111) films with known structural models [17, 18] from previous STM and LEED IV analysis studies. From these studies, it is known that the CoO(111) film is terminated by a hexagonal closed packed oxygen lattice, while the Co_3O_4(111) film is terminated with Co^{2+} ions sitting in a p(2×2) structure with a hexagonal oxygen layer below.

2. Experimental Section

The x-ray photoemission spectroscopy (XPS) and temperature programmed XPS (TP-XPS) experiments were performed at the beamline I311 at the MAX IV Laboratory (Lund, Sweden) [19]. All XP spectra were collected in normal emission with a photon energy of 625 eV for the O 1s core level. During measurements, the sample was scanned across the x-ray beam at a speed of 5 μm/s to avoid beam damage. The binding energy of all O 1s spectra were calibrated by measuring the Ir 4f region directly after recording the O 1s spectrum without changing the photon energy and by assuming fixed binding energy of Ir 4f of 60.85 eV. All O 1s spectra are normalized to the peak height and fitted with asymmetric pseudo-Voigt functions. For the deconvolution, we used a Lorentzian full width at half maximum (LFWHM) of 0.10 eV.

The Ir(100) crystal was cleaned by several cycles of Argon sputtering at room temperature and subsequent O_2 annealing ($1 \cdot 10^{-7}$ mbar, 5 min) at 1000 K, followed by vacuum annealing at

1273 K for 3 min. This preparation recipe produced an Ir(100)-(5×1)-hex reconstruction. Cleanness of the surface was confirmed by XPS and LEED [20]. The temperature of the sample was measured with a chromel−alumel thermocouple spot welded to the edge of the crystal.

The cobalt oxide films were grown following the recipes reported by Heinz and Meyer [18, 21]. An O_2 gas doser and a cobalt evaporator were mounted to allow simultaneous dosing. The O_2 gas doser allowed the local oxygen pressure at the surface to be well above $5 \cdot 10^{-6}$ mbar during the growth. The cobalt evaporation rate was calibrated by producing other two-dimensional cobalt oxide structures that require exact amounts of Co expressed in monolayer equivalents (MLEs) [22]. The $Co_3O_4(111)$ film was prepared on an Ir(100)-(2×1)-O surface. This surface was formed by cooling down the Ir(100)-(5×1)-hex phase from 1200 K to room temperature in $1 \cdot 10^{-8}$ mbar of oxygen. Subsequently, 15 MLE of Co were deposited in $5 \cdot 10^{-7}$ mbar of oxygen with a growth rate of 1ML/min at 300 K. The ~5nm thick films were finally annealed to 523 K in oxygen for 2 min and followed by flash annealing to 673 K to improve the ordering. The $Co_3O_4(111)$ film was converted to CoO(111) film by flashing at 900 K in UHV [21]. The ordering of both films was checked with LEED.

3. Results and Discussion

3.1 H_2O adsorption onto CoO(111)

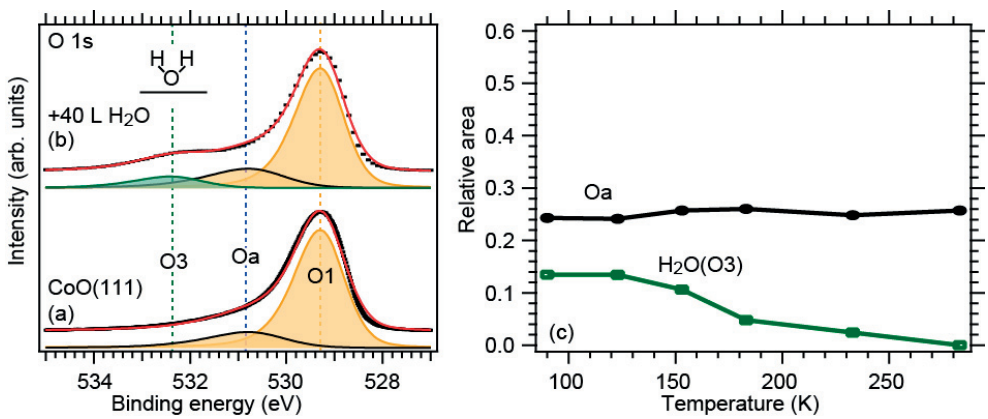

Figure 1: O 1s spectra of CoO(111) (a) before and (b) after exposure to 30 L of water at 90 K. The experimental O 1s spectrum is shown with black dots, the fit as a solid red line, while the filled curves represent the components of the fit. (c) Relative areas of the different components with respect to the O1 component as function of flashing temperature.

In figure 1 (a) and (b) we compare the O 1s spectra of CoO(111) thin film before (a) and after (b) exposure to 30 L H_2O ($1 \cdot 10^{-7}$ mbar for 400 sec) at 90 K. No sign of carbon contamination in the corresponding C 1s spectra (not shown) was observed before and after dosing H_2O. The

curve fitting of the O 1s spectra of the pristine surface reveals a main component located at 529.3 eV (O1) and a small shoulder component located at 530.8 eV, respectively (O_a). Upon water exposure, we observed the appearance of a new O3 component located at 532.3 eV and shifted by + 3.0 eV with respect to the O1 component.

The analysis of the TP-XPS measurements shown in figure 1 (c) demonstrates that the O3 component is fully removed after flashing to 283 K. This desorption temperature fits well to the desorption temperature of 170 K reported for physisorbed water adsorbed on FeO(111) films that are similar to the CoO(111) film and terminated by a closed surface layer of oxygen [23]. Therefore, we assign this peak to the adsorbed H_2O on the CoO(111) surface. As the relative intensity of the O3 component is small (0.14) and since the probing depth is equal to a few atomic layers the formation of multilayers of ice is unlikely at our experimental conditions. In contrast to the O1 component, no change in intensity of the O_a component is observed upon flashing. This O_a component we previously assigned to the intrinsic characteristics of the CoO(111) film itself [24].

3.2 Adsorption of hydrogen radicals onto CoO(111)

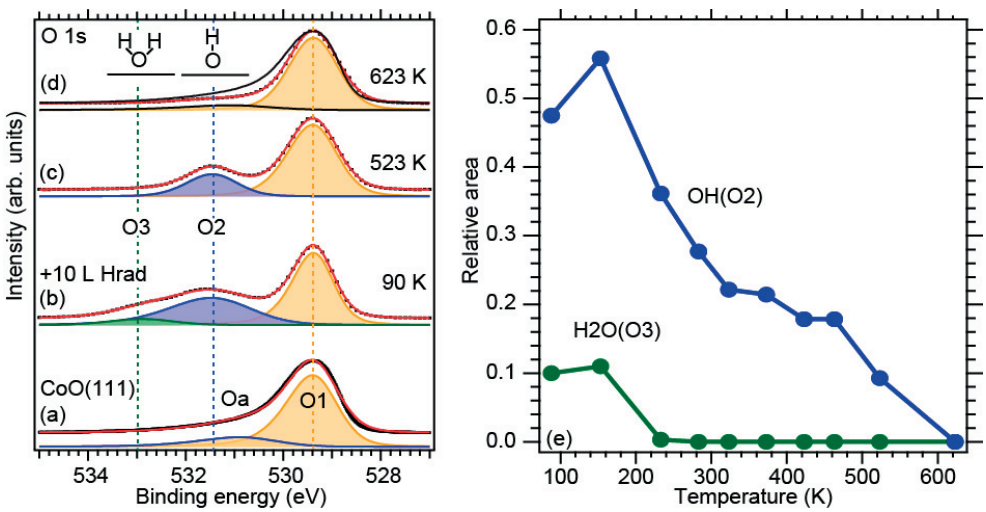

Figure 2: O 1s spectra of CoO(111) (a) before and (b) after exposure to hydrogen radicals at 90 K and after flashing to (c) 523 K and (d) 623 K ($2 \cdot 10^{-8}$ mbar for 11 min). The experimental O 1s spectrum is shown with black dots, the fit as a solid red line, and the filled curves represent the components of the fit. (e) Relative areas of the different components with respect to the O1 component as function of flashing temperature.

After having determined the adsorbed water component in the O 1s spectrum of CoO(111) we exposed the pristine film to hydrogen radicals (H_{rad}) at 90 K to identify the signature of hydroxyl groups on the surface. In figure 2 we compare the O 1s spectra of CoO(111) before (a) and

after (b) exposure to hydrogen radicals (H_{rad}) at 90 K. The O 1s of the clean CoO(111) film is deconvoluted by the O1 and O_a component as discussed above. However, upon exposure to H_{rad} the development of a broad shoulder at the high binding energy side is observed. Our curve fitting reveals that two components are necessary to obtain a reasonable fit of this broad shoulder, with components located at 531.4 eV (+2.1 eV) (O2) and 532.8 eV (+ 3.5 eV) (O3), respectively (see figure 2 (b)). In figure 2 (e) we show the data from the analysis of TP-XPS data recorded by flash heating the hydrogen radical exposed CoO(111) surface to stepwise increasing temperatures. Our analysis reveals that the O3 component is fully removed at 283 K and as we observed a similar desorption behavior for adsorbed water on CoO(111) in figure 1 it is natural to assign the O3 component to water. In contrast to the O3 component, the O2 component disappears in a broad temperature range between 200 K and 600 K. Similar work on the FeO(111)/Pt(111) [25] system have shown that OH groups are fully desorbed at 500 K and that O 1s component of OH groups are shifted by +2.2 eV with respect to the main peak. Since we observe a very similar BE shift of +2.1 eV for the O2 component on CoO(111) we assign this component to OH groups. Further, we note that the thermal stability of this component fits with what we expect for OH groups.

In figure 2 (c) and (d) selected O 1s spectra acquired after flashing to 523 K and 623 K, respectively, are shown. A few interesting observations can be made by comparing these spectra with the spectra of the clean and hydrogen radical exposed CoO(111) surface. First of all the width of the O2 component decrease substantially to 40% of its initial value upon flashing to 523 K. (GFWHM 0.9 eV => 0.5 eV). A second observation we make is that the area of the O_a component is reduced to 35% of the value of pristine CoO(111) film upon removal of the OH groups. Assuming that the OH groups desorb as water and partially reduce the film this observation suggest that the intensity of the O_a component is reduced for partially reduced films. We hope that our work will inspire future STM characterization of partially reduced CoO(111) films. As a final observation we compare the binding energies of pure water adsorbed on CoO(111) observed in in figure 1 (532.3 eV) with the coexisting structure of OH groups and water observed in figure 2 (532.8 eV) and note a 0.5 eV binding energy difference, most likely caused by a neighboring effect of the OH groups.

In summary, we identified the O 1s fingerprints of OH (+2.1 eV) and adsorbed water (+3.0 eV for a pure water film and +3.5 eV for water in a coexistence structure of OH and water). We found no evidence for water dissociation on the CoO(111) surface terminated by a hexagonal layer of oxygen atoms [26].

3.3 H_2O adsorption onto Co_3O_4(111)

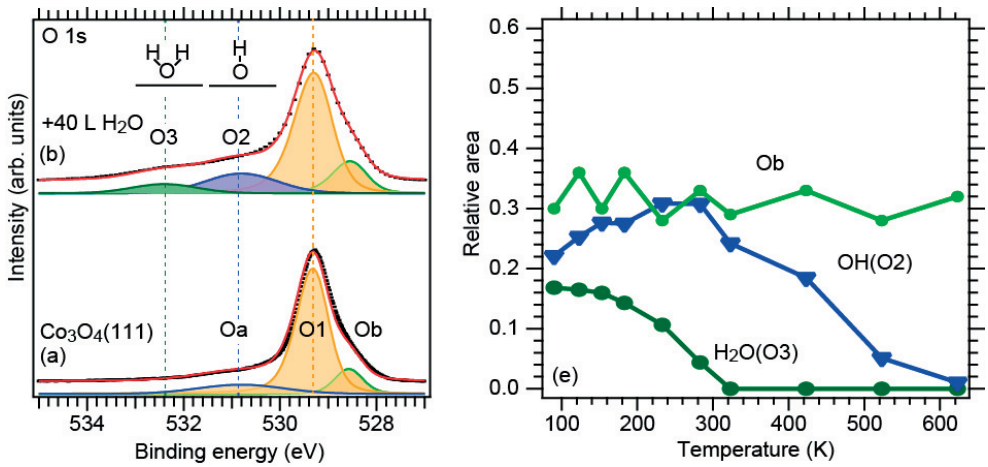

Figure 3: O 1s spectra of Co_3O_4(111) (a) before and (b) after exposure to 30 L of water at 90 K. The experimental O 1s spectrum is shown with black dots, the fit as a solid red line, while the filled curves represent the components of the fit. (c) Relative areas of the different components with respect to the O1 component as function of flashing temperature.

Figure 3 compares the O 1s spectra of the Co_3O_4(111) film before (a) and after (b) exposure to 30 L ($1 \cdot 10^{-7}$ mbar for 400 sec) H_2O at 90 K. Starting with the pristine Co_3O_4(111) surface we fitted it with one main component (O1) located at 529.3 eV and two shoulder components located at 528.6 eV (O_a), and at 530.8 eV (O_b) in accordance with our previous work.[27]

Upon water exposure we observe two new components located at 530.8 eV (O2) and 532.4 eV (O3). In contrast, the O_b component is unaffected by the water exposure. Figure 3 (c) shows the relative area evolution of the O2, O3, and O_b components as function of the flashing temperature. As the binding energy of the O2 component (530.8 eV) is identical to the binding energy of the O_a component we plotted the relative area of the O2 component after subtracting the area of the O_a component. Starting with the O3 component it is observed at 532.4 eV and shifted +3.1 eV with respect to the O1 component. It disappears fully after flashing the sample to 323 K, and this component is, therefore, assigned to adsorbed H_2O on the Co_3O_4(111) surface. We note that the + 3.1 eV shift observed here fits quite well to what is observed for pure water adsorption on CoO(111) (+ 3.0 eV).

The O2 component is then assigned to hydroxyl groups as its binding energy shift (+1.5 eV) and its high thermal stability fits well the characteristics of hydroxyl groups on the CoO(111) surface discussed above. Comparing the water exposed CoO(111) and Co_3O_4(111) surfaces in figure 1 (b) and 3(b) it is evident that it only is the Co_3O_4(111) surface that is able to dissociate water at 90 K. A final observation we make from figure 3 (c) is that the intensity of the OH component increase from 0.22 to 0.3 within the temperature interval where H_2O desorbs suggesting part of the H_2O molecules dissociate upon heating and increase the OH coverage.

3.4 Adsorption of hydrogen radicals onto $Co_3O_4(111)$

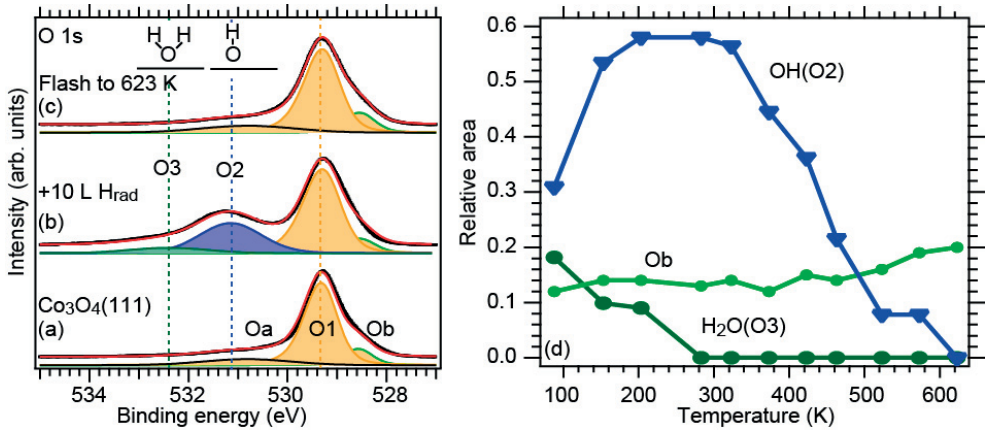

Figure 4: O 1s spectra of $Co_3O_4(111)$ (a) before and (b) after exposure to hydrogen radicals at 90 K and (c) after a subsequent flash to 623 K. The experimental O 1s spectrum is shown with black dots, the fit as a solid red line, and the filled curves represent the components of the fit. (d) Relative areas of the different components with respect to the O1 component as function of flashing temperature.

For comparison we also exposed the $Co_3O_4(111)$ to hydrogen radicals using the same conditions as for the CoO(111) surface. In figure 4 we compare the O 1s spectra of $Co_3O_4(111)$ before (a) and after (b) exposure to hydrogen radicals (H_{rad}) at 90 K and after subsequent desorption (c). Upon H_{rad} exposure we observe two new components located at 531.2 eV (O2) and 532.4 eV (O3). The O3 component we assign to adsorbed water molecules as its desorption profile and binding energy is identical to what we observed for the O3 component formed upon pure water exposure. The other O2 component is then naturally assigned to OH groups. Similar to what we observed upon pure water exposure we find clear evidence for H_2O dissociation after the first heating steps in figure 4 (d) as the OH coverage increase. Comparing the spectrum of pristine $Co_3O_4(111)$ (a) with the H_{rad} exposed and flashed spectrum (c) no changes are observed in contrast to the partial reduction discussed for the CoO(111) film. We also note that there is a small binding energy difference between the O2 component observed upon water exposure (530.8 eV) and upon exposure to hydrogen radicals (531.2 eV) for the $Co_3O_4(111)$ film. This difference could either be a coverage effect, as the OH coverage in figure 4 (b) is higher than in figure 3 (b) or it could be a coexistence effect as the relative water coverage is much higher in figure 3 (b). To differentiate between these two effects, we first flashed a $Co_3O_4(111)$ film exposed to hydrogen radicals to 463 K to desorb all water (see figure 5 (b)). At this point, the sample was kept at 90 K for 40 min in UHV (~$3 \cdot 10^{-10}$ mbar). Subsequently, we recorded the XPS spectrum again and clearly, a pronounce water

component developed at 532.4 eV, as shown in figure 5 (d) due to dissociation of H_2O molecules in the background gas. Interestingly, the water adsorption causes the OH component to shift from 531.2 eV to 530.8 eV. By flashing the sample again to desorb water, the OH component shift back to 531.2 eV again. Therefore, we conclude that the binding energy position of OH component on $Co_3O_4(111)$ surface is heavily affected by the presence of water molecules which could be due to the formation of OH/H_2O network structures which would affect the hydrogen bonding and as a consequence the O 1s binding energy. Another interesting observation can be made by comparing figure 3 (b) with figure 5 (c). In figure 3 (b) the $Co_3O_4(111)$ was exposed to 30 L water, while the maximum water exposure in figure 5 (c) is equal to $1 \cdot 10^{-9}$ mbar · 40 min = 2L. Clearly, much more water is able to adsorb (and partially dissociate) on the hydroxylated $Co_3O_4(111)$ surface even though the water dose is a factor of 10 lower than the dose used on the pristine $Co_3O_4(111)$ surface. A natural conclusion from this observation is that hydroxyl groups facilitate water adsorption onto the $Co_3O_4(111)$ surface, which makes a lot sense as adsorbed water molecules can form hydrogen bonds with the hydroxyl groups already present on the surface.

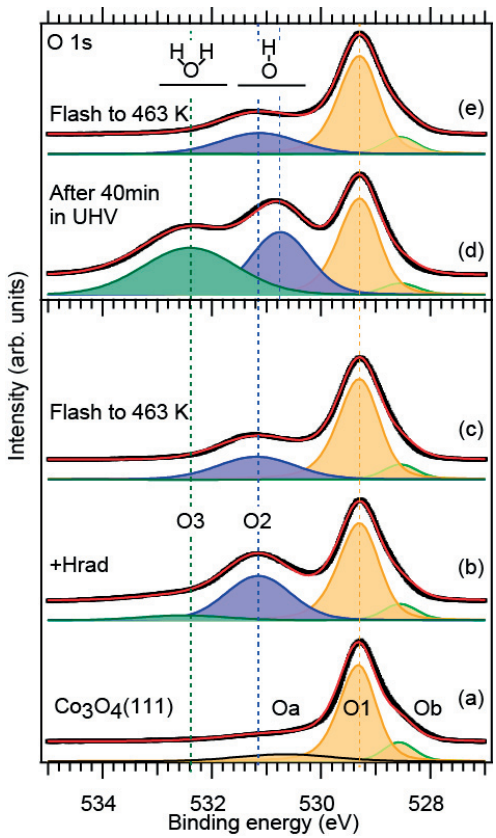

Figure 5: O 1s spectra of (a) pristine $Co_3O_4(111)$ thin film, (b) After exposure to radicals at 90 K, (c) after flashing to 463 K, (d) after keeping the sample in UHV for 40 min, and (e) after

flashing again to 463 K. The experimental O 1s spectrum is shown with black dots, the fit as a solid red line, and the filled curves represent the components of the fit. O_a, O_b, O1, O2, and O3 denote the different chemical species on the surface. See the text for details.

4. Conclusions

To conclude we have given a complete spectroscopic picture of water adsorption and dissociation and adsorption of hydrogen radicals onto CoO(111) and Co_3O_4(111) films grown on Ir(100). The study provides high resolution XPS fingerprints of physisorbed water, OH groups, and coexisting structures of OH and H_2O. Most importantly, we demonstrated that the oxygen-terminated surface of CoO(111) is inert with respect to water dissociation upon water exposure at 90 K. Only physisorbed water is here observed similar to what is observed on oxygen terminated iron oxide surfaces. In contrast, we find clear evidence for water dissociation on the Co_3O_4(111) film already at 90 K. We also conclude that a OH/H_2O network structure is formed on the Co_3O_4(111) surface upon low temperature water exposure as the BE position of the OH groups shift from 531.2 eV with co-adsorbed water to 530.8 eV without. Finally, we found very clear evidence for increased sticking of physisorbed water upon hydroxylation of the Co_3O_4(111) surface.

Exposure to hydrogen radicals were used to form hydroxyl groups both on the CoO(111) and the Co_3O_4(111) surfaces. Subsequent desorption of the hydroxyl groups from both films lead to significant changes in the O 1s spectrum of the CoO(111) film interpreted as partial reduction, while the spectrum of the flashed Co_3O_4(111) film was identical to the pristine film.

We hope that the present work will inspire future work in the water chemistry of cobalt oxide surfaces. In particular, STM imaging of the water exposed Co_3O_4(111) surfaces and the partially reduced CoO(111) films would be interesting.

Acknowledgement

The authors are grateful for financial support by the Röntgen-Ångström cluster (349-2011-6491) and by the project grant 2012-3850 both financed by the Swedish research council. Financial support from Nordforsk is also gratefully acknowledged. The MAX IV Laboratory personnel are acknowledged for support during measurements.

References

[1] M. A. Henderson, The interaction of water with solid surfaces: fundamental aspects revisited, Surf. Sci. Rep. 46 (2002) 1-308. http://dx.doi.org/10.1016/S0167-5729(01)00020-6

[2] G. S. Parkinson, Iron oxide surfaces, Surf. Sci. Rep. 71 (2016) 272. http://dx.doi.org/10.1016/j.surfrep.2016.02.001

[3] Y. Joseph, W. Ranke, W. Weiss, Water on FeO(111) and Fe_3O_4(111): adsorption behavior on different surface terminations, J. Phys. Chem. B, 104 (2000) 3224–3236. http://dx.doi.org/10.1021/jp9932012

[4] L.R. Merte, R. Bechstein, G. Peng, F. Rieboldt, C. a Farberow, H. Zeuthen, J. Knudsen, E. Lægsgaard, S. Wendt, M. Mavrikakis, F. Besenbacher, Water clustering on nanostructured iron oxide films, Nat. Commun. 5 (2014) 4193. http://dx.doi:10.1038/ncomms5193

[5] Xu, L. et al. Oxygen vacancy-induced novel low-temperature water splitting reactions on FeO(111) monolayer-thick film, J. Phys. Chem. C 116, 22921–22929 (2012). http://dx.doi.org/10.1021/jp307104a

[6] N. Johansson, L. R. Merte, E. Grånäs, S. Wendt, J. N. Andersen, J. Schnadt, J. Knudsen, Oxidation of Ultrathin FeO(111) Grown on Pt(111): Spectroscopic Evidence for Hydroxylation, Top Cat. 59 (2016) 506–515. http://dx.doi.org/10.1007/s11244-015-0521-7

[7] F. Ringleb, Y. Fujimori, H.F. Wang, H. Ariga, E. Carrasco, M. Sterrer, H.J. Freund, L. Giordano, G. Pacchioni, and J. Goniakowski, Interaction of Water with FeO(111)/Pt(111): Environmental Effects and Influence of Oxygen, J. Phys. Chem. C, 115 (2011), http://dx.doi.org//10.1021/jp207332n

[8] U. Leist, W. Ranke, K. Al-Shamery, Water adsorption and growth of ice on epitaxial Fe_3O_4(111), FeO(111) and Fe_2O_3(biphase), Phys. Chem. Chem. Phys.,5 (2003) 2435-2441. http://dx.doi.org/10.1039/b212163h

[9] K. T. Rim et al. Scanning tunneling microscopy and theoretical study of water adsorption on Fe_3O_4: implications for catalysis, J. Am. Chem. Soc. 134 (2012) 18979–18985. http://dx.doi.org/10.1021/ja305294x

[10] K. Heinz, L. Hammer, Epitaxial cobalt oxide films on Ir(100)—the importance of crystallographic analyses, J. Phys.: Cond. Matt. 25 (2013) 173001. http://dx.doi.org/10.1088/0953-8984/25/17/173001

[11] L. Gragnaniello, S. Agnoli, G. Parteder, A. Barolo, F. Bondino, F. Allegretti, S. Surnev, G. Granozzi, F. P. Netzer, Cobalt oxide nanolayers on Pd(100): The thickness-dependent structural evolution, Surf. Sci. 604 (2010) 2002. http://dx.doi.org/10.1016/j.susc.2010.08.012

[12] M. De Santis, A. Buchsbaum, P. Varga, M. Schmid, Growth of ultrathin cobalt oxide films on Pt(111), Phys. Rev. B. 84 (2011) 125430. http://dx.doi.org/10.1103/PhysRevB.84.125430

[13] J. Fester, M. Bajdich, A. S. Walton, Z. Sun, P. N. Plessow, A. Vojvodic, J. V. Lauritsen, J. V. Comparative Analysis of Cobalt Oxide Nanoisland Stability and Edge Structures on Three Related Noble Metal Surfaces: Au(111), Pt(111) and Ag(111), Top. Cat. (2016), 1-10. http://dx.doi.org/10.1007/s11244-016-0708-6

[14] I. Sebastian, H. Neddermeyer, Scanning tunneling microscopy on the atomic and electronic structure of CoO thin films on Ag(100), Surf. Sci. 454 (2000) 771 http://dx.doi.org/10.1016/S0039-6028(00)00060-1

[15] M. A. Arman, L. R. Merte, E. Lundgren, J. Knudsen, Co_3O_4(100) films grown on Ag(100): Structure and chemical properties, Accepted for publication in *Surf. Sci.*

[16] A. S. Walton, J. Fester, M. Bajdich, M. A. Arman, J. Osiecki, J. Knudsen, A. Vojvodic, J. V. Lauritsen, Interface Controlled Oxidation States in Layered Cobalt Oxide Nanoislands on Gold, ACS Nano 9 (2015) 2445. http://dx.doi.org/10.1021/acsnano.5b00158

[17] K. Biedermann, M. Gubo, L. Hammer, and K. Heinz, Phases and phase transitions of hexagonal cobalt oxide films on Ir(100)-(1×1), J. Phys.: Condens. Matter 21 (2009) 185003. http://dx.doi.org/10.1088/0953-8984/21/18/185003

[18] W. Meyer, K. Biedermann, M. Gubo, L. Hammer, K. Heinz, Surface structure of polar Co_3O_4(111) films grown epitaxially on Ir(100)-(1×1), Jour. phys. cond. matt. 20 (2008) 265011. http://dx.doi.org/10.1088/0953-8984/20/26/265011

[19] R. Nyholm, J. Andersen, U. Johansson, B. Jensen, I. Lindau, Beamline I311 at MAX-LAB: a VUV/soft X-ray undulator beamline for high resolution electron spectroscopy, Nucl. Instrum. Methhods A 467 (2001) 520. http://dx.doi.org/10.1016/S0168-9002(01)00399-0

[20] M. A. Arman, A. Klein, P. Ferstl, A. Valookaran, J. Gustafson, K. Schulte, E. Lundgren, K. Heinz, A. Schneider, F. Mittendorfer, L. Hammer, J. Knudsen, Adsorption of hydrogen on stable and metastable Ir(100) surfaces, Surf. Sci. 656 (2017) 66. http://dx.doi.org/10.1016/j.susc.2016.10.002

[21] K. Heinz, L. Hammer, Epitaxial cobalt oxide films on Ir(100)-the importance of crystallographic analyses., J. Phys. Condens. Matter. 25 (2013) 173001. https://doi.org/10.1088/0953-8984/25/17/173001.

[22] M. Gubo, C. Ebensperger, W. Meyer, L. Hammer, and K. Heinz, Structural elements in the oxidation process of a single cobalt layer on Ir(100)-(1×1), Phys. Rev. B 83 (2011) 075435. https://doi.org/10.1103/PhysRevB.83.075435

[23] U. Leist, W. Ranke, and K. Al-Shamery, Water adsorption and growth of ice on epitaxial Fe_3O_4(111), FeO(111) and Fe_2O_3(biphase), Phys. Chem. Chem. Phys., 5 (2003) 2435. http://dx.doi.org/10.1039/B212163H

[24] M. A. Arman, P. Ferstl, M.A. Schneider, L. Hammer, E. Lundgren, and J. Knudsen, Adsorption properties of CO and CO_2 onto CoO(111) and Co_3O_4(111) films studied with core level spectroscopy, *In Manuscript*

[25] J. Knudsen, L. R. Merte, L. C. Grabow, F. M. Eichhorn, S. Porsgaard, H. Zeuthen, R. T. Vang, E. Lægsgaard, M. Mavrikakis, F. Besenbacher, Reduction of FeO/Pt(1 1 1) thin films by exposure to atomic hydrogen, Surf. Sci. 604 (2009) 11. http://dx.doi.org/10.1016/j.susc.2009.10.008

[26] W. Meyer, K. Biedermann, M. Gubo, L. Hammer, and K. Heinz, Superstructure in the termination of CoO(111) surfaces: Low-energy electron diffraction and scanning tunneling microscopy, Phys. Rev. B 79 (2009) 121403(R). http://dx.doi.org/10.1103/PhysRevB.79.121403

[27] P. Ferstl, S. Mehl, M. A. Arman, M. Schuler, A. Toghan, B. Laszlo, Y. Lykhach, O. Brummel, E. Lundgren, J. Knudsen, L. Hammer, M.A. Schneider, and J. Libuda, Adsorption and activation of CO on Co_3O_4(111) thin films, J. Phys. Chem. C, 119 (2015) 16688. http://dx.doi.org/10.1021/acs.jpcc.5b04145

Paper V

Surface Science 657 (2017) 90–95

Contents lists available at ScienceDirect

Surface Science

journal homepage: www.elsevier.com/locate/susc

Co_3O_4(100) films grown on Ag(100): Structure and chemical properties

Mohammad A. Arman[a], Lindsay R. Merte[a], Edvin Lundgren[a], Jan Knudsen[a,b,*]

[a] Division of Synchrotron Radiation Research, Department of Physics, Lund University, Sweden
[b] MAX IV Laboratory, Lund University, Sweden

ARTICLE INFO

Keywords:
Cobalt oxide
Model catalysis
Photoelectron spectroscopy
Scanning tunneling microscopy
Ag(100)

ABSTRACT

Spinel type Co_3O_4(100) is successfully grown on Ag(100) at ultrahigh vacuum conditions and its structure, electronic and chemical properties are compared with those of Co_3O_4(111) grown on Ir(100). We find that the Co_3O_4(100) is unreconstructed. In contrast to the defect free Co_3O_4(111) surface the Co_3O_4(100) surface contains a high concentration of defects that we assign to subsurface cation vacancies analogous to those observed for Fe_3O_4(100). Our photoemission and absorption spectroscopy experiments reveal a very similar electronic structure of the Co_3O_4(111) and Co_3O_4(100) surfaces. The similar electronic structure of the two surfaces is reflected in the CO adsorption properties at low temperatures, as we observe adsorption of molecular CO as well as the formation of carbonate (CO_3) species on both surfaces upon CO exposure at 85 K.

1. Introduction

Oxides of cobalt have recently attracted attention due to their technical applications, particularly in the fields of heterogeneous catalysis [1–3] and electro-catalysis [4]. High catalytic and electro-catalytic activity has been observed for thermal decomposition of ammonium perchlorate [5], for the oxygen evolution reaction (OER) [6], and the oxygen reduction reaction (ORR) [7]. CO oxidation activity has also been observed over nanostructured Co_3O_4 far below room temperature [8,9]. The precise reasons for the high activity of these materials remain unclear, however, and elucidating the mechanisms and structure dependence of these reactions on Co_3O_4 surfaces is a major goal in fundamental research. Experiments utilizing controlled nanostructures of Co_3O_4 have revealed that the catalytic activity of the material is dependent on the crystallographic orientations of the exposed surfaces. For example, Chen et al. reported the facet dependence of oxygen evolution reaction (OER) activity and stability of Co_3O_4 nanocrystals [10]. In another study, Xie et al. demonstrated that Co_3O_4 nanorods which oxidize CO at low temperature predominantly exposed (110) facets [11] and Co_3O_4 nanosheets with (112) facets were shown to be particularly active for methane (CH_4) oxidation [12,13]. Well-controlled surface science studies using uniform, crystalline and atomically flat Co_3O_4 surfaces with controlled orientations promise to help to shed light on the atomistic mechanisms underlying the intriguing properties of this material. A series of elegant studies have been performed using thin films of cobalt oxide grown on Ir(100) [14], where under sufficiently oxidizing conditions, well-ordered Co_3O_4(111) is formed [15]. These model surfaces have enabled detailed studies of the adsorption properties under UHV conditions, showing, for example, the importance of under-coordinated Co ions at the surface in bonding to CO [16] below 100 K. To our knowledge, no study has been reported showing the formation of an atomically-flat Co_3O_4(100) film. Carson et al. reported that oxidation of CoO(100) under high-vacuum conditions gave rise to a Co_3O_4-like epitaxial phase, though this did not show low electron energy diffraction (LEED) features indicative of the (100) surface. Several studies on epitaxial growth of Co_3O_4 on MgO(100) by MOCVD [17], and on CoO(100) [18,19], have been reported, showing films with (100) orientation, but in these cases no surface characterization was performed. However, some density functional theory (DFT) studies have investigated the properties of Co_3O_4(100) surfaces, and shows that, this surface is active for OER [20,6]. An additional DFT study shows that the (100) plane of Co_3O_4 nanocrystals is active for CO oxidation [21] and CH_4 oxidation [22]. Here, we show that a well-ordered Co_3O_4 film can successfully be grown in the (100) orientation on Ag(100). The choice of the silver substrate was motivated by the fact that the lattice mismatch between of the cubic Co_3O_4 structure and Ag(100) is only ~0.8%, significantly smaller than on Ir(100) (~5%), where Co_3O_4 grows exclusively in a (111) orientation. Sebastian et al. furthermore reported growth of CoO(100) on Ag(100), characterized by scanning tunneling microscopy (STM), indicating that cobalt oxide growth with square surface orientation is possible on this substrate [23]. Another advantage of the silver substrate is its poor catalytic activity; catalytic tests performed on cobalt oxide grown on Ir(100) or other platinum group metals are complicated by the generally high catalytic activity of the substrate itself. Here, we present structural and electronic character-

* Corresponding author at: Division of Synchrotron Radiation Research, Department of Physics, Lund University, Sweden.
E-mail address: jan.knudsen@sljus.lu.se (J. Knudsen).

http://dx.doi.org/10.1016/j.susc.2016.11.011
Received 22 September 2016; Received in revised form 25 November 2016; Accepted 26 November 2016
Available online 30 November 2016

ization of a Ag(100) supported Co_3O_4(100) film as well as its chemical properties in terms of CO adsorption. These measurements are compared with similar measurements performed for CoO(111) and Co_3O_4(111) films grown on Ir(100).

2. Experimental details

The X-ray photoelectron spectroscopy (XPS) experiments were performed at beamline I311 at the MAX IV Laboratory (Lund, Sweden) [24]. All spectra were collected in normal emission with photon energies of 380 eV and 460 eV (C 1s), 460 eV (Ag 3d), 625 eV (O 1s), and 1000 eV (Co 2p). During our measurements we scanned the sample across the X-ray beam at a speed of 5 μm/s to avoid beam damage. Binding energies (BEs) of C 1s, O 1s, and Co 2p spectra are calibrated by measuring the Ir 4f/Ag 3d region directly after the spectra of interest without changing the photon energy and by assuming a fixed binding energy of Ir $4f_{7/2}$ of 60.85 eV/Ag $3d_{5/2}$ of 368.2 eV, determined by calibration to the Fermi level for clean surfaces. For the curve fitting we used pseudo Voigt components after subtracting a polynomial background. The Co 2p (L3) X-ray absorption spectroscopy (XAS) spectra were recorded in normal incidence in Auger yield mode by collecting electrons with kinetic energies between 647.8 and 652.2 eV. The photon energy of the XAS spectra was calibrated by measuring the kinetic energy of the Ag 3d/Ir 4f peaks with known binding energy before starting the acquisition of the XAS spectra. The Ag(100) crystal was cleaned by several cycles of Ar sputtering at room temperature and subsequent vacuum annealing at 723 K. The Ir(100) crystal was cleaned by sputtering at room temperature and subsequent oxygen annealing at 1000 K, followed by vacuum annealing at 1273 K. Cleanness of the Ag(100) and Ir(100) were confirmed with XPS, STM, and LEED. The Co evaporation rate was calibrated by producing two-dimensional cobalt oxide structures that require exact amounts of Co expressed in monolayer equivalents (MLEs) [25]. The preparation recipes for the different Co oxide films on Ag(100) are discussed throughout the text. The starting point for the preparation of the Co_3O_4(111) on Ir(100) film is the Ir(100)-(2×1)-O structure which we formed by cooling down the Ir(100)-(5×1)-hex reconstruction from 1200 K to room temperature in $1{\cdot}10^{-8}$ mbar oxygen. Subsequently, 15 MLE (1 MLE/min) of Co was deposited in $5{\cdot}10^{-7}$ mbar of O_2 at 300 K sample temperature. Finally, the 5 nm thick film was annealed at 523 K in $5{\cdot}10^{-7}$ mbar of O_2 for 2 min followed by vacuum flashing to 673 K to improve the ordering of the film. The CoO(111) film was formed from the Co_3O_4(111) film by flashing it to 900 K in UHV [14]. The ordering of both Co_3O_4(111) and CoO(111) on Ir(100) was checked by LEED.

3. Structure and electronic properties

As a starting point we used LEED to study how the annealing temperature affects the periodicity and ordering of Co oxide films grown on Ag(100). In Fig. 1 we compare LEED images acquired directly after reactive deposition of cobalt in O_2 at 473 K (b), and after sequential annealing at stepwise higher temperatures in $2{\cdot}10^{-5}$ mbar of O_2 (c), (d). For reference the LEED image of clean Ag(100) is shown in panel (a). Surface unit cells of Ag(100) (2.88 Å), CoO(100) (3.01 Å), and Co_3O_4(100) (5.71 Å) are superimposed with red, dotted blue, and black squares, respectively. Directly after deposition (b), the LEED image reveals broad 1×1 spots with the same orientation as Ag(100) consistent with a CoO(100) film that adapted the orientation of the substrate. The distinct cross-shaped spot profiles observed are most likely caused by CoO(100) patches slightly tilted against each other due to the lattice mismatch of ~4.4% between Ag(100) (2.88 Å) and rocksalt CoO(100) (3.01 Å). Similar spot profiles were observed for MgO(100)/Mo(001) films by Benia et al. [26], Stavale et al. [27], and Benedetti et al. [28]. Subsequent oxygen annealing at 573 K for 10 min results in sharp but weak (2×2) diffraction spots and cross-shaped (1×1) spot profiles in the LEED pattern (Fig. 1c). Since the lattice of Co_3O_4(100) (5.71 Å) fits almost perfectly with two times the lattice distance of Ag(100) (2·2.89 Å=5.78 Å) the (2×2) diffraction spots are assigned to diffraction from Co_3O_4(100) facets. In contrast, the cross-shaped (1×1) spots are due to diffraction from CoO(100). Therefore, Co_3O_4(100) and CoO(100) must co-exist on the surface after annealing to 573 K in oxygen. Further annealing at 573 K for 36 min in $1{\cdot}10^{-5}$ mbar O_2 did not cause any change to the LEED pattern suggesting that the CoO(100) facets are quite stable and inert towards O_2 exposure at this temperature. Increasing the oxygen annealing temperature further to 673 K the cross-shaped profile of the (1×1) spots almost disappear and all spots become sharper confirming the formation of a well-ordered Co_3O_4(100) film on Ag(100) (see Fig. 1d). The formation of a Co_3O_4 phase in this temperature (673 K) and pressure ($1{\cdot}10^{-5}$ mbar) interval fits well with the thermodynamic data of bulk Cobalt oxides [29].

Fig. 2a shows an overview STM image of the cobalt oxide film grown by reactive deposition of Co in O_2 at 473 K after one annealing step at 573 K in $2{\cdot}10^{-5}$ mbar of O_2. The LEED pattern of this film (not shown) is identical the one shown in Fig. 1c. The film exhibits large, atomically flat terraces. In this image, three different types of surface structures can be observed: (i) Co_3O_4(100), (ii) CoO(100), and (iii) bare Ag(100). The evidence for the assignment of the different surface structures is given in the following. The presence of CoO(100), a minority phase, is residual from the preparation. Considering the amount of Co deposited (~20 MLE), the presence of small patches of bare Ag(100) seems to be indicative of partial embedding of the cobalt oxide in the silver as a result of the relatively high annealing temperature used to oxidize it. The terraces of the Co_3O_4(100) phase exhibit distinct atomic-scale rows oriented along [011] and [0-11] directions, with a spacing of ~6 Å. The smallest steps observed between terraces are measured to be 1.9 Å in height, and the orientation of the rows on terraces separated by this type of step differ by a rotation of 90° (green arrows in Fig. 2a). Larger steps, ~3.8 Å in height, separate terraces whose rows are oriented in the same direction, and thus correspond simply to double steps. These features are characteristic of the cubic spinel structure; a ball model of Co_3O_4 is displayed in Fig. 2b; the lattice constant of this compound is 8.084 Å. The bulk stacking normal to the (100) plane consists of alternating layers of cobalt in octahedral (Co_{oct}, gray colored balls), and tetrahedral (Co_{tet}, green colored balls) coordination. The Co_{oct} ions form rows oriented along the unit cell diagonals while the Co_{tet} occupy interstitial pockets between these rows. Fig. 2c shows a top view of the Co_3O_4(100) surface, with a single step exposing two equivalent Co_{oct} layers separated by 1/4 of the unit cell height. In the model, we can observe that the orientations of the Co_{oct} rows in adjacent terraces are rotated by 90° with respect to each other. The Co_{tet} ions are located between the Co_{oct} rows and form a 5.7 Å square lattice corresponding to the bulk-truncated Co_3O_4(100) surface unit cell, reflected in the LEED as a p(2×2) pattern with respect to Ag(100) (Fig. 1d). The spacing between Co_{oct} rows (5.7 Å) and between equivalent Co_{oct} layers (2.0 Å) agree well with the STM measurement, and we propose that the Co_3O_4(100) surface forms the unreconstructed, Co_{oct}-terminated structure depicted in Fig. 2c. Surface reconstruction of the (100) surface of spinel compounds is expected, as these surfaces are polar. Therefore, it is surprising the Co_3O_4(100) film apparently is unreconstructed in contrast to the (100) surface of isomorphic Fe_3O_4, which exhibits a $(\sqrt{2} \times \sqrt{2})$R45° reconstruction caused by subsurface cation vacancies [30]. The subsurface Fe_{oct} vacancies enable filling of 1/2 of the unfilled tetrahedral interstitial pockets with Fe ions [31]. The presence of a tetrahedral interstitial atom causes the surface octahedral rows to bow inward, creating a distinctive wavy appearance in STM, and leads to additional strong reflexes in LEED. Such reflexes are clearly absent from our measured LEED pattern from Co_3O_4(100). However, in STM images we do observe some point defects which may be related to the Fe_3O_4(100) reconstruction. Fig. 3a shows a high-resolution STM image

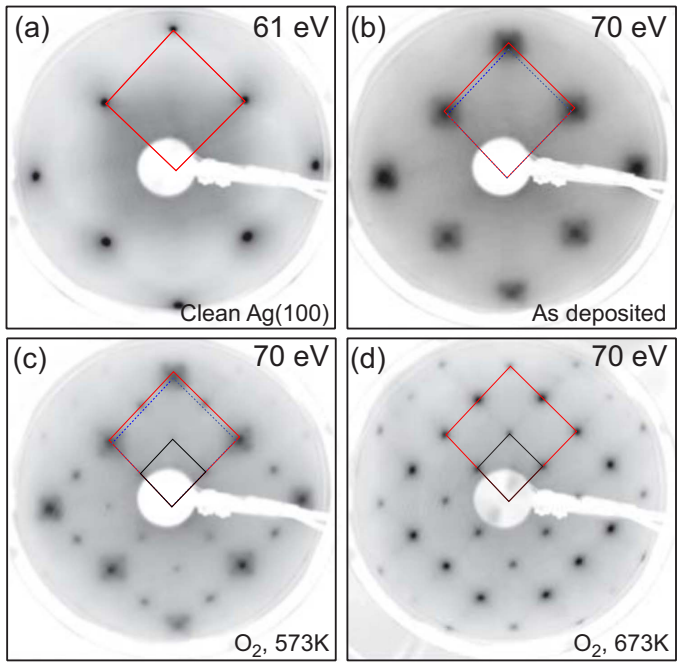

Fig. 1. LEED images of: (a) Ag(100), (b) after reactive Co deposition at 473 K, and after sequential oxygen annealing ($2{\cdot}10^{-5}$ mbar) for 10 min at (c) 573 K and (d) 673 K. The surface unit cells of Ag(100), CoO(100), and Co_3O_4(100) are indicated with solid red, dotted blue, and solid black lines, respectively. (For interpretation of the references to color in this figure legend, the reader is referred to the web version of this article.)

of the Co_3O_4(100) film taken from a single terrace. The most numerous defects observed in the image appear as small depressions (arrows in Fig. 3a) adjacent to the bright Co_{oct} rows. Careful inspection shows that these depressions always form as pairs centered on the trough between two Co_{oct} rows. Fig. 3b shows the same image overlaid with a grid corresponding to the 5.7 Å square lattice of Co_3O_4(100). Dashed white circles indicate the center points between pairs of depressions which constitute a single defect. Interpreted in this way, it can be seen that the defects are all centered at a single type of site on the Co_{tet} troughs. The minimum separation between defects along the rows and perpendicular to them (i.e. along the [0-11] and [011] directions) as indicated in Fig. 3a is 2 lattice spacings, while the minimum spacing overall, and one which is frequently observed in Fig. 3b, is $\sqrt{2}$, e.g. across the unit cell diagonal. Defects separated by two lattice spacings perpendicular to the Co_{oct} rows give rise to particularly deep depressions between them. Due to the symmetry, we find it unlikely that the observed defects correspond to oxygen vacancies. Other common defects such as metal atoms or adsorbed OH groups typically appear as bright protrusions under similar imaging conditions on oxide surfaces [32]. We propose instead that the observed defects correspond to subsurface cation vacancies analogous to those observed for Fe_3O_4(100). The presence of interstitial Co_{int} atoms in the tetrahedral interstitial pocket should cause the neighboring octahedral ions to bow inward, creating the appearance of depressions on either side in the STM image. The typical minimum separations between defects observed in Fig. 3b are also consistent with the $(\sqrt{2} \times \sqrt{2})$R45° arrangement characteristic of the Fe_3O_4(100) reconstruction. What causes the difference between iron and cobalt oxides is unclear. It may be related to the generally greater stability of Fe(III) oxides compared to Co(III), considering that the subsurface cation vacancies increase the overall oxidation state at the surface. The nominal thickness of 20 ML derived from the evaporator flux corresponds to ~6 nm thickness for Co_3O_4, which is comparable to that of Fe_3O_4(100) films grown on Pt(100) by Davis et al., which did show the same reconstruction as seen for bulk magnetite single crystals [33]. A thickness effect therefore appears unlikely. One difference between the Fe_3O_4 and Co_3O_4 oxide is, however, that while the Fe_3O_4 oxide has a half-metallic character at room temperature [34] the Co_3O_4 oxide is semiconductor with a band gap of the order of ~1.6 eV [35]. Future Scanning tunneling spectroscopy (STS) and ultraviolet photoemission spectroscopy (UPS) of the Co_3O_4(100) surfaces would definitely be very interesting and we hope our work can inspire such studies.

After presenting the structural model of the Ag(100) supported Co_3O_4(100) film we now discuss its spectroscopic characteristics. In Fig. 4 we compare Co 2p and O 1s XP spectra and Co 2p (L3) XAS spectra for: Ag(100) supported Co_3O_4(100) (top), Ir(100) supported Co_3O_4(111) (middle), and Ir(100) supported CoO(111) (bottom). The Ag(100) supported Co_3O_4(100) film was grown by a reactive deposition of 20 MLE Co at 473 K followed by annealing in oxygen ($2{\cdot}10^{-5}$ mbar) at 673 K until a sharp p(2×2) structure developed. The growth recipe of the Ir(100) supported reference structures are described in the Experimental section and in a previous publication [14]. Starting with the reference spectra of Ir(100) supported CoO(111) and Co_3O_4(111) shown at the bottom and middle, respectively, we note the following differences: (i) The satellite features appearing in the Co 2p spectra show greater intensity for CoO(111) compared to Co_3O_4(111), in

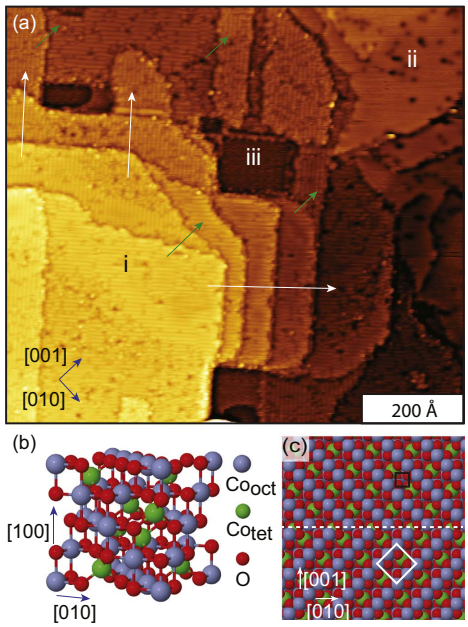

Fig. 2. Large-scale STM image (3.0 V, 350 pA) showing the co-existence of (i) Co_3O_4(100), (ii) CoO(100), and (iii) bare Ag(100). The image was acquired after cobalt oxide film growth by reactive deposition of Co in O_2 at 473 K after one annealing step at 573 K in $2{\cdot}10^{-5}$ mbar of O_2 (b) structural model of bulk Co_3O_4. (c) Ball model of bulk truncated Co_3O_4(100) surface, terminated at the Co_{oct} layer. The gray, green, and red balls correspond to Co_{oct}, Co_{tet}, and O, respectively. The bulk unit cell is indicated as a white square. The tetrahedral interstitial pocket is indicated as a black square. (For interpretation of the references to color in this figure legend, the reader is referred to the web version of this article.)

agreement with previous XPS studies of Co oxide bulk samples [36]. (ii) The Co 2p XAS spectrum of CoO(111) shows several strong peaks which are absent in the Co_3O_4(111) spectrum. (iii) The O 1s photoemission peak of CoO(111) is significantly broader than that of Co_3O_4(111). Comparing the spectrum of the Ag(100) supported Co_3O_4(100) with the fingerprint spectra of CoO and Co_3O_4, it is evident that the CoO features (i-iii) discussed above are fully absent and overall the spectrum of Ag(100) supported Co_3O_4(100) is very similar to Ir(100) supported Co_3O_4(111). Therefore, the photoemission spectroscopy experiments of Ag(100) supported Co_3O_4(100) gives additional support for the formation of spinel type film and they furthermore point towards very similar electronic structures of the Co_3O_4(100) and Co_3O_4(111) facets.

4. CO adsorption properties on Co_3O_4(100)

To probe the chemical properties of Ag(100) supported Co_3O_4(100) we studied CO adsorption with XPS. Fig. 5 shows O 1s and C 1s spectra before (a) and after (b) saturation with CO at 85 K. For reference similar data for Ir(100) supported Co_3O_4(111) also saturated with CO at 85 K are included in panel c [16]. Starting with the O 1s spectrum of clean Ag(100) supported Co_3O_4(100) curve fitting reveals a main component located at 529.15 eV (orange) and a shoulder component shifted by +1.75 eV (orange). For reference our previous work on the pristine Co_3O_4(111) supported by Ir(111) revealed similar components located at 529.30 eV (main) originating from the Co_3O_4(111) film and a shoulder component shifted by +1.5 eV tentatively assigned to oxygen vacancies [16]. Consistent with our previous study we therefore assign the 529.15 eV to oxygen in the Co_3O_4(100) film itself while the shoulder component shifted by +1.75 eV is assigned to defects. One clear difference between pristine Co_3O_4(100)/Ag(100) and Co_3O_4(111)/Ir(111) is that we in the case of pristine Co_3O_4(111)/Ir(111) observe an additional shoulder component with unknown identity at lower binding energy (528.55 eV), while no such component is observed for Co_3O_4(100)/Ag(100). Upon saturation the Co_3O_4(100) and Co_3O_4(111) films with CO at 85 K the intensity of the shoulder components shifted by +1.75 eV and +1.5 eV, respectively, increase. Furthermore, a new component appears at 534 eV and 533.8 eV for the two films, respectively. In previous work temperature programed XPS (TPXPS) was used to assign the increase in the +1.5 eV component to

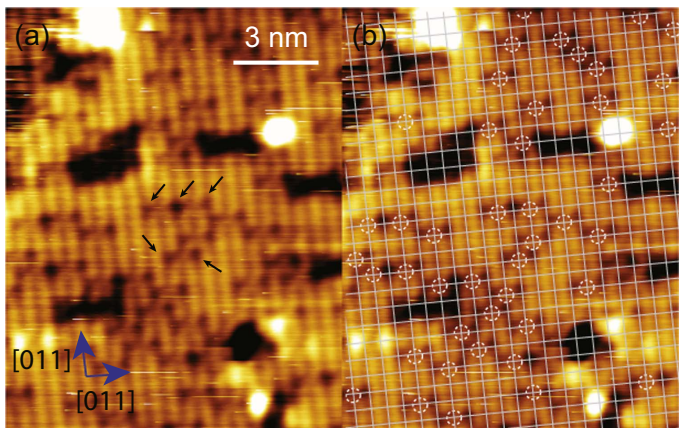

Fig. 3. (a) High resolution STM image (1.75 V, 200 pA) of the Co_3O_4(100) film. The image was acquired after annealing the cobalt oxide film in at 673 K in $2{\cdot}10^{-5}$ mbar of O_2. Arrows indicate point defects imaged as depressions, as discussed in the text. (b) The same image with a grid overlaid corresponding to the Co_3O_4(100)–(1×1) lattice. The white dotted circles correspond to individual point defects, each of which gives rise to two depressions at adjacent rows.

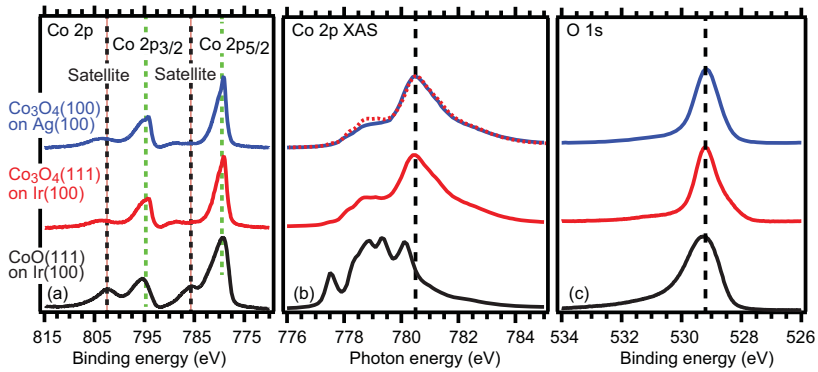

Fig. 4. XPS and XAS spectra of the $Co_3O_4(100)$ film, with corresponding spectra from previous studies of films grown on Ir(100) for comparison. The Ag(100) supported $Co_3O_4(100)$ film was grown by a reactive deposition of 20 MLE Co at 473 K followed by annealing in oxygen ($2{\cdot}10^{-5}$ mbar) at 673 K until a sharp p(2×2) structure developed. (a) Co 2p XPS. (b) Co 2p XAS. (c) O 1s XPS. The Co 2p spectrum of $Co_3O_4(111)$/Ir(100) (dashed red line) is superimposed on the spectrum of $Co_3O_4(100)$/Ag(100) (solid blue line) for direct comparison. (For interpretation of the references to color in this figure legend, the reader is referred to the web version of this article.)

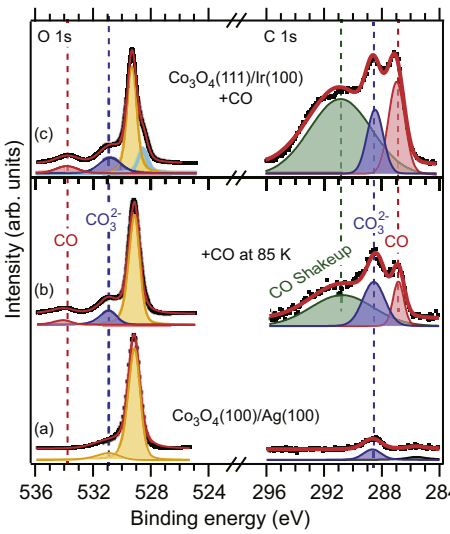

Fig. 5. O 1s and C 1s XP spectra of Ag(100) supported $Co_3O_4(100)$ before (a) and after (b) CO saturation at 85 K. For reference analog spectra of CO exposed $Co_3O_4(111)$ grown on Ir(100) are shown in (c). The experimental spectra are shown with black dots, the fit as a solid red line, and the filled curves represent the components of the fit. (For interpretation of the references to color in this figure legend, the reader is referred to the web version of this article.)

the formation of carbonates, while the new component at 533.8 eV was assigned to weakly adsorbed CO [16]. Based on this, and on the close similarity in binding energies of the respective components we make the same assignment here and conclude that CO adsorbs very similarly on the (100) and (111) surfaces of Co_3O_4. The C 1s spectra of the CO saturated $Co_3O_4(100)$ and $Co_3O_4(111)$ films can both be deconvoluted with three components: two narrow peaks at 287.0 eV (red) and 288.7 eV [$Co_3O_4(100)$/Ag(100)]/288.5 eV [$Co_3O_4(111)$/Ir(111)] (blue), and a broad feature centered at 290.9 eV (green). Based on the temperatures at which the different features disappear upon heating probed with TPXPS we previously attributed the components observed on $Co_3O_4(111)$ to carbonate (288.5 eV) and weakly adsorbed CO (287.0 eV). The broad component at 290.9 eV is a shake-up satellite of the main CO component at 287.0 eV.14 As we observe very similar components for the CO saturated $Co_3O_4(100)$/Ag(100) surface we make the same assignment and conclude that the C 1s spectra gives additional support for very similar adsorption of CO on the (100) and (111) surfaces of Co_3O_4. This is perhaps not surprising, considering the similarities of the two surfaces and their similarity in core-level spectra; the (100) and (111) surfaces of Co_3O_4 both expose potentially reactive Co and O ions, and the Co and oxygen XPS and XAS measurements suggested that these species are similar chemically. Geometrical effects related to the arrangement of these ions thus appear to be more subtle. Further measurements of the desorption temperature of CO on the two surfaces as well as detailed structural characterization of the adsorbed molecules could potentially shed further light on these subtler differences and how these influence the catalytic properties of Co_3O_4.

5. Conclusions

To conclude our work demonstrates that well-ordered $Co_3O_4(100)$ films can be grown on inert Ag(100). Therefore, our work paves the way for improved catalytic studies of cobalt oxide based model catalysts under near-realistic conditions eliminating the possible interference of the supporting substrate. Unlike $Fe_3O_4(100)$, the $Co_3O_4(100)$ surface is unreconstructed, but exhibits point defects which appear similar to the 'subsurface cation vacancies' that characterize the $Fe_3O_4(100)$ reconstruction. The Co 2p and O 1s core level spectra for the oxide appear almost identical to those of $Co_3O_4(111)$, which was studied previously, and CO adsorption at 85 K is likewise very similar, producing a mixture of molecular CO and more strongly bound CO_3. Further studies are therefore necessary to shed light on the structure-dependent catalytic properties of Co_3O_4 surfaces.

Acknowledgement

The authors are grateful for support by the Röntgen-Ångström cluster "Catalysis on the atomic scale" (Project No. 349-2011-6491) and by the Project Grant 2012-3850 both financed by the Swedish Research Council. The MAX IV Laboratory personnel are acknowl-

edged for support during measurements.

References

[1] L.F. Liotta, H. Wu, G. Pantaleo, A.M. Venezia, Co_3O_4 nanocrystals and Co_3O_4-MO_x binary oxides for CO, CH_4 and VOC oxidation at low temperatures: a review, Catal. Sci. Technol. 3 (2013) 3085–3102. http://dx.doi.org/10.1039/c3cy00193h.

[2] Y. Liang, Y. Li, H. Wang, J. Zhou, J. Wang, T. Regier, H. Dai, Co_3O_4 nanocrystals on graphene as a synergistic catalyst for oxygen reduction reaction, Nat. Mater. 10 (2011) 780–786. http://dx.doi.org/10.1038/NMAT3087.

[3] A.S. Walton, J. Fester, M. Bajdich, M.A. Arman, J. Osiecki, J. Knudsen, A. Vojvodic, J.V. Lauritsen, Interface controlled oxidation states in layered cobalt oxide nanoislands on gold, ACS Nano 9 (2015) 2445–2453. http://dx.doi.org/10.1021/acsnano.5b00158.

[4] C. Xu, Z. Tian, P. Shen, S.P. Jiang, Oxide (CeO_2, NiO, Co_3O_4, and Mn_3O_4)-promoted Pd/C electrocatalysts for alcohol electrooxidation in alkaline media, Electrochim. Acta 53 (2008) 2610–2618. http://dx.doi.org/10.1016/j.electacta.2007.10.036.

[5] L.-N. Jin, J.-G. Wang, X.-Y. Qian, D. Xia, M.-D. Dong, Catalytic activity of Co_3O_4 nanomaterials with different morphologies for the thermal decomposition of ammonium perchlorate, J. Nanomater., 2015, p. 854310, http://dx.doi.org/10.1155/2015/854310.

[6] Y. Zhang, F. Ding, C. Deng, S. Zhen, X. Li, Y. Xue, Y.-M. Yan, K. Sun, Crystal plane-dependent electrocatalytic activity of Co_3O_4 toward oxygen evolution reaction, Catal. Commun. 67 (2015) 78–82. http://dx.doi.org/10.1016/j.catcom.2015.04.012.

[7] J. Xiao, Q. Kuang, S. Yang, F. Xiao, S. Wang, L. Guo, Surface structure dependent electrocatalytic activity of Co_3O_4 anchored on graphene sheets toward oxygen reduction reaction, Sci. Rep., 3, 2013, p. 2300, http://dx.doi.org/10.1038/srep02300.

[8] J. Jansson, A. Palmqvist, E. Fridell, M. Skoglundh, L. Österlund, P. Thormahlen, V. Langer, On the catalytic activity of Co_3O_4 in low-temperature CO oxidation, J. Catal. 211 (2002) 387–397. http://dx.doi.org/10.1006/jcat.2002.3738.

[9] J. Jansson, Low-temperature CO oxidation over Co_3O_4/Al_2O_3, J. Catal. 194 (2000) 55–60. http://dx.doi.org/10.1006/jcat.2000.2924.

[10] Z. Chen, C.X. Kronawitter, B.E. Koel, Facet-dependent activity and stability of Co_3O_4 nanocrystals towards the oxygen evolution reaction, Phys. Chem. Chem. Phys. 17 (2015) 29387–29393. http://dx.doi.org/10.1039/c5cp02876k.

[11] X. Xie, Y. Li, Z.-Q. Liu, M. Haruta, W. Shen, Low-temperature oxidation of CO catalysed by Co_3O_4 nanorods, Nature 458 (2009) 746–749. http://dx.doi.org/10.1038/nature07877.

[12] Z. Fei, S. He, L. Li, W. Ji, C.-T. Au, Morphology-directed synthesis of Co_3O_4 nanotubes based on modified kirkendall effect and its application in CH_4 combustion, Chem. Commun. 48 (2012) 853–855. http://dx.doi.org/10.1039/c1cc15976c.

[13] L. Hu, Q. Peng, Y. Li, Selective synthesis of Co_3O_4 nanocrystal with different shape and crystal plane effect on catalytic property for methane combustion, J. Am. Chem. Soc. 130 (2008) 16136–16137. http://dx.doi.org/10.1021/ja806400e.

[14] K. Heinz, L. Hammer, Epitaxial cobalt oxide films on Ir(100) – the importance of crystallographic analyses, J. Phys. Condens. Matter 25 (2013) 173001. http://dx.doi.org/10.1088/0953-8984/25/17/173001.

[15] W. Meyer, K. Biedermann, M. Gubo, L. Hammer, K. Heinz, Surface structure of polar Co_3O_4(111) films grown epitaxially on Ir(100)-(1×1), J. Phys. Condens. Matter 20 (2008) 265011. http://dx.doi.org/10.1088/0953-8984/20/26/265011.

[16] P. Ferstl, S. Mehl, M.A. Arman, M. Schuler, A. Toghan, B. Laszlo, Y. Lykhach, O. Brummel, E. Lundgren, J. Knudsen, L. Hammer, M.A. Schneider, J. Libuda, Adsorption and activation of CO on Co_3O_4(111) thin films, J. Phys. Chem. C 119 (2015) 16688–16699. http://dx.doi.org/10.1021/acs.jpcc.5b04145.

[17] A. Mane, K. Shalini, A. Wohlfart, A. Devi, S. Shivashankar, Strongly oriented thin films of Co_3O_4 deposited on single-crystal MgO(100) by low-pressure, low-temperature MOCVD, J. Cryst. Growth 240 (2002) 157–163. http://dx.doi.org/10.1016/S0022-0248(02)00860-6.

[18] G. Carson, M. Nassir, M. Langell, Epitaxial growth of Co_3O_4 on CoO(100), J. Vac. Sci. Technol. A 14 (1996) 1637–1642. http://dx.doi.org/10.1116/1.580310.

[19] M. Langell, M. Anderson, G. Carson, L. Peng, S. Smith, Valence-band electronic structure of Co_3O_4 epitaxy on CoO(100), Phys. Rev. B 59 (1999) 4791–4798. http://dx.doi.org/10.1103/PhysRevB.59.4791.

[20] G.A. Kaptagay, T.M. Inerbaev, Y.A. Mastrikov, E.A. Kotomin, A.T. Akilbekov, Water interaction with perfect and fluorine-doped Co_3O_4(100) surface, Solid State Ionics 277 (2015) 77–82. http://dx.doi.org/10.1016/j.ssi.2015.03.012.

[21] H.-F. Wang, R. Kavanagh, Y.-L. Guo, Y. Guo, G. Lu, P. Hu, Origin of extraordinarily high catalytic activity of Co_3O_4 and its morphological chemistry for CO oxidation at low temperature, J. Catal. 296 (2012) 110–119. http://dx.doi.org/10.1016/j.jcat.2012.09.005.

[22] F. Zasada, W. Piskorz, J. Janas, J. Grybos, P. Indyka, Z. Sojka, Reactive oxygen species on the (100) facet of cobalt spinel nanocatalyst and their relevance in $^{16}O_2/^{18}O_2$ isotopic exchange, deN_2O, and $deCH_4$ processes-a theoretical and experimental account, ACS Catal. 5 (2015) 6879–6892. http://dx.doi.org/10.1021/acscatal.5b01900.

[23] I. Sebastian, H. Neddermeyer, Scanning tunneling microscopy on the atomic and electronic structure of CoO thin films on Ag(100), Surf. Sci. 454 (2000) 771–777. http://dx.doi.org/10.1016/S0039-6028(00)00060-1.

[24] R. Nyholm, J. Andersen, U. Johansson, B. Jensen, I. Lindau, Beamline I311 at MAX-LAB: a VUV/soft X-ray undulator beamline for high resolution electron spectroscopy, Nucl. Instrum. Methods A 467 (2001) 520. http://dx.doi.org/10.1016/S0168-9002.

[25] M. Gubo, C. Ebensperger, W. Meyer, L. Hammer, K. Heinz, Structural elements in the oxidation process of a single cobalt layer on Ir(100)-(1×1), Phys. Rev. B 83 (2011) 075435. http://dx.doi.org/10.1103/PhysRevB.83.075435.

[26] H.-M. Benia, P. Myrach, A. Gonchar, T. Risse, N. Nilius, H.-J. Freund, Electron trapping in misfit dislocations of MgO thin films, Phys. Rev. B 81 (2010) 241415. http://dx.doi.org/10.1103/PhysRevB.81.241415.

[27] F. Stavale, N. Nilius, H.-J. Freund, Cathodoluminescence of near-surface centres in Cr-doped MgO(001) thin films probed by scanning tunnelling microscopy, New J. Phys. 14 (2012) 033006. http://dx.doi.org/10.1088/1367-2630/14/3/033006.

[28] S. Benedetti, H.M. Benia, N. Nilius, S. Valeri, H.J. Freund, Morphology and optical properties of MgO thin films on Mo(001), Chem. Phys. Lett. 430 (2006) 330–335. http://dx.doi.org/10.1016/j.cplett.2006.08.130.

[29] M. Ivill, S.J. Pearton, S. Rawal, L. Leu, P. Sadik, R. Das, A.F. Hebard, M. Chisholm, J.D. Budai, D.P. Norton, Structure and magnetism of cobalt-doped ZnO thin films, New J. Phys., 10 http://dx.doi.org/10.1088/1367-2630/10/6/065002.

[30] R. Bliem, E. McDermott, P. Ferstl, M. Setvin, O. Gamba, J. Pavelec, M.A. Schneider, M. Schmid, U. Diebold, P. Blaha, L. Hammer, G.S. Parkinson, Subsurface cation vacancy stabilization of the magnetite (001) surface, Science 346 (2014) 1215–1218. http://dx.doi.org/10.1126/science.1260556.

[31] M. Fonin, R. Pentcheva, Y. Dedkov, M. Sperlich, D. Vyalikh, M. Scheffler, U. Rudiger, G. Guntherodt, Surface electronic structure of the Fe_3O_4(100): evidence of a half-metal to metal transition, Phys. Rev. B 72 (2005) 104436. http://dx.doi.org/10.1103/PhysRevB.72.104436.

[32] O. Gamba, J. Hulva, J. Pavelec, R. Bliem, M. Schmid, U. Diebold, G. Parkinson, The role of surface defects in the adsorption of methanol on Fe_3O_4(001), Nucl. Instrum. Methods A 467 (2001) 520. http://dx.doi.org/10.1016/S0168-9002.

[33] E.M. Davis, K. Zhang, Y. Cui, H. Kuhlenbeck, S. Shaikhutdinov, H.-J. Freund, Growth of Fe_3O_4(001) thin films on Pt(100): tuning surface termination with an Fe buffer layer, Surf. Sci. 636 (2015) 42–46. http://dx.doi.org/10.1016/j.susc.2015.02.004.

[34] J. Lee, S.G. Kwon, J.-G. Park, T. Hyeon, Size dependence of metal-insulator transition in stoichiometric Fe_3O_4 nanocrystals, Nano Lett. 15 (2015) 4337–4342. http://dx.doi.org/10.1021/acs.nanolett.5b00331.

[35] V.R. Shinde, S.B. Mahadik, T.P. Gujar, C.D. Lokhande, Supercapacitive cobalt oxide (Co3O4) thin films by spray pyrolysis, Appl. Surf. Sci. 252 (2006) 7487–7492. http://dx.doi.org/10.1016/j.apsusc.2005.09.004.

[36] H. Hagelin-Weaver, G. Hoflund, D. Minahan, G. Salaita, Electron energy loss spectroscopic investigation of Co metal, CoO, and Co_3O_4 before and after Ar^+ bombardment, Appl. Surf. Sci. 235 (2004) 420–448. http://dx.doi.org/10.1016/j.apsusc.2004.02.062.

Paper VI

Transformation between Co_3O_4 and CoO phases under reaction conditions

M. A. Arman[1], L. R. Merte[1], E. Lundgren[1], and J. Knudsen[1,2]

[1]*Division of Synchrotron Radiation Research, Lund University, Box 118, 22100 Lund, Sweden*

[2]*MAX IV Laboratory, Lund University, Box 118, 22100 Lund, Sweden*

Abstract

Using high pressure x-ray photoelectron spectroscopy Ag(100) supported Co_3O_4(100) and CoO(100) thin films are studied in a stoichiometric reaction mixture of O_2 and CO at a total pressure of 1.2 mbar. The Co_3O_4(100) phase is readily formed under these reaction conditions and remains stable in the temperature interval from 350 – 550 K, studied, here even if we start from the very inert CoO(100) phase. Only upon complete removal of CO from the gas mixture the Co_3O_4(100) phase transforms back to the CoO(100) phase. Metallic Co films are never observed. Carbonates are the only carbon containing adsorbate detected both on the CoO(100) and Co_3O_4(100) surfaces in the temperature range between 300 K and 450 K.

Keywords: high pressure x-ray photoelectron spectroscopy, Ag(100), Co_3O_4(100), CoO(100), O_2, CO.

1. Introduction

It is well known that transition metal oxides can change phase under reaction conditions. One extensively studied system is a Pt(111) supported bilayer iron oxide FeO(111) film that is transformed to a honeycomb-structured Fe_3O_2 film in mbar CO pressures [1] and a hydroxylated trilayer iron oxide FeO_2 film in mbar pressures of O_2 and O_2:H_2O mixtures at elevated temperatures [2,3]. In contrast to the extensively studied FeO(111) film conversion very little is known about the Co oxide film conversion under reaction conditions. For Au(111) supported cobalt oxide nano islands Walton *et al.* studied their conversion in low pressures of oxygen and showed that a CoO(111) phase develops upon synthesizing the islands at oxygen pressures of the order of $1 \cdot 10^{-6}$ mbar, while CoO_2(111) islands develop at 10 times higher oxygen pressures [4]. In a more recent study by Lukashuk *et al.* [5] the conversion of supported spinel particles was studied with high pressure x-ray photoelectron and absorption spectroscopy (HPXPS and HPXAS). This work revealed that the reduction of the Co_3O_4 particles sets in already at room temperature in 0.15 mbar of pure CO. At 523 K the particles are fully converted to CoO phase, and at 573 K metallic Co is observed. In the corresponding C 1s spectra carbonates (288.2 eV), CO or C-OH species (286.1 eV), and elementary carbon (284.7 eV) were detected. To the best of our knowledge, no studies have been performed on the conversion of well characterized single crystal surfaces of the CoO and Co_3O_4 phases.

In this short letter, we study the reduction and oxidation of Co_3O_4(100) and CoO(100) films grown on an Ag(100) substrate with high pressure x-ray photoelectron spectroscopy (HPXPS), low energy electron diffraction (LEED), and scanning tunneling microscopy (STM). We demonstrate that the Ag(100) supported CoO(100) film is immediately converted to a Co_3O_4 film in a reaction mixture of O_2 and CO at 550 K, while it converts back to CoO upon removal of oxygen from the reaction mixture. We also study the temperature dependence of the film conversion and identify carbonates as the only adsorbed carbon-containing species.

2. Experimental Section

The HPXPS experiments were performed at the SPECIES [6,7] beamline at the MAX IV Laboratory (Lund, Sweden). The base pressure of the endstation was ~$5 \cdot 10^{-10}$ mbar. All photoemission spectra (PES) were collected in normal emission with photon energies of 380 eV and 460 eV (C 1s), 625 eV (O 1s), and 1000 eV (Co 2p). Binding energies were calibrated by measuring the Ag 3d spectra directly after the spectra of interest without changing the photon energy and by assuming fixed binding energy of 368.2 eV of Ag 3d. For the curve fitting, we used symmetric Voigt components after subtracting a polynomial background. The Ag(100) crystal was cleaned by several cycles of Ar sputtering and annealing to 720 K. Cleanness of the crystal surface was confirmed with XPS and LEED. For the HPXPS we used 6N purity O_2 and 4.7N CO. CO was further purified with a commercial Gaskleen II purifier which removes volatile Ni-carbonyls. A chromel−alumel thermocouple spot welded to the side of the crystal was used for the temperature measurement.

The scanning tunneling microscopy (STM) experiments were performed at Lund University using a commercial room temperature STM (Omicron, STM1) having a base pressure of ~$1 \cdot 10^{-10}$ mbar.

The growth of Co_3O_4(100) on Ag(100) has been discussed in our previous work [8]. In short, the preparation consists of ~20 MLE of Co evaporated in oxygen ($5 \cdot 10^{-6}$ mbar) with a growth rate of ~1ML/min at 470 K. The deposition rate of Co was calibrated on Ir(100). Here the Co evaporation rate was calibrated by producing and identifying the LEED pattern of two-dimensional cobalt oxide structures that require exact amounts of Co expressed in monolayer equivalents (MLEs) [9]. One MLE is here equivalent to a full monolayer coverage of the two dimensional c(8×2) cobalt oxide film grown on the Ir(100)-(1×1) surface [9]. Subsequently, the Ag(100) was placed in the same position as the Ir(100) crystal and Co was deposited onto Ag(100) with identical flux reading on the EFM-3 source (50 nA). After reactive Co deposition, the thick films were annealed at 670 K in $2 \cdot 10^{-5}$ mbar oxygen for 10 min in steps until a sharp (2×2) pattern was observed in LEED.

3. Results and Discussion

The structural properties of the Co_3O_4(100) phase have been studied previously with STM, LEED, and XPS [8]. From this previous study, it is known that the surface of the Co_3O_4(100) film is terminated with Co_{oct} rows oriented along [011] and [0-11] directions, with a spacing of ~6 Å. The LEED image of Co_3O_4(100) surface shows a (2×2) pattern (figure 1(a)). In contrast, the CoO(100) films exhibit a (1×1) pattern (figure 1(e)). Figure 1(b) and (f) show STM images of the Co_3O_4(100) and CoO(111) phases, respectively, while panels (c) and (f) show the structural models of the two phases.

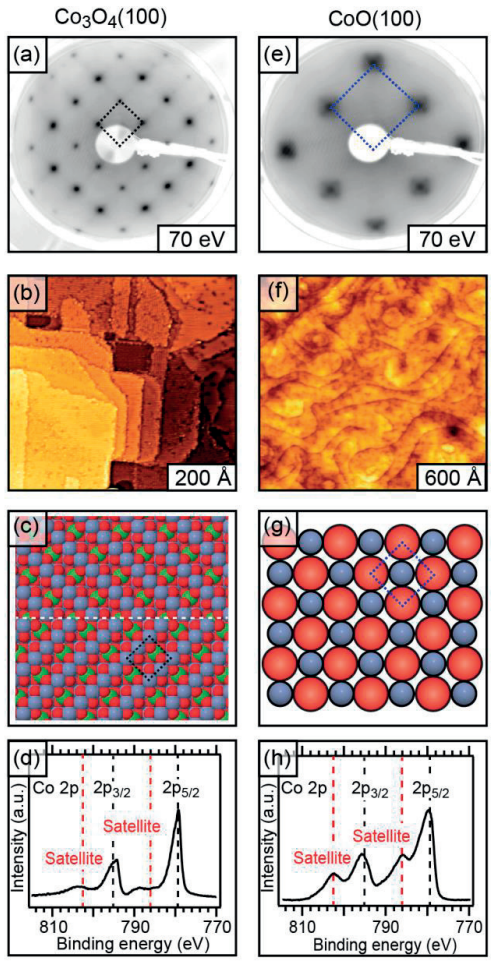

Figure 1: (a) LEED, (b) STM, (c) structural model, and (d) Co 2p XP spectrum of Co_3O_4(100). (e) LEED, (f) STM, (g) structural model, and (h) Co 2p XP spectrum of CoO(100). The red and blue balls correspond to oxygen and cobalt atoms. The blue and green balls in (c) correspond to cobalt in ocbtahedral (Co_{oct}), and tetrahedral (Co_{tet}) coordination. Unit cells are shown in the LEED and in the structural models.

In figure 1(d) and (h) Co 2p spectra of the Co_3O_4(100) and CoO(100) phases are compared revealing that the main line of the CoO(100) phase is much wider than the Co_3O_4(100) phase. Further, the satellite features show larger intensity for CoO compared to the Co_3O_4 phase. Both observations are in agreement with previous XPS studies of Co oxide bulk samples [10] and our previous work on Co_3O_4(111) and CoO(111) thin films grown on Ir(100) [11].

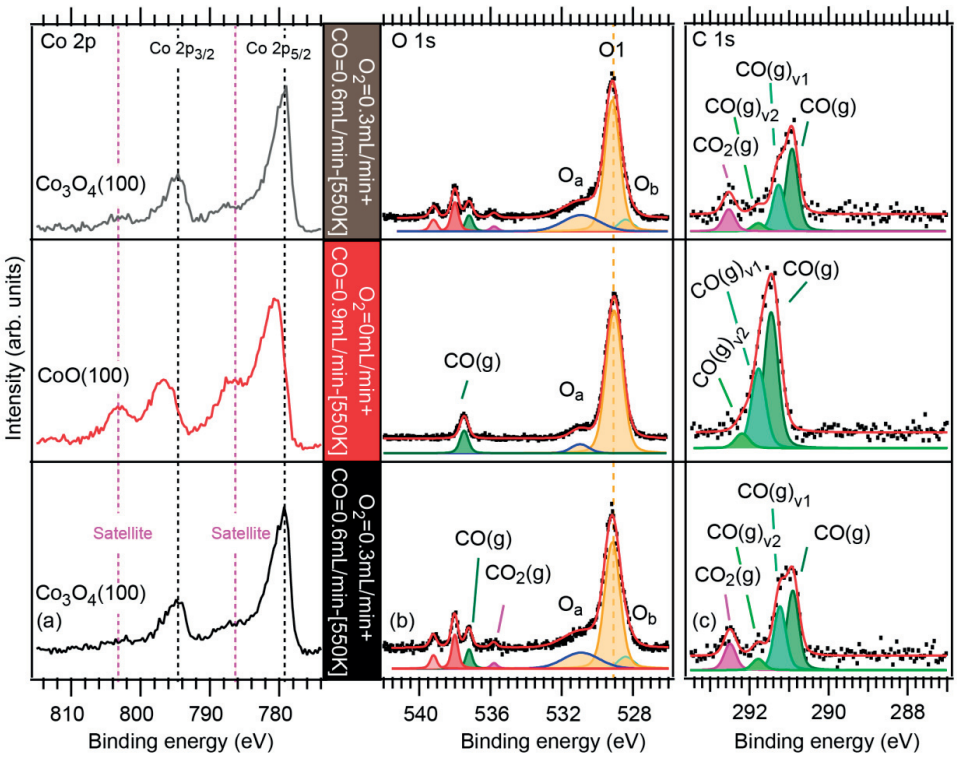

Figure 2: (a) Co 2p, (b) O 1s, and (c) C 1s spectra of the cobalt oxide films grown on Ag(100) exposed to different reactant mixtures.

After briefly characterizing the Co_3O_4(100) and CoO(100) films supported by Ag(100) with LEED, STM, and XPS we exposed the Co_3O_4(100) film to reaction mixtures of CO and O_2 at elevated temperatures. The bottom of figure 2(a) shows the Co 2p spectrum of this surface acquired at 550 K in a 2:1 reaction mixture of CO:O_2 at a total pressure of 1.2 mbar. The low intensity of the satellite features appearing in the Co 2p spectrum is clear evidence for the presence of a Co_3O_4 structured film. In the corresponding O

1s spectrum shown in the lower part of panel (b) the main peak (O1) is observed at 529.2 eV, while two shoulder components are observed at 530.9 eV (O_a) and 528.4 eV (O_b) also consistent with a Co_3O_4 phase [11]. The additional O 1s components located at 539.2 eV (O_2), 538.0 eV (O_2), 537.2 eV (CO), and 535.8 eV (CO_2) originate from gas phase molecules as indicated in the figure. In the corresponding C 1s spectrum in the bottom of panel (c) no surface adsorbates are observed. Only the gas phase CO with the main peak located at 290.9 eV and vibrational components at 291.2 eV and 291.7 eV in addition to the CO_2 gas phase peak located at 292.5 eV are observed. To summarize, the Ag(100) supported Co_3O_4(100) film exposed to the reaction mixture of CO and O_2 at 550 K remains heavily oxidized as the film has all the XPS fingerprints expected for Co_3O_4(100).

In the second step, we changed the gas from a mixture of CO and O_2 to a pure CO gas, while the temperature was maintained at 550 K. XP spectra acquired in the pure CO gas are shown in the middle of figure 2. Compared to the Co 2p spectrum of the Co_3O_4(100) phase measured in a mixture of CO and O_2 the spectrum measured in pure CO shows much higher intensities of the Co 2p satellite features and the O_b component disappeared completely in the O 1s spectrum. These observations are clear evidence that the Co_3O_4(100) film transformed into a CoO(100) film in the pure CO gas. In the gas phase region of the O 1s and C 1s spectra, we observed CO gas phase peaks at 537.6 eV (O 1s) and 291.4 eV (C 1s, main peak). Compared to the binding energies positions observed for gas phase CO above the Co_3O_4(100) phase (537.2 eV and 290.9 eV) phase are shifted by + 0.4 eV (O 1s) and + 0.5 eV (C 1s). These shifts in the gas phase CO peaks we explain by a work function shift between the Co_3O_4(100) and CoO(100) surfaces of 0.5 eV, as the binding energies of gas phase molecules are pinned to the vacuum level which again is determined by the surface work function [12].

In the final step, the reaction gas mixture was changed from pure CO and back to the CO and O_2 mixture. As soon as the reaction gas mixture was changed to the reaction mixture containing O_2 all spectra became identical to the ones observed for the Co_3O_4 phase in the bottom of the figure. The CoO phase is thus oxidized immediately to the Co_3O_4 phase in the $CO:O_2$ mixture.

After demonstrating that it is easy to transform between the CoO and Co_3O_4 phases in reaction mixtures at elevated temperatures, we examine the temperature

dependence of the conversion. The starting point for this work was a CoO(100) film grown on Ag(100). The Co 2p spectrum shown at the bottom of

figure 3(a) was recorded under UHV conditions before high pressure exposure and the shake-up peaks are clear evidence for the CoO(100) phase. The corresponding O 1s shows a single component consistent with the CoO(100) phase, while the corresponding C 1s spectrum shows the absent of any carbon on the surface. After characterizing the CoO(100) film in UHV it was exposed to a reaction mixture consisting of a 1:2 mixture of $CO:O_2$ at a total pressure of 1.2 mbar. Subsequently, the film was heated in 50 K steps from 300 K to 550 K while the evolution of the Co 2p, O 1s, and C 1s regions was followed with HPXPS.

Starting with the Co 2p region, we observe that the intensity of the shake-up peak features of the CoO(100) phase decreased gradually upon heating to 400 K in the reaction mixture. Above 400 K no shake-up features are observed indicating that the film is fully transformed to the Co_3O_4(100) phase at 400 K and above.

In the O 1s spectra, we observe a broad component at 530.9 eV assigned to carbonate species [13] as soon as the film is exposed to the reaction mixture. A maximum intensity of the carbonate component is observed at a temperature of 350 K. Above that temperature the intensity gradually becomes smaller and at a temperature of 500 K the carbonate species are fully removed. The asymmetric tail towards the low binding energy side described by an O_b component and characteristic for the Co_3O_4(100) phase is also observed upon heating the film to 400 K.

In the C 1s spectrum recorded at 300 K in the reaction mixture, two peaks located at 288.7 eV and 291.2 eV are observed. The component found at 288.7 eV we assign to carbonates as its binding energy is close to the value reported for carbonates [13]. The intensity of this component first increases upon heating and reaches a maximum at a temperature of 350 K. With increasing temperature, the intensity of the carbonate components decreases, and at 500 K it fully disappears, consistent with the O 1s data. The complete removal of carbonates at a temperature of 500 K matches well the desorption behavior of carbonates on Ir(100) supported Co_3O_4(111) films studied under UHV conditions [13]. In contrast to the work of Lukashuk *et al.* [5] on supported Co_3O_4 particles that also identified CO or C-OH species and elementary carbon, carbonate is the only surface adsorbate that is identified in our work. The remaining component in the C 1s spectrum located at 291 eV at room temperature is assigned to CO in the gas phase. The observed gradual shift in the gas phase CO component

from 291.3 to 290.8 eV is due to the work function shift between the CoO(100) and the Co_3O_4(100) surfaces of +0.5 eV discussed above. Finally, we observe a CO_2 gas phase peak in the C 1s spectrum recorded at temperatures of 500 and 550 K at a position of 292.4 eV, which suggests CO_2 production on the Co_3O_4(100) phase. CO_2 production was, however, also observed on pure Ag(100) sample at similar gas mixtures, pressures, and temperatures and we are therefore unable to correlate the observed CO_2 production with the presence of the Co_3O_4 phase.

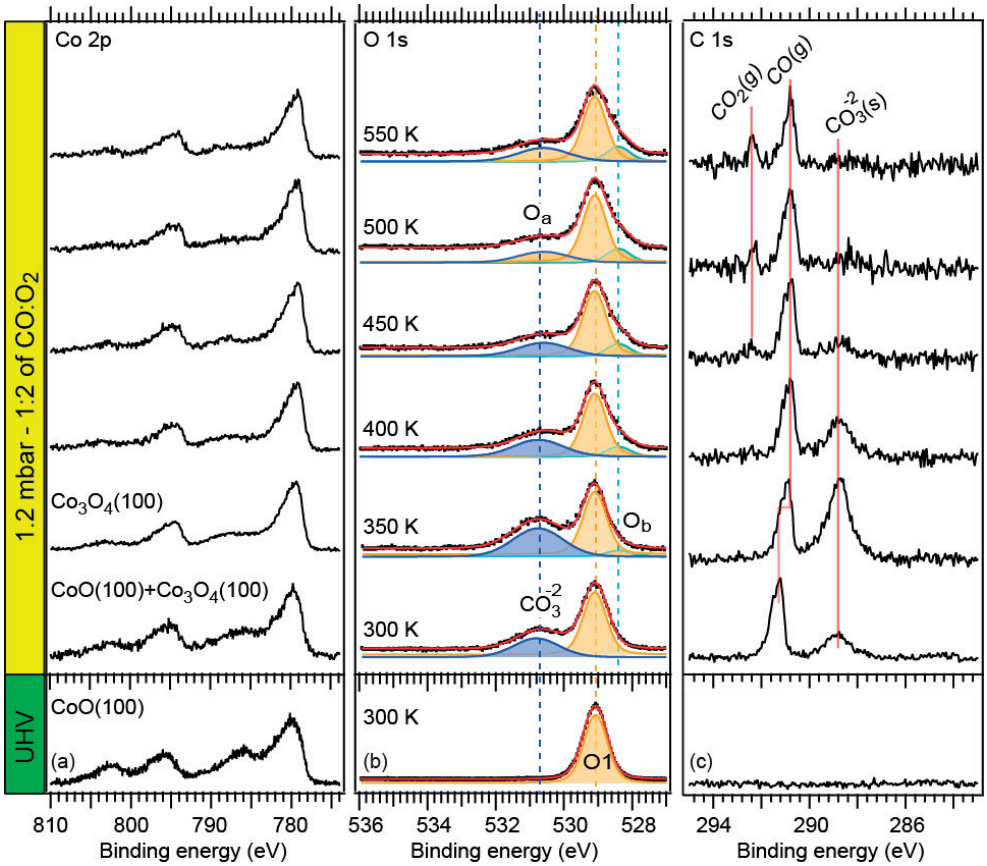

Figure 3: (a) Co 2p, (b) O 1s, and (c) C 1s spectra of Ag(100) supported CoO(100) acquired in UHV at room temperature (bottom) and in 1.2 mbar of a 1:2 $CO:O_2$ mixture at stepwise increasing temperature.

4. Conclusions

To conclude, we have shown that an Ag(100) supported CoO(100) film readily converts to a Co_3O_4(100) film at 550 K in a 1:2 reaction mixture of CO:O_2 at a total pressure of 1.2 mbar. Only upon complete removal of O_2 in the gas mixture, the film is transformed back to the CoO(100) film, while no evidence for metallic Co is observed. Temperature programmed HPXPS measurements revealed that the CoO(100) to Co_3O_4(100) transformation is completed at a temperature of 400 K in the same reaction mixture. The experiments also revealed that carbonate is the only carbon containing species present on the surface in the temperature range between 300 K and 450 K.

Acknowledgement

The authors are grateful for financial support by the Röntgen-Ångström cluster (349-2011-6491) and by the project grant 2012-3850 both financed by the Swedish research council. Financial support from Nordforsk is also gratefully acknowledged. The MAX IV Laboratory personnel are acknowledged for support during measurements.

References

[1] L.R. Merte, J. Knudsen, F.M. Eichhorn, S. Porsgaard, H. Zeuthen, L.C. Grabow, E. Lægsgaard, H. Bluhm, M. Salmeron, M. Mavrikakis, F. Besenbacher, CO-induced embedding of Pt adatoms in a partially reduced FeOx film on Pt(111), J. Am. Chem. Soc. 133 (2011) 10692–10695. http://dx.doi:10.1021/ja2015923.

[2] N. Johansson, L. R. Merte, E. Grånäs, S. Wendt, J. N. Andersen, J. Schnadt, J. Knudsen, Oxidation of Ultrathin FeO(111) Grown on Pt(111): Spectroscopic Evidence for Hydroxylation, Top Catal (2016) 59 506. http://dx.doi:10.1007/s11244-015-0521-7.

[3] F. Ringleb, Y. Fujimori, H.-F. Wang, H. Ariga, E. Carrasco, M. Sterrer, H.-J. Freund, L. Giordano, G. Pacchioni, J. Goniakowski, Interaction of Water with FeO(111)/Pt(111): Environmental Effects and Influence of Oxygen, J. Phys. Chem. C. 115 (2011) 19328–19335. http://dx.doi:10.1021/jp207332n.

[4] A.S. Walton, J. Fester, M. Bajdich, M.A. Arman, J. Osiecki, J. Knudsen, A. Vojvodic, J. V. Lauritsen, Interface controlled oxidation states in layered cobalt oxide nanoislands on gold, ACS Nano. 9 (2015) 2445–2453. http://dx.doi:10.1021/acsnano.5b00158.

[5] L. Lukashuk, K. Föttinger, E. Kolar, C. Rameshan, D. Teschner, M. Hävecker, A. Knop-Gericke, N. Yigit, H. Li, E. McDermott, M. Stöger-Pollach, G. Rupprechter, Operando XAS and NAP-XPS studies of preferential CO oxidation on Co_3O4 and CeO_2-Co_3O_4 catalysts, J. Catal. 344 (2016) 1–15. http://dx.doi:10.1016/j.jcat.2016.09.002.

[6] S. Urpelainen, C. Såthe, W. Grizolli, M. Agåker, A. R. Head, M. Andersson, S.-W. Huang, B. N. Jensen, E. Wallen, H. Tarawneh, R. Sankari, R. Nyholm, M. Lindberg, P. Sjöblom, N. Johansson, B. N. Reinecke, M. A. Arman, L. R. Merte, J. Knudsen, J. Schnadt, J. N. Andersen, F. Hennies, The SPECIES beamline at the MAX IV Laboratory: a facility for soft x-ray RIXS and APXPS, J. Synchrotron Radiat. 24 (2017), https://doi.org/10.1107/S1600577516019056.

[7] J. Schnadt, J. Knudsen, J.N. Andersen, H. Siegbahn, A. Pietzsch, F. Hennies, N. Johansson, N. Mårtensson, G. Öhrwall, S. Bahr, S. Mähl, O. Schaff, The new ambient-pressure X-ray photoelectron spectroscopy instrument at MAX-lab, J. Synchrotron Radiat. 19 (2012) 701–704. http://dx.doi.org/10.1107/S0909049512032700

[8] M. A. Arman, L. Merte, E. Lundgren, J. Knudsen, Co_3O_4(100) films grown on Ag(100): Structure and chemical properties, Accepted for publication in *Surf. Sci.*

[9] M. Gubo, C. Ebensperger, W. Meyer, L. Hammer, K. Heinz, Structural elements in the oxidation process of a single cobalt layer on Ir(100)-(1×1), Phys. Rev. 83 (2011) 1–8. http://dx.doi.org/10.1103/PhysRevB.83.075435

[10] J. Jansson, Low-Temperature CO Oxidation over Co_3O_4/Al_2O_3, J. Catal. 194 (2000) 55–60. http://dx.doi.org/10.1006/jcat.2000.2924

[11] M. A. Arman, P. Ferstl, M. A. Schneider, L. Hammer, E. Lundgren and J. Knudsen Adsorption properties of CO and CO_2 onto CoO(111) and Co_3O_4(111) films studied by core level spectroscopy, In Manuscript.

[12] H. Bluhm, Photoelectron spectroscopy of surfaces under humid conditions, J. Electron Spectros. Relat. Phenomena. 177 (2010) 71–84. http://dx.doi.org/10.1016/j.elspec.2009.08.006

[13] P. Ferstl, S. Mehl, M. A. Arman, M. Schuler, A. Toghan, B. Laszlo, Y. Lykhach, O. Brummel, E. Lundgren, J. Knudsen, L. Hammer, M. A. Schneider, J. Libuda, Adsorption and Activation of CO on Co_3O_4(111) Thin Films, J. Phys. Chem. C. 119 (2015) 16688–16699. http://dx.doi:10.1021/acs.jpcc.5b04145.

Paper VII

Interface Controlled Oxidation States in Layered Cobalt Oxide Nanoislands on Gold

Alex S. Walton,[†] Jakob Fester,[†] Michal Bajdich,[‡] Mohammad A. Arman,[§] Jacek Osiecki,[⊥] Jan Knudsen,[§,⊥] Aleksandra Vojvodic,[‡] and Jeppe V. Lauritsen*[,†]

[†]Interdisciplinary Nanoscience Center (iNANO), Aarhus University, 8000 Aarhus C, Denmark, [‡]SUNCAT Center for Interface Science and Catalysis, SLAC National Accelerator Laboratory, 2575 San Hill Road, Menlo Park, California 94025, United States, [§]Division of Synchrotron Radiation Research, Department of Physics, Lund University, 221 00 Lund, Sweden, and [⊥]MAX IV Laboratory, Lund University, 221 00 Lund, Sweden

ABSTRACT Layered cobalt oxides have been shown to be highly active catalysts for the oxygen evolution reaction (OER; half of the catalytic "water splitting" reaction), particularly when promoted with gold. However, the surface chemistry of cobalt oxides and in particular the nature of the synergistic effect of gold contact are only understood on a rudimentary level, which at present prevents further exploration. We have synthesized a model system of flat, layered cobalt oxide nanoislands supported on a single crystal gold (111) substrate. By using a combination of atom-resolved scanning tunneling microscopy, X-ray photoelectron and absorption spectroscopies and density functional theory calculations, we provide a detailed analysis of the relationship between the atomic-scale structure of the nanoislands, Co oxidation states and substrate induced charge transfer effects in response to the synthesis oxygen pressure. We reveal that conversion from Co^{2+} to Co^{3+} can occur by a facile incorporation of oxygen at the interface between the nanoisland and gold, changing the islands from a Co−O bilayer to an O−Co−O trilayer. The O−Co−O trilayer islands have the structure of a single layer of β-CoOOH, proposed to be the active phase for the OER, making this system a valuable model in understanding of the active sites for OER. The Co oxides adopt related island morphologies without significant structural reorganization, and our results directly demonstrate that nanosized Co oxide islands have a much higher structural flexibility than could be predicted from bulk properties. Furthermore, it is clear that the gold/nanoparticle interface has a profound effect on the structure of the nanoislands, suggesting a possible promotion mechanism.

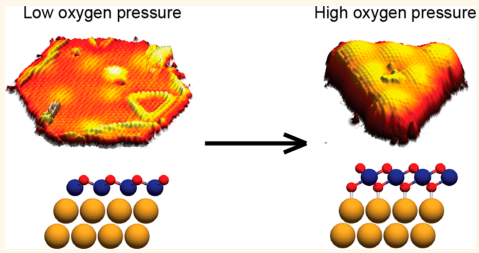

KEYWORDS: water splitting · electrocatalysis · nanocatalysis · cobalt oxide · two-dimensional materials · reducible metal oxides

Electrochemical water splitting is a highly promising new technology for the production of clean, renewable fuel. However, in order to be commercially viable, efficient catalysts are needed for the two half reactions: oxygen evolution (OER) and hydrogen evolution. The OER is a particular challenge, with few materials showing significant activity for this reaction, the majority of which are noble metal oxides. Cobalt oxide is one of the few non-noble metal oxides which shows significant catalytic activity for water oxidation in alkaline solution.[1,2] A key barrier to development of better OER catalysts is a lack of understanding of the surface chemistry of the active phase for OER. Cobalt can form several oxides, containing different formal cobalt valencies and coordinations, leading to large differences in activity. In previous reports of OER, the starting material is often the spinel Co_3O_4 phase, displaying complex surfaces exposing tetrahedrally coordinated Co^{2+} and octahedrally coordinated Co^{3+} species. However, it has been recently revealed that the active phase in electrochemical water oxidation is in fact so-called β-CoOOH, consisting of O−Co−O layers with intercalated hydrogen, where the edges are the active sites for the OER.[3−6] Creating model systems which mimic the properties of this phase and using these models to search for the active sites of these materials is crucial for the rational design of cobalt oxide OER catalysts. It has also been reported that there are synergistic effects

* Address correspondence to jvang@inano.au.dk.

Received for review July 29, 2014 and accepted February 18, 2015.

Published online February 18, 2015
10.1021/acsnano.5b00158

between gold and cobalt oxide, with the presence of a gold/cobalt oxide interface greatly enhancing OER activity;[5,7] however, no consensus has been reached on a mechanism for this effect. Furthermore, the detailed structure of cobalt oxide particles on the nanoscale is known to influence activity, but the role of nanoparticle edges and atomic defects, which often control catalytic activity, have also not been explored.

In this study, we synthesized cobalt oxide nanoislands on a single crystal surface, Au(111), by physical vapor deposition of cobalt in an oxygen environment and subsequent annealing in the same environment. This method allowed us to systematically investigate the structure and composition of the nanoislands as a function of oxygen pressure and temperature using a powerful combination of scanning tunneling microscopy (STM) (for direct, real space imaging of the structure) and X-ray photoelectron and absorption spectroscopies (XPS and XAS) (providing information about the composition, oxidation states and surface chemistry of the nanoislands). To further our understanding at the atomic level, thin films of cobalt oxide supported on Au(111) were modeled using density functional theory (DFT).

Gold was chosen as substrate here so that we could explore the synergistic Au/cobalt oxide interaction and its implications for the catalytic behavior of the resultant nanoislands. Gold is also an excellent substrate for model catalyst studies as (non-nanostructured) gold is catalytically inert, allowing the catalytic properties of the islands and the gold/island interface to be easily determined in future studies. The (111) surface was chosen as the "herringbone" reconstruction facilitates the creation of well-dispersed nanoislands by providing a regular array of nucleation sites for Co.[8,9] Thin films of cobalt oxide on Ir(100) crystals have been extensively studied,[10−12] cobalt oxide has also been investigated on Pd(100)[13] and Pt(111)[14] and there have been some investigations into cobalt oxide on Au(111),[15−17] but to date no analysis of atomic-scale structure of cobalt oxide nanoislands as a function of oxygen pressure has been carried out.

The key finding from our work is that the synthesized Co oxide islands on gold are remarkably structurally flexible during an increase in the formal oxidation state from Co^{2+} to Co^{3+}. As the synthesis oxygen pressure is increased, the structure of the islands changes from a Co−O bilayer with 2+ cobalt to an O−Co−O trilayer with 3+ cobalt, the same structure as a single layer of β-CoOOH. We propose that this structure is stabilized due to charge transfer from the gold to the nanoislands. We propose this will be of great interest as a model system in the search for the active sites of cobalt oxide-based OER catalysts.

RESULTS AND DISCUSSION

Our synthesis procedure consisted of electron beam evaporation of cobalt onto the Au(111) surface in an oxygen environment and a postanneal of the crystal in the same oxygen pressure. We have explored the synthesis procedure for different postanneal temperatures and oxygen pressures. The best synthesis procedure was found for a postanneal temperature fixed at 523 K, and all syntheses at this temperature produced well-dispersed, crystalline nanoislands of cobalt oxide located on the terraces of the Au(111) surface. Postanneal temperatures lower than 473 K were observed to be insufficient to produce crystalline nanoislands and those above 673 K caused coalescence of the nanoislands into large, poorly crystalline structures. Between these two temperatures, there was no obvious temperature dependence on the nanoisland morphology. In contrast, the oxygen pressure during synthesis had a dramatic effect on the nanoisland morphology, with abrupt structural changes observed within a narrow range of oxygen partial pressures. The strongest effect is seen between two pressure regimes, "low" oxygen pressure (1×10^{-6} mbar) and "high" oxygen pressure (1×10^{-5} mbar).

Low Oxygen Pressure: Stoichiometric CoO Islands. At the low oxygen pressure (1×10^{-6} mbar), the surface is covered with atomically flat, 5−10 nm wide nanoislands with two distinct apparent heights (1.7 ± 0.2 Å or 4.0 ± 0.2 Å) and appearances (Figure 1a). Hereafter these will be referred to as Type A and Type B islands, respectively. Both nanoisland types show a truncated hexagonal morphology. Figure 1b,c show atomic resolution STM images of both types of nanoisland and reveal that the surface atoms are arranged in a regular lattice with hexagonal symmetry. As both stable bulk phases of cobalt oxide (CoO and Co_3O_4) have a cubic unit cell, the hexagonal packing of the surface atoms is only compatible with a (111) surface. Measurements of the interatomic spacing on both types of islands show a periodicity of 3.3 ± 0.1 Å with no significant distortion within the basal plane and no dependence on the crystallographic orientation. This surface periodicity is inconsistent with a spinel Co_3O_4(111) surface. The Co_3O_4(111) surface can display a variety of terminations, but only one of the bulk truncated surfaces results in a regular hexagonal periodicity, the Co^{2+} terminated surface. However, the periodicity of the Co^{2+} surface is 5.7 Å,[18] far larger than our observed periodicity. The other spinel surfaces display a kagome lattice structure (Co^{3+} terminated) or a significantly distorted hexagonal structure (O terminated).[19] The observed surface periodicity is closer to the expected spacing for the rocksalt CoO(111) surface, which displays a regular hexagonal lattice with a 3.02 Å periodicity in the close packed directions. Moreover, the difference in apparent heights between the two particle types is 2.3 ± 0.2 Å which is similar to the repeat unit distance between (111) layers in rocksalt CoO(111), 2.46 Å, but far too small for Co_3O_4(111) (4.67 Å).[18] At this point it is

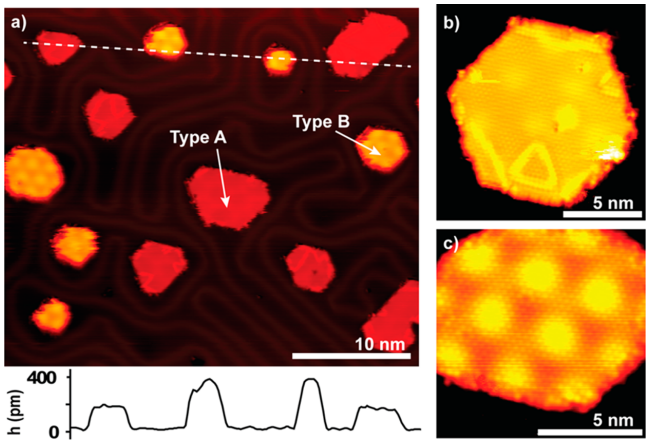

Figure 1. Cobalt oxide nanoislands on Au(111) synthesized at 1×10^{-6} mbar oxygen pressure. (a) Large scale STM image showing distribution and morphology of Type A and Type B nanoislands and different nanoisland types ($V = -558$ mV, $I = 0.36$ nA). Graph shows an apparent height profile along the dotted line. (b) Zoomed-in atom-resolved STM image of a Type A nanoisland ($V = -386$ mV, $I = 0.50$ nA). (c) Zoomed-in atom-resolved STM image of a Type B nanoisland ($V = -174$ mV, $I = 0.70$ nA).

important to emphasize that care should be used when using apparent heights of features measured in STM as the STM image is a convolution of topographic and electronic effects.[20] When measuring the height difference between two dissimilar materials (Au and cobalt oxide in this case) significant deviations from real heights can be observed. However, the height difference between the two types of nanoisland (as they are both cobalt oxide) should be less strongly affected by electronic contributions and therefore closer to a real height difference. It was found that the apparent height of the nanoislands was essentially bias independent at biases < -750 mV, and all reported apparent height measurements were taken in this bias independent regime. Previous STM investigations of thick Co_3O_4 films demonstrate a 5.7 Å in plane periodicity and a 4.67 Å minimum step height.[18] We therefore conclude that the Type A and B structures are single and double layer CoO(111)-like islands, respectively, although with a significant relaxation of the surface in-plane atomic spacing.

A striking feature common to both types of nanoisland is a regular array of diffuse protrusions with the same hexagonal symmetry as the surface atoms (see Figure 1b,c) but much longer range periodicity. This is a moiré pattern formed from overlaying and/or rotating two dissimilar lattices, seen on many other heteroepitaxial films.[11,12,21,22] It differs between the two particle types. In the Type A islands, it has a periodicity of $\lambda_{typeA} = 37 \pm 2$ Å and displays a slight rotation with respect to the atomic lattice of $\theta_{typeA} = 8 \pm 2°$. The moiré corrugation is weak and only just visible over the corrugation due to the surface atoms (0.11 ± 0.02 Å). In the Type B the moiré periodicity is shorter, ($\lambda_{typeB} = 31 \pm 2$ Å) and no rotation is observed between the moiré pattern and the atomic lattice $\theta_{typeB} = 0°$. Here, the moiré corrugation is much stronger (0.28 ± 0.03 Å). The reduction in moiré periodicity between Type A and B islands could reflect a slight expansion of the in-plane lattice constant between Type A and B which our measurements are not precise enough to detect.

Expansion of the in-plane lattice constant of ultrathin heteroepitaxial oxide films relative to bulk values is a commonly observed phenomenon, occurring with, for example, FeO, CoO and ZnO on various substrates.[14,23,24] A common interpretation is that this reduces the surface dipole by moving the oppositely charged metal and oxygen layers closer together, necessitating an in-plane expansion. It should be mentioned that nanoscale cobalt oxide can also adopt the wurtzite crystal structure[25] and that thicker rocksalt CoO films are found to be terminated with a pseudomorphic wurtzite layer.[26] This is also believed to compensate surface polarity as the Co−O spacing can be much closer in wurtzite than in rocksalt.[14]

Taking into account the observations regarding the apparent height and interatomic periodicity of the top layer for the Type A and B islands, we propose the following model for the islands' structure: the Type A consist of one bilayer (*i.e.*, one Co−O unit) of rocksalt CoO(111) with a significantly expanded lattice constant of 3.3 ± 0.1 Å. The Type B are higher and therefore are interpreted as double bilayer islands (two Co−O units). The change in moiré periodicity and apparent moiré corrugation are indicators of both structural and electronic changes within the island, so we propose that the thicker Type B films are in fact wurtzite rather than rocksalt structure (with tetrahedral cobalt coordination rather than octahedral) in accordance with recent observations of two-layer CoO on both Pt(111) and Ir(001).[14,27] Ball

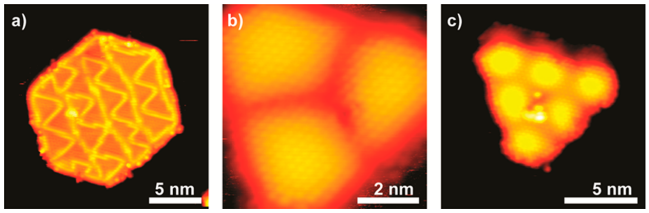

Figure 2. Cobalt oxide nanoislands synthesized at 1×10^{-5} mbar oxygen pressure. (a) High defect density Type A particle (−508 mV 0.41 nA). (b,c) Type C islands in atomic resolution (−321 mV, 0.53 nA, −691 mV, 0.40 nA).

models of the proposed Type A and B structures are shown in Figure 3a,b. Detailed first-principle calculations of these and additional structures are performed to test our hypothesis, see discussion below.

A further noteworthy difference between the two particle types is that Type A nanoislands also possess a low density of linear features (Figure 1b) not seen in the Type B islands. We interpret these as oxygen adatom line dislocations as observed in FeO ultrathin films, which form as a result of an additional strain release mechanism.[28] The structure and dynamics of the line dislocations will be discussed in detail in a forthcoming publication.

High Oxygen Pressure: Oxygen Rich Islands. Increasing the oxygen pressure during synthesis to 1×10^{-5} mbar caused large changes in the resultant islands which restructure in order to accommodate more oxygen. Type A nanoislands with a high density of linear features were still present in small numbers (Figure 2a), but a third distinct nanoisland morphology is now the majority structure present (Type C, see Figure 2b,c). The Type C islands had an apparent height in between that of the Type A and B islands of 2.9 ± 0.2 Å. There were also a small number of islands with the same morphology as Type C but a significantly larger apparent height of 5 ± 0.2 Å. The surface of the Type C islands was extremely corrugated, even more so than the Type B islands (0.59 ± 0.07 Å). The interatomic spacing was the same as the Type A and B nanoislands (3.3 ± 0.1 Å). The moiré corrugation was less regular than in the Type A and B islands, often appearing distorted, particularly in smaller islands, but had the same periodicity and rotation as the Type B nanoislands. Similar cobalt oxide structures were recently observed on Au(111) and proposed to be spinel Co_3O_4.[17] However, as our atom-resolved images reveal the Type C islands have the same interatomic periodicity and symmetry as the Type A and B structures, they are incompatible with any surface of spinel Co_3O_4 as discussed earlier.

Instead, these islands closely resemble structures that have been observed at high oxygen pressure in FeO films on Pt and Pd(111)[28,29] which also show extremely strong moiré corrugation. In these works, such structures were explained as FeO_2 trilayers, *i.e.*, an extra layer of oxygen exists between the support and the Fe layer. Given the similarities between Fe and Co oxides and the increase in oxygen chemical potential, we propose that the Type C nanoislands consist of a O−Co−O trilayer with the rocksalt structure. The higher islands observed are therefore interpreted as an O−Co−O trilayer with an extra bilayer of Co−O on top (analogous to the Type B structures observed at lower pressures). The effect of increased oxygen chemical potential is therefore the incorporation of an extra layer of oxygen atoms between the Au and the first cobalt layer of the nanoislands, which increases the nominal oxidation state of Co with almost no structural change to the islands. Figure 3c shows a cross-sectional ball model of the proposed Type C island structure. In previous reports of the formation of FeO_2, very high chemical potential of oxygen is required, either by using atomic oxygen[28] or very high oxygen pressures in the mbar regime.[29] Our CoO_2 trilayer islands form at a much lower pressure. This could suggest that oxygen intercalation is much easier than in the FeO/Pt system.

DFT Simulations of Ultrathin Cobalt Oxide Layers on Au. We performed density functional theory (DFT) simulations to elucidate the atomic structure of the different experimentally observed supported CoO_x nanoislands under different oxygen pressure. Surface structural models of the nanoislands were constructed as infinite thin CoO_x films on-top of three layers of Au(111), using the equilibrium lattice constant of Au (a_{lat} = 4.157 Å, see also Supporting Information). These structural models are used as a first order approximation of the nanoislands as they are able to capture the stability order between overlayers with different structures, various Co to O stackings and Co−O bonding coordination, different terminations and CoO_x/Au interfaces. Figure 3 shows the structural models, some of which are proposed based on experimental findings as discussed above. The different considered films consisted of 1 ML of rock-salt (RS) CoO (Type A) (a), 2 ML of wurtzite (WZ) CoO (Type B) (b) and 1 ML of RS CoO_2 (Type C) (c) with extra oxygen layer compared to (a). Additionally, we have also tested the stability of 2 ML spinel Co_3O_4 structures, interfaced to gold *via* either Co (d) or *via* oxygen (e) as well as the stability of 1 ML Co_2O_3 in a k-phase arrangement (f).[30] The proposed structures reflect both types of metal−oxygen bonding: purely octahedral (a) and (c), and purely tetrahedral type (b). The spinel type structures (d) and (e) have both types of bonding.

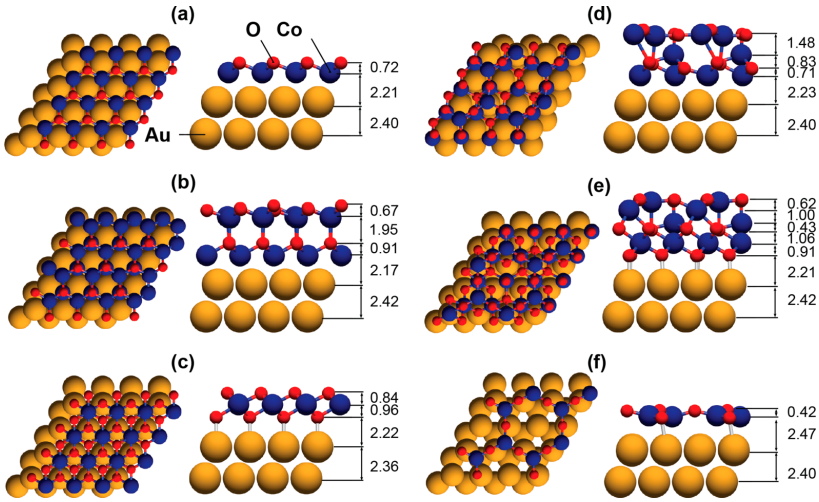

Figure 3. Atomic representation of different CoO_x films adsorbed on the Au(111) surface. (a) Type A structure with 1 ML of RS CoO. (b) Type B structure with 2 ML of WZ CoO. (c) Type C structure with CoO_2 stoichiometry. (d) 2 ML of spinel Co_3O_4. (e) Same as (d) but with extra oxygen layer near Au. (f) 1 ML of Co_2O_3 in a k-phase arrangement.[30] The labels indicate distances in Å.

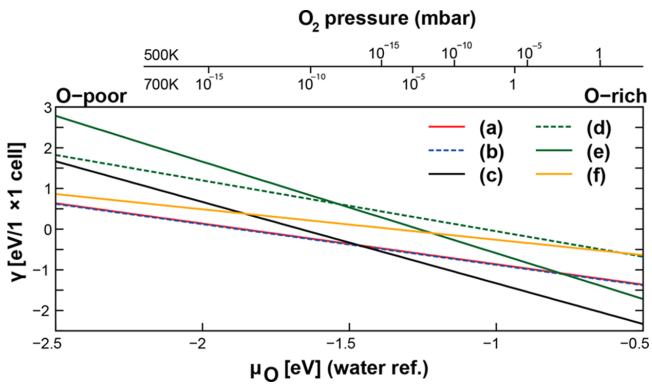

Figure 4. Surface stability per 1 × 1 unit cell of different CoO_x films on the Au(111) surface (A = 7.49 Å^2) as a function of the chemical potential of oxygen. The corresponding structures are shown in Figure 3. The pressure scales for T = 500 K and T = 700 K were constructed according to ref 31.

The cobalt oxide films were adapted to fit the 2 × 2 hexagonal cell of the Au(111) surfaces; *i.e.*, the films are strained to fit the gold support. This allows for determination of the oxide film stability, however, it is not able to capture the moiré pattern as this requires a larger super cell approach. Several possibilities of adsorption of the films on top of the Au surface were investigated. The Co-terminated films prefer adsorption on Au-hollow sites, while oxygen terminated films layer adsorb on top of the Au surface metal atoms. The optimized film structures with indicated layer spacings are shown in Figure 3. Adjusted for the covalent radius of Au (1.34 Å), the heights of the optimized structures are 1.59, 4.36 and 2.68 Å for (a), (b) and (c) structures. This compares very favorably with observed heights of Type A, B and C nanoislands, measured as 1.70 ± 0.2 Å, 4.0 ± 0.2 Å and 2.9 ± 0.2 Å.

The calculated surface stabilities γ (eq 1) of the cobalt oxides films are shown in Figure 4. We find that the Type A and B structures are nearly degenerate and are the most stable structures at low oxygen pressures. At higher oxygen pressures, a more oxidized Type C surface structure is the most stable structure. Depending on the temperature, the calculated structure transition occurs at 10^{-16} to 10^{-6} mbar of oxygen for 500 to 700 K. Lastly, we also test for the stability of 2 ML spinel type structures and Co_2O_3. However, neither of the investigated spinel structures, (d) or (e), nor the Co_2O_3 (f) are stable at the conditions probed by the experiment. The above computationally obtained picture

TABLE 1. Bader Charge and Magnetic Moment Contributions to Co, Au and O Atoms in the Three Most Stable Structures: Type A, B and C

	Co		Au (top layer)	O (near Au)
	Bader charge	mag mom [μ_B]	Bader charge	Bader charge
Type A (AFM)	+1.14	|1.74|	−0.18	–
Type B (AFM)	+1.32 (top) +1.06 (bottom)	|2.11| (top) |2.04| (bottom)	−0.22	–
Type C (FM)	+1.51	0.42	+0.20	−0.92
O−Co−O (no Au)	+1.57	0.80	–	−0.79
Au(111)	–	–	−0.02	–

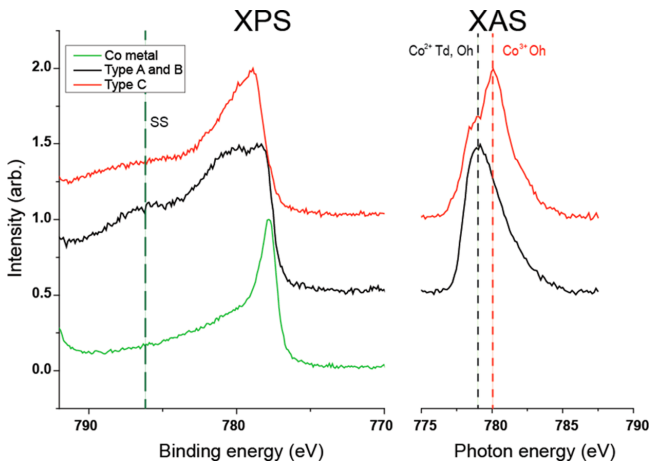

Figure 5. XPS and XAS spectra of the Co $2p_{3/2}$ peak of cobalt oxide nanoislands synthesized at different oxygen pressures. "SS" indicates the position of the shakeup satellite. "Co^{2+} Td,Oh" and "Co^{3+} Oh" indicates the peaks corresponding to tetrahedrally/octahedrally coordinated Co^{2+} and octahedrally coordinated Co^{3+} respectively.

is consistent with our experimental observations of coexistence of Type A and B nanoislands at low oxygen pressure conditions ($p < 10^{-6}$ mbar, $T = 573$ K) and appearance of Type C nanoislands at higher oxygen pressures ($p > 10^{-5}$ mbar, $T = 573$ K).

The obtained magnetic structures reflect the apparent oxidation states of each system and are listed in Table 1. The (a) and (b) structures have high spin magnetic moment [(a): ~1.7 μ_B per Co site, (b): ~2.1 μ_B per Co site] and AFM ordering within layers, which is consistent with cobalt in the 2+ oxidation state (for plots of density of states refer to Figure S2 of the Supporting Information). The Au atoms in contact with Co act as weak electron acceptors in the two cases. The more oxidized (c) structure consists of Co sites with lower magnetic moments (~0.4 μ_B per Co-site) in a FM ordering, which more closely resembles a Co^{3+} character. Contrary to (a) and (b) structures, the charge from Co and Au is transferred toward the intercalating oxygen atoms, with the net result of a small positive charge for the uppermost Au layer. Both spinel structures [(d) and (e)] have metal sites in high magnetic moments (~2 μ_B per Co site) with the only exception being the octahedrally coordinated Co-sites near the Au interface (e), that show Co-sites with lower magnetic moment (~0.3 μ_B per Co-site) consistent with a Co^{3+} character.

XPS and XAS Measurements of Co Valency. The cobalt oxidation states predicted by DFT were tested by XPS and XAS spectra acquired on three samples, a mixed A/B synthesis (1×10^{-6} mbar synthesis O_2 pressure), a Type C synthesis (1×10^{-5} mbar synthesis O_2 pressure) and a control of cobalt metal evaporated in UHV conditions (Figure 5). Both the cobalt oxide syntheses show a significant shift to higher binding energies from the cobalt metal peak, confirming that oxidation is complete in both synthesis and no metallic-character cobalt remains. The Type A/B synthesis gave rise to a strong satellite peak and broad main peak in the XPS spectrum and a single peak at low photon energy in the XAS. The Type C synthesis showed much weaker satellite peaks, a narrower main peak and the appearance of a higher energy peak in the XAS spectrum.

The satellite peak and the broad main peak observed in the XPS spectrum of the Type A/B synthesis are indicative of a paramagnetic (high spin) cobalt

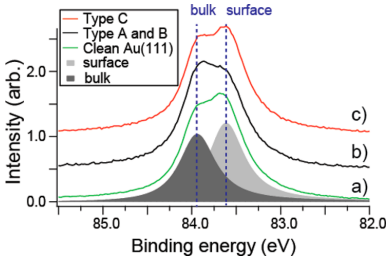

Figure 6. Au $4f_{7/2}$ spectra taken at $h\nu$ = 110 eV on (a) a clean Au(111) surface, (b) Type A and B cobalt oxide islands on Au(111) and (c) Type C cobalt oxide islands on Au(111).

species, as the unpaired electrons in the d shell of the cobalt give rise to shakeup excitations (causing the satellite peak) and multiplet splitting of the main peak.[32,33] Conversely, for the Type C synthesis, the XPS spectrum of the Type C synthesis shows strongly suppressed shakeup structure and a narrower main peak suggesting a low spin species. This is fully consistent with the DFT predictions of cobalt valency for the A,B and C structures, with the Type A/B synthesis consisting of high spin Co^{2+} species and the Type C synthesis of low spin Co^{3+}. These spectra are also consistent with bulk reference data, with the spectrum from the Type A/B synthesis qualitatively resembling high spin CoO and the Type C resembling reference data for Co_3O_4 (which is predominantly low spin Co^{3+}) and CoOOH (which is entirely low spin Co^{3+}).[32,33]

XAS spectra are also very sensitive to cobalt valency and coordination and can be used to discriminate between different cobalt oxides.[34,35] Tetrahedral and octahedral Co^{2+} give a broad peak at low photon energy, whereas octahedral Co^{3+} gives rise to a narrower peak at a significantly higher energy (a shift of 2.5 eV). The appearance of a higher energy peak in the XAS spectrum for the Type C synthesis is therefore consistent with the emergence of octahedral Co^{3+} species. The continued presence of a small Co^{2+} peak in this spectrum is attributed to the small amount of Type A islands present at the this pressure and the small number of high Type C islands with an extra layer of Co−O (while the lower cobalt layer is 3+, the upper layer will be in the 2+ state as for Types A and B).

Figure 6 shows Au $4f_{7/2}$ XPS spectra recorded at a photon energy of 110 eV, resulting in a very high surface sensitivity. On the clean Au (111) surface, the peak can be deconvoluted into two components corresponding to the contributions from the surface gold atoms and the bulk gold atoms (Figure 6a). The binding energy shift in the surface component is due to undercoordination of the surface atoms relative to the bulk.[36] When a Type A/B synthesis is made on a gold surface (Figure 6b), a strong reduction in the intensity of the surface component is seen relative to the clean surface. This loss of the surface component implies a strong interaction between the islands and the gold surface, as the surface gold atoms underneath the islands have increased their coordination and become "bulk-like". However, if a Type C synthesis is made on the gold (at the same coverage), no loss of surface component is observed (Figure 6c). This points to a clear structural difference in the islands, as now the underlying gold is not strongly interacting with the islands, and retains its "surface-like" character. The addition of an oxygen layer underneath the cobalt in the islands would explain this change in interaction strength—as this extra oxygen is likely to bind much more strongly to the cobalt and only weakly interact with the gold.

CONCLUSIONS

In summary, we demonstrate based on a combination of experimental and computational findings that the gold/nanoisland interface is central in defining the properties of the cobalt oxide nanoislands. Three distinct types of cobalt oxide nanoislands are observed, two under an oxygen-poor and one under an oxygen-rich environment. For the latter charge transfer from the metal substrate and a change in cobalt valency from 2+ to 3+ stabilizes an extra oxygen layer at the metal/island interface, as has been observed for ultrathin oxides on other metal supports (for example FeO on Pt[28] and CoO on Ir(100)[37]). The degree of charge transfer stabilization is dependent on both the metal support and the oxide chosen and has important implications for the structure's reactivity. In the case of cobalt oxide on gold, it offers a potential explanation for the promotional effect of Au on cobalt oxide catalysts, namely the stabilization of highly active oxygen at the Au/Co oxide interface. In addition, the system of supported ultrathin cobalt oxide nanoislands could be of interest as a catalyst in its own right as part of an emerging new class of catalytic materials, as has been demonstrated for other ultrathin film systems.[28,29,38,39] Finally, we emphasize that the Type C island's structure is identical to that of a single layer of β-CoOOH, reported as the active phase for electrochemical water oxidation[3,4] (*i.e.*, an O−Co−O trilayer), and as such, the study of water's interaction with this structure could yield valuable insight into the nature of the active sites of this important catalytic material.

METHODS

Clean and flat Au(111) surfaces were obtained by cycles of Ar ion sputtering and subsequent annealing. Submonolayer amounts of cobalt were deposited onto the crystal using an electron beam evaporator. The crystal was held at a slightly elevated temperature of 380 K during deposition. For STM

analysis, the same evaporation conditions were used, resulting in a coverage of ~15% ML cobalt oxide. To increase signal-to-noise ratio in XPS analysis, the cobalt coverage was increased such that ~30% ML cobalt oxide was formed (kept constant for all XPS measurements). Deposition of Co was done in an oxygen environment and the sample was subsequently postannealed at 573 K in the same oxygen environment for 15 min. The oxygen pressure at the sample was varied between $1 \times 10^{-6} - 1 \times 10^{-5}$ mbar.

All analysis was performed under UHV conditions (10^{-10} mbar or better). STM analysis was performed in UHV using a home-built "Aarhus" type STM capable of high speed, atomic-resolution imaging on a routine basis.[40] XPS and XAS analysis was carried out at the I311 beamline at the MAX IV Laboratory.[41] All spectra were recorded at normal emission and photon energies of 110 and 1000 eV were used for acquisition of the Au 4f and Co 2p spectra, respectively. All spectra are calibrated to the Fermi edge and a polynomial background was removed. The Co 2p XAS experiments were performed in Auger yield mode and the photon energy scale was calibrated by recording Au 4f in half and second order mode.

Density functional theory (DFT) calculations have been performed within the Vienna ab initio simulation package[42,43] (VASP) using the projector augmented wave (PAW) potentials.[44] Similar to the study of CoO(111) on Ir(100),[11] we adapted the Perdew–Burke–Ernzerhof[45] (PBE) exchange-correlation functional together with the Hubbard-U approach of Dudarev[46] with a fixed value of $U - J = U_{eff} = 1$ eV for the localized *d*-electrons of the Co atoms (DFT+U). This value of U_{eff} was shown to be the best compromise between an accurate description of structural and electronic properties (see also SI for additional electronic description). In all calculations, we have employed a 400 eV energy cutoff, 1600 eV density cutoff, and $8 \times 8 \times 8$ Monkhorst–Pack type *k*-point mesh for a $(1 \times 1 \times 1)$ bulk unit cell and a $4 \times 4 \times 1$ gamma centered *k*-point mesh for the (2×2) surfaces. The CoO structures were placed on-top of three layers of Au(111) of which the bottom two layers were fixed at bulk equilibrium positions, and 16 Å of vacuum was used to separate the Au layers. The structures were relaxed with the maximum force threshold of 0.05 eV/Å subject to small dipole corrections.

To model the stability of the films under different synthesis and operating conditions, we compared the relative thermodynamic surface stability of these structures by calculating the surface free energy γ per single surface area *A* as

$$\gamma = (G_{Co_xO_y/Au(111)} - G_{Au(111)} - N_{CoO}\mu_{CoO} - N_{Co}\mu_{Co} - N_O\mu_O)/A \quad (1)$$

where $G_{Co_xO_y/Au(111)}$ and $G_{Au(111)}$ are free energies of the slabs with and without cobalt oxide on top of Au(111) with subtracted energy contributions of N_{CoO} complete CoO bulk units and remaining N_{Co} of cobalt and N_O of oxygen surface atoms of the slab. This approach allows for comparison of structures of different thickness and stoichiometry. The free energies of the slabs are approximated by their total energies and the chemical potentials, μ_{CoO} and μ_{Co}, are referenced to total energies of the most stable bulk phases, which were found to be bulk RS CoO ($\mu_{CoO} = E_{CoO}^{total}$) and that of metallic bulk Co ($\mu_{Co} = E_{Co}^{total}$) (see also Supporting Information). The chemical potential of oxygen, for any given temperature *T* and pressure *p*, is bounded by the formation energy of bulk RS CoO (oxygen poor) and half of the total energy of an O_2 molecule (oxygen rich) as $E_{CoO}^{free} < \mu_O(p,T) - 1/2E_{O_2}^{total} < 0$. Because of the well-known inaccuracy of $E_{O_2}^{total}$ within our PBE-DFT approach, higher accuracy is achieved by referencing $E_{O_2}^{total}$ relative to 2×1.23 eV thermodynamic equilibrium of water and hydrogen gas as $E_{O_2}^{total} = E_{H_2O}^{total} - E_{H_2}^{total} - 2.506$ eV, which also includes ZPE corrections.[47] Lastly, for a fixed temperature, the correspondence between oxygen chemical potential and oxygen pressure is established following the procedure of Reuter and Scheffler.[31]

Conflict of Interest: The authors declare no competing financial interest.

Acknowledgment. The iNANO group acknowledges support from the Lundbeck Foundation and the European Research Council (ERC Grant no. 239834 (OxideSynergy)). We also acknowledge the Nordforsk network "An interdisciplinary approach to atomistic design of new catalysts" and COST Action CM1104 "Reducible metal oxides". Support from the U.S. Department of Energy Office of Basic Energy Science to the SUNCAT Center for Interface Science and Catalysis is gratefully acknowledged.

Supporting Information Available: Further details of computational methodology and projected density of states for bulk CoO and the three experimentally observed structures (Types A, B and C). This material is available free of charge *via* the Internet at http://pubs.acs.org.

REFERENCES AND NOTES

1. Liao, L.; Zhang, Q.; Su, Z.; Zhao, Z.; Wang, Y.; Li, Y.; Lu, X.; Wei, D.; Feng, G.; Yu, Q.; *et al.* Efficient Solar Water-Splitting Using a Nanocrystalline CoO Photocatalyst. *Nat. Nanotechnol.* **2014**, *9*, 69–73.
2. Rosen, J.; Hutchings, G. S.; Jiao, F. Ordered Mesoporous Cobalt Oxide as Highly Efficient Oxygen Evolution Catalyst. *J. Am. Chem. Soc.* **2013**, *135*, 4516.
3. Bajdich, M.; García-Mota, M.; Vojvodic, A.; Nørskov, J. K.; Bell, A. T. Theoretical Investigation of the Activity of Cobalt Oxides for the Electrochemical Oxidation of Water. *J. Am. Chem. Soc.* **2013**, *135*, 13521–13530.
4. Friebel, D.; Bajdich, M.; Yeo, B. S.; Louie, M. W.; Miller, D. J.; Sanchez Casalongue, H.; Mbuga, F.; Weng, T.-C.; Nordlund, D.; Sokaras, D.; *et al.* On the Chemical State of Co Oxide Electrocatalysts During Alkaline Water Splitting. *Phys. Chem. Chem. Phys.* **2013**, *15*, 17460–17467.
5. Yeo, B. S.; Bell, A. T. Enhanced Activity of Gold-Supported Cobalt Oxide for the Electrochemical Evolution of Oxygen. *J. Am. Chem. Soc.* **2011**, *133*, 5587–5593.
6. Song, F.; Hu, X. Exfoliation of Layered Double Hydroxides for Enhanced Oxygen Evolution Catalysis. *Nat. Commun.* **2014**, *5*, 4477.
7. Gorlin, Y.; Chung, C.-J.; Benck, J. D.; Nordlund, D.; Seitz, L.; Weng, T.-C.; Sokaras, D.; Clemens, B. M.; Jaramillo, T. F. Understanding Interactions between Manganese Oxide and Gold That Lead to Enhanced Activity for Electrocatalytic Water Oxidation. *J. Am. Chem. Soc.* **2014**, *136*, 4920–4926.
8. Helveg, S.; Lauritsen, J. V.; Lægsgaard, E.; Stensgaard, I.; Nørskov, J. K.; Clausen, B. S.; Topsøe, H.; Besenbacher, F. Atomic-Scale Structure of Single-Layer MoS_2 Nanoclusters. *Phys. Rev. Lett.* **2000**, *84*, 951–954.
9. Gong, J. Structure and Surface Chemistry of Gold-Based Model Catalysts. *Chem. Rev.* **2011**, *112*, 2987–3054.
10. Heinz, K.; Hammer, L. Epitaxial Cobalt Oxide Films on Ir(100)—the Importance of Crystallographic Analyses. *J. Phys.: Condens. Matter* **2013**, *25*, 173001.
11. Tröppner, C.; Schmitt, T.; Reuschl, M.; Hammer, L.; Schneider, M. A.; Mittendorfer, F.; Redinger, J.; Podloucky, R.; Weinert, M. Incommensurate Moiré Overlayer with Strong Local Binding: CoO(111) Bilayer on Ir(100). *Phys. Rev. B: Condens. Matter Mater. Phys.* **2012**, *86*, 235407.
12. Ebensperger, C.; Gubo, M.; Meyer, W.; Hammer, L.; Heinz, K. Substrate-Induced Structural Modulation of a CoO(111) Bilayer on Ir(100). *Phys. Rev. B: Condens. Matter Mater. Phys.* **2010**, *81*, 235405.
13. Gragnaniello, L.; Barcaro, G.; Sementa, L.; Allegretti, F.; Parteder, G.; Surnev, S.; Steurer, W.; Fortunelli, A.; Netzer, F. P. The Two-Dimensional Cobalt Oxide (9×2) Phase on Pd(100). *J. Chem. Phys.* **2011**, *134*, 184706–184708.
14. De Santis, M.; Buchsbaum, A.; Varga, P.; Schmid, M. Growth of Ultrathin Cobalt Oxide Films on Pt(111). *Phys. Rev. B: Condens. Matter Mater. Phys.* **2011**, *84*, 125430.
15. Sebastian, I.; Heiler, M.; Meinel, K.; Neddermeyer, H. Growth of Epitaxial Layers of Co and CoO on Au(111). *Appl. Phys. A: Mater. Sci. Process.* **1998**, *66*, S525–S528.
16. Li, M.; Altman, E. I. Cluster-Size Dependent Phase Transition of Co Oxides on Au(111). *Surf. Sci.* **2014**, *619*, L6–L10.
17. Li, M.; Altman, E. I. Shape, Morphology, and Phase Transitions During Co Oxide Growth on Au(111). *J. Phys. Chem. C* **2014**, *118*, 12706–12716.

18. Meyer, W.; Biedermann, K.; Gubo, M.; Hammer, L.; Heinz, K. Surface Structure of Polar Co_3O_4 (111) Films Grown Epitaxially on Ir(100)-(1 × 1). *J. Phys.: Condens. Matter* **2008**, *20*, 265011.
19. Rasmussen, M. K.; Meinander, K.; Besenbacher, F.; Lauritsen, J. V. Noncontact Atomic Force Microscopy Study of the Spinel $MgAl_2O_4$(111) Surface. *Beilstein J. Nanotechnol.* **2012**, *3*, 192–197.
20. Tersoff, J.; Hamann, D. R. Theory of the Scanning Tunneling Microscope. *Phys. Rev. B: Condens. Matter Mater. Phys.* **1985**, *31*, 805–813.
21. Yankowitz, M.; Xue, J.; Cormode, D.; Sanchez-Yamagishi, J. D.; Watanabe, K.; Taniguchi, T.; Jarillo-Herrero, P.; Jacquod, P.; LeRoy, B. J. Emergence of Superlattice Dirac Points in Graphene on Hexagonal Boron Nitride. *Nat. Phys.* **2012**, *8*, 382–386.
22. Sun, Y.-N.; Giordano, L.; Goniakowski, J.; Lewandowski, M.; Qin, Z.-H.; Noguera, C.; Shaikhutdinov, S.; Pacchioni, G.; Freund, H.-J. The Interplay between Structure and Co Oxidation Catalysis on Metal-Supported Ultrathin Oxide Films. *Angew. Chem., Int. Ed.* **2010**, *49*, 4418–4421.
23. Weiss, W.; Ranke, W. Surface Chemistry and Catalysis on Well-Defined Epitaxial Iron-Oxide Layers. *Prog. Surf. Sci.* **2002**, *70*, 1–151.
24. Deng, X.; Yao, K.; Sun, K.; Li, W.-X.; Lee, J.; Matranga, C. Growth of Single- and Bilayer ZnO on Au(111) and Interaction with Copper. *J. Phys. Chem. C* **2013**, *117*, 11211–11218.
25. Risbud, A. S.; Snedeker, L. P.; Elcombe, M. M.; Cheetham, A. K.; Seshadri, R. Wurtzite CoO. *Chem. Mater.* **2005**, *17*, 834–838.
26. Meyer, W.; Hock, D.; Biedermann, K.; Gubo, M.; Müller, S.; Hammer, L.; Heinz, K. Coexistence of Rocksalt and Wurtzite Structure in Nanosized CoO Films. *Phys. Rev. Lett.* **2008**, *101*, 016103.
27. Roy, S.; Meyerheim, H. L.; Mohseni, K.; Tian, Z.; Sander, D.; Hoffmann, M.; Adeagbo, W.; Ernst, A.; Hergert, W.; Felici, R.; *et al.* X-Ray Analysis of Wurtzite-Type CoO(111) Films on Ir(001): Correlation of Structure, Stress, Electronic, and Magnetic Properties. *Phys. Rev. B: Condens. Matter Mater. Phys.* **2014**, *89*, 165428.
28. Zeuthen, H.; Kudernatsch, W.; Peng, G.; Merte, L. R.; Ono, L. K.; Lammich, L.; Bai, Y.; Grabow, L. C.; Mavrikakis, M.; Wendt, S.; *et al.* Structure of Stoichiometric and Oxygen-Rich Ultrathin FeO(111) Films Grown on Pd(111). *J. Phys. Chem. C* **2013**, *117*, 15155–15163.
29. Giordano, L.; Lewandowski, M.; Groot, I. M. N.; Sun, Y. N.; Goniakowski, J.; Noguera, C.; Shaikhutdinov, S.; Pacchioni, G.; Freund, H. J. Oxygen-Induced Transformations of an FeO(111) Film on Pt(111): A Combined DFT and STM Study. *J. Phys. Chem. C* **2010**, *114*, 21504–21509.
30. Kresse, G.; Surnev, S.; Ramsey, M. G.; Netzer, F. P. First-Principles Calculations for V_xO_y Grown on Pd(111). *Surf. Sci.* **2001**, *492*, 329–344.
31. Reuter, K.; Scheffler, M. Composition, Structure, and Stability of RuO_2(110) as a Function of Oxygen Pressure. *Phys. Rev. B: Condens. Matter Mater. Phys.* **2001**, *65*, 035406.
32. Chuang, T. J.; Brundle, C. R.; Rice, D. W. Interpretation of the X-Ray Photoemission Spectra of Cobalt Oxides and Cobalt Oxide Surfaces. *Surf. Sci.* **1976**, *59*, 413–429.
33. Casella, I. G.; Guascito, M. R. Anodic Electrodeposition of Conducting Cobalt Oxyhydroxide Films on a Gold Surface. XPS Study and Electrochemical Behaviour in Neutral and Alkaline Solution. *J. Electroanal. Chem.* **1999**, *476*, 54–63.
34. Morales, F.; de Groot, F. M. F.; Glatzel, P.; Kleimenov, E.; Bluhm, H.; Hävecker, M.; Knop-Gericke, A.; Weckhuysen, B. M. *In Situ* X-Ray Absorption of Co/Mn/TiO_2 Catalysts for Fischer−Tropsch Synthesis. *J. Phys. Chem. B* **2004**, *108*, 16201–16207.
35. Papaefthimiou, V.; Dintzer, T.; Dupuis, V.; Tamion, A.; Tournus, F.; Hillion, A.; Teschner, D.; Hävecker, M.; Knop-Gericke, A.; Schlögl, R.; *et al.* Nontrivial Redox Behavior of Nanosized Cobalt: New Insights from Ambient Pressure X-Ray Photoelectron and Absorption Spectroscopies. *ACS Nano* **2011**, *5*, 2182–2190.
36. Heimann, P.; van der Veen, J. F.; Eastman, D. E. Structure-Dependent Surface Core Level Shifts for the Au(111), (100), and (110) Surfaces. *Solid State Commun.* **1981**, *38*, 595–598.
37. Gubo, M.; Ebensperger, C.; Meyer, W.; Hammer, L.; Heinz, K. Structural Elements in the Oxidation Process of a Single Cobalt Layer on Ir(100)-(1 × 1). *Phys. Rev. B: Condens. Matter Mater. Phys.* **2011**, *83*, 075435.
38. Fu, Q.; Li, W.-X.; Yao, Y.; Liu, H.; Su, H.-Y.; Ma, D.; Gu, X.-K.; Chen, L.; Wang, Z.; Zhang, H.; *et al.* Interface-Confined Ferrous Centers for Catalytic Oxidation. *Science* **2010**, *328*, 1141–1144.
39. Martynova, Y.; Shaikhutdinov, S.; Freund, H.-J. Co Oxidation on Metal-Supported Ultrathin Oxide Films: What Makes Them Active? *ChemCatChem* **2013**, *5*, 2162–2166.
40. Walton, A. S.; Lauritsen, J. V.; Topsøe, H.; Besenbacher, F. MoS_2 Nanoparticle Morphologies in Hydrodesulfurization Catalysis Studied by Scanning Tunneling Microscopy. *J. Catal.* **2013**, *308*, 306–318.
41. Nyholm, R.; Andersen, J. N.; Johansson, U.; Jensen, B. N.; Lindau, I. Beamline I311 at Max-Lab: A VUV/Soft X-Ray Undulator Beamline for High Resolution Electron Spectroscopy. *Nucl. Instrum. Methods Phys. Res., Sect. A* **2001**, *467−468*, 520–524.
42. Kresse, G.; Furthmüller, J. Efficiency of *Ab-Initio* Total Energy Calculations for Metals and Semiconductors Using a Plane-Wave Basis Set. *Comput. Mater. Sci.* **1996**, *6*, 15–50.
43. Kresse, G.; Hafner, J. *Ab Initio* Molecular Dynamics for Liquid Metals. *Phys. Rev. B: Condens. Matter Mater. Phys.* **1993**, *47*, 558–561.
44. Kresse, G.; Joubert, D. From Ultrasoft Pseudopotentials to the Projector Augmented-Wave Method. *Phys. Rev. B: Condens. Matter Mater. Phys.* **1999**, *59*, 1758–1775.
45. Perdew, J. P.; Burke, K.; Ernzerhof, M. Generalized Gradient Approximation Made Simple. *Phys. Rev. Lett.* **1996**, *77*, 3865–3868.
46. Dudarev, S. L.; Botton, G. A.; Savrasov, S. Y.; Humphreys, C. J.; Sutton, A. P. Electron-Energy-Loss Spectra and the Structural Stability of Nickel Oxide: An LSDA+U Study. *Phys. Rev. B: Condens. Matter Mater. Phys.* **1998**, *57*, 1505–1509.
47. Ebensperger, C.; Meyer, B. First-Principles Study of the Reconstruction and Hydroxylation of the Polar NiO(111) Surface. *Phys. Status Solidi B* **2011**, *248*, 2229–2241.

Printed by Media-Tryck, Lund University 2017 | Nordic Ecolabel 3041 0903

Mohammad Alif Arman was born in 1984 in Nilphamari, Bangladesh. He completed his Bachelor of Science (B.Sc.) degree from American International University - Bangladesh in 2006. After completing his B.Sc. degree in Electrical and Electronic Engineering (EEE) he continued his master studies at Lund University. For his master project he performed research under the supervision of Dr. Jan Knudsen and Prof. Jesper N. Andersen and studied the chemistry of graphene.

In July 2012, he was selected as a PhD student for a project under supervision of Dr. Jan Knudsen and Prof. Edvin Lundgren. His PhD project has been focused on obtaining a profound knowledge of the catalytic properties of Cobalt oxide surfaces. In addition, to his own PhD project he also been involved research projects focused on graphene chemistry and iron oxide film chemistry. He performed numerous experiments in particular at the MAX IV laboratory and at the other synchrotron facilities around the world. He also acted as a local contact for guiding other PhD students or researchers through the working of complex instruments and research.

LUND UNIVERSITY
Faculty of Science
Deptartment of Physics
ISBN 978-91-7753-140-1 (print)
978-91-7753-141-8 (pdf)